

NON-INTRUSIVE EXPERIMENTAL INVESTIGATION OF MULTI-SCALE FLOW
BEHAVIOR IN ROD BUNDLE WITH SPACER-GRIDS

A Dissertation

by

ELVIS EFREN DOMINGUEZ ONTIVEROS

Submitted to the Office of Graduate Studies of
Texas A&M University
in partial fulfillment of the requirements for the degree of

DOCTOR OF PHILOSOPHY

May 2010

Major Subject: Mechanical Engineering

NON-INTRUSIVE EXPERIMENTAL INVESTIGATION OF MULTI-SCALE FLOW
BEHAVIOR IN ROD BUNDLE WITH SPACER-GRIDS

A Dissertation

by

ELVIS EFREN DOMINGUEZ ONTIVEROS

Submitted to the Office of Graduate Studies of
Texas A&M University
in partial fulfillment of the requirements for the degree of

DOCTOR OF PHILOSOPHY

Approved by:

Chair of Committee,	Yassin A. Hassan
Committee Members,	Kalyan Annamalai
	William Marlow
	Victor Ugaz
Head of Department,	Dennis L. O'Neal

May 2010

Major Subject: Mechanical Engineering

ABSTRACT

Non-Intrusive Experimental Investigation of Multi-Scale Flow Behavior
in Rod Bundle With Spacer-Grids. (May 2010)

Elvis Efren Dominguez Ontiveros, B.S., Instituto Politecnico Nacional, Mexico City,
Mexico; M.S., Texas A&M University

Chair of Advisory Committee: Dr. Yassin A. Hassan

Experiments investigating complex flows in rod bundles with spacer grids that have mixing devices (such as flow mixing vanes) have mostly been performed using single-point measurements. Although these measurements allow local comparisons of experimental and numerical data they provide little insight because the discrepancies can be due to the integrated effects of many complex flow phenomena such as wake-wake, wake-vane, and vane-boundary layer interactions occurring simultaneously in a complex flow environment. In order to validate the simulations results, detailed comparison with experimental data must be done.

This work describes an experimental database obtained using Time Resolved Particle Image Velocimetry (TR-PIV) measurements within a 5 x 5 rod bundle with spacer-grids. Measurements were performed using two different grid designs. One typical of Boiling Water Reactors (BWR) with swirl type mixing vanes and the other typical of Pressurized Water Reactors (PWR) with split type mixing vanes. High quality data was obtained in the vicinity of the grid using the multi-scale approach. One of the unique characteristic of this set-up is the use of the Matched Index of Refraction (MIR) technique employed in this investigation. This approach allows the use of high temporal

and spatial non-intrusive dynamic measurement techniques to investigate the flow evolution below and immediately above the spacer. The experimental data presented includes explanation of the various cases tested such as test rig dimensions, measurement zones, the test equipment and the boundary conditions in order to provide appropriate data for comparison with Computational Fluid Dynamics (CFD) simulations. Turbulence parameters of the obtained data are analyzed in order to gain insight of the physical phenomena. The shape of the velocity profile at various distances from the spacer show important modifications passing the grid which delineates the significant effects of the presence of the grid spacer. Influence of the vanes wake in the global velocity was quantified to be up to a distance of 4 hydraulic diameters from the edge of the grid. Spatial and temporal correlations in the two measured dimensions were performed to quantify the time and length scales present in the flow in the vicinity of the grids and its influence in the flow modification induced by the vanes. Detection of vortex cores was performed using the vorticity, swirl strength and Galilean decomposition approach. The resulted cores were then tracked in time, in order to observe the evolution of the structures under the influence of the vanes for each grid. Vortex stretching was quantified in order to gain insight of the energy dissipation process normally associated with the phenomena. This work presents data in a single-phase flow situation and an analysis of these data for understanding complex flow structure. This data provide for the first time detailed temporal velocity full field which can be used to validate CFD codes.

ACKNOWLEDGMENTS

I wish to express my gratitude to my advisor, committee chair, Dr. Yassin A. Hassan for his guidance, patience, enthusiasm, knowledge and time throughout this entire project. I would also like to thank the committee members, Dr. Kalyan Annamalai, Dr. William Marlow and Dr. Victor Ugaz for their assistance and patience. Special thanks to Mr. Aaron Markwardt who helped me during the preparation of this manuscript and plotting process, Mr. Ramiro Martinez for his guidance and precise words of advice, Mr. Carlos Ortiz, Mr. Carlos Estrada-Perez and my fellow graduate students for their professional help.

NOMENCLATURE

A	Quantity being averaged
b	Point where the correlation coefficient becomes zero
$\underline{\underline{D}}^{2-D}$	Two dimensional form of the velocity tensor
dP	Pressure drop
f	Fraction of the mean velocity
g	Acceleration due to gravity
D_h	Hydraulic diameter
L_{ij}	Integral length scale
N	Total number of realizations
N_T	Number of velocity fields
P	Pressure
Q_w	water flow rate
$R(s)$	Autocorrelation of $I(X)$
Re	Reynolds number
Re_d	Reynolds number based on hydraulic diameter
$R_{ij}(\Delta r)$	Two-point correlation coefficient
$R_{ij}(\Delta t)$	Autocorrelation coefficient
S_{ij}	Average rate of strain
s_{ij}	Fluctuating rate of strain
t_τ	Viscous time scale
T_L	Integral time scale

U	Bulk velocity
u	Instantaneous streamwise velocity
U	Average or mean velocity
u'	Streamwise fluctuating velocity component
u'	Streamwise velocity fluctuation
u'_s	Fluctuating velocity from spatial decomposition
U_b	Bulk velocity
u_c	Velocity deviation
U_c	convection velocity
U_e	velocity at the free stream [m/s]
u_{rms}	Streamwise turbulence intensity
U_s	Mean velocity obtained by spatial averaging
$-\overline{u'v'}$	Reynolds stresses
v'	Normal fluctuating velocity component
V_l	Liquid volume
v_{rms}	Normal turbulence intensity
x	Distance
\overline{X}	Position vector
x_j	Spatial coordinate in the jth direction
Greek letters	
ω	Vorticity

ν	Kinematic viscosity
λ	Eigen value
σ	Surface tension
κ	Kármán constant
δ_{99}	Boundary layer thickness
λ_{ci}	Swirling strength
Superscript	
$'$	Fluctuation
$-$	Average or mean
Subscript	
i	Component
j	Component
l	Liquid
z	Spanwise direction

TABLE OF CONTENTS

	Page
ABSTRACT.....	iii
ACKNOWLEDGMENTS.....	v
NOMENCLATURE.....	vi
TABLE OF CONTENTS.....	ix
LIST OF FIGURES.....	xii
LIST OF TABLES.....	xxi
CHAPTER	
I INTRODUCTION.....	1
1.1 Motivation.....	1
1.2 Previous Works.....	2
II EXPERIMENTAL SET UP AND TECHNIQUES.....	17
2.1 Channel Flow Facility.....	17
2.2 Aluminum Frame.....	22
2.3 U-Channel.....	28
2.4 Particle Tracking Velocimetry and Optical System.....	33
2.5 Data Acquisition System.....	36
2.6 Fluorescent Particles.....	37
2.7 Matching Refractive Index.....	40
2.7.1 MRI Experiments.....	47
2.7.2 FEP Experiments.....	51
2.8 Pressure System.....	58
2.8.1 Photographic Pressure Fluctuations Evaluation Method.....	61
2.9 Bundle Array and Grids.....	68
2.9.1 Grid 1.....	68
2.9.2 Grid 2.....	76

CHAPTER	Page
III DATA ANALYSIS.....	81
3.1 Background.....	81
3.1.1 Equations of Motion.....	82
3.2 Statistics.....	83
3.2.1 Turbulence Intensities and Reynolds Shear Stress.....	85
3.2.2 Correlation Coefficients.....	86
3.2.2.1 Two-point Correlation Coefficients.....	86
3.2.2.2 Autocorrelation Coefficient.....	87
3.2.2.3 Two-dimensional Two-point Correlation Coefficients.....	88
3.2.3 Vorticity.....	89
3.2.4 Rate of Strain.....	90
3.3 Visualization Techniques.....	91
3.3.1 Modified Reynolds Decomposition.....	91
3.3.2 Spatial Decomposition.....	92
3.3.3 Vortex Identification.....	93
IV ROD BUNDLE ARRAY WITH SPACER-GRIDS RESULTS AND DISCUSSION.....	95
4.1 Grid 1.....	95
4.1.1 Interchannel Scale.....	99
4.1.2 Sub-channel Scale.....	116
4.1.3 Micro-Scale.....	137
4.2 Grid 2.....	141
4.2.1 Inter-channel Scale.....	145
4.2.2 Sub-channel Scale.....	171
3.3.3 Vortex Identification.....	93
V CONLCUSIONS.....	206
5.1 Grid 1.....	206
5.2 Grid 2.....	208
REFERENCES.....	210
APPENDIX A	215
APPENDIX B.....	224

	Page
APPENDIX C.....	234
VITA.....	259

LIST OF FIGURES

	Page
Figure 1. Hydraulic loop.	18
Figure 2. Reservoir tank, pump, and filtering system.	19
Figure 3. Variable frequency pump controller.	19
Figure 4. Insertion propellor type flow meter.	20
Figure 5. Air mixing chamber.	21
Figure 6. Test section, (a) top view, (b) isometric view, (c) real frame picture.	25
Figure 7. Flow straightener (a) CAD drawing, (b) Position inside aluminum frame.	26
Figure 8. Aluminum frame interior with flow straightener.	27
Figure 9. Perspective view with respect to channel's inlet.	27
Figure 10. Exploded view of aluminum frame, U-shaped channel and front observation window.	29
Figure 11. U-shaped polycarbonate channel inside aluminum frame (a) picture (b) top view schematic.	30
Figure 12. Aluminum frame with two internal polycarbonate sheets and grids.	31
Figure 13. Grid with rods and square channel.	32
Figure 14. Optical system and location with respect to test section.	35
Figure 15. Image acquisition time chart.	38
Figure 16. Tracer particles for PIV with average diameter of 10 μm . (a) Polystyrene particles before coating (powder) (b) Polystyrene particles after coating process (solution).	40
Figure 17. Refractive index matching experiments. (a) target (b) Petri dish with PMMA beads and air (c) Petri dish with PMMA beads and water and (d) Petri dish with PMMA beads and NaI.	40

Figure 18. Refractive index matching for (a) p-cymene (b) isopropyl alcohol and diethyl phthalate (c) ethanol and methylnaphthalene and (d) ethanol and benzyl alcohol.....	40
Figure 19. Refractive index matching experiment using an FEP tube in water.	53
Figure 20. A 5x5 spacer grid segment filled with FEP tubes emulating a fuel-bundle. (a) Pipes immersed in water (b) Pipes immersed in air.	54
Figure 21. Pictorial of the achieved transparency in the facility.	55
Figure 22. Rods of varying materials immersed in water. The camera setting are modified (white balance: incandescent, ISO:400, Exposure:Auto, Manual focus).	56
Figure 23. Matched index of refraction inside the channel.	57
Figure 24. Laser sheet passing across the rod bundle without distortion due to a good matching index of refraction.	58
Figure 25. Pressure transducer model PDCR 4020.	59
Figure 26. Wall pressure tap flushed in the back observation window.	60
Figure 27. Pressure transducer location.	62
Figure 28. Sketch of the meniscus formed at the selected tube.	64
Figure 29. Example of the meniscus formed inside the pipe and the image template	67
Figure 30. AREVA's Ultraflow™ spacer design.	69
Figure 31. Subsection of Ultraflow used for experimentation (a) Picture of the subsection (b) CAD of the subsection.	70
Figure 32. Experimental rod bundle assembly.	70
Figure 33. Plastic rod with end caps (a) Aluminum coned cap (b) Rod with end caps.....	71
Figure 34. Spacers with rods.....	72
Figure 35. Aluminum frame with two internal polycarbonate sheets and grids.	73

Figure 36. Rod bundle with spacer grid 1 and channel envelope dimensions.	74
Figure 37. Channel mounted on base frame (a) General view (b) Close-up measurement zone.	75
Figure 38. 5x5 subsection of the second grid used for experimentation (generic Westinghouse) (a) Isometric view (b) Top view.	77
Figure 39. Spacer grid distance.	78
Figure 40. Rod bundle with spacer grid 2 and channel envelope dimensions.	79
Figure 41. Measured planes for grid 1.	96
Figure 42. Multi-scale approach.	98
Figure 43. Macroscale measurement viewing areas (all channel) for test grid 1.	100
Figure 44. Average streamwise component of the velocity vector (U) for the three positions measured in the inter-channel scale, Plane C, Re=15000.	102
Figure 45. Average normal component of the velocity vector (V) for the three positions measured in the inter-channel scale, Plane C, Re=15000.	104
Figure 46. Average streamwise component of the velocity vector (U) for the three positions measured in the inter-channel scale, Plane B2, Re=15000.	106
Figure 47. Average normal component of the velocity vector (V) for the three positions measured in the inter-channel scale, Plane B2, Re=15000.	107
Figure 48. Averaged streamwise component (U) velocity profile for the three measured postions at the interchannel scale, Plane C , Re=15000.	109
Figure 49. Averaged normal component (V) velocity profile for the three measured postions at the interchannel scale, Plane C , Re=15000.	110
Figure 50. Averaged turbulence intensity for the stramwise component (u_{rms}) for the three measured postions at the interchannel scale, Plane C , Re=15000.	111

Figure 51. Averaged turbulence intensity for the normal component (v_{rms}) for the three measured postions at the interchannel scale, Plane C , Re=15000.....	112
Figure 52. Averaged Reynolds stress ($u'v'$) for the three measured postions at the interchannel scale, Plane C , Re=15000.....	113
Figure 53. Averaged streamwise component (U) velocity profile for the three measured postions at the interchannel scale, Plane B2 , Re=15000.	114
Figure 54. Averaged normal component (V) velocity profile for the three measured postions at the interchannel scale, Plane B2 , Re=15000.	114
Figure 55. Averaged turbulence intensity for the stramwise component (u_{rms}) for the three measured postions at the interchannel scale, Plane B2 , Re=15000.....	115
Figure 56. Averaged turbulence intensity for the normal component (v_{rms}) for the three measured postions at the interchannel scale, Plane B2 , Re=15000.....	115
Figure 57. Averaged Reynolds stress ($u'v'$) for the three measured postions at the interchannel scale, Plane B2 , Re=15000.....	116
Figure 58. Sub-channel scale measurement viewing areas (zoom) for test grid 1.....	118
Figure 59. Average streamwise component of the velocity vector (U) for the three positions measured in the sub-channel scale, Plane C, Re=15000.....	120
Figure 60. Average normal component of the velocity vector (V) for the three positions measured in the sub-channel scale, Plane C, Re=15000.	121
Figure 61. Typical instantaneous velocity field for subchannel scale. Positions BGP1 and AGP1, plane C, Re= 6400.	123
Figure 62. Averaged velocity field with overlapped streamlines for subchannel scale . Positions BGP1 and AGP1, plane C, Re= 6400.	124
Figure 63. Averaged velocity field for subchannel scale . Positions BGP1 and AGP1, plane C, Re= 6400.....	125

Figure 64. Typical instantaneous velocity field for subchannel scale. Positions BGP1 and AGP1, plane B2, Re= 6400.	127
Figure 65. Averaged velocity field for subchannel scale . Positions BGP1 and AGP1, planeB2, Re= 6400.....	128
Figure 66. Averaged velocity field with overlapped streamlines for subchannel scale . Positions BGP1 and AGP1, plane B2, Re= 6400.	129
Figure 67. Averaged streamwise component (U) velocity profile for subchannel scale, positions BGP1 (down) and AGP1 (up), Plane C , Re=3250 (q20), Re= 9700 (q60) and Re=15000 (q90).....	129
Figure 68. Averaged normal component (V) velocity profile for subchannel scale, positions BGP1 (down) and AGP1 (up), Plane C , Re=3250 (q20), Re= 9700 (q60) and Re=15000 (q90).	133
Figure 69. Averaged turbulence intensity for the streamwise component (u_{rms}) velocity profile for subchannel scale, positions BGP1 (down) and AGP1 (up), Plane C , Re=3250 (q20), Re= 9700 (q60) and Re=15000 (q90).	134
Figure 70. Averaged turbulence intensity for the normal component (v_{rms}) velocity profile for subchannel scale, positions BGP1 (down) and AGP1 (up), Plane C , Re=3250 (q20), Re= 9700 (q60) and Re=15000 (q90).	135
Figure 71. Averaged Reynolds stress ($u'v'$) for subchannel scale, positions BGP1 (down) and AGP1 (up), Plane C , Re=3250 (q20), Re= 9700 (q60) and Re=15000 (q90).	136
Figure 72. Micro scale viewing area	138
Figure 73. Typical instantaneous velocity field for micro scale. Positions BGP1 (down)and AGP1 (up), plane C, Re= 6400.	139
Figure 74. Typical instantaneous velocity field with overlapped streamlines for micro scale. Positions BGP1 (down) and AGP1 (up), plane C, Re= 6400.	140
Figure 75. Location of the various 2D PIV measurement planes.	142
Figure 76. Side view of test section showing position of measurement planes.	144

Figure 77. Equivalent viewing area #1 (all channel).	146
Figure 78. Typical PIV image for equivalent viewing area #1 (all channel).	148
Figure 79. Average velocity fields before and after grid. Color code represents streamwise component of velocity vector (U) with red color = 2500 mm/s dark blue = 0 mm/s. Re= 16300.	150
Figure 80. Average velocity fields and overlapped streamtraces for the downstream grid case. Color code represents streamwise component of velocity vector (U) with red color = 2500 mm/s dark blue = 0 mm/s. Re= 16300.	152
Figure 81. Average velocity fields and overlapped streamtraces for the upstream grid case. Color code represents streamwise component of velocity vector (U) with red color = 2500 mm/s dark blue = 0 mm/s. Re= 16300.	153
Figure 82. Average velocity fields and overlapped streamtraces for the upstream grid case. Color code represents spanwise component of velocity vector (V) with red color = -200 mm/s dark blue = 200 mm/s. Re= 16300.	155
Figure 83. Average velocity fields and overlapped streamtraces for the downstream grid case. Color code represents spanwise component of velocity vector (V) with red color = -200 mm/s dark blue = 200 mm/s. Re= 16300.	156
Figure 84. Averaged streamwise component of the velocity vector (U) for the A, B, and C, D planes downstream and upstream the grid. Re= 16300.	158
Figure 85. Averaged streamwise component of the velocity vector (U) for the A1, B1, C1, D1, Bypass planes downstream and upstream the grid. Re= 16300.	159
Figure 86. Averaged spanwise component of the velocity vector (V) for the A, B, and C, D planes downstream and upstream the grid. Re= 16300.	161
Figure 87. Averaged spanwise component of the velocity vector (V) for the A1, B1, C1, D1, Bypass planes downstream and upstream the grid. Re= 16300.	162

Figure 88. Averaged turbulence intensities for the streamwise component of the velocity vector (u') for the A, B, and C, D planes downstream and upstream the grid. $Re = 16300$	164
Figure 89. Averaged turbulence intensities for the streamwise component of the velocity vector (u') for the A1, B1, C1, D1, Bypass planes downstream and upstream the grid. $Re = 16300$	165
Figure 90. Averaged turbulence intensities for the spanwise component of the velocity vector (v') for the A, B, and C, D planes downstream and upstream the grid. $Re = 16300$	166
Figure 91. Averaged turbulence intensities for the spanwise component of the velocity vector (v') for the A1, B1, C1, D1, Bypass planes downstream and upstream the grid. $Re = 16300$	167
Figure 92. Averaged Reynolds stresses ($u'v'$) for the A, B, C, D planes downstream and upstream the grid. $Re = 16300$	169
Figure 93. Averaged Reynolds stresses ($u'v'$) for the A1, B1, C1, D1, Bypass planes downstream and upstream the grid. $Re = 16300$	170
Figure 94. Equivalent viewing area #2 (sub-channel scale) for positions BGP1 (down) and AGP1 (up).	172
Figure 95. Typical PIV image for equivalent viewing area #1 (zoom) for positions BGP1 (down) and AGP1 (up).	174
Figure 96. Average velocity fields before and after grid for the sub-channel scale cases. Color code represents streamwise component of velocity vector (U) with red color = 2500 mm/s dark blue = 0 mm/s. $Re = 16300$	175
Figure 97. Average velocity fields and overlapped streamtraces for the downstream grid sub-channel scale case. Color code represents streamwise component of velocity vector (U) with red color = 2500 mm/s dark blue = 0 mm/s. $Re = 16300$	177
Figure 98. Average velocity fields and overlapped streamtraces for the upstream grid sub-channel scale case. Color code represents streamwise component of velocity vector (U) with red color = 2500 mm/s dark blue = 0 mm/s. $Re = 16300$	178

Figure 99. Average velocity fields and overlapped streamtraces for the downstream grid sub-channel scale case. Color code represents spanwise component of velocity vector (V) with red color = 2500 mm/s dark blue = 0 mm/s. $Re = 16300$	179
Figure 100. Average velocity fields and overlapped streamtraces for the upstream grid sub-channel scale case. Color code represents spanwise component of velocity vector (V) with red color = 2500 mm/s dark blue = 0 mm/s. $Re = 16300$	180
Figure 101. Averaged streamwise component of the velocity vector (U) for the A, B, C, D (sub-channel scale) planes downstream and upstream the grid. $Re = 16300$	182
Figure 102. Averaged streamwise component of the velocity vector (U) for the A1, B1, C1, D1, Bypass (sub-channel scale) planes downstream and upstream the grid. $Re = 16300$	183
Figure 103. Averaged spanwise component of the velocity vector (V) for the A, B, C, D (sub-channel scale) planes downstream and upstream the grid. $Re = 16300$	184
Figure 104. Averaged spanwise component of the velocity vector (V) for the A1, B1, C1, D1, Bypass (sub-channel scale) planes downstream and upstream the grid. $Re = 16300$	185
Figure 105. Averaged turbulence intensities for the streamwise component of the velocity vector (u') for the A, B, C, D (sub-channel scale) plane downstream and upstream the grid. $Re = 16300$	187
Figure 106. Averaged turbulence intensities for the streamwise component of the velocity vector (u') for the A1, B1, C1, D1, Bypass (sub-channel scale) plane downstream and upstream the grid. $Re = 16300$	188
Figure 107. Averaged turbulence intensities for the spanwise component of the velocity vector (v') for the A, B, C, D (sub-channel scale) plane downstream and upstream the grid. $Re = 16300$	189
Figure 108. Averaged turbulence intensities for the spanwise component of the velocity vector (v') for the A1, B1, C1, D1, Bypass (sub-channel scale) plane downstream and upstream the grid. $Re = 16300$	190

Figure 109. Averaged Reynolds stresses ($u'v'$) for the A, B, C, D (sub-channel scale) planes downstream and upstream the grid. $Re = 16300$	192
Figure 110. Averaged Reynolds stresses ($u'v'$) for the A1, B1, C1, D1, Bypass (sub-channel scale) planes downstream and upstream the grid. $Re = 16300$	193
Figure 111. Average strain rate for sub-channel scale , plane B1.	195
Figure 112. Average strain rate for sub-channel scale , plane C.	196
Figure 113. Swirl strength sub-channel scale, plane B1.	198
Figure 114. Swirl strength for sub-channel scale , plane C.	199
Figure 115. R_{uu} correlation for sub-channel scale, plane B1.	201
Figure 116. R_{vv} correlation for sub-channel scale, plane B1.	202
Figure 117. R_{uu} correlation for sub-channel scale, plane C.....	203
Figure 118. R_{vv} correlation for sub-channel scale, plane C.....	204

LIST OF TABLES

	Page
Table 1 Main physical properties of Zelux polycarbonate	23
Table 2 Refractive index for solids	43
Table 3 Possible matching refractive index fluids and their properties	44
Table 4 Measurements of areas with high 2D correlation for sub-channel scale.	205

CHAPTER I

INTRODUCTION

1.1 Motivation

The core of a Light Water Reactor (LWR) is formed by cylindrical rods of about 3.5 m long and diameter in the 0.010 m range. The rods contain Uranium pellets which generate energy by fission of the uranium fuel. In practical terms, the cylindrical rods are thermal energy sources whose energy is utilized to produce electricity. In order to have a controlled chain reaction, the LWR's use thousands of cylindrical rods arranged in a specific geometry. The location of the rods is achieved by the use of spacers which place the rods at a desired distance from each other and provide structural rigidity to the core. Water is used as coolant for this kind of reactor. The water flows around the cylindrical rods and removes the energy released during the nuclear reaction occurring inside the fuel. The water increases its enthalpy and this change is utilized to produce electricity by using a turbine.

It can be imagined that a good part of the reactor performance depends on the physics occurring in the heat removal process. This process involves solving two main problems: the hydraulic part and heat transfer part. The first takes care of the flow characteristics and distribution in the geometry specified. The second quantifies the

amount of energy that is taken away from the rod surface and being carried by the fluid. The spacer grids used in the core design greatly affect the flow distribution between the rods. Therefore the whole energy production system is modified by these devices. There are different designs of spacer-grids in the current nuclear reactors. The design of each of the former represents a great investment from the designing team and it directly affects the final performance of the reactor system. Improvements in the performance of specific spacer-grids may increase the power operation of existing LWR's which may signify economical benefits for the utilities. In addition, the study of the detailed physics caused by a specific grid design may improve the current mathematical models that simulate the core behavior under specific circumstances.

1.2 Previous Works

Fluid flow around circular cylinders is one of the classical problems of fluid mechanics and has been well studied because of its common occurrence in many forms and in different applications. Cylinder-like structures can be found both alone and in groups in the designs for heat exchangers, cooling systems for nuclear power plants, offshore structures, power lines, struts, grids, screens, and cables, in both single and multi-phase flows. A complete understanding of the fluid dynamics for the flow around a circular cylinder includes such fundamental subjects as the boundary layer, separation, the free shear layer, the wake, and the dynamics of vortices. The flow fields of multiple-cylinder configurations involve complex interactions between the shear layers, vortices and Karman vortex streets (Zdravkovich 1987). The problem is further complicated by

the large number of configurations encountered in practice, resulting in different flow patterns, and by the effect of their interactions.

One of the applications of paramount importance in this study is fluid flow in fuel rod bundles of Light Water Reactors (LWR). In this type of nuclear reactor, optimum heat removal from the surface of fuel elements is the subject of many studies for researchers in order to determine reactor thermal margin and safety. In this case, the spacer grids which support the fuel assembly are used as an effective mixing device by attaching various types of flow deflectors. Several recent works focused on the development of numerical simulations that predict the complex behavior of fluid flow close to grid spacers and between fuel assemblies.

However, the validity of the produced results from Computational Fluid Dynamics (CFD) is still under scrutiny for several cases in real world conditions. Moreover, the existing models for multiphase flows produce results that are generally recognized as unreliable. Development of better models for multiphase simulation requires an improved understanding of the evolution of the flow with dynamic interaction of the flow multi-scales. Therefore, experimental data is urgently needed for validation of the models.

Channels of various complex forms are widely used in nuclear reactors, steam generators, and heat exchangers. The heat transfer in such channels depends considerably on the velocity distribution of the heat carrier over the flow cross section. There have been widespread experimental studies of the hydrodynamics of complex channels, but it is a very laborious matter to study all the channels found in practice. There is thus a great

need for developing a database to benchmark CFD on the basis of physical laws emerging from the analysis of existent experimental data.

The analysis of the physics underlying the flow in rod bundles has been intensively studied in an effort to develop better predictions of the basic physics observed in the former configuration. Most of the known experimental studies of the fluid dynamics in packs of rods were carried out in order to obtain data on coefficients of friction. Only some isolated investigations were devoted to the measurement of local characteristics of the flow. Overestimated values of the coefficients of friction and limited information on the velocity distribution made it difficult to use these data in practice. A brief historic description of the experimental and computational works regarding flow in rod bundles is presented in the following sections.

In 1959, the primary concern of the thermal hydraulic reactor designer was with the fully turbulent region in rod bundles at Reynolds numbers above 25000. This concern arose from the need to obtain faithful friction factors in a rod configuration. The heat transfer to water flowing parallel to tube bundles was investigated experimentally in square and triangular lattices without spacer grids by Weisman. Colburn equation (dimensionless heat-transfer equation to calculate the natural convection movement of heat from vertical surfaces or horizontal cylinders to fluids flowing past these surfaces) was compared against experimental data. The author concluded that lower fluid velocities can be used to obtain high heat transfer coefficients for the cases studied but no explanation about the phenomena was presented. Ibragimov (1966) proposed a method for calculating tangential wall stresses, velocity fields, and hydraulic resistances in straight, smooth channels with cross sections of various shapes. The calculations were

valid for hydrodynamically stabilized flow of liquid in a developed turbulent condition ($Re > 10^4$). The results of the stress calculations were used to find coefficients of turbulent heat transfer required for solving problems connected with the determination of temperature fields and heat transfer coefficients. The information of structure and scale of turbulent eddies in complex channels allowed the establishment of the tangential stress as a function of distance from the wall. The variation of tangential stress over the perimeter of a complex channel was closely connected with the transfer of momentum along the perimeter in the Z axis. Nijsing (1966) presented a simple model for the description of fluid flow and heat transfer in a non-circular channel like that presented by the triangular array of parallel rods. The main objective of the study was to gain information regarding convective heat transfer in a bundle of parallel heating rods for conditions of turbulent flow and fluids having a Prandtl number larger than 1. Analysis of the flow was aimed to provide velocity distributions to be used for the heat transfer calculations.

Eifler and Nijsing (1967) described the determination of velocity distribution and flow resistance for fully developed flow parallel to triangular array of rods. The effects of Reynolds number and rod spacing were investigated. The results obtained agree satisfactorily with theoretical predictions.

Velocity measurements were done using a test probe in combination with a manometer. Injection needles were used as the test probes. Investigations were carried out mainly to obtain the velocity distribution normal to the rod surface. Skinner (1969) studied transverse temperature differences in a coolant flowing axially along a rod cluster. He concluded that tube bundle heat transfer was reduced by diffusion of heat from one sub-channel to another through the gaps between the rods or tubes. This process

called mixing for convenience was studied experimentally using a mass transfer analogy. Mixing rates were found to be greater than can be explained by turbulent diffusion theory. They were attributed to the action of secondary velocities. The results were used to predict the extent to which mixing reduced temperature differences within fuel clusters of advanced gas-cooled reactors. Pitot probes were used to measure velocity at pre-determined locations inside the bundle array. The probes were transverse in order to obtain flow distributions based on the assumption of using a truly isokinetic sampling technique (with no azimuthal or radial deflection of the flow before it was sampled). In order to measure secondary flow a mix of Nitrous Oxide was used. The concentrations of the nitrous oxide-air mix gave the velocity at the test probe.

The heat transfer characteristics of non-concentric annuli with various eccentricities and of a seven-rod cluster were experimentally determined by means of mass transfer technique (Tachibana *et al.* 1969). A coating of naphthalene was applied to the surface of the test rod and changes in its thickness were measured. The mass transfer coefficient was represented in terms of Colburn's j-factor with which both the average and local values were analyzed. The existence of secondary flow in the seven-rod cluster was also discussed for a pitch to diameter ratio (P/D) of 1.125. The length of the test section was 15 times the equivalent channel diameter.

This work showed a correlation for the entrance effect given by:

$$\frac{L}{D} = 0.693 Re^{\frac{1}{4}}$$

The authors mentioned the possibility of including turbulence promoters or swirl generators in high power density reactor fuel assemblies. They found that local heat transfer characteristics were more complex than expected, although a clear periodicity

was observed in the circumferential variation. The anisotropy of turbulence caused these former variations and the secondary flow caused the circumferential variations in heat transfer coefficients.

Single-phase liquid energy-exchange experiments were carried out in a four rod cluster by Van Der Ros (1970). The amount of flow mixing was determined by measuring enthalpy increase. The data was analyzed by using the eddy diffusivity approach. By means of the Prandtl mixing length theory an analytical explanation was obtained for the fact that the mixing coefficient was roughly inversely proportional to the gap width. The authors attributed this effect to the fact that the velocity gradient in the gap, a mixing promoter, was about inversely proportional to the gap width. In an effort to clarify the phenomena at hand, Levchenko et al. (1972) studied the local tangential stresses experimentally in a triangular rod array. The hypothesis of approximated universal character of the velocity profiles along the normals to the walls of channels with sufficiently small curvature of the perimeter was experimentally sustained. This hypothesis is widely used in computational –theoretical investigations. The coefficients of friction of the channels, computed from the measured pressure gradient along the channels and the tangential stresses at the wall, coincided.

Rowe (1973) focused on the effect of flow channel geometry on fully developed turbulent flow in clean rod bundle flow channels. Axial components of the velocity, turbulence intensity and eulerian autocorrelation function were the primary measurements used in order to understand cross flow mixing between rod sub channels with Reynolds number range from 50000 to 200000. Autocorrelation function provided an indication of the dominant frequency of turbulence and an estimate of the longitudinal

macro-scale by using Taylor's hypothesis. Experiments were done with pitch-to-diameter ratios of 1.25 and 1.125. Decreasing the rod gap spacing increased the turbulence intensity, longitudinal macro-scale, and the dominant frequency of turbulence. These turbulence parameters were found to be rather insensitive to Reynolds number. The turbulence parameters within a rod gap were found to be insensitive to the shape of adjacent sub-channels and only slightly affected by the amount of lateral freedom allowed by the various size flow models. The results indicate that macroscopic flow processes existed adjacent to the rod gap. This included secondary flows and increased scale and frequency pulsations when the rod gap spacing is reduced.

Carajilescov and Todreas (1976) developed a one-equation statistical model of turbulence to compute the detailed description of velocity field (axial and secondary flows) and the wall shear stress distribution of steady, fully developed turbulent flows within triangular arrays of rods with different aspect ratios. Furthermore, experimental measurements of the distributions of the axial velocity, turbulent kinetic energy, and Reynolds stresses were performed using LDA. From the experimental results a new mixing length distribution was proposed. The statistical model for turbulence was able to reasonably predict the axial velocity, wall shear stress, eddy diffusivity distribution and friction factor for rod bundle sub-channels. The experimental investigation presented evidence of two swirls of secondary flows for a triangular array of rods that agreed with analytic predictions of the test geometry utilized.

Tapucu and Merilo (1977) performed experimental work of axial pressure variations of two parallel channels with single phase flows communicating by a long lateral slot. Using mass and momentum conservation principles, the axial pressure

variations were derived. A pressure difference oscillation between channels along the slot was detected having a sinusoidal form with wave lengths depending on the gap clearance. Flow visualization allowed observation of particle flow paths in the slot region. The pattern showed was of sinusoidal shape which was similar to the results obtained in the present investigation. The authors reported that the oscillations came from the pressure difference in the sub-channels.

Rehme (1978) investigated the transport properties of turbulent flow through sub-channels of rod bundles without spacers. The author provided measurements of the mean velocity, turbulent intensities in all directions, turbulent kinetic energy, shear stress and wall shear stress for a Reynolds number of 8.7×10^4 . Eddy viscosities in the directions normal and parallel to the walls in rod bundles were calculated for the first time. The author stated that precise experimental results on the turbulence anisotropy factor and its local distributions were therefore necessary to verify the assumptions made or adjust the codes. The authors mentioned that computational codes such as VELASCO were used in the calculations. The code required the user to enter the value for anisotropy factor. Measurements were made using a Pitot tube for mean quantities and hotwire for fluctuating ones. Wall shear stress was measured using Preston tubes. Preston tubes. - Preston 1954 proposed a method of measuring skin friction which promised to be both accurate and convenient. It depended upon the assumption that close to the wall in turbulent shear flow there is a region in which the flow is substantially determined by the surface shear stress and the relevant properties of the fluid, independent of the nature of the outer turbulent flow and such quantities as pressure gradient and surface curvature. The author concluded that the momentum transport in rod bundles is highly non-

isotropic. The anisotropic factor showed a strong dependence on the local position. Time-mean velocity and wall shear stress were affected much less by secondary flows. However, the axial turbulent intensity and the kinetic energy or turbulence showed influence on secondary flows.

Seale (1979) presented axial velocity contours, temperature contours and the amount of inter-subchannel mixing by turbulent diffusion and secondary flow for turbulent flow in ducts simulating smooth bare rod bundles both experimentally and analytically. The analytical work was performed by solving the basic differential equations of the turbulent flow and heat flux using a k - ϵ turbulent model. The authors claimed that this turbulent model was applied for the first time to the prediction of inter-subchannel mixing. A comparison between the computer predictions and the results of experimental work revealed that secondary flows were not important to determine the mixing rate. The predictions obtained from calculations assumed that the effective eddy diffusivity was isotropic which did not agree with experimental results. In order to account for the effects of anisotropy, the eddy diffusivity in a direction parallel to the wall was increased by an anisotropy factor. Since anisotropy was essentially a wall effect the amount of anisotropy was expected to rapidly fall from a maximum value near the wall to a factor of unity at some distance from the wall. This implies that it would be difficult to deduce accurate anisotropies from measurements of the axial velocity distribution alone. The inclusion of an anisotropic factor improved the results but still was not sufficient to reproduce the flow correctly. The results of his experimental work confirmed major findings in other works, in particular that the inter-subchannel mixing rates were considerably higher than predicted by simple diffusion theory, and were relatively insensitive to variations in the

gap width between the rods. Effective diffusivities through the gap appeared to be strongly anisotropic and there was no evidence of secondary flows.

In order to establish reliable design and performance criteria for tube bundle models, better velocity data is needed. Simonin et al. (1988) conducted experiments using Laser Doppler Anemometry (LDA) within a specific tube arrangement. Although they gathered some velocity data in the cross-flow over a tube bundle, the data points were limited and detailed velocity distributions, or whole flow field data was not available due to the nature of the LDA technique. (Chang *et al.* 2008) used 2D-LDA measurements in a 5x5 rod bundle array scaled to be 2.6 times larger than the actual bundle size. This work focused on the performance and mixing characteristics of two kinds of spacers with turbulence enhancement vanes. The spacer grids used were of the typical split and swirl type for Pressurized Water Reactors (PWR). The experiments were performed at a condition of $Re=48,000$ and pressure of 1.5 bar. They reported the velocity at various axial positions ranging from one hydraulic diameter (D_h) to 16 hydraulic diameters. The reported accuracy of the measurements is about 1.6% for velocity measurements. However, the use of Laser Doppler Velocimetry (LDV) methods was restricted by the existence of invisible regions in fuel rod bundles and insufficient spatial resolution for the narrow gaps in rod bundles. (Ikeda and Hoshi 2006) developed a miniaturized LDV system embedded in a fuel cladding. The rod-embedded fiber LDV can be inserted in an arbitrary grid cell instead of a fuel rod without disturbing the flow. They obtained flow velocity data in a 5x5 rod bundle typical of a Pressurized Water Reactor (PWR). Measurements were carried out for a central rod with a pitch-to-diameter ratio $P/D=1.326$ with $D_h = 9.75$ mm. The Re used was 57,000. The reported uncertainty in velocity data

was 2.1%. In their work, the conditioning grid was without mixing vanes. They showed results of axial and cross flow data. The cross flow data showed that positions close to the grid had velocities 40% greater than positions farther from the grid. The velocity fluctuations of such positions also increased as much as 100% from positions far from the grid to positions close to the grid. In the case of the axial-flow velocity, the mean flow velocity at $X=3.1 D_h$ was smaller than at $X=20.5 D_h$ and fluctuations were bigger closer to the grid. This work found that for this type of grid the flow recovers after about a ratio of $x/D_h=10$ for axial flow velocity. For the case of cross flow the fluctuations remain constant after $x/D_h=10$ but the mean value of the velocity component decreases with distance from the grid. Mean cross flow velocity and turbulence in the fuel bundle are bigger near the spacer grid; recovery of mean flow velocity and a reduction in turbulence were observed downstream. These flow behaviors were assumed to be mainly due to the mixing vanes. The results indicate that the mixing vane effect has a strong influence to around $X=10 D_h$ downstream of the spacer grid. (Conner *et al.* 2005) presents the experimental results of a 5x5 fuel bundle with spacer grids. Several spacer types typical of PWR's were tested in an air loop with fully heated rods. The work focuses on heat transfer measurements using an especially design thermocouple holder that can be moved axially inside the bundle. The Re number tested ranged from 15,000 to 37,000 based on the hydraulic diameter, $D_h = 11.77 \text{ mm}$. The results were calculated based on temperature measurements at discrete positions inside the bundle. Conner et al. found an improvement in the heat transfer after the spacer-grids but did not provide any explanation about the probable mechanism behind these improvements.

(Yang and Chung 1998) have studied the influence of the spacer grids on the turbulent mixing within square sub-channel geometry. They analyzed the generation and decay of turbulent energy from LDA measurement results. (Neti *et al.* 1982) measured the lateral velocity profiles within sub channels using 2D LDA and they claimed that the magnitudes were less than 1% of the average axial velocity. However, detailed secondary flow features were unclear. (Rehme 1987) performed measurements using Hot Wire Anemometry (HWA) in order to confirm the existence of lateral flow pulsations between the sub-channels. He concluded that the thermal mixing in sub-channel geometry is mostly influenced by almost periodic macro scale flow pulsations caused by the flow instability rather than the secondary flow from the Reynolds stress gradients.

Regarding computational work, several attempts have been made to model the thermal hydraulic behavior of fuel rod bundles. (Tzanos 2004) simulated the flow in a 7x7 rod bundle typical of a PWR. The spacers were simulated as plates with no thickness and the blockage ratio of the spacer was used as controlling parameter. The simulations were made using various turbulence models with symmetric and periodic boundary conditions. Tzanos concluded that far from components that cause significant flow deflections the agreement of mean velocity predictions with measurements was good. However, near such components the discrepancy between velocity predictions and measurements could be large. These discrepancies were attributed to shortcomings of the k- ϵ models. Even in rod bundles without flow deflectors, the turbulence predictions of standard k- ϵ models showed significant discrepancy with measurements. (Ikeno and Kajishima 2006) used Large Eddy Simulation (LES) coupled with the immersed boundary method in an effort to represent the effect of flow geometry and compare some

of their results with PIV focusing on developing swirl. The Re for these investigations was $Re=4100$. Their method includes a SGS model because the dynamic procedure would not require a near-wall correction for SGS viscosity nor an averaging operation of dynamic operation. The results reproduced the effects of flow geometry: the flow around mixing-vanes caused the swirl with large-scale fluctuation, enhancing heat transfer, and vortices were produced in the rod gap enhancing enthalpy mixing between channels. This model successfully explained the mechanism of decaying swirl in the rod bundle: a developing vortex in the rod gap and the decreasing wake behind the mixing-vanes promoted the decay of swirl more strongly than in a pipe. (Lee and Choi 2007) focused on the computational analysis of turbulence intensities, maximum surface temperatures of the rod bundle, heat transfer coefficients and pressure drops of four kinds of mixing vanes. The authors used a 17×17 rod bundle since they considered that vortex size effect may not be represented correctly with a smaller rod array. (Caraghiaur and Anglart 2007) measured the axial velocity in three different sub-channels of 5×5 rod bundle with spacers using LDV. The results were compared with CFD predictions using a $k-\varepsilon$ and SSG turbulence models. It should be noted that the spacer did not have any turbulence enhancement device such as mixing vanes. In this study both turbulence models over-predicted the rate of the velocity decrease downstream of the spacer. In addition, the behavior of the root mean square values of the axial velocity did not agree with the predicted ones from the CFD codes. Caraghiaur et al concluded that the pressure drop over a spacer was under-predicted by 20-30% with the CFD code and model used. There was reasonable agreement between axial velocity distribution downstream of the spacer and they recommended a larger CFD model i.e. half of the bundle geometry to remove

the influence of symmetry boundary conditions imposed on sub-channel boundaries on the results of CFD predictions.

To date, experimental data has not exposed major flaws in computational models for fluid flow in a rod bundle with spacers. However, even small discrepancies should force us to ask ourselves if it is safe for nuclear engineers and other people working in this field to assume the validity of computational predictions. Verification and validation (V&V) are the primary means to assess the accuracy and reliability of computational simulations. V&V methods and procedures have fundamentally improved the credibility of simulations in several high-consequence fields, such as nuclear reactor safety.

The field of nuclear reactor safety has not focused on code verification benchmarks but it has placed great emphasis on developing validation benchmarks. Many of these validation benchmarks are closely related to the operations of actual reactors at near-safety-critical conditions, as opposed to being more fundamental-physics benchmarks.

The importance of computer simulations in the design and performance assessment of engineered systems has increased dramatically during the last three decades. To have justified confidence in this evolving culture, there must be major improvements in the transparency and maturity of the computer code used, the clarity of the physics included and excluded in the modeling, and the comprehensiveness of the uncertainty assessment performed. Commercial codes should be applied to the flows where dominant physics are clarified.

Thus, the ultimate goal of this work is to contribute to a better understanding of presupposed and existent events that could affect the safety of nuclear power plants by

using state-of-the-art measurement techniques that may elucidate the fundamental physics of fluid flow in rod bundles with spacer grids. In particular, this work concerns the development of an experimental data base with high spatial and temporal resolution of flow measurements inside 5x5 rod bundles with spacer grids. The data base is intended to validate CFD codes at various scales. Measurements are carried out using Dynamic Particle Image Velocimetry (DPIV) inside an optically transparent rod bundle utilizing the MIR approach. This work presents results showing full field velocity vectors and turbulence statistics for the bundle under single phase flow conditions.

CHAPTER II

EXPERIMENTAL SET UP AND TECHNIQUES

This chapter describes the experimental facility designed and used for this investigation. The experimental set-up was divided into several subsections in order to provide a more comprehensive approach for the reader. Detailed information about geometry used and technical considerations of the main equipment utilized were compiled into the following sections.

2.1 Channel Flow Facility

The experiments were performed at the Optical Multi-phase Flow Research Laboratory in the Nuclear Engineering Department of Texas A&M University. The experimental facility consisted of two main systems: the hydraulic loop and the test section as shown in figure 1. Both systems were coupled together in order to obtain flow representations of the studied phenomena.

The closed loop configuration consisted of a plastic reservoir tank with capacity for 570 liters (150 gallons), a 2 HP centrifugal pump (Berkeley model: S39538) with modified o-rings for high temperature operation, CPVC valves, filters, and CPVC piping, and various pressure gages. The tank was located 25.4 cm (10 inch) above the pump intake in order to provide a constant water head to the pump during normal operation. In addition, this configuration avoided the pump purging due to air trapped in the piping connecting the tank to the pump's intake. The fluid passed through a series of filters

(Keystone filter division model: MMTGB20) that limit the size of suspended particles in the fluid during experiments to $50\text{e-}6\text{ m}$.

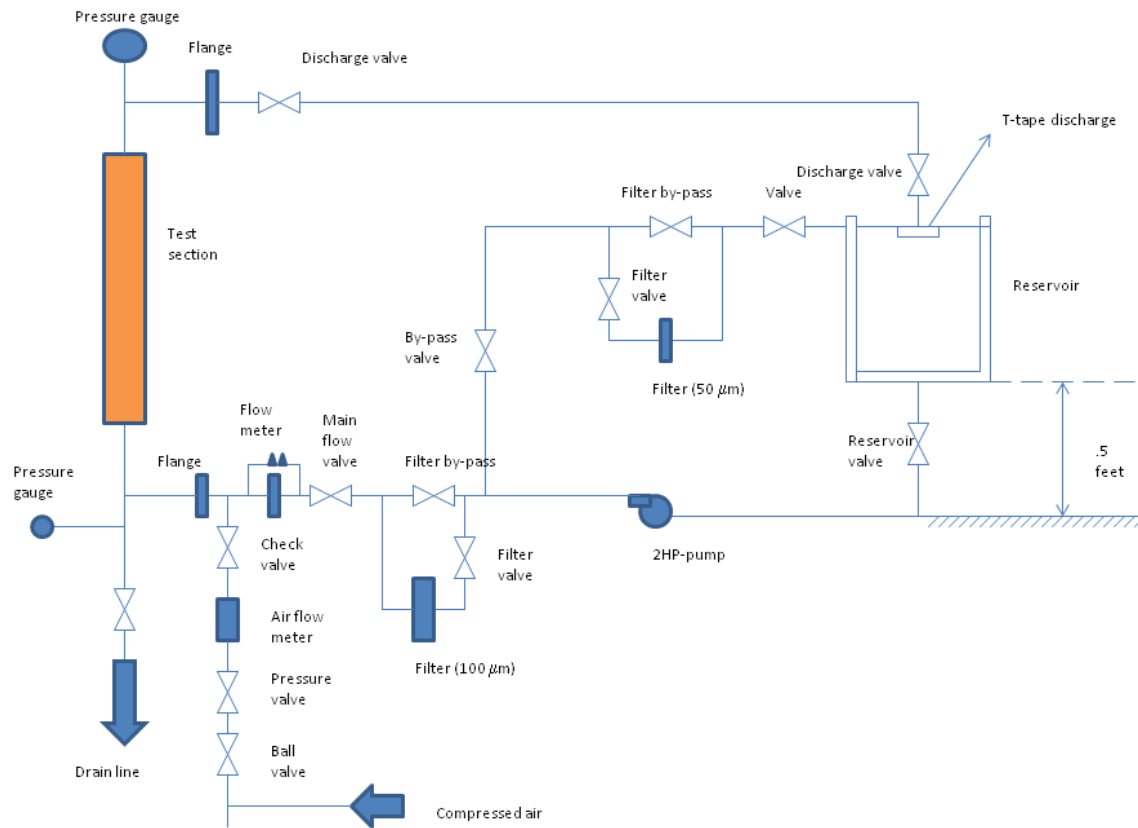


FIGURE 1. Hydraulic loop.

The pump was controlled by a variable frequency controller (Polyspeed Electronics Dallas Texas model: XLT25-20C) in order to assure reproducibility of flow rates and constant torque in the pump impeller at various operation frequencies. Figure 2 and figure 3 show a pictorial of the reservoir tank and variable frequency pump controller respectively. An insertion propeller type flow meter (Data Industrial SDI flow sensor model : SDI 1D1N10-0200) was located downstream at a distance of 228.6 cm (90 inch)

from the pump's exit to measure the volumetric flow rate delivered to the test section as shown in figure 4.

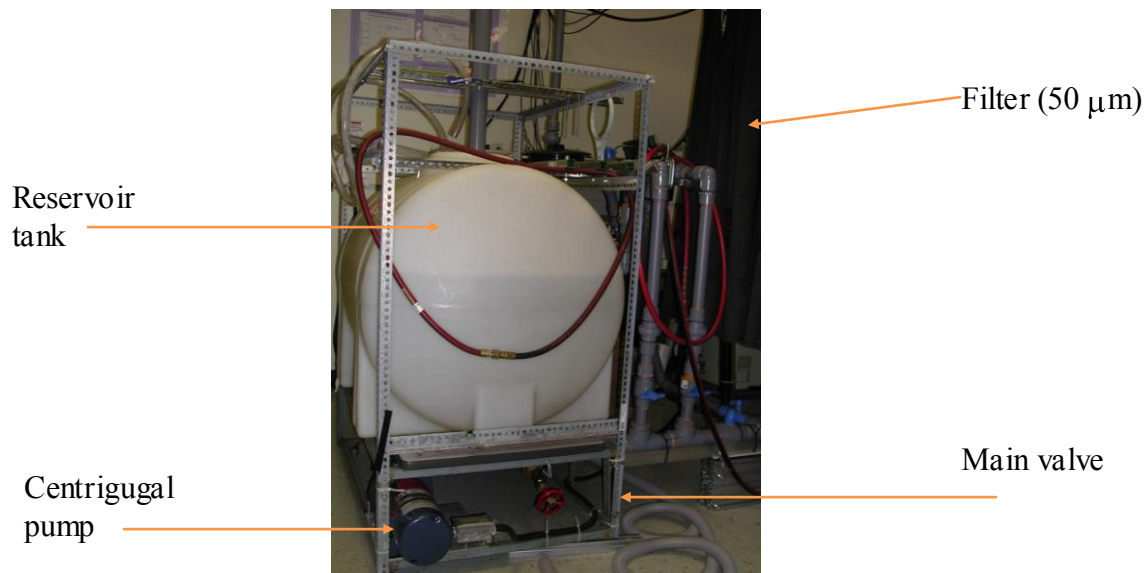


FIGURE 2. Reservoir tank, pump, and filter ring system.

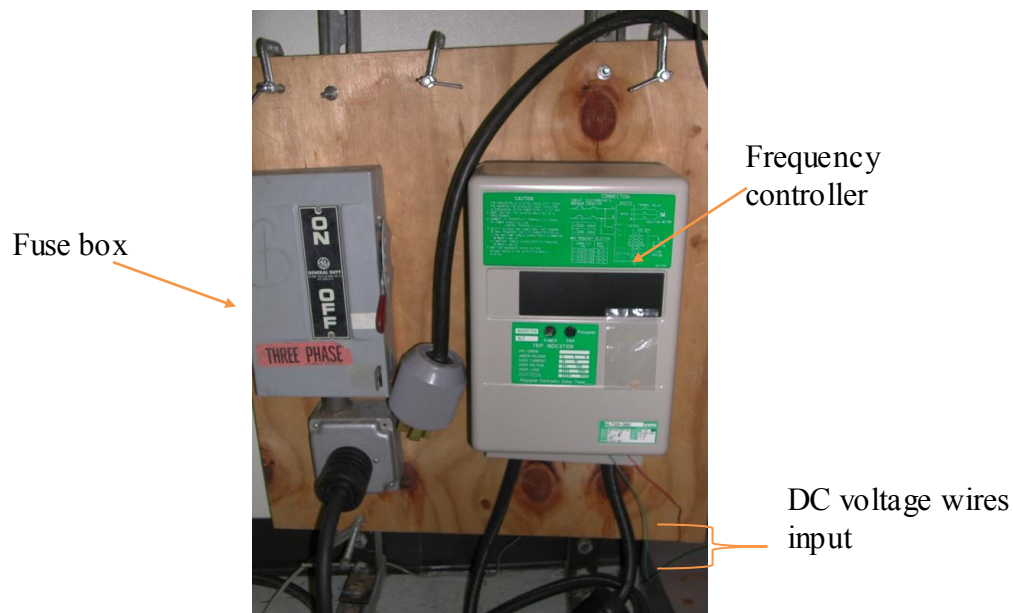


FIGURE 3. Variable frequency pump controller.

An air mixing chamber was included in the design of the hydraulic loop in order to inject gas into the main flow stream. A porous media cylinder was introduced into the chamber as shown in figure 5. The air line was connected to a compressed air line available in the laboratory with working pressures that range from 2- 100 psi. A gas flow meter (Alicat Scientific model: MC-100 SLPM-D (N2)) was placed at the gas inlet of the mixing chamber to monitor the gas flow rate. A pressure gauge was located at the same gas pipe line. The porous cylinder delivered the air into the main stream by producing bubbles, the average diameter of which was dependent on the main flow rate.

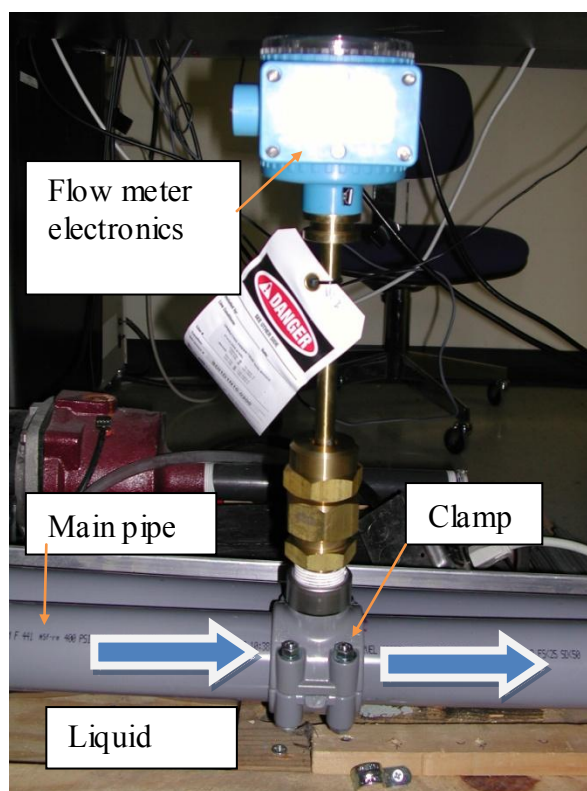


FIGURE 4. Insertion propellor type flow meter.

The position of the flow meter was selected according to the instructions manual by leaving about 45 pipe diameters upstream and downstream the flow meter location. The maximum volumetric flow rate attained by the pump in the hydraulic loop without the test section was 416 liters per minute (110 gpm) which correspond to a maximum Reynolds number in the piping system based on the piping diameter of $Re=1.74e5$. It should be noticed that the former was the maximum Reynolds number achievable in the hydraulic loop when the test section was not attached to the loop. The reproducibility of the flow rates was of 99% when working inside the specified limits.

Figure1 shows a drawing of the flow loop used in this study. The locations of relevant components are specified to provide a reasonable description of the hydraulic facility.

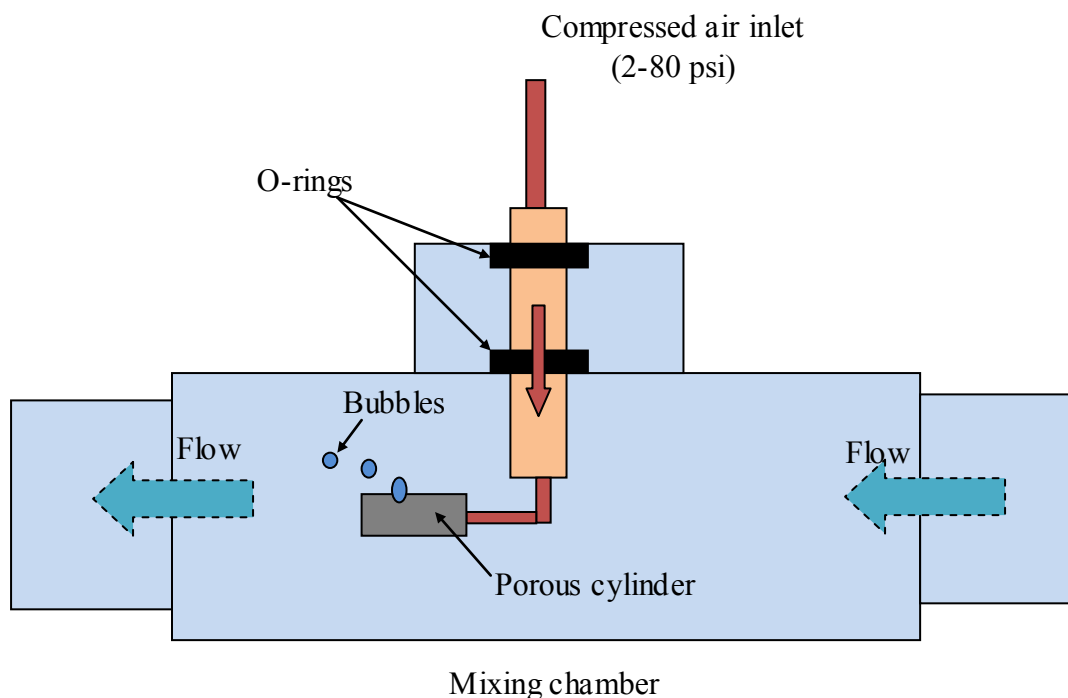


FIGURE 5. Air mixing chamber.

2.2. Aluminum Frame

The ultimate goal of this work is the development of a database for benchmark CFD simulations. With the former goal in mind, the first step towards this objective is the accurate characterization of the test section which is formed by two main components. 1) An aluminum frame channel with visualization windows and 2) A U-shaped transparent polycarbonate interior channel that encages the spacer-grids and rods. This work presents the testing of two different typical spacer-grids. Therefore, geometric and construction descriptions for both configurations are presented in this section.

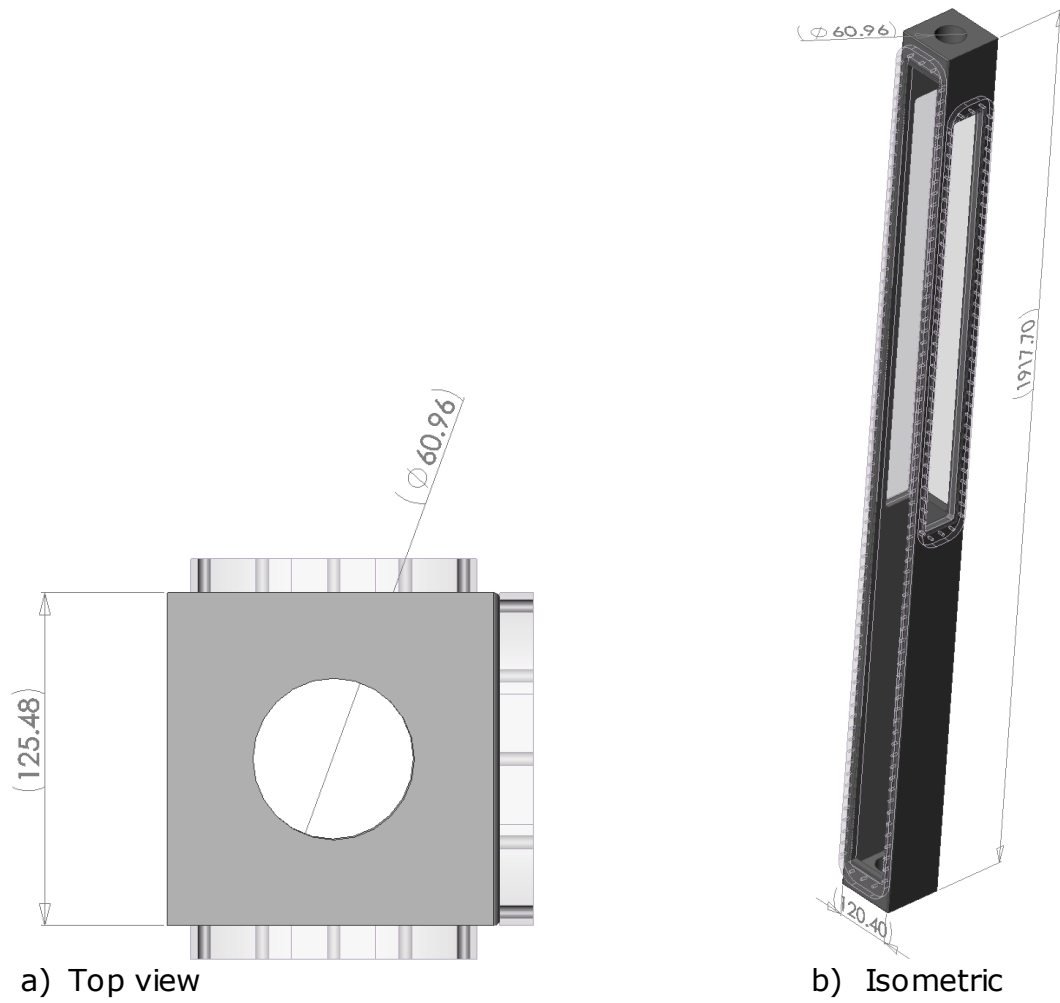
Aluminum frame

The frame was an aluminum rectangular box shaped channel of length 1790.7 mm (70.65 inch) and a square cross section with a side length of 122.9 mm (4.84 inch). The channel had a total of four (4) rectangular windows on each of the longest faces of the box (one window per side) which served as observation windows. Three of the windows had dimensions of 107.95 x 965.2 mm (4.25 x 39 inches) and one with dimensions of 107.95 x 1790 mm (4.9 x 70 inches). The other two faces of the box had an orifice of 60.9 mm (2.4 inches) in diameter which served as the inlet and outlet of the channel as shown in figure 6. The construction of the channel was made of a single aluminum rectangular brick to avoid any welding in the process. Optically transparent polycarbonate rectangular sheets were used as windows for the channel. Zelux type plastic was used for all the polycarbonate pieces. This polycarbonate has operating temperatures of -40 to 121 C and tensile strength of about 65 MPa (9500 psi). Table 1 shows the main properties for the used polycarbonate.

TYPICAL PROPERTIES of ZELUX POLYCARBONATE			
ASTM or UL test	Property	Unfilled	30% Glass
PHYSICAL			
D792	Density (lb/in ³) (g/cm ³)	0.043 1.2	0.052 1.43
D570	Water Absorption, 24 hrs (%)	0.12	0.12
MECHANICAL			
D638	Tensile Strength (psi)	9,500	19,000
D638	Tensile Modulus (psi)	320,000	-
D638	Tensile Elongation at Break (%)	60	10
D790	Flexural Strength (psi)	15,000	23,000
D790	Flexural Modulus (psi)	375,000	1,100,000
D695	Compressive Strength (psi)	12,000	18,000
D695	Compressive Modulus (psi)	240,000	500,000
D785	Hardness, Rockwell	M70 / R118	M92
D256	IZOD Notched Impact (ft-lb/in)	13	2
THERMAL			
D696	Coefficient of Linear Thermal Expansion (x 10 ⁻⁵ in./in./°F)	3.9	1.2
D648	Heat Deflection Temp (°F / °C) at 264 psi	270 / 132	295 / 146
D3418	Glass Transition Temp (°F / °C)	293 / 145	300 / 149
-	Max Operating Temp (°F / °C)	250 / 121	270 / 132
C177	Thermal Conductivity (BTU-in/ft ² -hr-°F) (x 10 ⁻⁴ cal/cm-sec-°C)	1.3 6.9	1.3 6.9
UL94	Flammability Rating	H-B / V-0*	H-B / V-0*
ELECTRICAL			
D149	Dielectric Strength (V/mil) short time, 1/8" thick	390	470
D150	Dielectric Constant at 60 Hz	3.17	3.35
D150	Dissipation Factor at 60 Hz	0.0009	0.0011
D257	Volume Resistivity (ohm-cm)at 50% RH	1016	1016

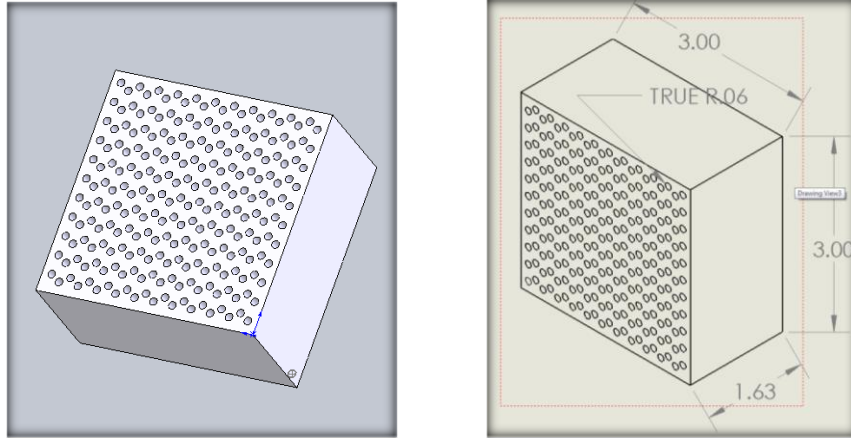
Table 1 Main physical properties of Zelux polycarbonate

The sealing between the plastic windows and the aluminum channel was accomplished by the use of an EPDM o-ring placed inside a groove carved in the aluminum frame. This type of o-ring has an operation temperature of -40 C to 121 C which fulfilled the design operation temperatures for this part of the project. However, the o-ring can be easily replaced by a different material in case that different operation conditions are needed. The plastic windows were attached to the aluminum frame by the use of more than 500 stainless steel screws T-10-32 x 0.75" evenly distributed along the windows. The screws were tightened by the use of a torque wrench with a preset torque of 4.5 ft-lb which was previously calculated to hold the pressure force of the expected flow inside the chamber. The polycarbonate windows attached to the aluminum frame were made of single plastic rectangular pieces with 2.54 cm (1 inch) thickness. The windows were machined in such a way that the windows have a smooth transition from the aluminum surface to the plastic in the interior faces of the frame. The windows were designed to have a tight fitting with the aluminum frame. Conversely, a gap of 1.5 mm (0.0625 inch) around the perimeter was allowed between the plastic and aluminum surfaces in order to account for the thermal expansion of both materials under heating conditions. A square cross section flow straightener with a side length of 93.66 mm (3.68 inch) and thickness of 38.1 mm (1.5 inch) was placed at 304.8 mm (12 inch) from the channel's inlet. Its purpose was to homogenize the incoming flow and to obtain uniform velocity fluctuations at the entrance of the test section. Figure 7 shows a drawing of the flow straightener with its corresponding dimensions. The through perforations forming the flow straightener have a smooth finish in order to minimize flow disturbances caused by surface roughness.

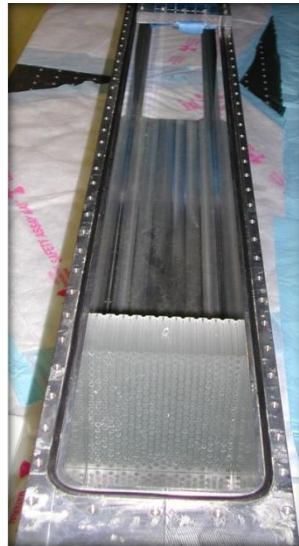


c)

FIGURE 6. Test section, (a) top view, (b) isometric view, (c) real frame picture.



a)



b)

FIGURE 7. Flow straightener (a) CAD drawing, (b) Position inside aluminum frame.

Figure 8 shows the interior of the aluminum frame and the position of the flow straightener with respect to the channel's flow inlet. It should be noticed that the u-shaped polycarbonate channel is not presented in figure 8. Figure 9 shows a perspective of the channel's inlet and location of flow straightener for better appreciation.

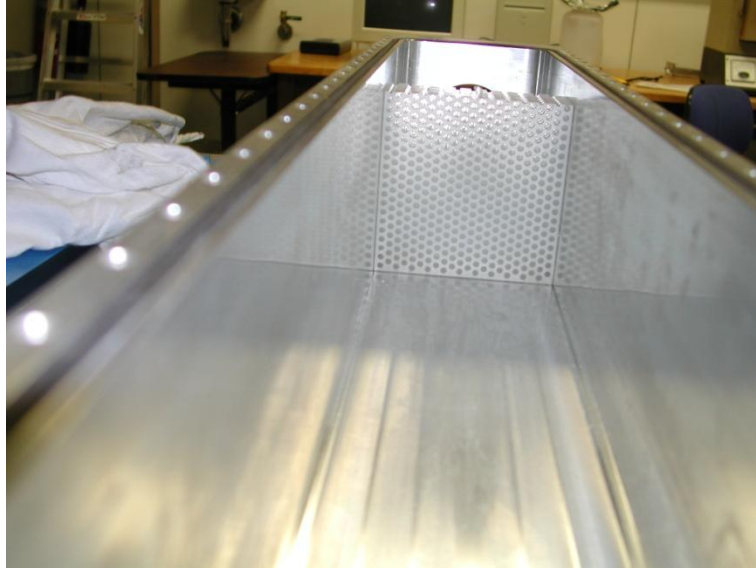


FIGURE 8. Aluminum frame interior with flow straightener.

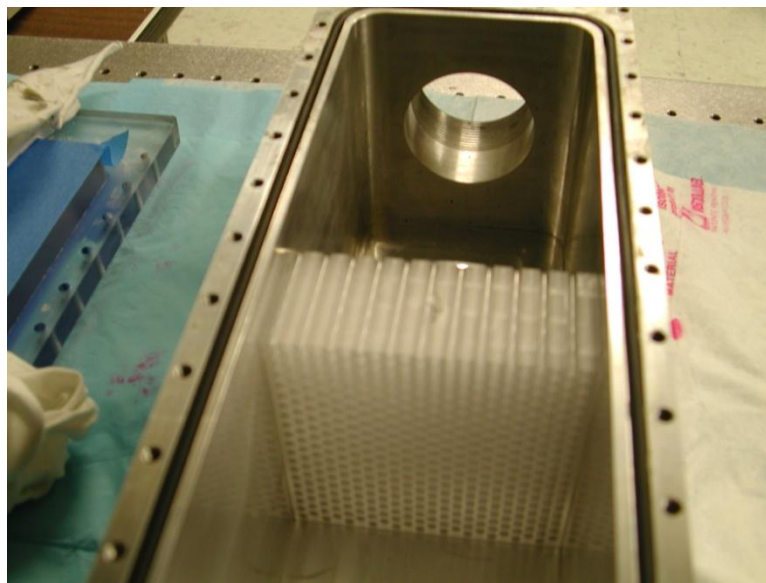


FIGURE 9. Perspective view with respect to channel's inlet.

2. 3 U-channel

A second polycarbonate channel was placed inside the sealed windowed aluminum frame in order to have an even cross section and wall smoothness inside the test section. A correction in cross section was considered necessary since the machining process required a small step in the aluminum frame to assure the correct sealing of the observation windows. Therefore by placing a u-shaped channel inside the main channel, it assures the free flow of the fluid and a constant smoothness along the test section. These approaches were considered important details taken into account that may avoid geometry problems in the Computational Fluid Dynamics (CFD) simulations by providing a simple geometry model that accurately represents the real geometry in the channel without overlooking significant details. Two different spacer-grids designs were tested in this investigation. Therefore, two slightly different u-shaped channels were needed, one for each tested grid type. The geometric characteristics for each of them are provided in the following sections. Figure 10 shows an exploded view of the aluminum frame, u-shaped plastic channel and the observation window. It should be noticed that the interior plastic channel has a length of 1555.75 mm because it was placed right after the flow straightener. Therefore, it runs along the channel with one edge placed in contact with the straightener and the other edge in contact with the aluminum channel outlet.

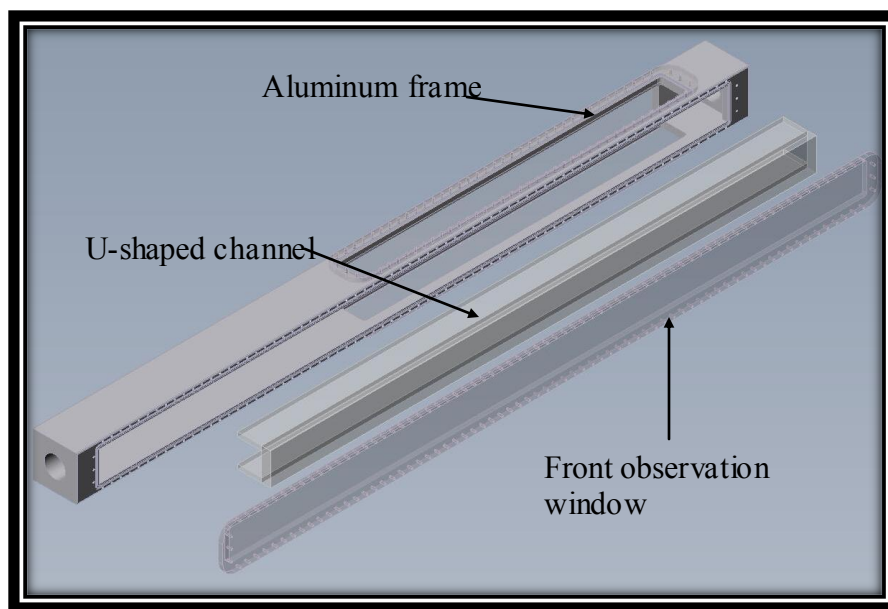


FIGURE 10. Exploded view of aluminum frame, U-shaped channel and front observation window.

Figure 11 shows the u-shaped channel inside the aluminum frame formed by the two lateral polycarbonate sheets named as right internal polycarbonate sheet and left polycarbonate sheet. The top polycarbonate sheet has a thickness of 25.4 mm. The side polycarbonate sheets had a thickness of 12.7 mm each. The joints of the u-shaped channels had a compressible EPDM type gasket to assure correct sealing between the polycarbonate sheets. The sealing was achieved by compression of the gasket. The compression force was applied on the top polycarbonate sheet when the observation window was attached to the aluminum frame through the stainless steel screws. Figure 12 shows the position of the interior plastic walls located inside the aluminum frame. The position of the flow straightener can be appreciated in the lower part of this figure.

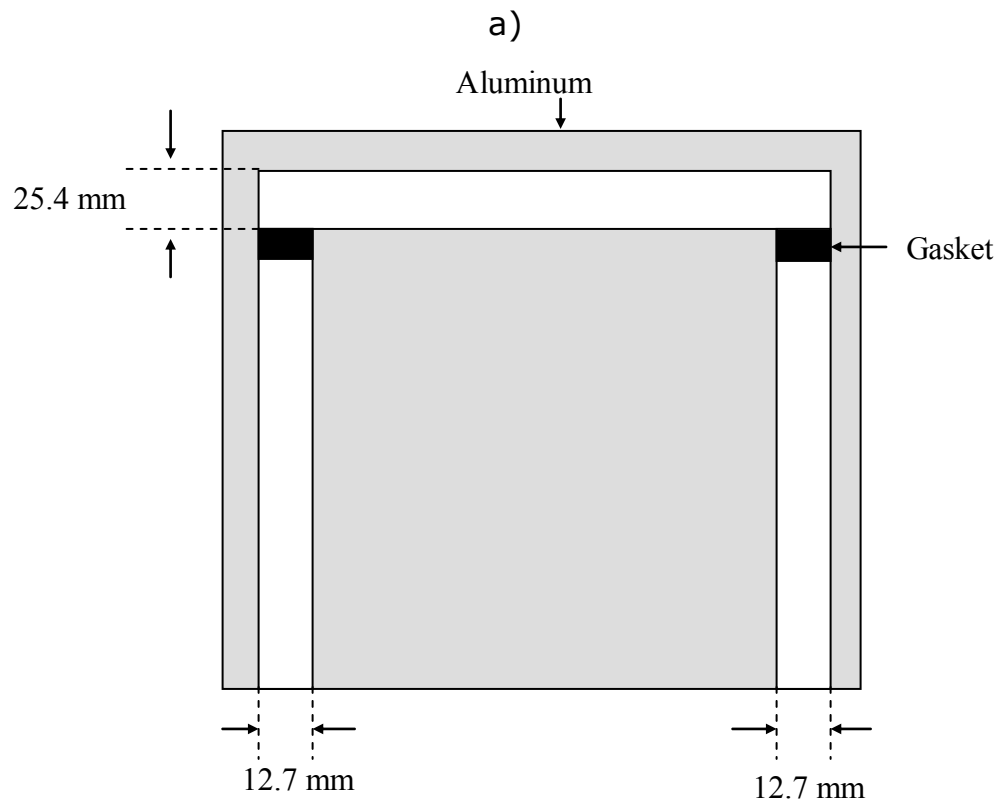
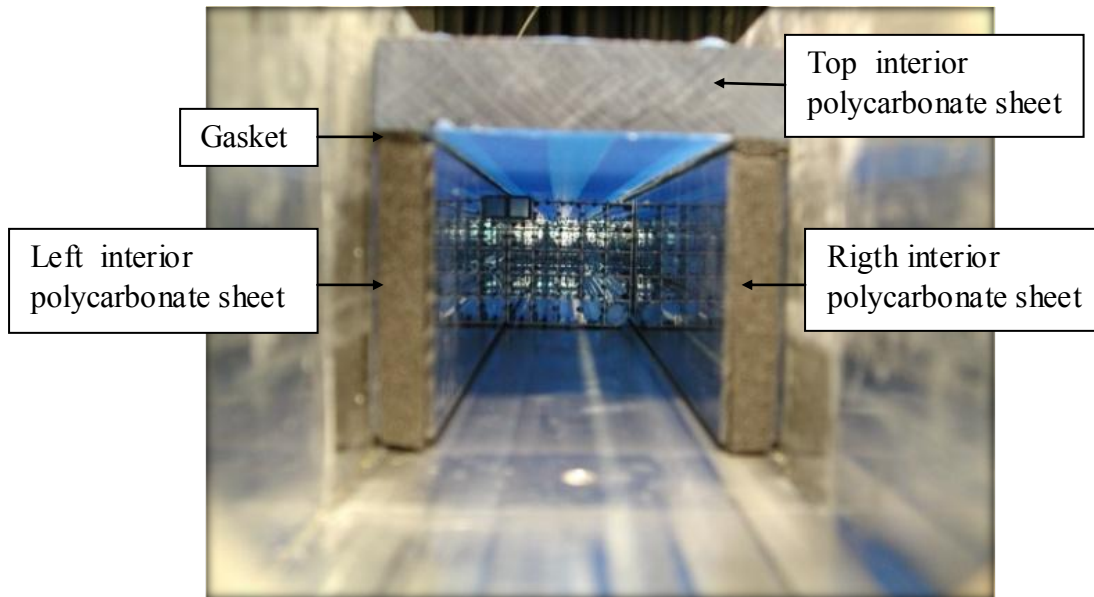


FIGURE 11. U-shaped polycarbonate channel inside aluminum frame (a) picture (b) top view schematic.

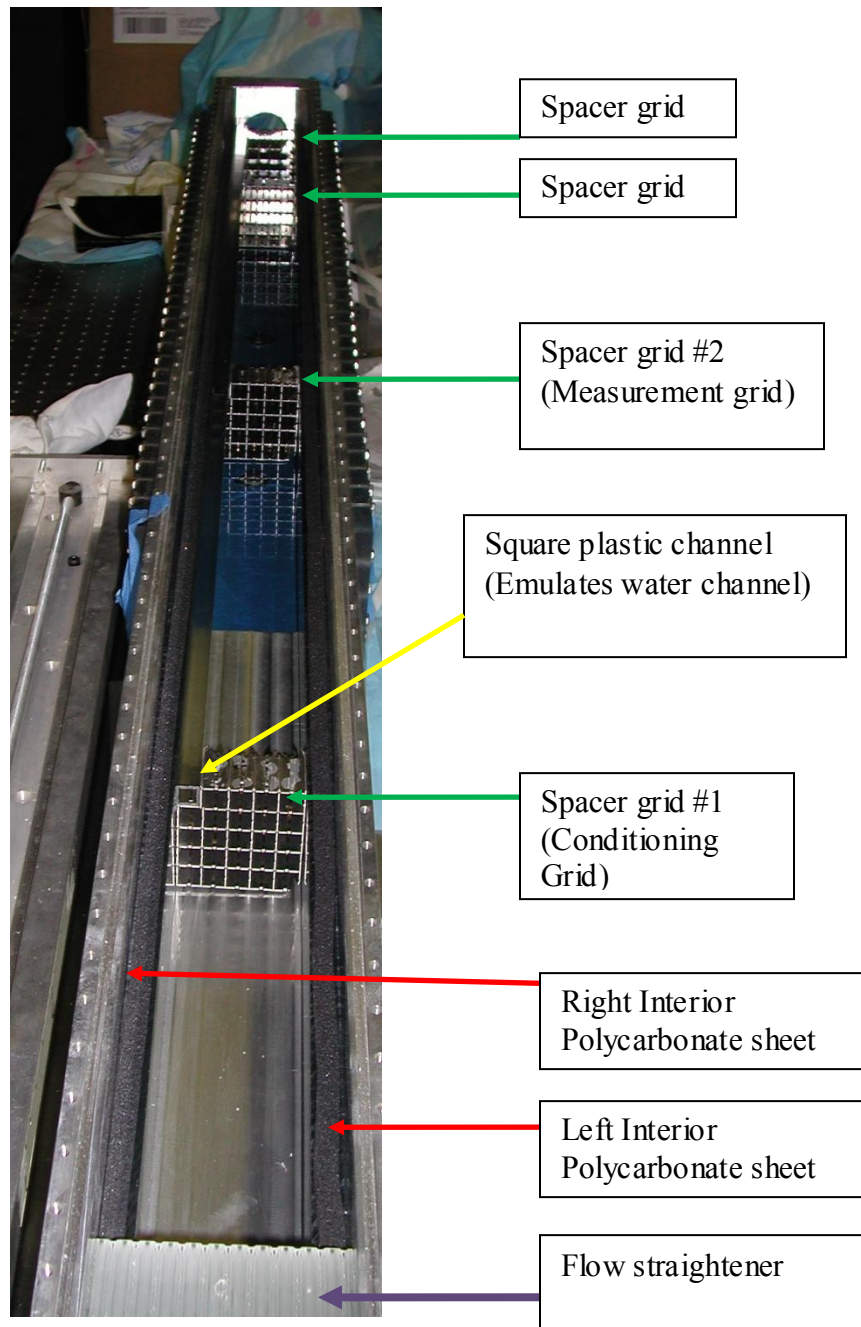


FIGURE 12. Aluminum frame with two internal polycarbonate sheets and grids.

Figure 13 shows the spacer grid holding the 24 plastic rods and the square plastic channel. The 25 components were sealed at both ends of its geometry. It is important to highlight that no flow passed through the square channel or any of the rods. Therefore, the rods and

square plastic channel can be treated as solids where fluid flow cannot trespass the solid boundary.

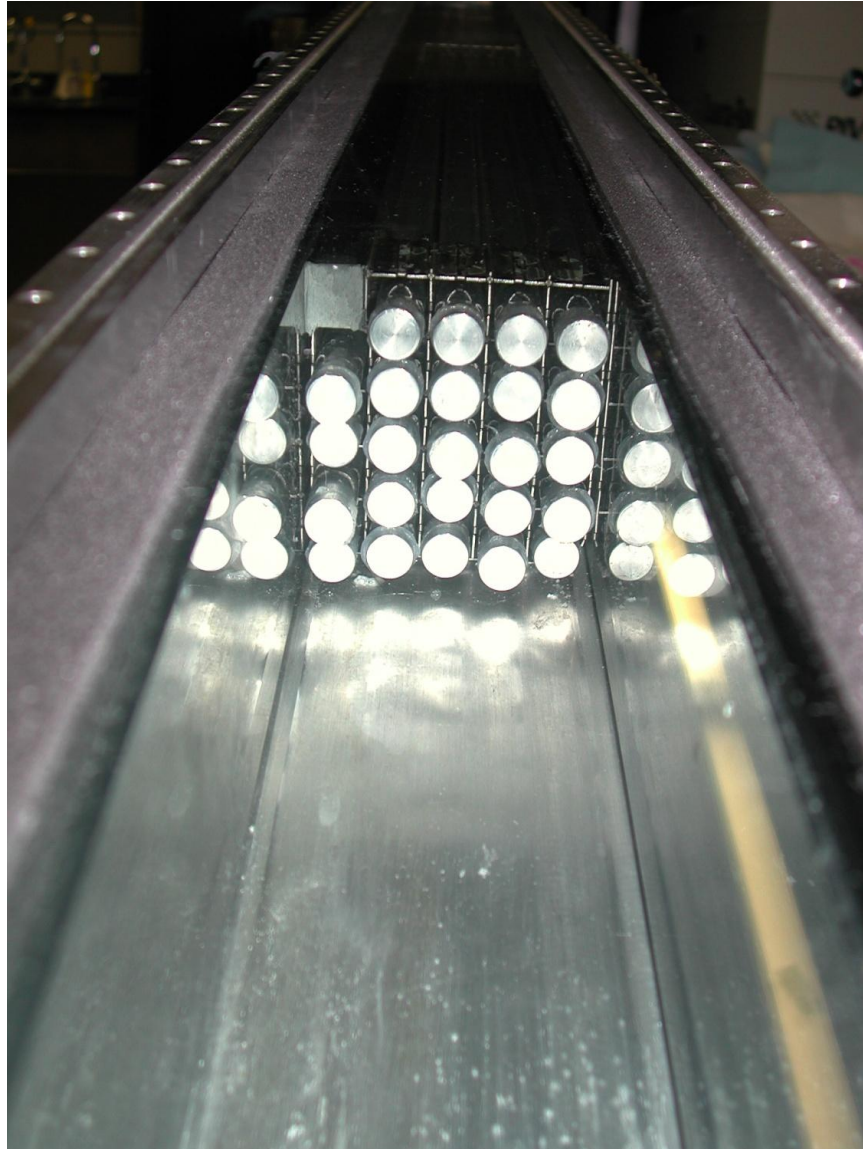


FIGURE 13. Grid with rods and square channel.

2.4 Particle Tracking Velocimetry and Optical System

The optical elements of the experiment included a twin high repetition Nd:YAG class IV laser (New Wave/Pegasus PIV), a beam splitter, mirrors, holders and motorized translation stages. The Nd:YAG laser produced the illumination light for the experiments. It has a maximum power output of 10 mJ per laser (20 mJ total) with a wavelength of 527 nm. The light coming from the laser was directed towards a 50% mirror which allowed passing through 50% of the laser beam energy and reflected the other 50% towards a series of 90 % reflection mirrors. This splitter allowed forming two different laser sheets at the test section. The first laser sheet was parallel to the front face of the channel forming a uniform laser illumination volume of 100 mm high, 200 mm long and 1 mm thick. The second illumination volume had a perpendicular orientation with respect to the front channel face. The second illumination volume had similar dimensions as the illumination volume one. The laser sheet volumes were formed by using a set of three cylindrical lenses. Figure 14 shows a schematic of the optical system used for the experiments.

The particle detection and vector calculation was performed using an in-house Particle Tracking Velocimetry (PTV) algorithm. The computer code for PTV has been improved over the years and its reliability tested in several occasions (PIV challenge reference). Estrada-Perez (2004) showed that the code has an averaged error of 0.1 pixels for particle detection and velocity calculation. The window size used for the present investigation varied according to the data set. However, for most cases the interrogation window was set to 32 x 24 pixels with an overlap of 50 %.

The PTV code output is a velocity field for every pair of images tested. The acquisition rate for the experiments was set to 8000 fps. The optimal particle displacement for the cases tested was found to be 8 pixels. One of the advantages of using the high speed PTV system described in this section is the acquisition of high speed consecutive flow images. Therefore, the optimum particle displacement for the analysis can be selected by the user. For example, for a case with low flow velocity the particles may have an averaged displacement of 2 pixels in two consecutive images which lead to an increase in the particle detection error (Estrada-Perez 2004). For this case the averaged particle displacement can be increased by changing the number of images to skip. Therefore, if 4 images are skipped for the analysis, the averaged displacement between image number one and image number four is 8 pixels. This approach is possible due to the high acquisition rate of the used PTV system. The instantaneous velocity fields obtained by the PTV algorithm was filtered using a statistic filter. The filter used different methods to detect spurious vectors in the field such as 1) deviation from the mean, 2) vector magnitude outliers, and 3) correlation threshold. It is important to notice at this point that the output of the PTV algorithm and the filter is a velocity field with scatter validated vectors. In other words, the vectors are “real vectors” and no interpolation was done for the resulting instantaneous vectors. The calculation of the statistics presented in chapter IV was done with the instantaneous vector fields, therefore no error due to interpolation was added to the resulted statistics. Once that the statistics were calculated using “real vectors” only, the resulted averaged statistics were organized into a grid for calculation of further parameters such as derivatives which require the existence of a structured grid for its computation.

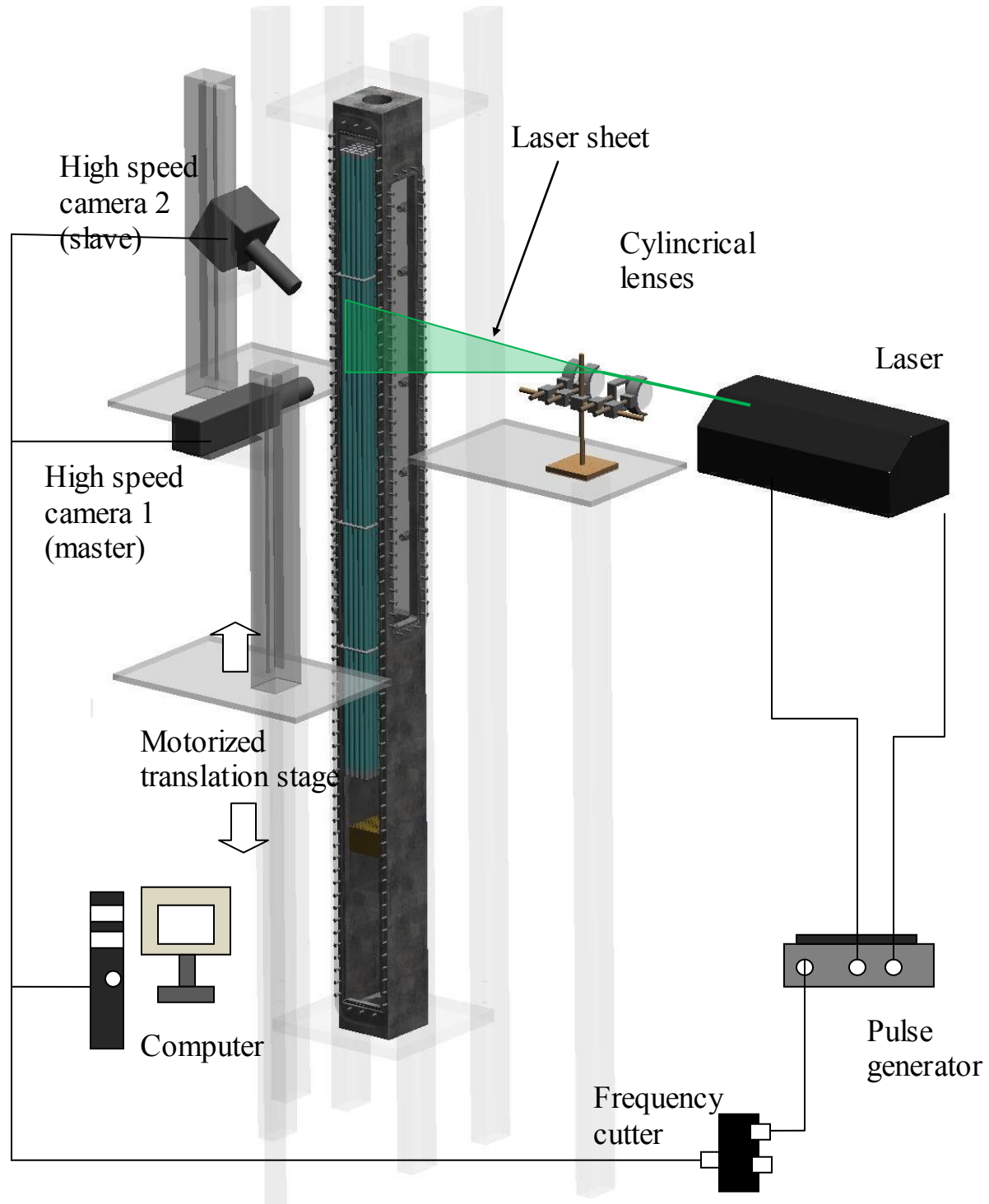


FIGURE 14. Optical system and location with respect to test section.

2. 5 Data Acquisition System

The data acquisition system included two high-speed/ high-resolution cameras, a frequency cutter circuit, a pulse generator, trigger circuit, and desktop computers for data storage. The cameras were CMOS type sensor Phantom 7.1 and Phantom 7.3 (Vision research). These cameras have a CMOS sensor of 800 x 600 pixels with 4GB of on-board memory and 12 bit pixel depth. The cameras were synchronized with the laser at various frame rates. For frame rates less than 4000 fps, the camera was configured to provide the pertinent digital pulses needed to control the laser. Therefore no additional stages were needed for frame rates of up to 4000 fps. However for acquisition frequencies exceeding the former limit, a frequency cutter circuit was necessary to assure the correct synchronization of the cameras with the laser shots. The frequency cutter circuit consisted of a pair of type D flip-flops with its clock inputs interconnected in order to cut the frequency of the incoming pulses to half the original value, more details can be found in (Dominguez-Ontiveros *et al.* 2006). A high accuracy pulse generator (Stanford research) was connected to the output of the frequency cutter circuit to generate the laser trigger pulses. The pulse generator has the capability to receive a pulse and generate an independent pulse with the programmed time delay for each of its outputs. In this work, two channels were used (one per laser) with a programmed time delay depending on the frame acquisition rate (typically 125 μ s). The CMOS cameras were used in a master-slave configuration. In this configuration, the master camera generates the pulses necessary to synchronize the image acquisition of both cameras. The frame rate set in the master camera dictate the maximum acquisition rate in order to assure the acquisition of

simultaneous frames. The cameras used various optical accessories such as telecentric lenses, filters, ring extenders, in order to capture the desired image resolution and working distances necessary. A second electronic circuit was designed to provide a trigger pulse to the acquisition system. The circuit consisted of a monostable pulse circuit using a 555 Integrated Circuit (IC). A monostable circuit produces one pulse of a set length (time period T) in response to a trigger input such as a push button. The output of the circuit stays in the low state until there is a trigger input, hence the name "monostable" meaning "one stable state". This type of circuit is ideal for use in a "push to operate" system for a model displayed at exhibitions. A visitor can push a button to start a model's mechanism moving, and the mechanism will automatically switch off after a set time. The monostable circuit was used to synchronize the picture acquisition and other sensors acquisition (i.e. pressure sensors) which will be explained in the next sections. Figure 15 shows the simplified time chart for the image acquisition process.

2.6 Fluorescent Particles

The fluorescent particles used as fluid tracers in this investigation were produced in-house using the following procedure. The particle production was based in the idea of adding a film coating of a fluorescent dye to the regular Polystyrene microspheres used for PIV. The thin coating should firmly adhere to the bead surface and the selected dye should be excited with the available illumination source. A Nd:YAG class IV laser with emission wavelength of 527 nm which fall in the green light spectrum of visible light was

used for particle excitation. Therefore, the selected dye should be excited in the near region of the 527 nm and had its emission peak wavelength in a desirable range far from

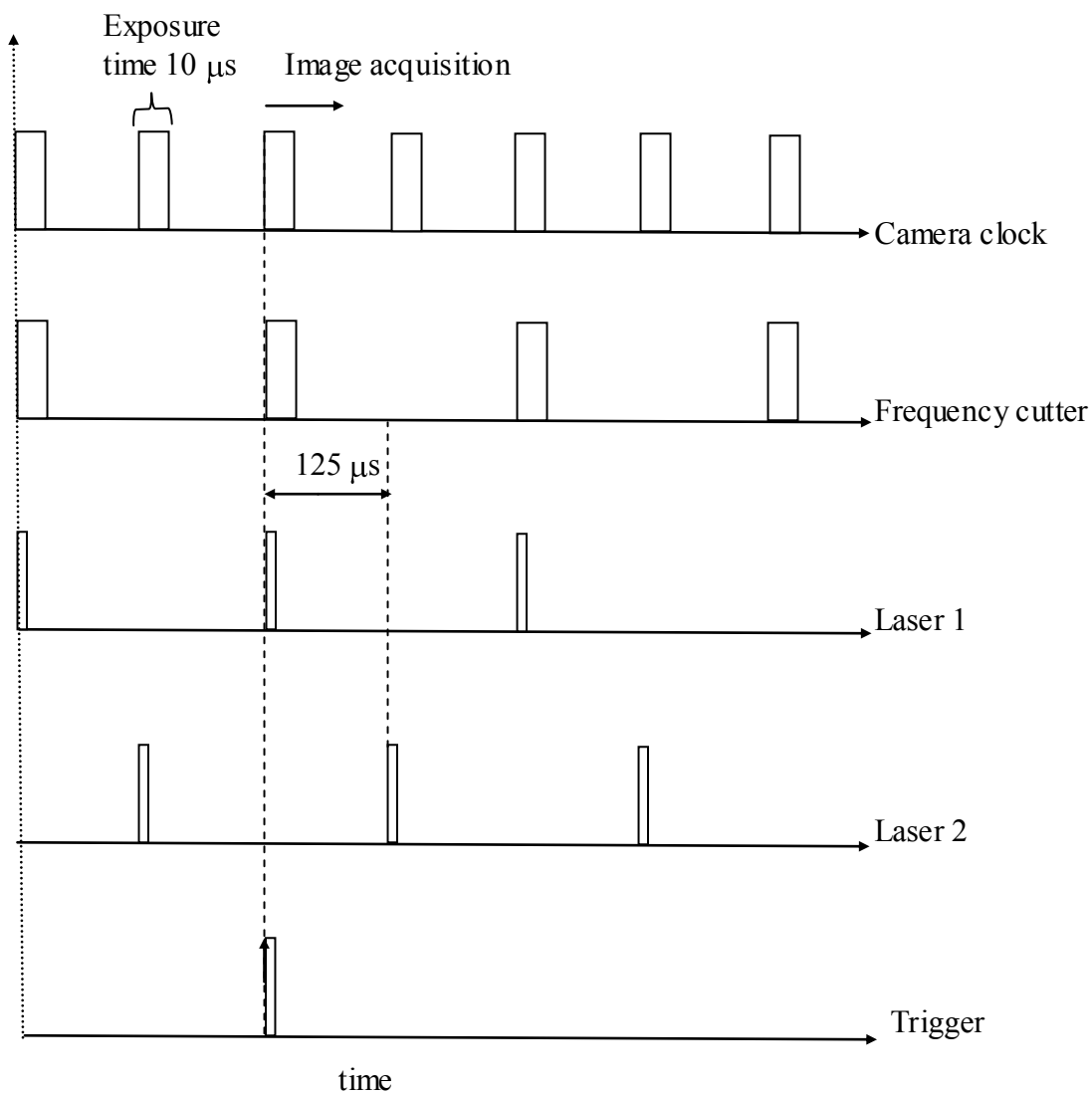


FIGURE 15. Image acquisition time chart.

the excitation band. The selected fluorescent dye was Rhodamine B which fulfilled the requirements mentioned above. Rhodamine B was acquired from a commercial vendor (Sigma-aldrich) in a dye form. Polystyrene particles with average diameter of 10 μm (Expancel UE/ Nobel Industries Sweden) were used as the base surface to be coated.

A solution of 0.78 g of rhodamine B and 75 ml of ethanol was prepared in a glass container. The solution was mixed by stirring the liquid for 1 minute with a regular metallic spoon. Rhodamine B is highly soluble in ethanol therefore no additional mixing device was needed at this point. An additional 500 ml glass container was filled with 55 g of the polystyrene spheres. The ethanol-rhodamine solution previously prepared was poured into the 500 ml glass with the polystyrene particles. A magnetic stirring device was introduced into the new solution rhodamine-ethanol-particles and mixed for 45 minutes. The solution was then placed on a hot plate capable of stirring the solution using the magnetic device and heats the solution simultaneously. The hot plate was set to a temperature of 80 C and the solution was heated for 2 hours. The purpose of the previous step was to evaporate the ethanol from the solution. At this point, the solution became a solid mass exhibiting a pink color. The obtained pink mass was mixed with 737 g of distilled water using the magnetic stirring device. The new liquid solution containing pink colored particles mixed with water was sonicated for 2 hours. The final result was a high concentration water-fluorescent particles ready to be used in the PIV experiments. Figure 16 presents the raw particles on the right side of the picture and the fluorescent fabricated particles in a water solution.

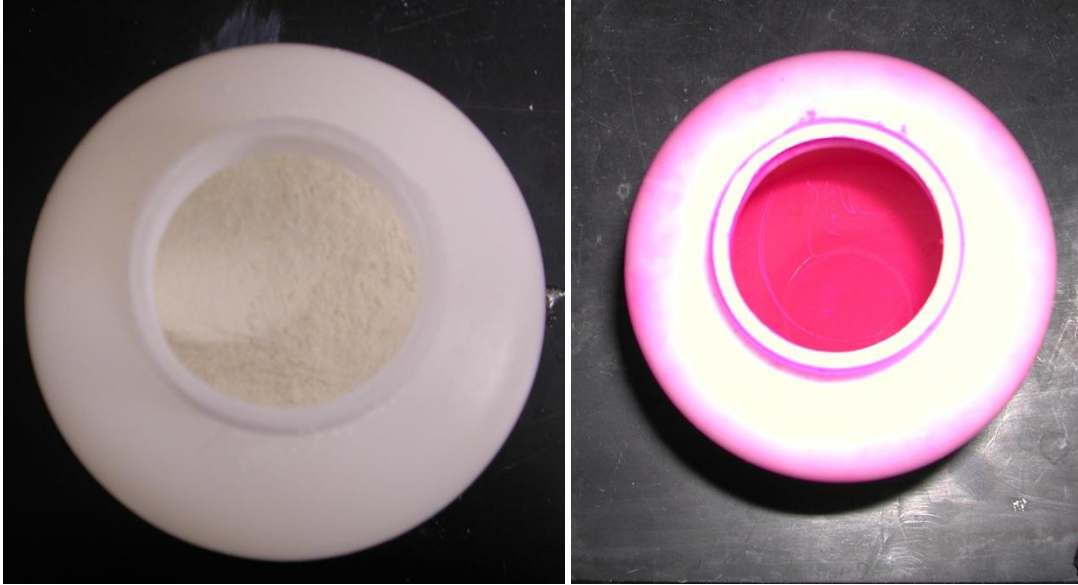


FIGURE 16. Tracer particles for PIV with average diameter of 10 μm . (a) Polystyrene particles before coating (powder) (b) Polystyrene particles after coating process (solution).

2.7 Matching Refractive Index

Optical flow studies of complex geometries such as packed beds are possible through matching the refractive index (RI) of the solid test section with that of the working fluid. When light passes through materials with a different RI, the light will bend at the interface of the materials which could lead to phenomena such as distortion or hidden areas within field of study. However, by matching the RI of the materials, the bending of the light will be minimized or eliminated, making the field of interest accessible and the test section optically transparent. Refractive index matching techniques have been used extensively in past studies. However, advancements in the materials used, coupled with state-the-art measurement techniques such as PIV, have kept

the use of MRI at the forefront of new research. Although the method of matching the RI of the solid and liquid material is not difficult, other material concerns such as price, viscosity, density, toxicity, flammability, compatibility, etc. can complicate the selection process. During the period of this experimental process the author worked to improve its understanding of MRI and has included pertinent information below this section.

A literature reviewed, performed by Budwig (1994) gives insight into MRI techniques. The use of curved walls or boundaries in the test section must be accounted for and Budwig suggests equations that account for curvature through measurements in a cylindrical pipe or the use of a flat wall correction box that is filled with the working fluid. Using a correction box, complex geometries can be used without the loss of clarity due to refraction. Blind spots, complete loss of the certain sections of the image, can develop in complex geometries. Table 2 and table 3 summarize solid and liquid materials and their properties for possible use in MRI experiments.

A popular choice for a fluid in past studies has been an aqueous salt solution. In a study by (Hendriks and Aviram 1982) an aqueous solution of zinc iodide was used to match the RI of polymethylmethacrylate (PMMA) to study the flow in ink-jet aspirators. This study provided data that established the refractive index as a function of ZnI_2 concentration with a refractive index as high as 1.619 at a zinc iodide concentration of 81.05 % wt.. Also data for kinematic viscosities of fluid as a function of refractive index are presented. At low concentrations aqueous solutions have a low kinematic viscosity, which is useful when it is desirable to have a working fluid similar to water. Although this solution does possess the possibility to match the RI of multiple materials by changing the concentration of the salt and the price is moderate, and the toxicity is high

(www.sigmaaldrich.com). An aqueous solution of sodium iodide has also been a popular choice in past studies. (Chen and Fan 1992) used a 60 % wt. sodium iodide solution to match glass beads ($RI \approx 1.5$). Refractive index is a function of the temperature, concentration and the wave length of the light passing through the material (Narrow *et al.* 2000). Narrow *et al.* developed a model to predict the refractive index of sodium iodide as a function of these variables. It was also suggested that a very small concentration of sodium thiosulfate ($\approx 1\%$ wt.) be used to reduce discoloration of the solution due to the formation of I_3^- . Uzol *et al.* (2007) used the solution at concentrations up to 64 % wt. to match the RI of PMMA. They found that the I_3^- was formed by exposure to light and oxygen and suggested deaerating test apparatuses and minimizing exposure to light.

Oils have been suggested in past studies for MRI facilities (Dybbs and Edwards 1984), (Northrup *et al.* 1991), (Stohr *et al.* 2003), and (Stoots *et al.* 2001). Northrup *et al.* (1991) used a 27 % wt. L42 organosilicone fluid manufactured by Union Carbide Co. and 73 % wt. 550 fluid manufactured by Dow Chemical Co. to match the refractive index of a PMMA test section along with fluorescent PIV (FPIV) techniques to measure flow in a porous media. They suggested the use of FPIV, with a band pass filter to reduce noise due to reflections from inhomogeneities in the PMMA material. The RI of the fluid was then fine tuned by controlling the temperature of the experiment. Stohr *et al.* (2003) experimented with other fluids from Dow Chemical Company (200, 556 and 710 fluid), however the health, flammability and viscosity proprieties of these fluids were not ideal. Stoots *et al.* (2001) used a mineral oil to create a large-scale MRI facility. The mineral oil was chosen for its price due to the large scale of the facility.

Material	Refractive Index	Reference
Borosilicate (Pyrex)	1.47-1.49	Budwig 1994
Optical Glasses	1.45-1.96	Budwig 1994
Acrylic (PMMA)	1.49	Budwig 1994
Polycarbonate	1.58	Budwig 1994
FEP	1.33	Dominguez <i>et al.</i> 2008
Teflon AF	1.29-1.31	Dominguez <i>et al.</i> 2008
K8 glass	1.51	Pokusaev <i>et al.</i> 2004
Styrene -		
divinyl-benzene	1.5903	Cui and Adrian 1997
Silica gel	1.452	Cui and Adrian 1997
Fused quartz	1.4584	

Table 2 Refractive index for solids

Fluid	Refractive Index	Hazard	Density [g/cm ³]	Boiling Point / (Melting Point) [C]	Flash Point [C]	Dynamic Viscosity [cP]	Cost	Reference
water	1.33		1	100		1		
glycerin	1.47	1	1.262	182	160	934	\$\$	Budwig (1994)
zinc iodide solution	1.33-1.62	3	4.74	(445)		1-10	\$\$\$\$	Hendricks and Avram (1982)
sodium iodide solution	1.33-1.5 (60%)	2	3.67	(651)			\$\$	Narrow <i>et al.</i> (2000)
potassium thiocyanate sol.	133-1.49	1	1.89	(173)		1-2.4	\$	Budwig (1994)
ammonium thiocyanate sol.	1.33-1.5	1	1.3	(152)		1-2.1	\$\$	Budwig (1994)
sodium thiocyanate sol.	1.33-1.48	2	1.74	(287)		1-7.5	\$	Budwig (1994)
kerosene	1.45	2	0.8	175-325	82		\$	Budwig (1994)
silicone oil mixture	1.47	0	1.102		316	90-110	\$\$\$\$	Dybbs and Edwards (1984)
mineral oil	1.48	0	0.862				\$	Dybbs and Edwards (1984)
turpentine	1.47		0.87	150	35	1.49		Dybbs and Edwards (1984)
solvent naphtha	1.5		0.67					Dybbs and Edwards (1984)
soybean oil	1.47		0.93			69	\$\$\$	Dybbs and Edwards (1984)
olive oil	1.47		0.92			84		Dybbs and Edwards (1984)
caster oil	1.48		0.96	313		986	\$\$\$	Dybbs and Edwards (1984)
tung oil	1.52		0.93				\$	Dybbs and Edwards (1984)
cassia oil	1.6							Budwig (1994)
dibutylphthalate	1.49	2	1.043	340	171		\$	Budwig (1994)
tetraline	1.541	2	0.969	204	75		\$\$\$	Budwig (1994)
benzyl alcohol	1.54	2	1.044	90	96	5	\$\$\$	Cui and Adrian (1997)
ethyl alcohol	1.362	2	0.79	78	14		\$\$\$	Cui and Adrian (1997)
methylnaphthalene	1.615	3	1.001	240	82		\$\$\$\$	Cui and Adrian (1997)
chloronaphthalene	1.632	2	1.194	111	121		\$\$\$\$	Cui and Adrian (1997)
200 fluid (Dow Corning)	1.404	1	0.816	152	30	1		Stohr <i>et al.</i> (2003)
550 fluid (Dow Corning)	1.4935	0	1.065	35	101	125		Northrup <i>et al.</i> (1991)

Table 3 Possible matching refractive index fluids and their properties

Fluid	Refractive Index	Hazard	Density [g/cm ³]	Boiling Point / (Melting Point) [C]	Flash Point [C]	Dynamic Viscosity [cP]	Cost	Reference
556 fluid (Dow Corning)	1.46	3	0.98	65	101	20		Stohr <i>et al.</i> (2003)
710 fluid (Dow Corning)	1.533	0	1.11	35	101	500		Stohr <i>et al.</i> (2003)
Cargille RI matching fluids	1.3-2.3						\$\$\$\$	Cargillei-Sacher (2010)
d-limonene	1.473	3	0.843	176	48	0.8	\$\$\$\$	Nguyen <i>et al.</i> (2004)
methylsalicylate	1.526	2	1.184	219	96	4.09	\$\$\$\$	Nguyen <i>et al.</i> (2004)
diethylphthalate	1.504	0	1.118	294	156	12	\$\$	Nguyen <i>et al.</i> (2004)
para-cymene	1.491	2	0.857	177	47	0.876	\$\$	Haam <i>et al.</i> (2000)
isopropyl alcohol	1.378	2	81	12	81		\$\$	Haam <i>et al.</i> (2000)

Table 3 (cont'd)

By mixing two or more miscible liquids with refractive indexes above and below the desired value, RI matching can be accomplished. (Cui and Adrian 1997) used a mixture of 1-methanaphthalene, 1-chloronaphthalene, and tetraline to match styrene-divinyl-benzene particles and a benzyl and ethyl alcohol mixture to match silica gel particles. The toxicity of the first mixture is high due to the 1-methanaphthalene component, while the second mixture is highly flammable and may corrode certain plastics. Cargille Labs also produces custom mixtures with refractive indexes from 1.3-2.3. However, these fluids are prohibitively expensive for large scale facilities and can be highly toxic. (Nguyen *et al.* 2004) proposed a method for matching the refractive index and kinematic viscosity of a blood analog for flow visualizations. This same technique could be used to match the kinematic viscosity of water and the RI of the test section material. A mixture of diethyl phthalate and ethanol was chosen by Nguyen *et al.* for their experiments. This group was able to develop equations to predict the kinematic viscosity and refractive index of the fluid mixture as a function of temperature and concentration to approximately 1% error. The use of ethanol required low temperatures and exposure times. (Wedd 2003) also proposes a mixture of isopropyl alcohol and methylnaphthalene.

(Haam *et al.* 2000) suggested the use of p-cymene (1.491) to match the RI of PMMA (RI=1.49). By using a single fluid that matches the refractive index of the test section material, the complicated process of mixing and matching the fluid is eliminated. This in turn reduces experimental setup time and eliminates the possibility of the refractive index changing due to evaporation of the fluid. P-cymene is an aromatic

hydrocarbon and has a rather unpleasant smell and is mildly corrosive with plastic materials. For this reason the test loop section and flow loop must be drained and cleaned for long term storage.

The RI of a solid may also be matched to that of water, effectively eliminating unwanted properties of the fluid. Fluorinated ethylene-propylene (FEP) has a refractive index similar to that of water, however the material is not completely transparent and thick test sections could not be used. This is very limiting as the strength of the material is low and thick cross sections must be used in order to achieve a static test section. (Leis *et al.* 2005) also suggests Teflon AF which has a RI slightly lower than that of water and Nafion. Nafion is a hydrophilic material which allows it to absorb water, further aiding the MRI process. However, this absorption must be accounted for and complicates mass transfer computations.

2.7.1 MRI Experiments

Once an extensive literature review was performed several refractive index fluid candidates were selected for further experimentation and testing: 1) sodium iodide solution 2) p-cymene 3) isopropyl alcohol and methylnaphthalene 4) ethanol and diethyl phthalate and 5) ethanol and benzyl alcohol. To test MRI capabilities of the fluids, a background target was placed beneath a Petri dish filled with 5mm diameter PMMA beads as depicted in figure 17. Finally, MRI fluid was added to the dish and pictures were taken. An Abbe refractometer was used to measure the fluids' RI before they were

added to the Petri dish. All experiments were performed at room temperature (21°C) to eliminate uncertainties generated by temperature differences. The quality of MRI can be determined by observing the distortion of the target behind the Petri dish.

Figure 17 shows the process using water and a sodium iodide (NaI) solution, respectively with MRI. It can be seen that without the MRI the target has been distorted by the PMMA bead but with MRI, the distortion of the target has been reduced or eliminated.

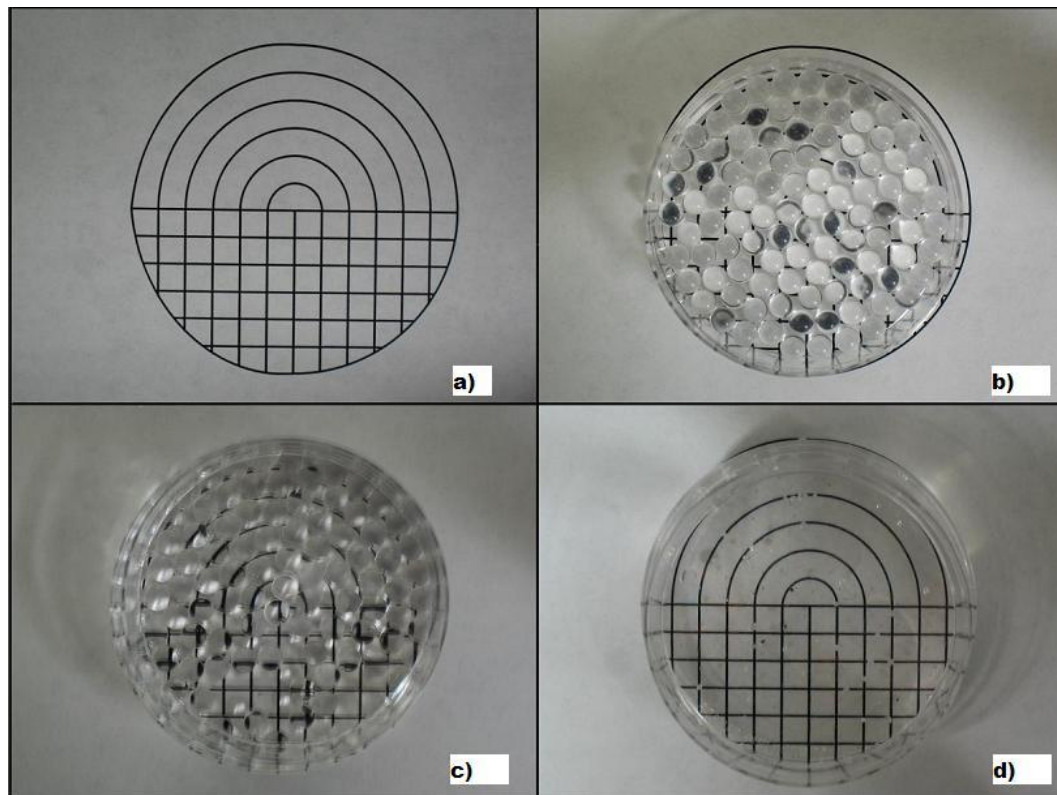


FIGURE 17. Refractive index matching experiments. (a) target (b) Petri dish with PMMA beads and air (c) Petri dish with PMMA beads and water and (d) Petri dish with PMMA beads and NaI.

NaI produced a clear target picture in comparison with the fluids that were tested. The solution was carefully made by weighing the amount of NaI added to the water and thoroughly mixing the solution. The solution was then fine tuned to match the refractive index of the PMMA beads (RI=1.49) using the Abbe refractometer. To test the stability of the fluid two mixtures were made, one was not modified and the other was modified using a 0.1% concentration of sodium thiosulfate ($\text{Na}_2\text{S}_2\text{O}_3$) as recommended by Narrow et al. A measurement of the RI of the mixture solution after the sodium thiosulfate was added indicated a slight decrease. To counteract this effect more sodium iodide was added to the solution to match the RI to that of PMMA. Once the two samples were prepared the mixtures were left in open air containers for two weeks. At the end of the trial, the original solution had turned yellow due to the formation of the I^{3-} , while the mixture containing sodium thiosulfate remained clear. To eliminate the discoloration of the mixture sodium thiosulfate can be added and the solution will return to the clear state. A concentration of ~64 wt. % was needed to match the RI of PMMA. This makes the sodium iodide solutions expensive due to the large amount of NaI needed relative to that of other fluids. P-cymene was chosen because its refractive index (1.491), as measured by the Abbe refractometer, is similar to that of the PMMA particles. The representation of the p-cymene fluid in figure 18 reveals that the slight difference in RI does produce a clear transmission of the target underneath. It should be noted that the large distortion on the left side of the figure is due to the presence of an air bubble. Although the RI of the fluid does not exactly match that of the PMMA, it is very close and produces good images. The p-cymene is aggressive with the PMMA material and

after leaving the fluid in the Petri dish for 1-2 days the PMMA beads began to melt. This reaction necessitated the draining and cleaning of the test section and flow loop after each test. Three alcohol based solutions 1) isopropyl alcohol and diethyl phthalate 2) ethanol and methylnaphthalene and 3) ethanol and benzyl alcohol were also used to match the refractive index and are shown in figure 18.

The refractive indexes of these mixtures were matched PMMA refractive index using the Abbe refractometer. The refractive indexes of isopropyl and ethyl alcohol are lower than that of PMMA, while diethyl phthalate, methylnaphthalene and benzyl alcohol have higher refractive indexes. By mixing fluids with refractive indexes lower and higher than the target value, the refractive index of the mixture can be matched to the target value. The ethanol and methylnaphthalene mixture was found to be the most capable of achieving the desired RI and was followed by the ethanol and benzyl alcohol mixture. Although these mixtures were able to match the refractive index well, other factors such as flammability and reactivity were a concern. The ethanol and benzyl alcohol are highly flammable making them unattractive for use in a large scale experiment. Additionally the ethanol is very aggressive with plastics such as PMMA and immediately starts to melt the beads and Petri dish. The isopropyl alcohol and diethyl phthalate did not achieve matching the refractive index as well as the ethanol solutions; however the mixture was less aggressive than the ethanol solutions and reacted similar to p-cymene liquid.

FEP, a common material used for tubing, has a RI similar to that of water and allows direct MRI. A sample of FEP was tested in water for its RI matching capabilities.

To test the material, a plastic column was filled half way with water and a target was placed behind the column, as depicted in figure 19. A sample of the FEP tubing was placed in the column of water and the quality of the MRI was determined by observations of the distortion of the target due to the FEP tube. In figure 19, the target is less distorted near the mid plane of tube than on the periphery. This is due to increased refraction from the higher contact angle between the water and the tubing. It can also be observed that although the refraction due to the tubing is minimal, the opaqueness of the material still makes it visible in the water. For this reason the thickness of the material must be minimized in order to maximize clarity.

2.7.2 FEP Experiments

The facility achieves optical transparency by the use of matched index of refraction. In this work, the plastic rods are immersed into water with a similar index of refraction. The plastic rods are made out of FEP which has a refractive index of 1.338 and filled with a solution of water and chlorine as was previously explained with a refractive index of 1.333. By matching the index of refraction of both materials the optical transparency is achieved. The working fluid for the tests is water, therefore no correction is necessary and the transparency of the test section is assured.

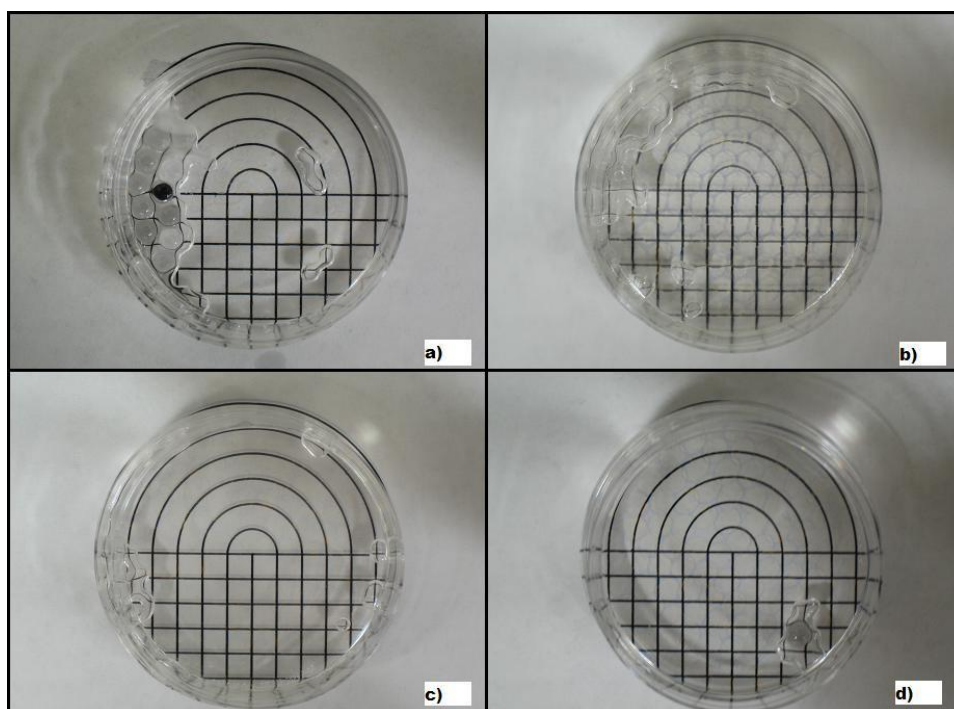
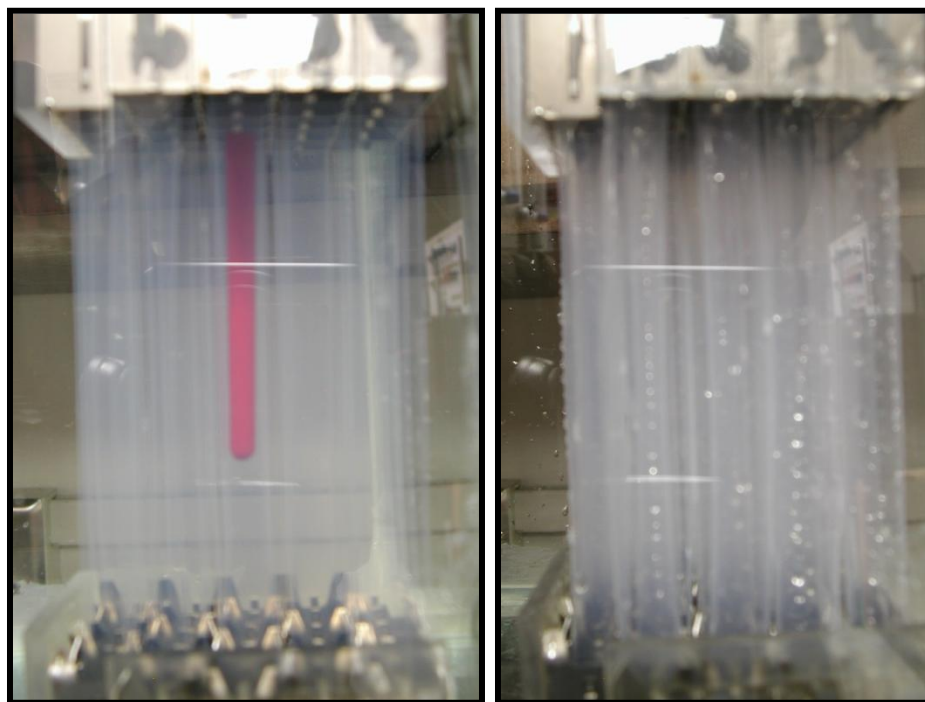


FIGURE 18. Refractive index matching for (a) p-cymene (b) isopropyl alcohol and diethyl phthalate (c) ethanol and methylnaphthalene and (d) ethanol and benzyl alcohol.

Figure 20 shows an emulated hot-rod (red color) embedded in the central rod position. The rod is optically accessible when the bundle is submerged in water. The matched refractive index of water and the FEP pipes allows the visualization of the central rod without considerable disturbances from the rod-layers surrounding it. Figure 20 presents another pictorial of the achieved transparency in the facility. The vertical channel is filled with water up to a certain level in order to demonstrate the immediate clearness and accessibility to any point inside the grid spacer. Figure 20 shows the unobstructed path of a light sheet formed using a blue laser as it passes through the rod

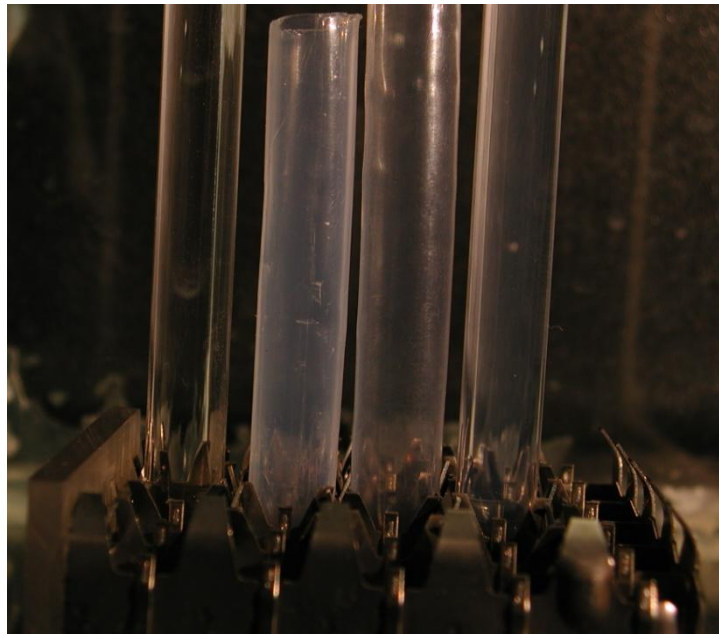
have a wall thickness of 0.254 mm. Figure 22 shows the four rods tested: glass, FEP tube with 0.762 mm wall thickness, FEP with 0.254 wall thickness and Maxphion material. It can be observed that the best match with tap water was achieved by the use of the thin wall thickness in the FEP material. The Maxphion rod provides an exceptional performance in refractive index which is complemented by a good strength (since it is a solid rod) but it proved to be prohibitively expensive.



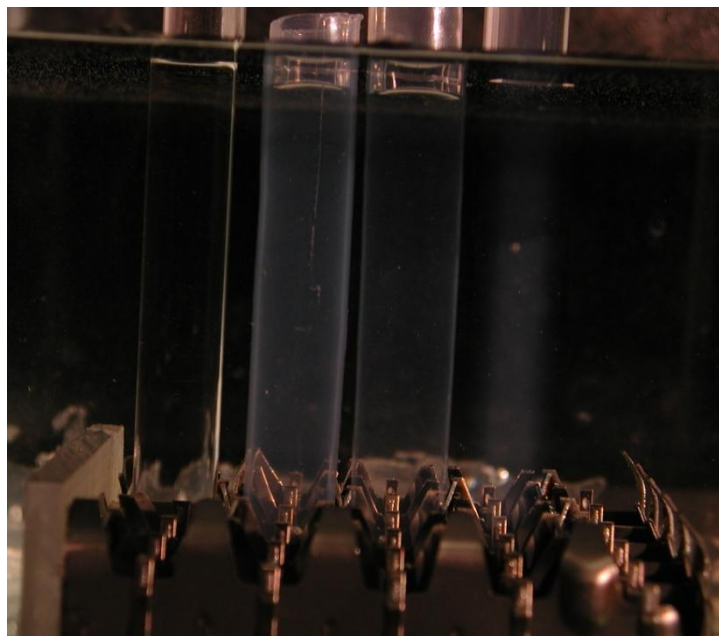
(a) Water
Matched Refractive Index

(b) Air
Not Matched Refractive Index

FIGURE 20. A 5x5 spacer grid segment filled with FEP tubes emulating a fuel-bundle. (a) Pipes immersed in water (b) Pipes immersed in air.



Rods immersed in air



Rods immersed in water

FIGURE 21. Pictorial of the achieved transparency in the facility.

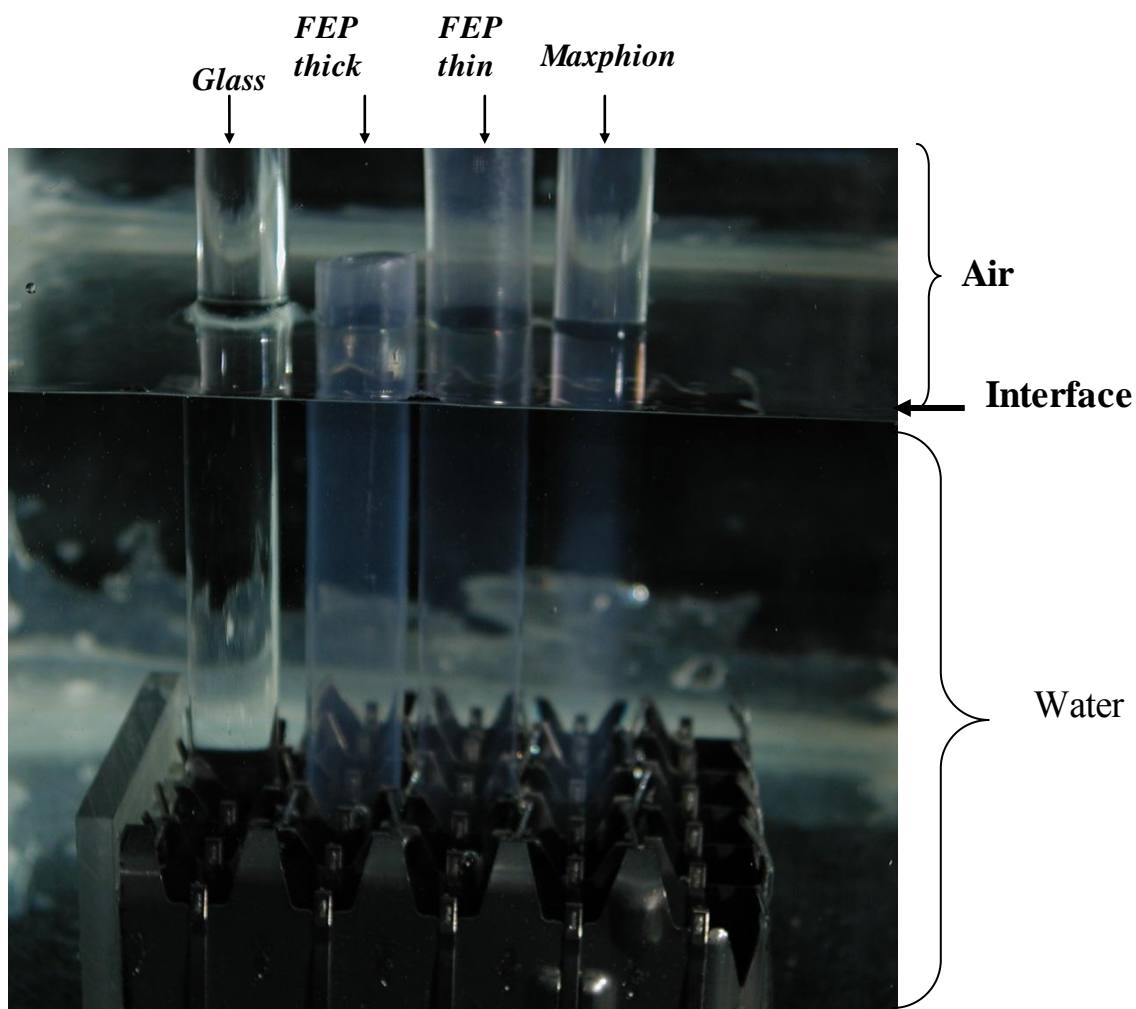


FIGURE 22. Rods of varying materials immersed in water. The camera settings are modified (white balance: incandescent, ISO:400, Exposure:Auto, Manual focus).

The refractive index was matched using FEP tubes with thin walls as the working solids and water as the working liquid. The 5x 5 rod bundle in a spacer grid is shown in figure 23. In order to further demonstrate the quality of the matched refractive index achieved a blue laser light sheet was used to pass through the 5 x 5 rod bundle as shown in figure 24. The laser light passes across the test section without significant reflections.

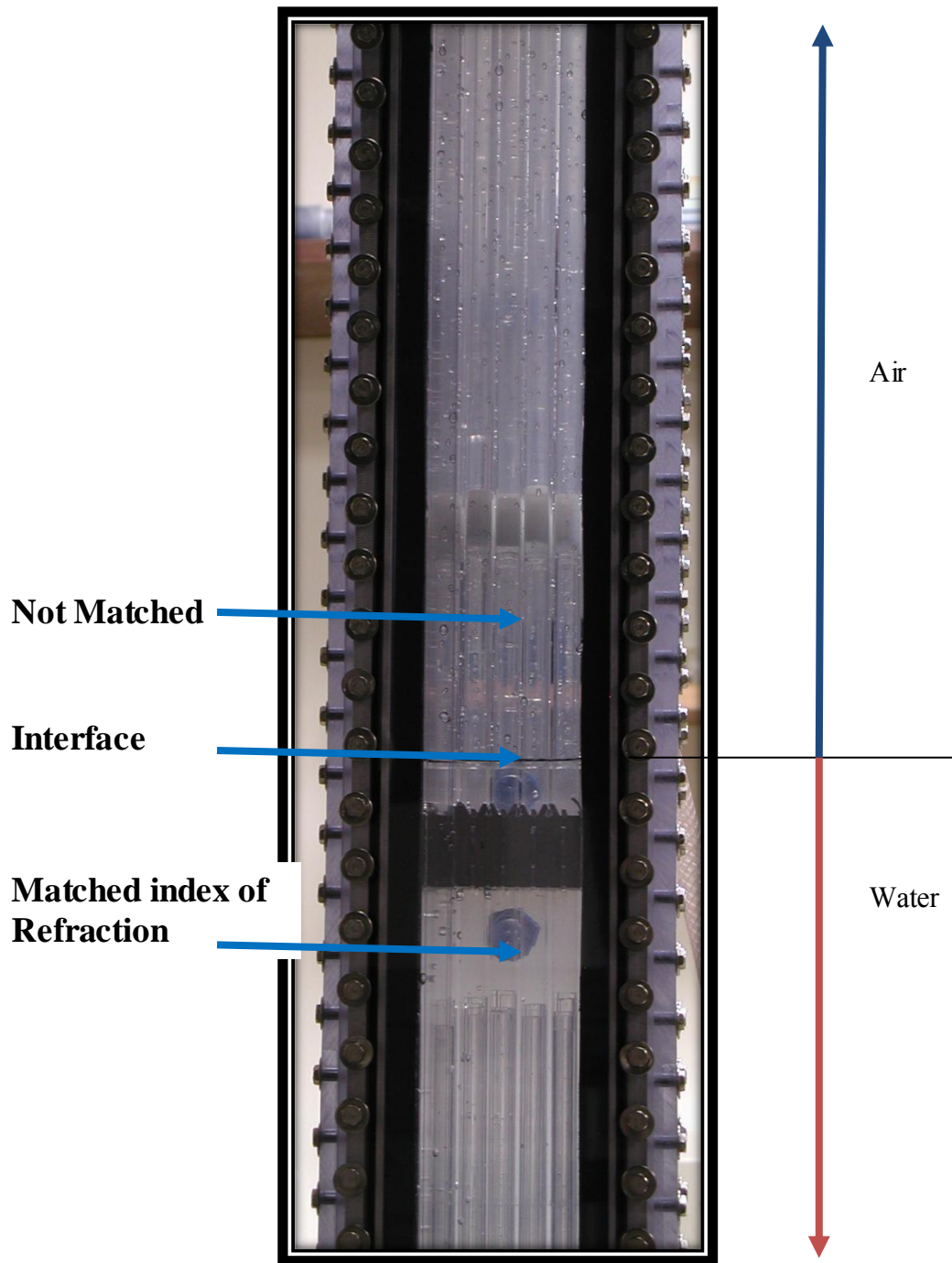


FIGURE 23. Matched index of refraction inside the channel.

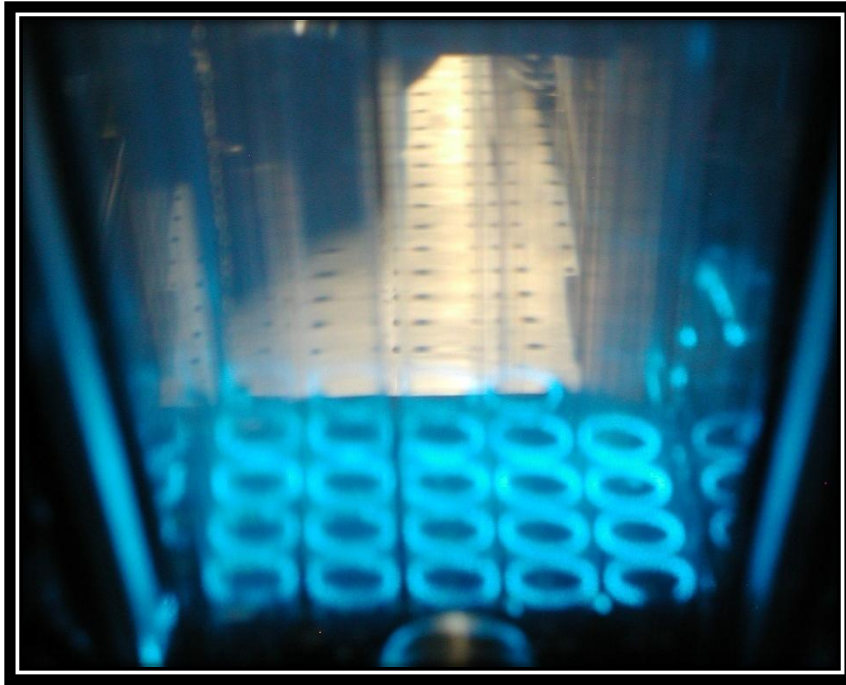


FIGURE 24. Laser sheet passing across the rod bundle without distortion due to a good matching index of refraction.

2.8 Pressure System

Various other techniques such as shadowgraphy for flow visualization and pressure measurements were implemented along with PIV in order to obtain additional relevant information about the complex flow characteristics. This section describes in more detail the pressure acquisition system. The pressure acquisition system consists of five gage pressure transducers purchased from GE sensing company (Druck 4020) which were wall flushed at specific locations along the experimental facility. These pressure gages have a manufacturer accuracy of $\pm 0.08\%$ FS of Best Straight Line (BSL) and their acceleration sensitivity is 0.04% FS/g at 350 mbar (5psi).

Figure 25 shows the physical description of the transducers used. Technical characteristics of this sensor can be found at manufacturer's website .



FIGURE 25. Pressure transducer model PDCR 4020.

The wall flush procedure was of relevance in this work since it was considered that the ratio boundary layer thickness (δ) to the Tap diameter (D) was of importance for accurate measurements. In this case, the influence of this ratio was considered in the design process. The tap diameter for pressure acquisition is 0.1 cm and was drilled with a 60 degree internal cone connection. In other words, the 0.1 cm diameter did not persist across the wall thickness and the diameter increases gradually from 0.1 to 1.8 cm in order to fit the pressure connector as shown in figure 26.

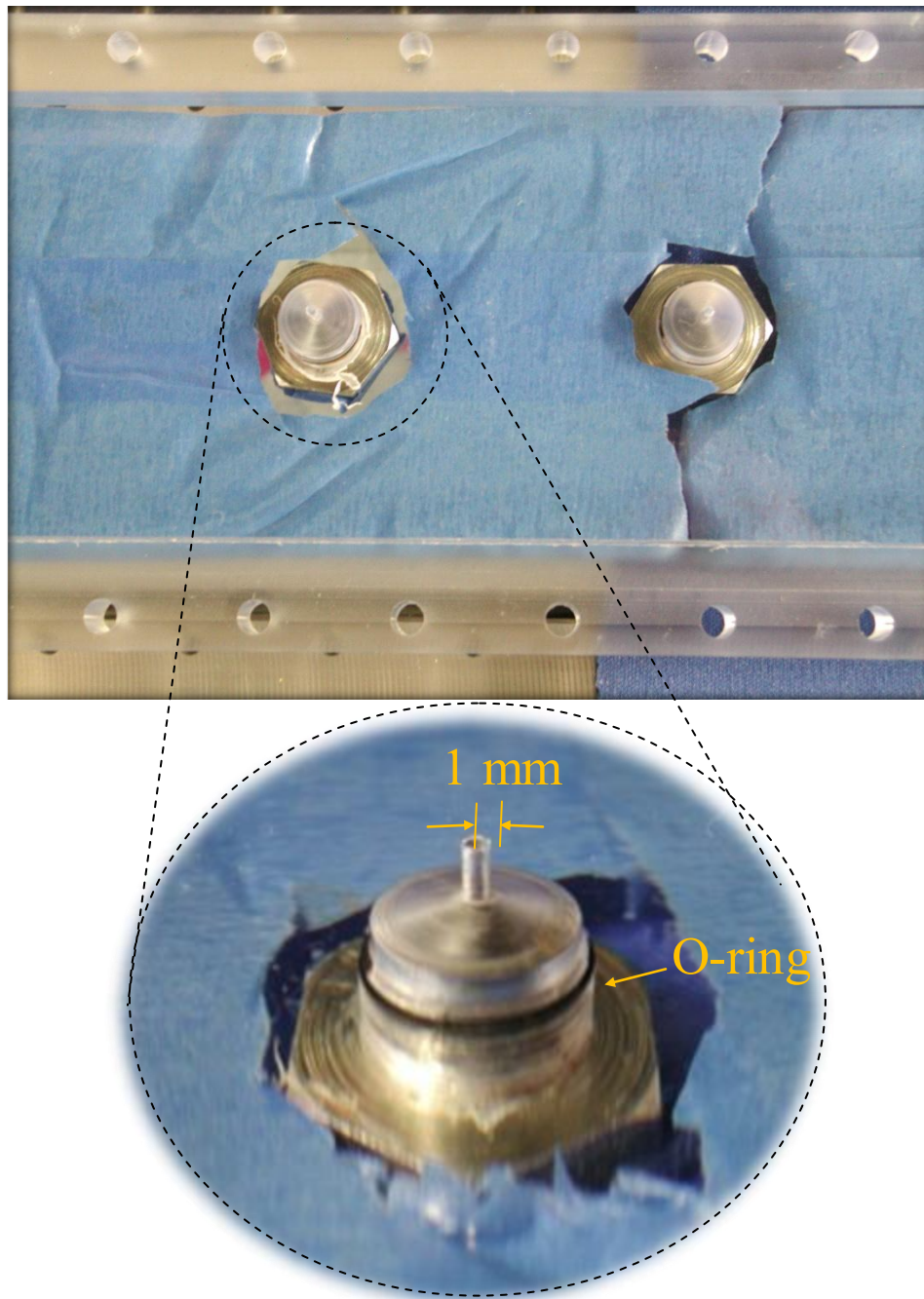


FIGURE 26. Wall pressure tap flushed in the back observation window.

The pressure transducers were located immediately below and above of two of the spacer grids. The fifth transducer was located between two of the spacer grids as shown in figure 27 in a spacer free zone. The output voltage signal from the pressure transducers was conditioned using a signal conditioning module NI-SCXI 1600-1314. This module had a 16 bit analog to digital converter and provided the excitation source for the transducers. In-house developed manual electronic triggers and counters were used in addition to the former equipment for pressure data acquisition.

The acquired data sets were intended to get acquainted with the level of pressure fluctuations in the system. The acquired data was recorded at different sampling rates and for various time spans in an effort to maximize the efficiency of the data collection. Two main sampling rates were used: 1000 and 500 Hz. The time span proposed for these experiments are in the range of 10 to 100 seconds of continuous pressure recording. The tests were conducted independently at various flow conditions and repeatability of the flow behavior tested. The pressure measurements were synchronized with velocity measurements as explained previously in the data acquisition section.

2.8.1 Photographic Pressure Fluctuations Evaluation Method

A novel pressure fluctuation evaluation method was implemented during this investigation. The method consisted in acquiring photographic images of a water tested volume contained in the FEP tubes. The images were then analyzed using an in-house

pattern recognition technique to detect pressure fluctuations caused by the flow. This section describes the photographic system for pressure fluctuations detection.

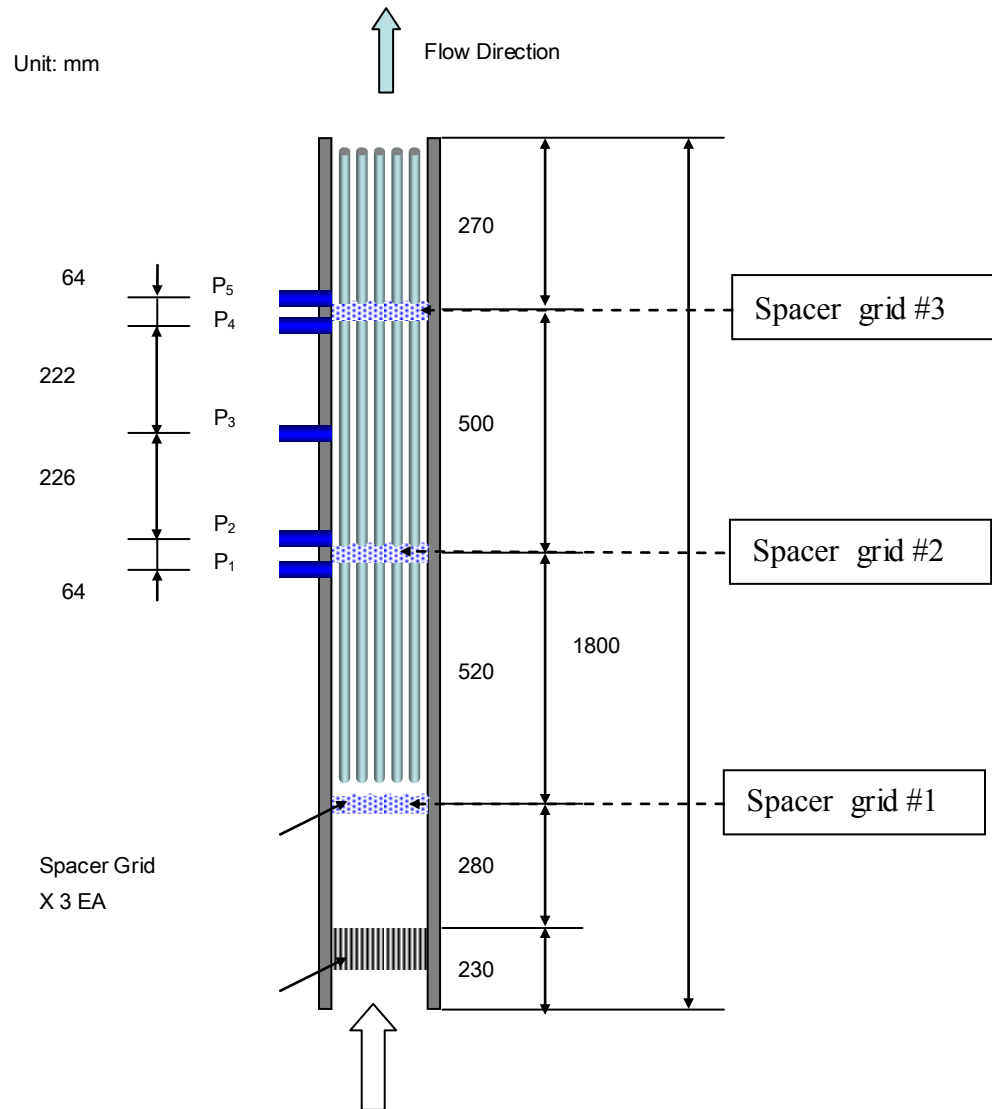


FIGURE 27. Pressure transducer location.

The present research work used FEP hollow tubes to simulate the fuel rods of nuclear reactors. The tubes were filled with a water-chlorine solution from bottom to top and sealed in both ends, more details about the pipes can be found in the bundle array section of this work. In three of the pipes, the water-chlorine solution was allowed to have an air filled section therefore the water solution formed a meniscus in this section. The meniscus formed inside the tube due to the surface tension of the water was used as an indicative of the pressure fluctuations induced by the liquid flowing along the rods outside surface area. Figure 28 shows a sketch of the meniscus formed at the selected tube. The technique took advantage from the change in density and refractive index of the air and water contained in the pipe. Changes in the outside pressure affected the meniscus position which was tracked using a pattern recognition technique.

The main idea behind the matching technique was to perform a cross-correlation calculation of the meniscus position when there was a stagnant fluid condition in the channel and compare the change in its position when the fluid was flowing through the test section. The pictures were taken using a back-illumination (shadowgraphy) set-up and the results cross-correlated with a template. The following section describes the algorithm basic principle.

The pattern matching algorithm consisted of two phases: the template learning phase and the matching phase. The template learning phase was time consuming and was best performed offline. Once this phase was completed, however, the matching phase was sped up considerably and could be performed in real time if desired. The learning phase consisted of three parts: pseudo-random sampling, stability analysis, and

edge detection. In the pseudo-random (or sub-random) sampling phase, a set of pixels was taken from the template image using a low-discrepancy sequence, such as Sobol or Halton.

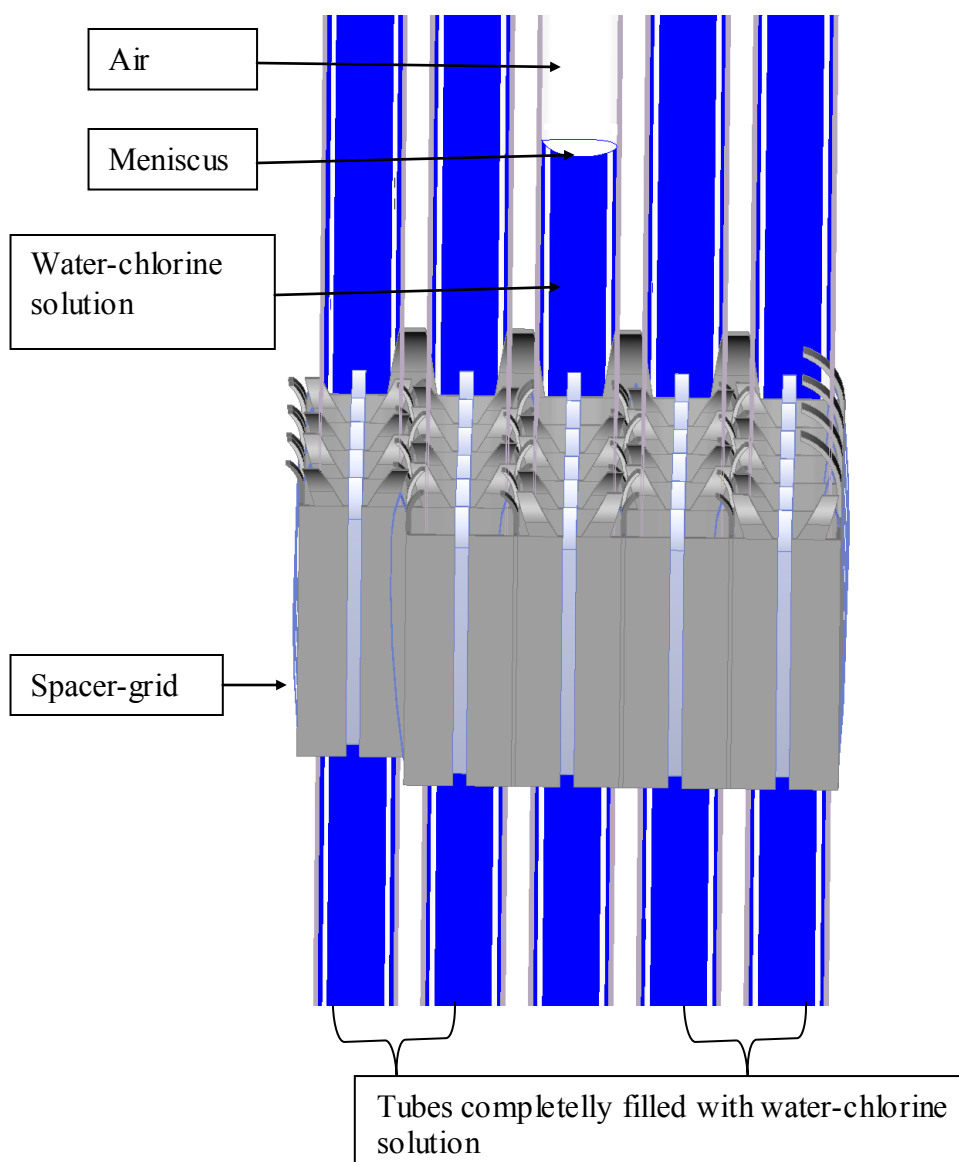


FIGURE 28. Sketch of the meniscus formed at the selected tube.

These pixels were used during the matching phase to detect likely template locations in the image while significantly reducing the number of comparisons that need to be made. After this subset of pixels was determined, a stability analysis was performed to determine the radius around each chosen pixel for which the neighboring pixel values correlate highly to the chosen pixel. Optionally, sampled pixels can be discarded that do not have a stable neighborhood of a sufficient size as determined by the user. This further reduced the number of pixels that will be used for comparison purposes without negatively impacting the accuracy of the algorithm. The algorithm then sorted the chosen pixel subset according to stable neighborhood size (2x2, 3x3, etc.). These neighborhood sizes were used by the algorithm to determine an appropriate step size for later cross correlation. The stability neighborhood and step size data was associated with each chosen pixel and these values were stored for matching purposes later. The matching phase consisted of a correlation calculation with a number of iterations that were performed in a coarse-to-fine manner. First the subset of pixels that were sampled during the learning phase with the largest stability neighborhood was compared with the target image using an appropriately determined step size. For example, a subset of pixels with a stability neighborhood of size $(n \times n)$ pixels was compared to the target image using a stepsize of n . The locations in the target image for which the correlation calculation returned an appropriately high correlation factor were recorded. Then, the subset of pixels from the learning phase with the next smallest stability neighborhood was chosen. These pixels were then compared to the target image using the same correlation calculation but only for the more promising locations

recorded in the first iteration with high correlation values. The correlation values from this second iteration were then used to eliminate locations chosen for the first iteration for which the finer-grained correlation calculation did not return an appropriately high correlation factor. The algorithm proceeded in this manner, using progressively finer-grained searches (and correspondingly finer step sizes) until all of the sampled pixels from the learning phase was used. Alternatively, the algorithm may also at this point perform a final correlation calculation using all pixels from the template at the remaining promising locations. Figure 29 shows an example of the photographed meniscus inside the tube. The template used for the image recognition pattern is shown along with a plot of the cross-correlation coefficient obtained. The boxes delineated by the light blue lines represent each of the templates used during the image recognition process. It can be observed that the meniscus delineates a straight line under stagnant conditions. When template number one was used, the discrepancies of the shadow produced by the meniscus through time were captured by the cross-correlation calculation, denoting a low value when the meniscus “crosses” the small image template formed by box 1 shown in figure 29.

The figure shows the evolution of the cross correlation factor along with example images of the meniscus in order to provide a better visual understanding of the meniscus fluctuations. The fluctuations frequency was calculated by performing a Fast Fourier Transform (FFT) of the cross-correlation signal used for the image pattern recognition technique. The plot represents the evolution of the cross-correlation coefficient through time.

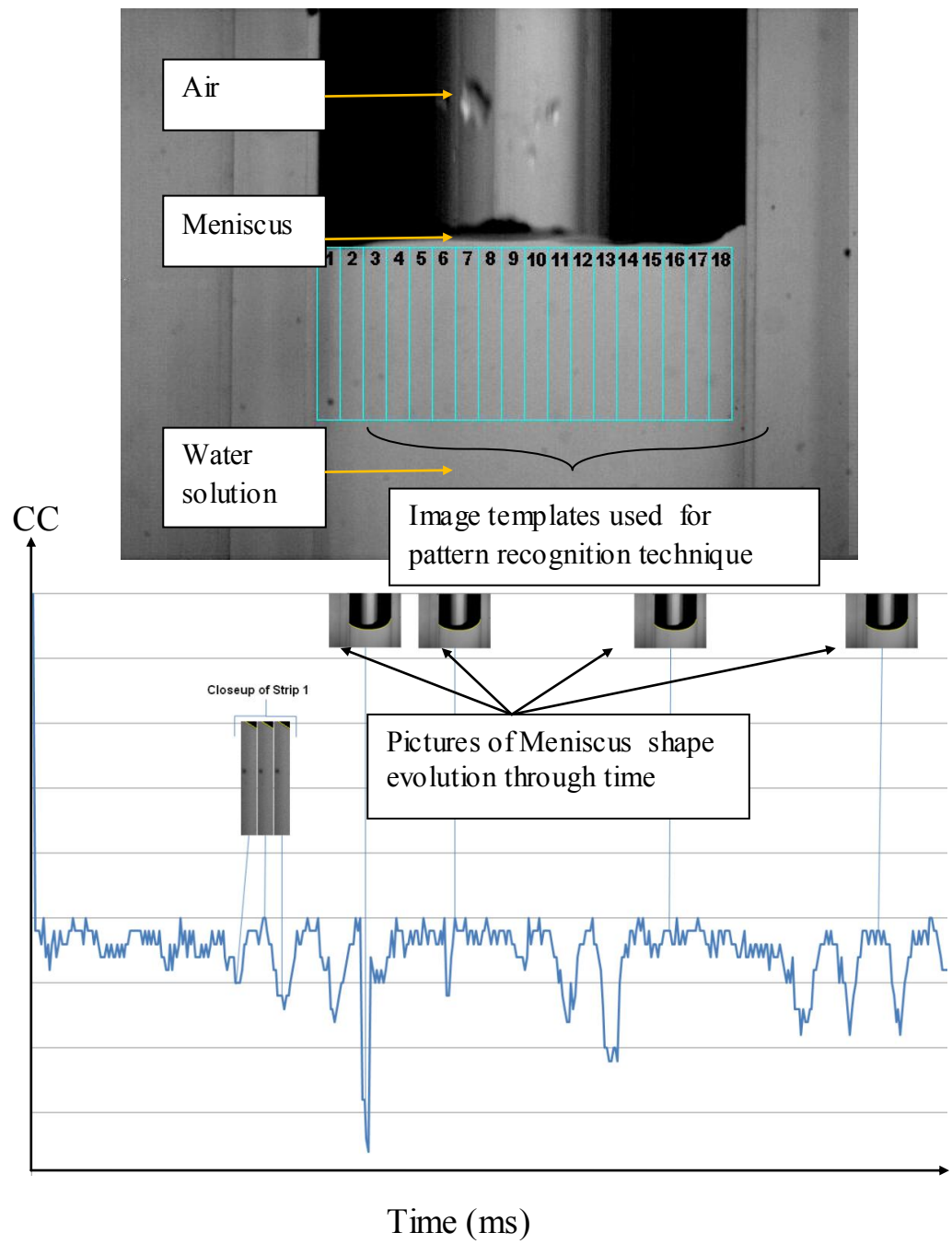


FIGURE 29. Example of the meniscus formed inside the pipe and the image template .

2.9 Bundle Array and Grids

Two different spacer-grids were tested in this investigation. The first investigated grid was a typical grid used for Boiling Water Reactors (BWR) with swirl vanes. The second tested grid was typical of Pressurized Water Reactor (PWR) with swirl type vanes. The following section describes the pertinent details for each bundle configuration. A similar experimental approach was followed for each tested grid; however the dimension in the test rig varied for each case.

2.9.1 Grid1

The first task of the present work was focused on obtaining a detailed fluid flow structure and an understanding of the complex flow within a fuel bundle with spacer grids. The first selected spacer grid was the AREVA UltraflowTM spacer which is part of the ATRIUMTM 10 fuel assembly design for Boiling Water Reactors (BWR). The UltraflowTM design was characterized by an egg-crate shape with swirl vanes and strip springs as shown in figure 30. This particular design holds 91 rods arranged into a 10 x 10 configuration with a central square water channel.

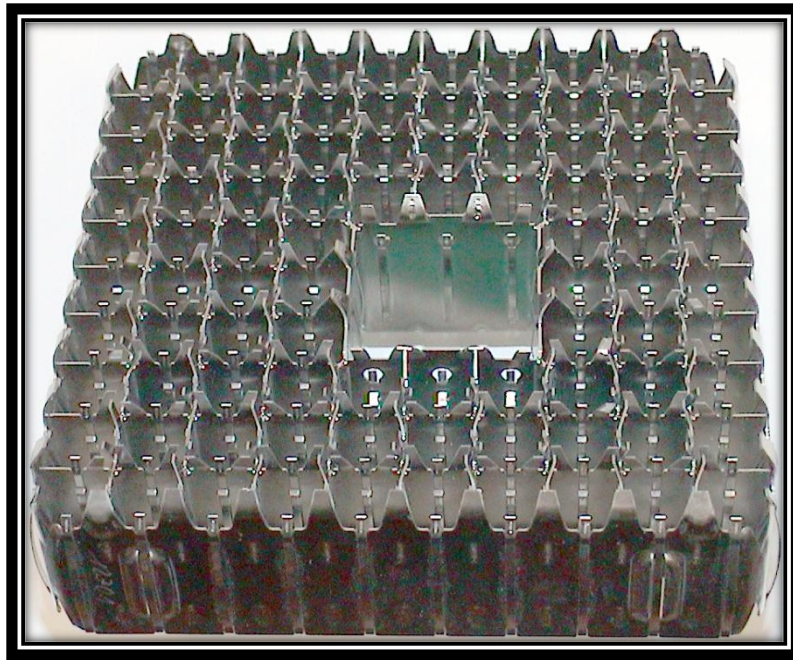


FIGURE 30. AREVA's Ultraflow™ spacer design.

In this study, a subsection of the Ultraflow™ spacer was used to perform experimentation on it. This subsection was extracted directly from one of the real spacers having a final geometry containing 24 egg-crate spaces and a void space designated for a water channel as shown in figure 31. The experimental rod assembly was composed of 24 plastic rods placed inside the egg-crated spaces of the spacer subsection and one square plastic channel arranged into a 5 x 5 matrix configuration as shown in figure 32..

The rods are fabricated using a fluorinated ethylene-propylene (FEP) plastic with dimensions of 10.6 OD x 10.16 ID x 1270 mm long with a ± 0.0762 mm tolerance in all dimensions.

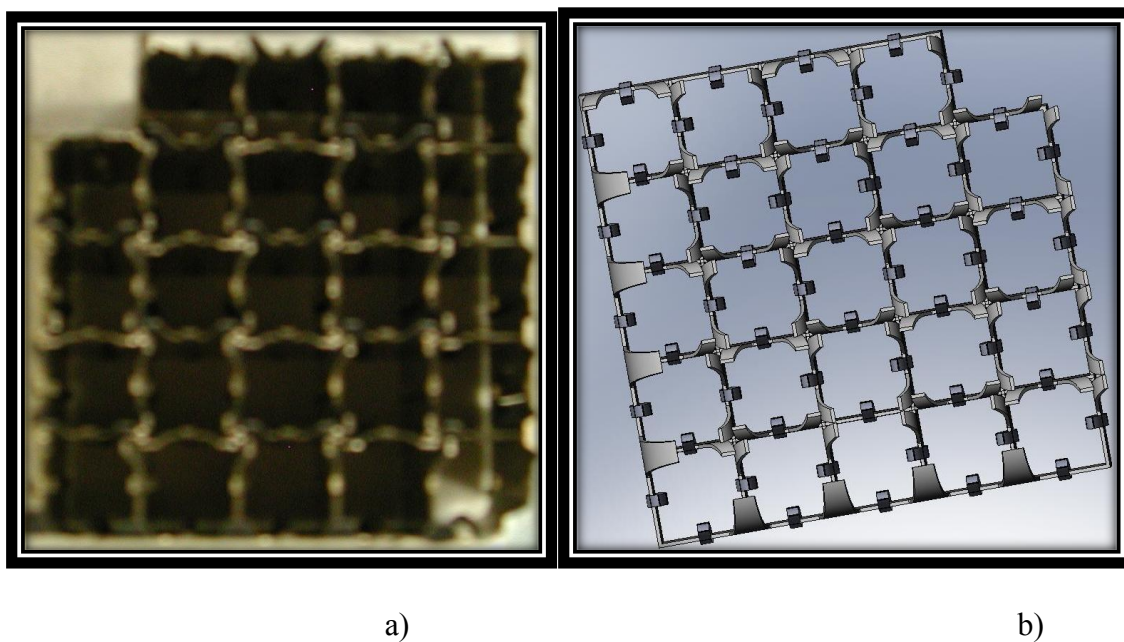


FIGURE 31. Subsection of Ultraflow used for experimentation (a) Picture of the subsection (b) CAD of the subsection.

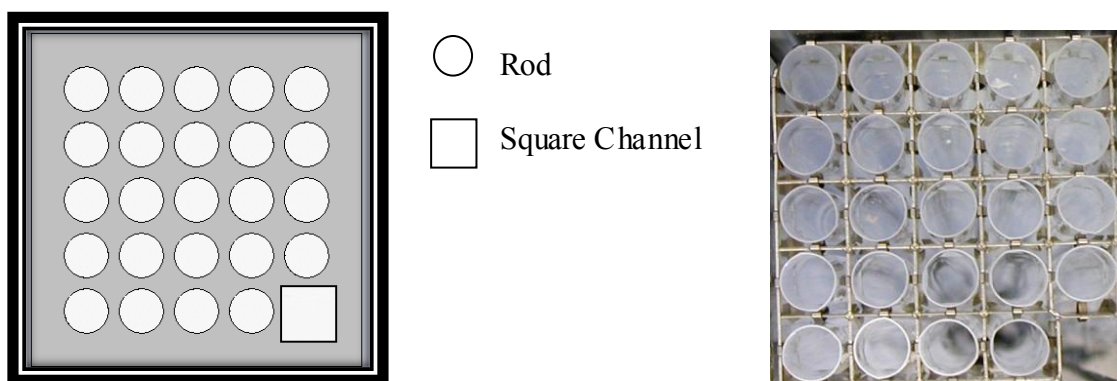


FIGURE 32. Experimental rod bundle assembly.

These dimensions followed closely the dimensions of the real fuel rod used in the Ultraflow spacers. The rods were closed at each end using a coned aluminum caps as

shown in Figure 33 and filled with a solution of water and chlorine in a 5% by volume concentration.

This solution allowed keeping the refractive index of water close to its original value of 1.33 and the chlorine restricted the growth of any kind of bacteria or algae in the fluid which may alter the optical transparency of the stagnant solution inside the rods.

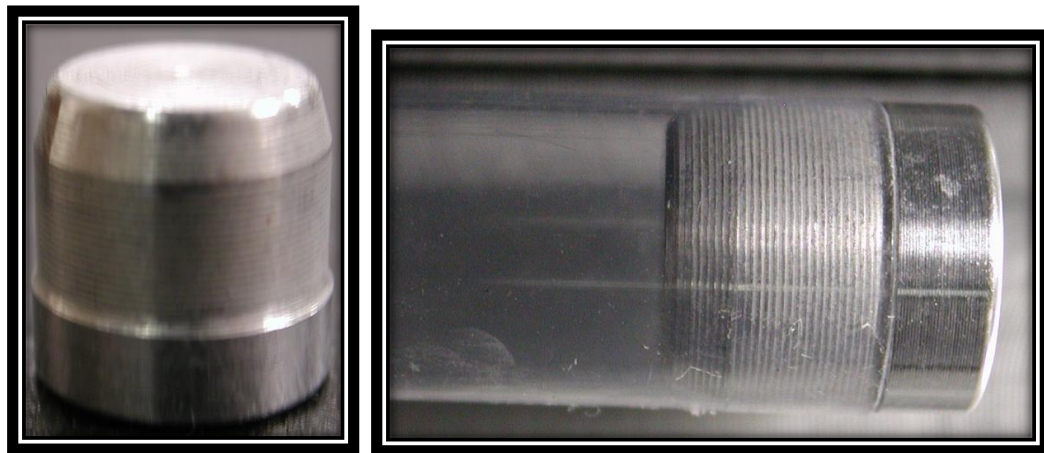


FIGURE 33. Plastic rod with end caps (a) Aluminum coned cap (b) Rod with end caps.

The 24 rods were reinforced with solid plastic rods that added strength to the rods. The reinforcement was done by introducing solid plastic rods inside the FEP shallow rods at strategic locations along the rods. The test section where the PIV measurement was obtained did not have the solid rods. This allowed a clear test section for flow visualization and PIV measurements. Therefore, the “strength- rods” did not disturb in any way the original shape, smoothness, geometry or properties of the FEP

rods. Figure 34 shows the spacers with the rods in place inside the channel. The position of the four spacer-grids used in this investigation is shown in figure 35. The interior plastic u-shaped channel and the grid dimensions are shown in figure 36. This figure presents the main characteristics of the geometry containing the grids for the CFD simulations.

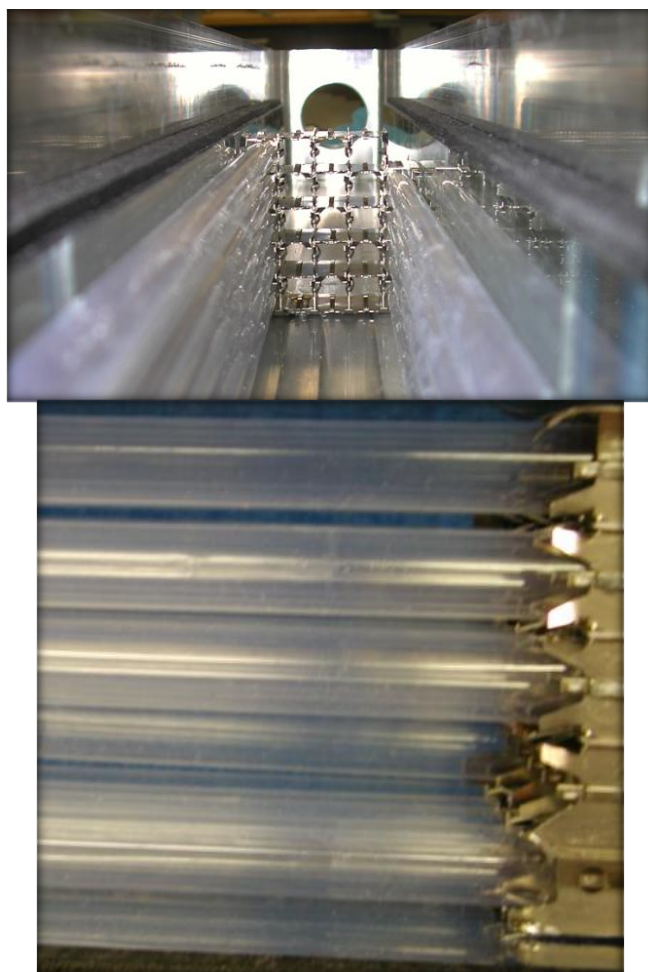


FIGURE 34. Spacers with rods.

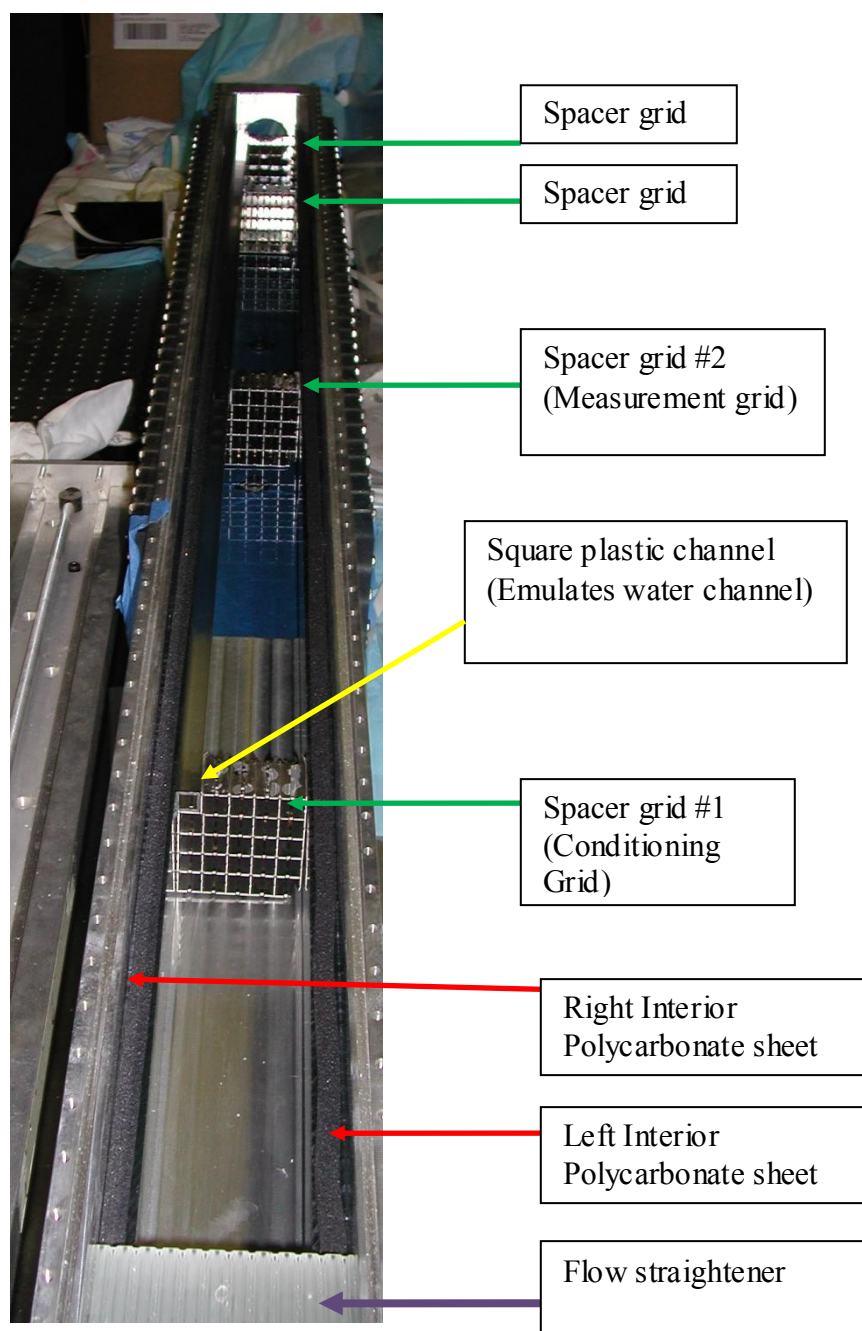


FIGURE 35. Aluminum frame with two internal polycarbonate sheets and grids.

The test facility consisted of four (4) grid spacers distributed along the rod's height. The spacer grids had a pitch of 510.54 mm. This pitch was similar to the one in the Ultraflow spacer of the BWR. It should be noticed that the last spacer had a different pitch of 254 mm with respect to the spacer located immediate before. This spacer was located near the channel's outlet and after the measurement zone and it also provided strength and stability to the rod array.

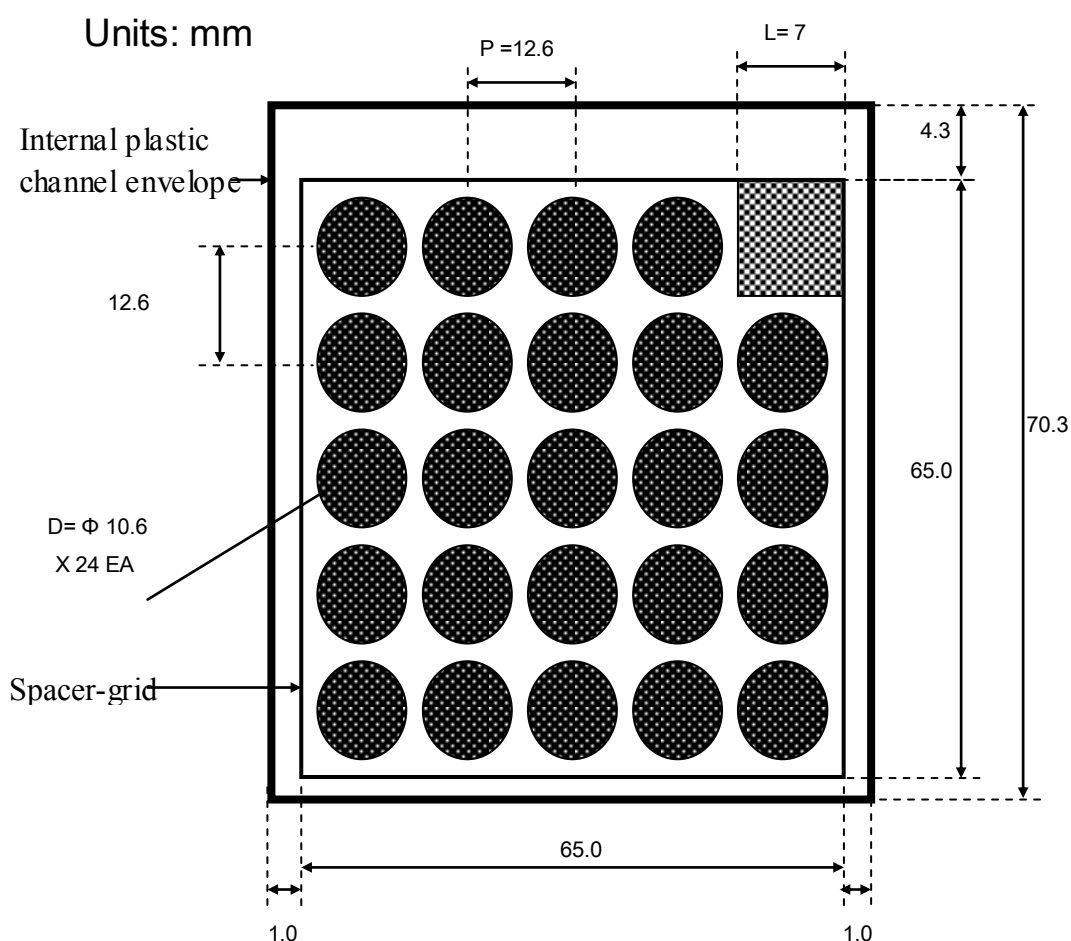


FIGURE 36. Rod bundle with spacer grid 1 and channel envelope dimensions.

The channel and all its internal components were placed on a prefabricated base frame that assured the verticality of the channel with respect to the floor as shown in figure 37. The base was fabricated of a combination of stainless-steel and aluminum.

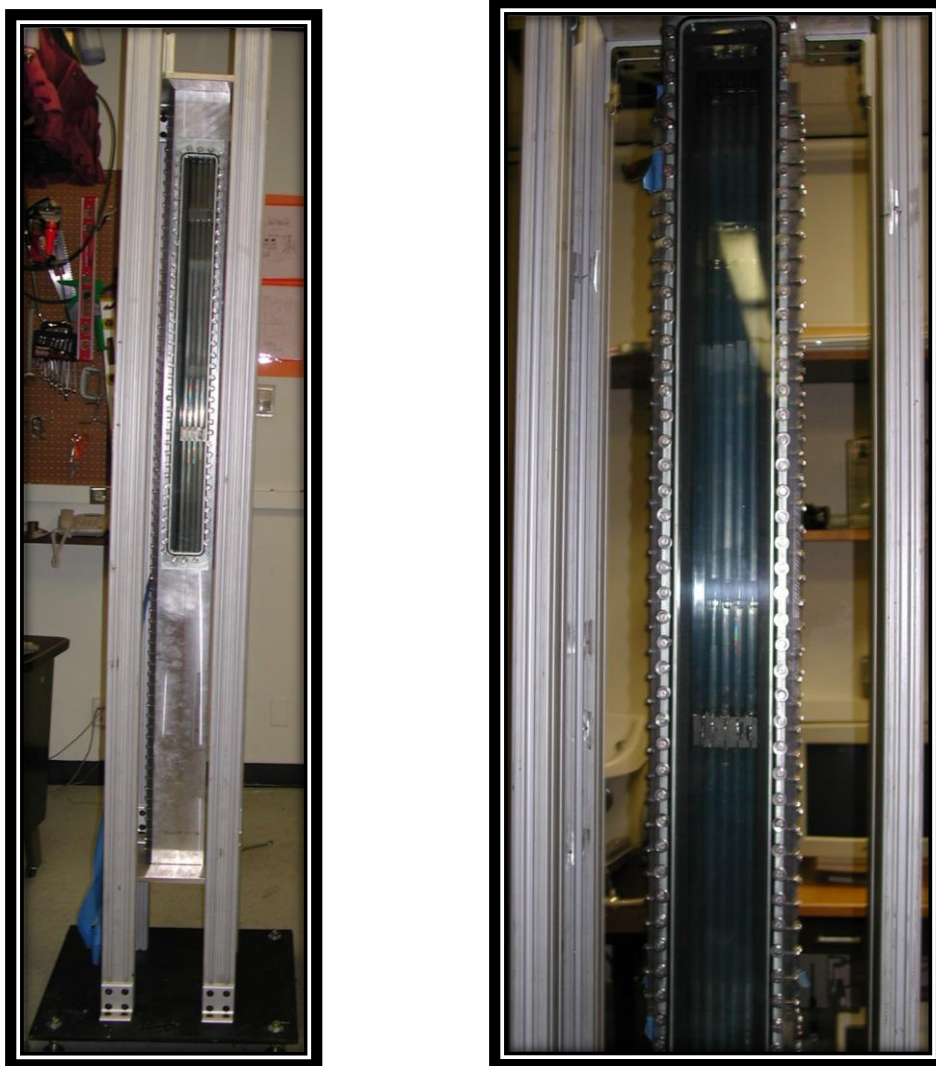


FIGURE 37. Channel mounted on base frame (a) General view (b) Close-up measurement zone.

Three ball type inclinometers were attached to the channel's face walls in order to correct the vertical position of the channel with respect to the floor with an accuracy of ± 0.5 degree. The vertical position of the channel was verified by the use of a laser level and six bubble levels placed at the four channel faces and three sides of the base

2.9.2 Grid 2

A similar procedure for the bundle construction was followed for the second spacer grid tested. The second selected spacer grid was the generic WestinghouseTM spacer fuel assembly design for Pressurized Water Reactors (PWR). The Westinghouse design was characterized by an egg-crate shape with split vanes. In this study, a subsection of the WestinghouseTM spacer was used to perform experimentation on it. This subsection was extracted directly from one of the real spacers having a final geometry containing 25 egg-crate spaces in a configuration of 5 x 5 rods as shown in figure 38.

The rods were fabricated using a fluorinated ethylene-propylene (FEP) plastic with dimensions of 9.5 OD x 9 ID x 1270 mm long with a ± 0.0762 mm tolerance in all dimensions. These dimensions followed closely the dimensions of the real fuel rod used in the generic Westinghouse spacers. The rods were closed at each end using a coned aluminum caps as shown in figure 33 and filled with a solution of water and chlorine in a 5% by volume concentration. This solution allowed keeping the refractive index of water close to its original value of 1.33 and the chlorine restricted the growth of any kind of

bacteria or algae in the fluid which may alter the optical transparency of the stagnant solution inside the rods.

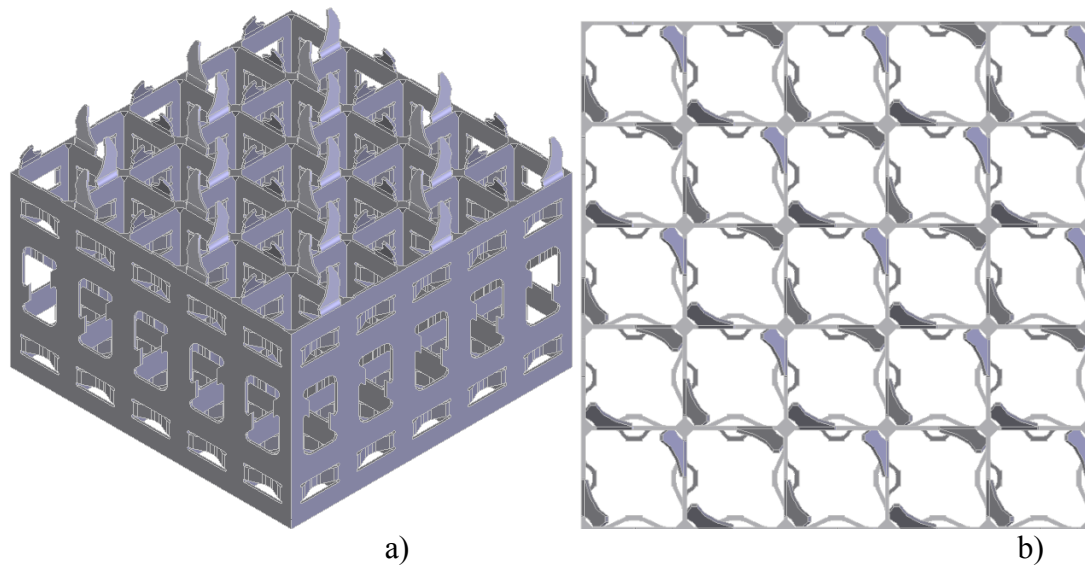


FIGURE 38. 5x5 subsection of the second grid used for experimentation (generic Westinghouse) (a) Isometric view (b) Top view.

As mentioned previously, a similar procedure was used to locate the FEP tubes inside the grid. This configuration also utilized solid plastic rods in order to increase the strength and stability of the FEP rods. It should be noticed that there was a change in the inner dimension of the internal plastic channel envelope. However, the aluminum frame was the same as the one used for the testing of grid 1. The test facility consisted of four (4) grid spacers distributed along the rod's height. The spacer grids had a distance between the lower edges of the first grid to the second one of 510.54 mm. This rod pitch was similar to the one in the generic Westinghouse spacer of the PWR, $P = 12.6$ mm. It should be noticed that the last spacer had a different spacer pitch of 254 mm with respect

to the spacer located immediate before. This spacer was located near the channel's outlet and after the measurement zone and it also provided strength and stability to the rod arrays shown in figure 39.

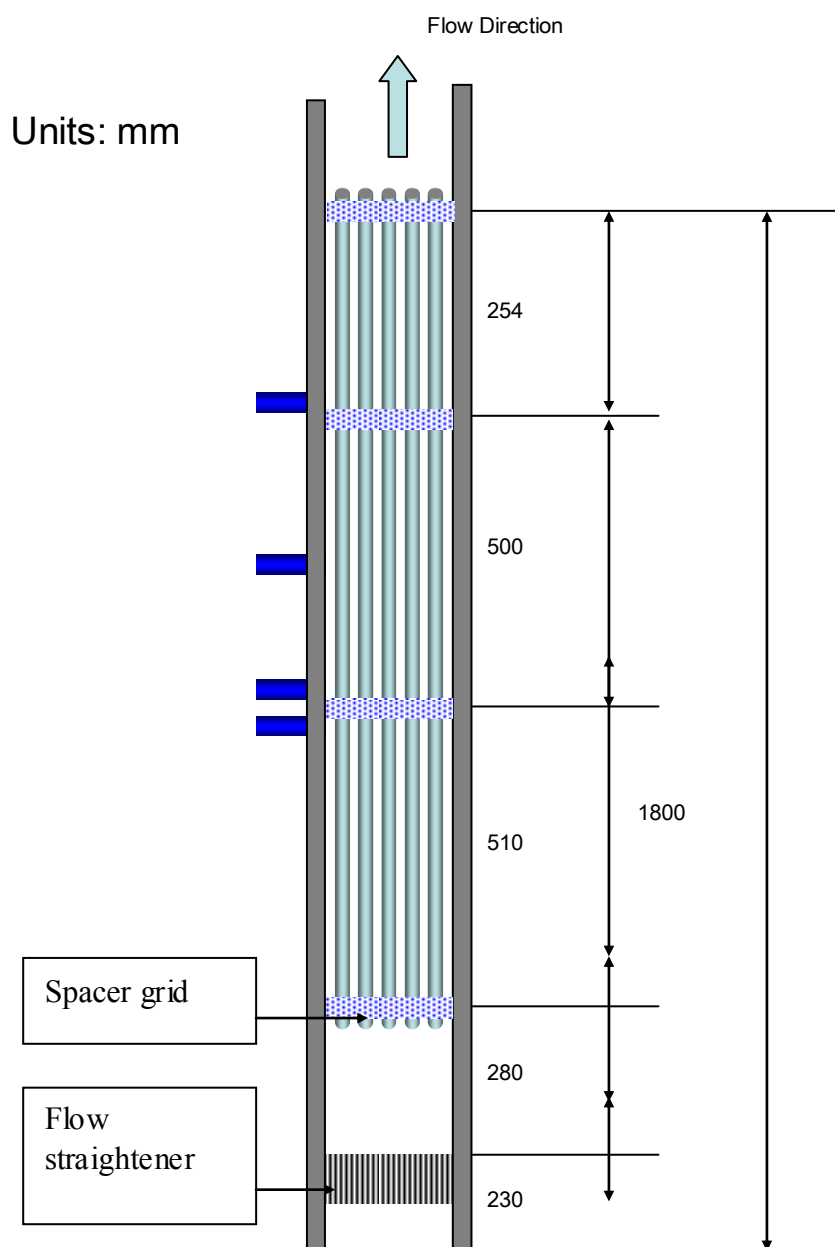


FIGURE 39. Spacer grid distance.

The dimensions of the spacer-grid when located inside the envelope plastic channel for the grid 2 are shown in figure 40. It should be noticed that there was a gap between the edge of the grid and the interior wall of the plastic channel. This space was denominated as bypass flow and the results will refer to this space with the same name.

A summary of the main dimensions of both grids and their respective flow casing is shown in Table 4.

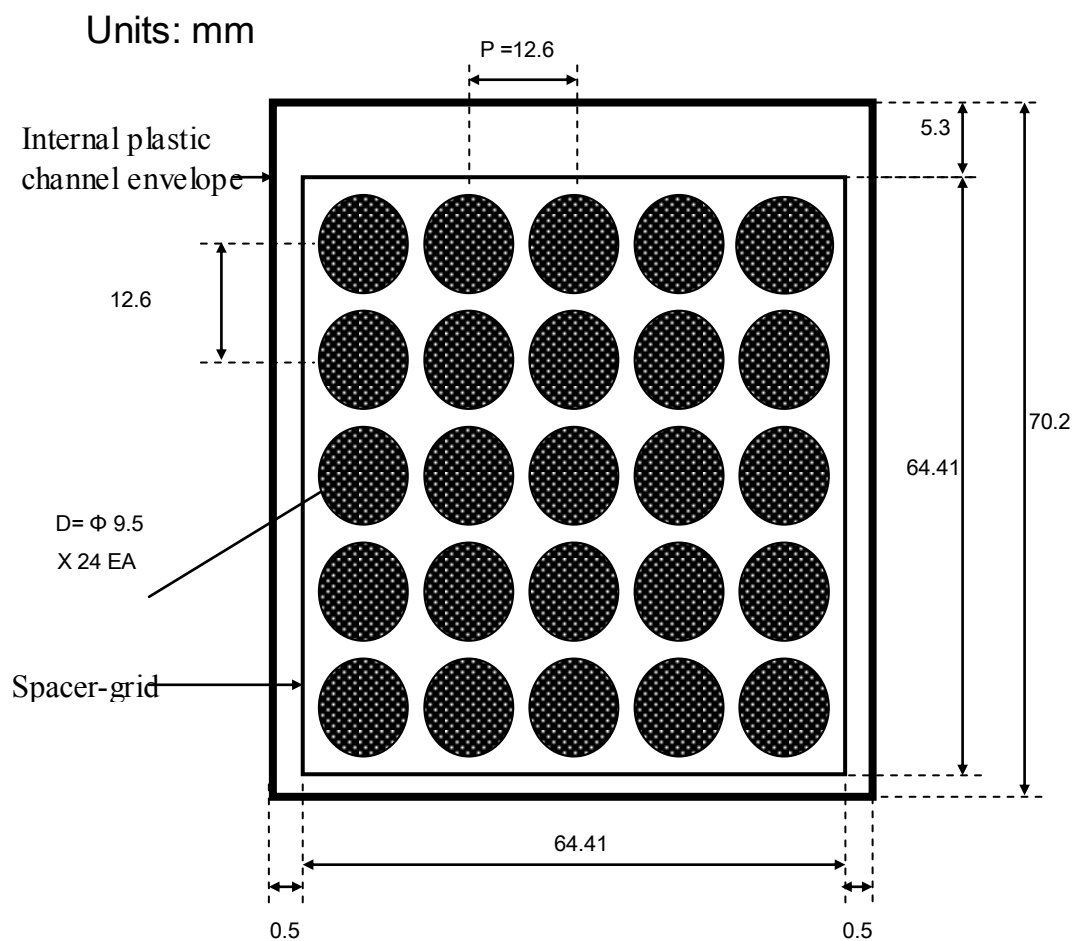
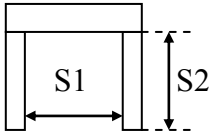
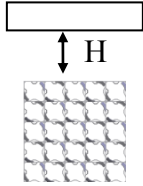
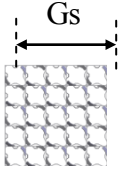


FIGURE 40. Rod bundle with spacer grid 2 and channel envelope dimensions.

	U-shaped plastic internal channel dimensions (mm)	By-pass gap height (mm)	Grid dimensions (mm)
			
Grid 1	67 x 70.3	4.3	65
Grid 2	65.41 x 70.2	5.3	64.41

	Pitch (P) (mm)	Average rod outside diameter (mm)	Hydraulic diameter (Dh)	Distance between spacers (mm)
Grid 1	12.6	10.6	10.49	510.54
Grid 2	12.6	9.5	11.78	510.54

Table 4 Comparison table showing the two grids tested and their respective u-shaped plastic internal channel dimensions

CHAPTER III

DATA ANALYSIS

The obtained data using the experimental set-up explained in chapter II was analyzed using different methodologies. This chapter will address the basic background necessary for a better understanding of the results presented in chapter IV. The turbulent flow contains many interacting vortical structures. These structures are so complex in their spatial distribution and temporal evolution that the dynamical cause and effect relationships are difficult to clarify. In order to attain a better understanding of the complicated dynamics found in turbulent flow in rod bundles, several analysis techniques were applied. These techniques are presented in this chapter.

3.1 Background

Turbulence is the most common, the most important and the most complicated kind of fluid motion. The equations which express Newton's second law for a Newtonian viscous fluid are the Navier-Stokes equations. There are three, one for each of the components of momentum. They can be derived by control volume analysis. The fourth equation, which completes the set for the four variables U , V , W and p , is the continuity equation. Despite their physical simplicity, the equations are very difficult to solve: the four variables U , V , W and p are in general functions of x , y , z and t and the spatial scales of their variation can, in principle, take any values between those imposed

by the size of the container in which the fluid is flowing and those of the molecular motion. Except in low-density gas flows and shock waves, viscosity prevents spatial scales from extending down into the molecular range and the fluid can be regarded as a continuum. The most general case of fluid motion, exhibiting all the complications allowed by the Navier-Stokes equations is called turbulence and its study leans heavily on experiments.

3.1.1 Equations of Motion

The principles of conservation of mass and momentum are expressed in the continuity and Navier-Stokes equations respectively:

$$\frac{\partial u_i}{\partial x_i} = 0 \quad (1)$$

$$\frac{\partial u_i}{\partial t} + u_j \frac{\partial u_i}{\partial x_j} = -\frac{1}{\rho} \frac{\partial p}{\partial x_i} + \nu \nabla^2 u_i \quad (2)$$

where u_i is the i th component of velocity, x_j is the spatial coordinate in the j th direction, p is the pressure, ρ is the fluid density, ν is the fluid kinematic viscosity. For turbulent flows, the instantaneous velocity u is decomposed into mean and fluctuating components using the “Reynolds decomposition” as it is shown in equation (3).

$$u = U + u' \quad (3)$$

where U is the mean velocity and u' is the velocity fluctuation.

The average process to obtain the mean component of the velocity was carried out using equation (4).: Substituting the instantaneous velocity in its decomposed form into the streamwise component of the Navier-Stokes equation, averaging each term and enforcing conservation of mass and the mean momentum equation in the streamwise direction: The transport of momentum by velocity fluctuations is represented by the product of the individual velocity fluctuating component as expressed in equation (5) by the additional term on the right hand side $-\overline{u'v'}$. This term is commonly known as turbulent stress or Reynolds stress. For fully developed two-dimensional channel flow equation (5) can be reduced to equation (6) where ρ is density, ν is kinematic viscosity of the fluid, and U , the local mean velocity. The terms inside the brackets are the Newtonian viscous stress and the Reynolds shear stress respectively.

$$U_i = \frac{1}{N_T} \sum_{k=1}^{N_T} u_{i(k)} \quad (4)$$

$$U_j \frac{\partial U_i}{\partial x_j} = -\frac{1}{\rho} \frac{\partial P}{\partial x_i} + \frac{\partial}{\partial x_j} \left(\frac{\partial U_i}{\partial x_j} - \overline{u'v'} \right) \quad (5)$$

$$0 = -\frac{1}{\rho} \frac{\partial P}{\partial x_1} + \frac{\partial}{\partial x_2} \left(\frac{\partial U_1}{\partial x_2} - \overline{u'v'} \right) \quad (6)$$

3.2 Statistics

The statistical quantities that are desirable to measure in turbulence studies are those connected with

- (i) The spatial distribution of the Reynolds stresses themselves.
- (ii) The rates, at which turbulent kinetic energy, or the individual Reynolds stresses, are produced, destroyed or transported from one point in space to another.
- (iii) The contribution of different sizes of eddy to the Reynolds stresses
- (iv) The contribution of different sizes of eddy to the rates mentioned in (ii), and the rate at which energy or Reynolds stresses are transferred from one range of eddy size to another.

Several different techniques were used to analyze the behavior of the channel flow. Velocity statistics were obtained from PIV measurements in the x-y plane. These velocity statistics are determined by ensemble averaging over the number of velocity fields,

$$\overline{A} = \frac{\sum_{i=1}^N A_i(\overline{x})}{N} \quad (7)$$

where A is the quantity being averaged, \overline{x} is the position vector, and N is the total number of realizations. The result from equation (7) is a two-dimensional average vector field. Further averaging can be done in the x-direction due to the assumption of fully developed channel flow. The fluctuating velocity fields were obtained using the Reynolds decomposition for each vector in each instantaneous velocity field.

3.2.1 Turbulence Intensities and Reynolds Shear Stress

The intensity of turbulence is defined as the rms value of the fluctuating velocities. The streamwise (u_{rms}) and normal (v_{rms}) turbulent intensities were calculated using

$$u_{rms}(x, y) = \sqrt{\frac{1}{N} \sum_{i=1}^N [u_i(x, y) - U(x, y)]^2} \quad (8)$$

The total shear stress, τ_t , across half height of the channel can be determined from

$$\tau_t = \mu \frac{dU}{dy} - \rho \overline{u'v'} \quad (9)$$

where $\mu \frac{dU}{dy}$ is the viscous stress and $-\rho \overline{u'v'}$ is the Reynolds shear stress. The viscous component of the total shear stress can be determined from the measured streamwise velocity profile. The derivative $\frac{dU}{dy}$ is calculated using a central difference scheme.

The Reynolds shear stress is the contribution of the turbulent motion to the main stress tensor.

Reynolds shear stress can be measured directly from PIV using

$$\overline{u'v'}(x,y) = \frac{1}{N} \sum_{i=1}^N \{[u'_i(x,y)][v'_i(x,y)]\} \quad (10)$$

3.2.2 Correlation Coefficients

Velocity correlation measurements are useful for obtaining direct estimates of the turbulence length scales. In this work, several correlation coefficients calculations were used to analyze the turbulent flow.

3.2.2.1 Two-point Correlation Coefficients

The two-point or Eulerian correlations play a leading part in turbulence theory. In general, the velocity correlations can be expected to be dependent on two things: a) distance between the two points, and b) the absolute value of the velocities.

The correlations values depend on distance because as we move the measuring points apart, it is expected that the correlation will die away. Furthermore, the magnitude of the correlations at a fixed separation must also depend on the absolute values of the measured velocities.

The first suggestion of the use of the statistical correlation in the analysis of turbulence was made by (Taylor 1935). He pointed out that without any regard of the definition of the diameter of an eddy, if the separation of two points in space is small compared with the eddy diameter, there must be a high degree of correlation between the

velocities at those points. If such points are taken so far apart that the distance between them is larger than the diameter of an eddy, little correlation can be expected. The two-point correlation coefficient, also called Eulerian correlation, can be obtained from

$$R_{ij}(\Delta r) = \frac{\overline{u'_i(r)u'_j(r + \Delta r)}}{u_{rms_i}(r)u_{rms_j}(x + \Delta r)} \quad (11)$$

where u' is the fluctuating velocity, u_{rms} is the rms velocity fluctuation of turbulence intensity at the point in question, and Δr is the distance separation between the two points.

The integral length scale can be calculated from the value of the two-point correlation function, using the area under the velocity two-point correlation curve. This scale is thought to be the average size of the eddies. This scale can be calculated from

$$L_{ij} = \int_0^b R_{ij}(\Delta r) dr \quad (12)$$

where L_{ij} is the integral length scale, R_{ij} is the two-point correlation coefficient, and 0 and b are the limits of the span region where R_{ij} is positive, i.e. b is the point where the correlation coefficient becomes zero.

3.2.2.2 Autocorrelation Coefficient

For statistically stationary processes, the simplest multi-time statistic that can be considered is the autocorrelation coefficient (Pope 2000), also known as the Lagrangian correlation, which can be expressed as

$$R_{ij}(\Delta t) = \frac{\overline{u'_i(t)u'_j(t + \Delta t)}}{\overline{u'_{rms_i}(t)u'_{rms_j}(t + \Delta t)}} \quad (13)$$

The autocorrelation function has the properties

$$R_{ij}(0) = 1 \quad (14)$$

$$|R_{ij}(\Delta t)| \leq 1 \quad (15)$$

For processes present in turbulent flows, the correlation diminishes as the lag time Δt increases.

The definition of the Lagrangian integral time-scale T_L is given by

$$T_L = \int_0^b R_{ij}(\Delta t) dt \quad (16)$$

3.2.2.3 Two-dimensional Two-point Correlation Coefficients

The computation of the 2D correlation coefficient function is very advantageous due to the possibility to measure the correlations in any arbitrary direction on the measurement plane (Piiro *et al.* 2001). The two-dimensional correlation function can be obtained from

$$R_{ij}(\Delta x, \Delta y) = \frac{\overline{u'_i(x, y)u'_j(x + \Delta x, y + \Delta y)}}{\overline{u'_{rms_i}(x, y)u'_{rms_j}(x + \Delta x, y + \Delta y)}} \quad (17)$$

3.2.3 Vorticity

A better understanding of many aspects of turbulent flows can be gained from the dynamics of the vorticity field. Vorticity is a local property of the flow field (Panton 1996), which is a measure of the rotation of a fluid element as it moves in the flow field (Fox and McDonald 1998).

$$\omega = \nabla \times \mathbf{U} \quad (18)$$

where \mathbf{U} is the fluid velocity. Vorticity can be calculated using the average, the instantaneous, or the fluctuating velocity field. One of the advantages of PIV measurements is that it can offer information about the vorticity field from the spatial distribution of velocity. In this case, since measurements are carried out in the x-y plane, just one component (spanwise) of the vorticity vector can be obtained. Therefore, the expression for instantaneous spanwise vorticity is

$$\omega_z = \left(\frac{\partial u}{\partial y} - \frac{\partial v}{\partial x} \right) \quad (19)$$

The derivative calculation is carried out using central difference scheme. Substituting the fluctuating components of the velocity in equation (19), the fluctuating spanwise vorticity can be obtained. Likewise, the substitution of the average velocity components will yield the average vorticity field.

3.2.4 Rate of Strain

Straining or deformation is important because is related to the stresses in the fluid. The total straining velocity is directly proportional to the symmetric part of the velocity gradient tensor, which is called the strain-rate tensor or the rate of deformation tensor. For mean flow, the rate of strain tensor can be obtained from

$$S_{ij} = \frac{1}{2} \left(\frac{\partial U_i}{\partial x_j} + \frac{\partial U_j}{\partial x_i} \right) \quad (20)$$

From the mean rate of strain the Turbulent Energy Production can be obtained from

$$P = -\overline{u_i u_j} S_{ij} \quad (21)$$

The rate at which viscous stresses perform deformation work against the fluctuating strain rate is called viscous dissipation. It can be expressed as

$$\varepsilon = 2\nu \overline{s_{ij} s_{ij}} \quad (22)$$

where ν is the kinematic viscosity of the fluid and s_{ij} is the fluctuating rate of strain, which can be expressed as

$$s_{ij} = \frac{1}{2} \left(\frac{\partial u'_i}{\partial x_j} + \frac{\partial u'_j}{\partial x_i} \right) \quad (23)$$

The fluctuating strain rate s_{ij} is larger than the mean rate of strain S_{ij} when the Reynolds number is large. This implies that the eddies contributing most to the dissipation of energy have very small convective time scale compared to the time scale of the flow (Tennekes and Lumley 1974).

3.3 Visualization techniques

Although Reynolds decomposition of velocity into mean and fluctuating components is the standard method to characterize turbulent velocity fields, and offers the right bases for statistical analysis of the turbulent flows, it is not always the best method for visualizing turbulent structures in the flow.

When the primarily objective is investigate the dynamics of small-scale vortices or any other structures, then the use of different methods for detection of such structures is the better path to follow.

3.3.1 Modified Reynolds Decomposition

To improve the detection of vortices or any other kind of coherent structures in a turbulent velocity field, a modification of the Reynolds decomposition is proposed. This technique is based on the concepts of the traditional Reynolds decomposition and the Galilean decomposition.

The traditional Reynolds decomposition was already discussed in this chapter and stated mathematically in equation (8). In the Galilean transformation the total velocity is represented as the sum of a constant convection velocity, U_c , plus the deviation

$$\mathbf{u} = \mathbf{U}_c + \mathbf{u}_c \quad (24)$$

In 2000, Adrian, et al. selected different fractions of the centerline velocity as the convection velocity to implement the Galilean transformation technique.

From these concepts, a new decomposition technique was proposed by (Hassan *et al.* 2005). In this case, a time averaging process is carried out to obtain the mean velocity, just as it is done in the Reynolds decomposition; however, to obtain the fluctuating component of the velocity, just a fraction of this mean velocity is subtracted from the instantaneous velocity, this can be expressed as

$$u = fU + u' \quad (25)$$

where U is the mean velocity, f is any number between 0 and 1 (if $f = 1$ this constitute the traditional Reynolds decomposition), and u' is the fluctuating velocity obtained.

3.3.2 Spatial Decomposition

This is another method used to elucidate structures in fluctuating velocity fields. In this case, the mean velocity is calculated from spatial averaging in a statistically homogenous direction. In this case, that direction is the streamwise (y – direction), since the flow is fully developed. This decomposition can be expressed as

$$u = U_s + u'_s \quad (26)$$

where U_s is the mean velocity obtained by spatial averaging in the x -direction for each y position.

3.3.3 Vortex Identification

Vorticity analysis is generally used to identify locations of vortices. However, vorticity not only identifies vortex cores, but also detects any shearing motion in the flow. Strong shear layers are very common near the wall region in turbulent wall-bounded flows. These regions frequently mask the presence of eddies or vortices in vorticity maps.

In (Chong *et al.* 1990), suggested that a vortex core is a region of space where the vorticity is sufficiently strong to cause the rate-of-strain tensor to be dominated by the rotation tensor, i. e., the rate-of-deformation tensor has complex eigenvalues. This definition depends only on the properties of the deformation tensor; it is independent of the frame of reference.

In three dimensions, the rate of deformation tensor will have a real eigenvalue (λ_r) and a pair of complex conjugate eigenvalues ($\lambda_{cr} \pm \lambda_{ci}$) when the discriminant of its characteristic equation is positive. If this is true, the particle trajectories about the eigenvector corresponding to λ_r exhibits a swirling, spiral motion; λ_{ci}^{-1} represents the period required for a particle to swirl once about the λ_r -axis. If $\lambda_{ci} > 0$, the fluid particle corresponds to short almost circular ellipses, i.e. eddies. This technique has been successfully applied by Zhou et al. (1996, 1999) for three dimensional flows, where it was shown that the strength of any local swirling motion is quantified by λ_{ci} .

The application of this particular technique in two-dimensional velocity fields obtained from PIV measurements was presented by Adrian, et al. (2000). For two-

dimensional measurements, an equivalent two-dimensional form of the velocity gradient tensor is used

$$\underline{\underline{D}}^{2-D} = \begin{bmatrix} \frac{\partial u_i}{\partial x_i} & \frac{\partial u_i}{\partial x_j} \\ \frac{\partial u_j}{\partial x_i} & \frac{\partial u_j}{\partial x_j} \end{bmatrix} \quad (27)$$

In this case, $\underline{\underline{D}}^{2-D}$ will either have two real eigenvalues or a pair of complex conjugate eigenvalues. Hence, vortices can be identified by plotting regions where $\lambda_{ci} > 0$.

CHAPTER IV

ROD BUNDLE ARRAY WITH SPACER-GRIDS RESULTS AND DISCUSSION

This chapter presents selected results for both tested grids. The results were divided into two main sections: results for grid 1 and results for grid 2. A multi-scale approach was used for all the results included in this section. The geometry and appropriate details used for each case are presented in a compacted plot. However, detailed plots for each measured position and scale can be found at the corresponding appendix section. The main results presented in this section still having dimensions according to the quantity in question in order to avoid possible confusion when compared with CFD simulations.

4.1 Grid 1

The measurements for axial velocity at the investigated region were performed at several planes using a multi-scale approach. This approach consisted of performing measurements on various viewing areas of the test section. The scales were selected based on the physical constrictions and the desired resolution of the velocity fields. The measured planes for grid1 are shown in figure 41. Five planes were measured for grid 1 which are represented by green lines in the figure. The planes were formed by the laser light where the light passes through the test section. The planes were identified using the number assigned to each of them or by the corresponding notation using the first three

letters from the alphabet. For this case plane A was the closest plane to the by-pass flow plane explained in chapter II. The main differences between the measured planes was the distance of the plane with respect to the front observation window and the “obstacles” found by the light path in its way through the test section. Planes C, B and A (1, 3, and 5) respectively lie between the cylindrical rods and Planes B2 and A1 (2 and 4) did not have any physical obstacle in its way through the test section. The data collection process included the measurement of every scale at various planes inside the 5 x 5 bundle. The selected planes were parallel to the frontal channels’ window and they varied in distance from the wall to the center of the bundle by changing the position of the optical set-up and cameras using automatic motorized positioning stages.

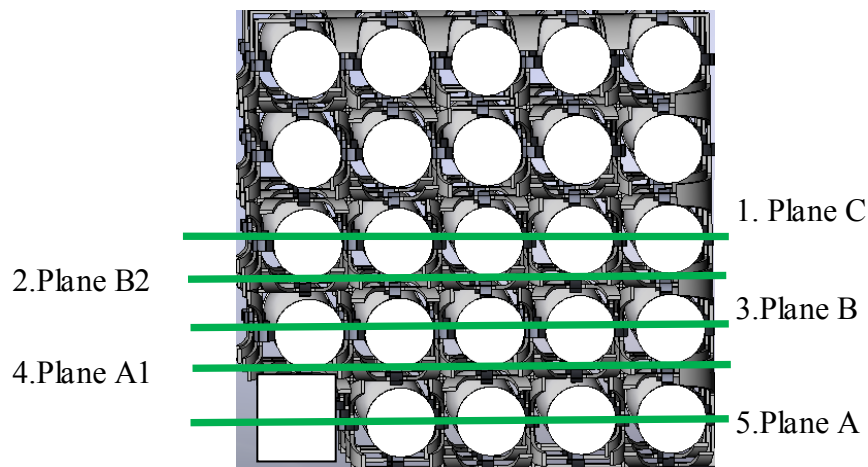


FIGURE 41.Measured planes for grid 1.

Figure 42 shows the different scales used in this work. The first scale examined the flow behavior in the planes that cover the five rods and its respective sub-channels which are denoted by the yellow dashed line. At this scale the interaction between sub-channels and general characteristics of the flow were captured. The equivalent viewing area of the cameras for this scale was 65 x 49 mm. The second scale is denoted by the area marked with a dashed red line in Figure 42. This scale captured the flow characteristics of a central sub-channel with an equivalent camera viewing area of 65 x 12 mm. At this scale the flow evolution in the sub-channel could be observed. The third scale is denoted by the red dashed line in figure 42 and it has an equivalent viewing area of 5 x 4 mm. This scale was intended to resolve the local flow behavior, such as boundary layer thickness, turbulence energy production, turbulent energy dissipation, eddy size, coherent structures identification, among other important parameters of interest.

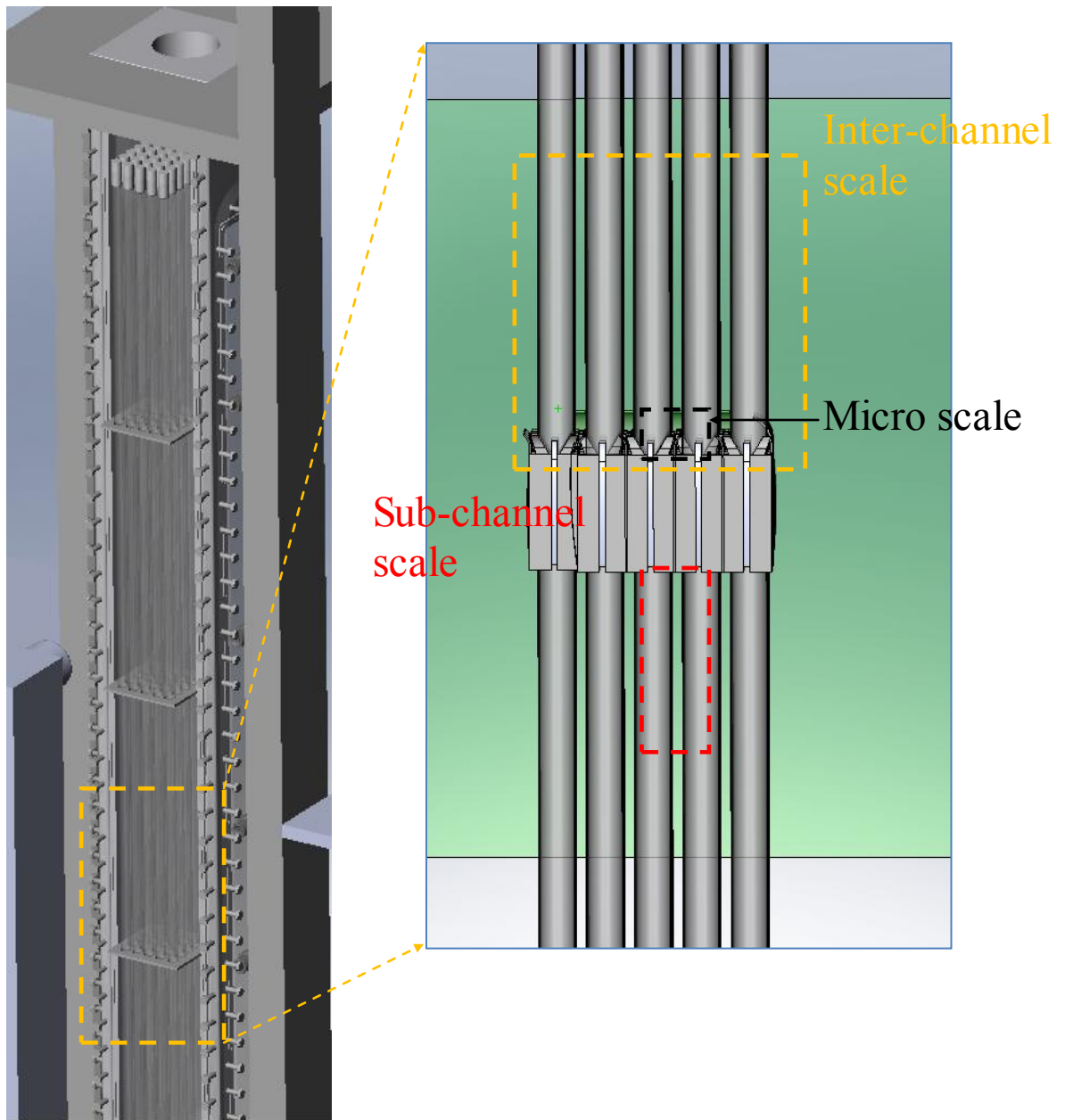


FIGURE 42. Multi-scale approach.

4.1.1 Inter-channel scale

Figure 43 shows a pictorial of the three positions measured using the viewing area covering the inter-channel scale. Each of the black dotted lines represents one measured position. Each position was assigned with a representative name using the following logic. All measured positions upstream from the grid were denominated as “Before Grid” (BG) and the positions downstream from the grid were denominated as “After Grid” (AG). The corresponding nomenclature for each position was included in the name by using the abbreviation and the corresponding number. i.e., AGP1 represents the After Grid position 1 measurement zone. The distance covered by each measurement volume was measured from the edge of the grid without including the mixing vanes. Figure 43 shows the three measurement volumes used for the inter-channel scale and its corresponding distance from the grid in length units (mm) and equivalent hydraulic diameters (D_h). The distance range for positions after the grid varied from 0 (grid edge) to $9.3 D_h$ (tip of measured volume 2, AGP2). From the before grid case (upstream grid) only one position was measured and its corresponding distance from the grid edge to the tip of the viewing area was $4.5 D_h$. The flow direction with respect to the measured positions is indicated in the figure by a white arrow pointing upwards. The averaged velocity fields for plane C in the three measured positions upstream and downstream the grid are shown in figure 44 and figure 45.

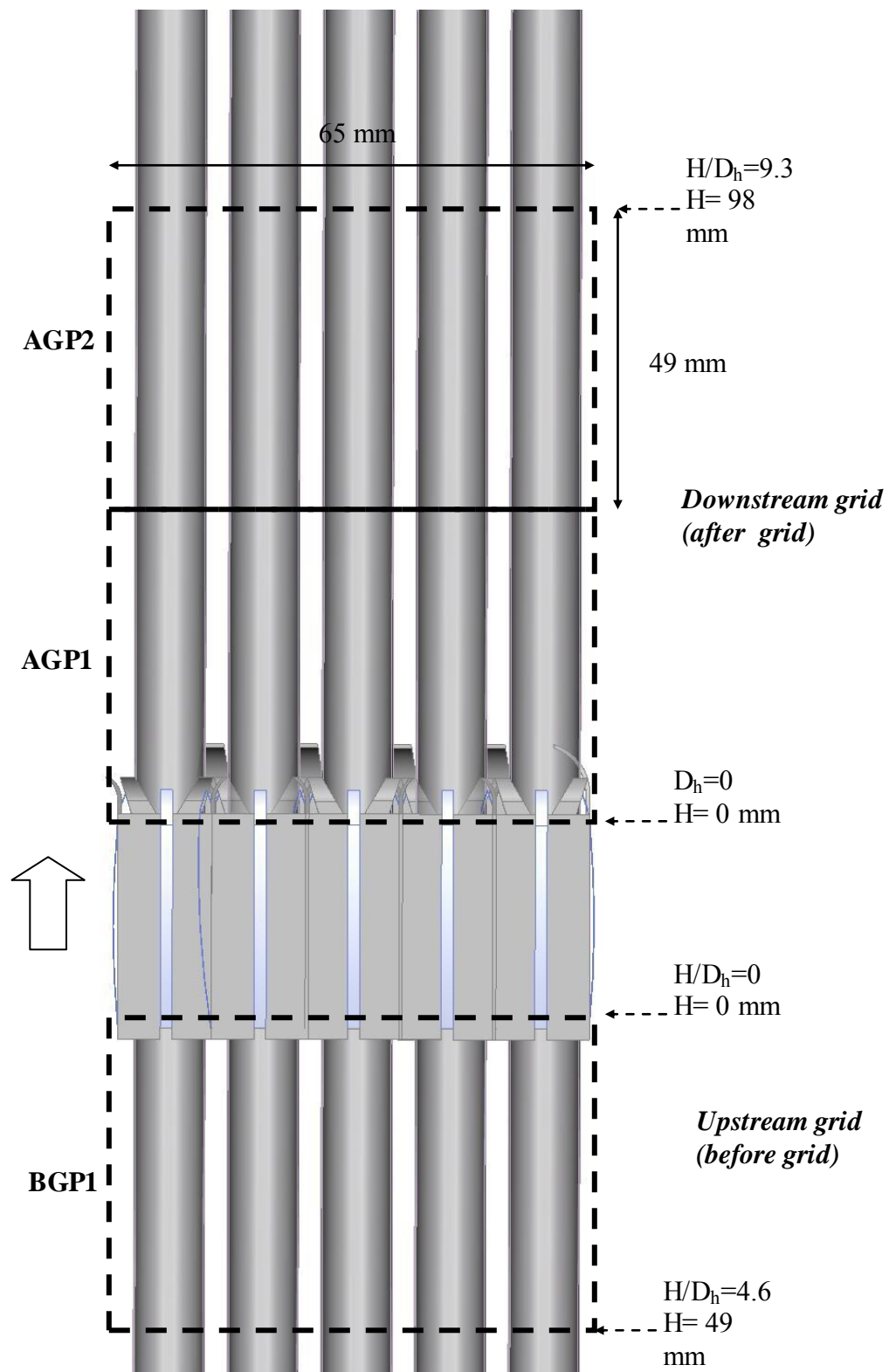


FIGURE 43. Macroscale measurement view wing areas (all channels) for test grid 1.

Each figure presents the velocity fields in vector form with its corresponding component of the velocity vector represented by the color in the plot. The color scale is presented at the top of position AGP2. Each position is framed by a dotted frame with a color code for an easy identification. The square channel (water channel) used in the experiment is represented by a black rectangle in the left side of the velocity contours. Since the rectangular channel obstructed the light reflected by the seeded particles, no vectors are presented in this section of the image. The position of the cylindrical rods is included in the pictorial (gray cylinders) and the position of the grid is represented by a gray color rectangle. It is observed that the streamwise component of the velocity vector (U) in figure 44 has a maximum value of 2000 mm/s for position BGP1. This value is consistent in the three main sub-channels. However, the upstream component denoted a decrease after passing through the grid. The decrease is considerable as denoted by the contour plot of position AGP1 in the vicinity of the mixing vanes. The streamwise component shows a recovery in position AGP2. In the three positions presented there is a smaller value of velocity in the sub-channels located near the square channel and the right wall of the u-shaped channel. This behavior was expected since the flow should enforce the non slip condition at the boundary of solid surfaces.

The effect of the container walls and the non-symmetric configuration of the mixing vanes are noted in figure 44 by a decrease in the streamwise component of the velocity vector in the regions near the walls. A full size plot for each position is presented in the appendix section for better appreciation.

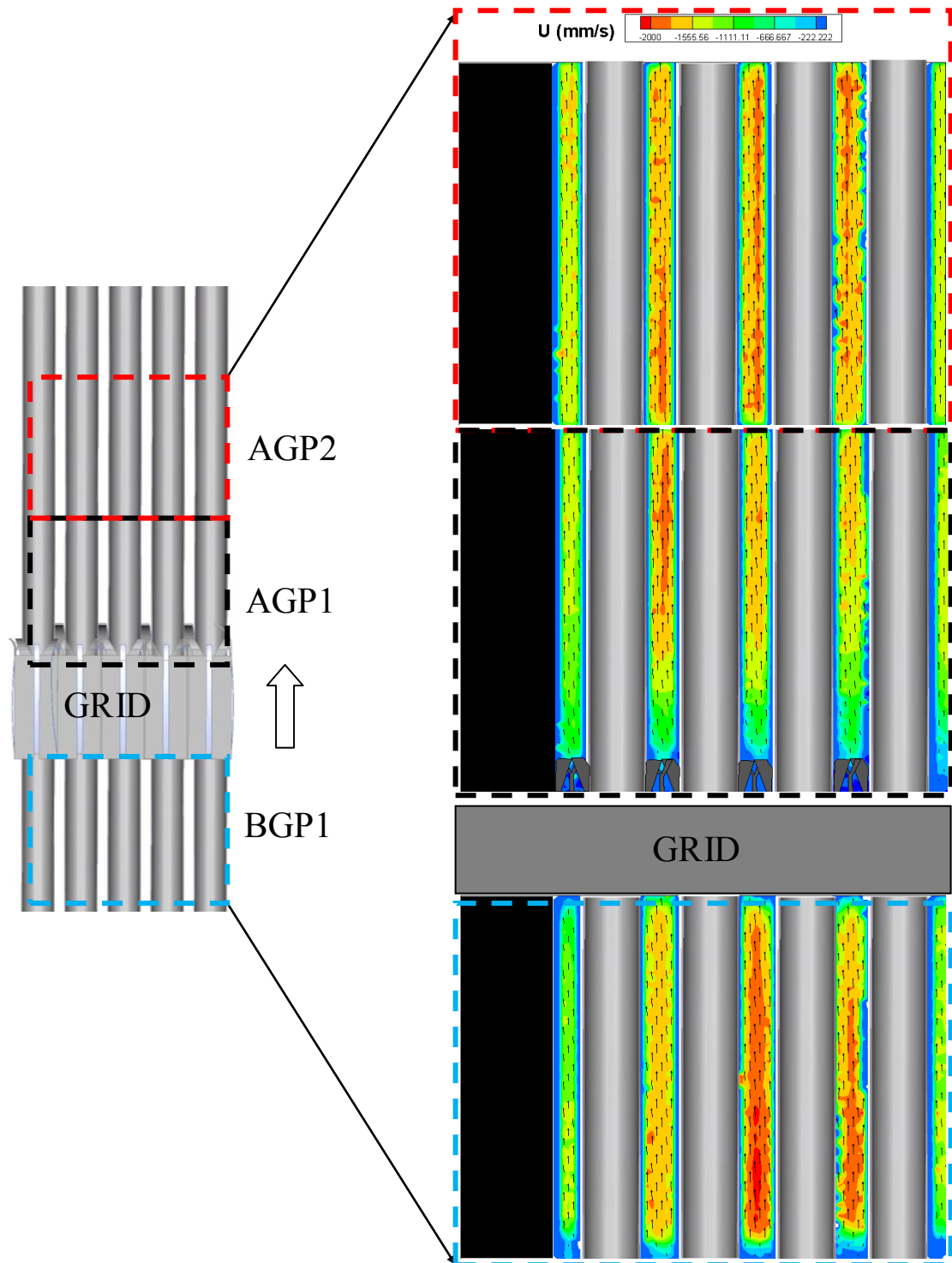


FIGURE 44. Average streamwise component of the velocity vector (U) for the three positions measured in the inter-channel scale, Plane C, $Re=15000$.

The average normal component of the velocity vector (V) is presented in figure 45 for the three positions measured at the inter-channel scale. Since this component represents the changes in the normal component, the scale representing this value can have positive and negative values. The positive values represent displacements toward the right side of the paper in the X-Y plane and the negative values represent displacements toward the left side. Figure 45 shows the evolution of the normal component (V) upstream the grid and its evolution downstream of the spacer. It is observed that there is an average of 30 mm/s contours for the three interchannels at the center of the image for position BGP1. Once, the flow passes through the grid, the component has an increase in the region nearby the mixing vanes. There are well delineated zones where red color is dominant, indicating an increase in the positive direction of the normal component with an average value of 50 mm/s. This increment is due to the inclination angle of the mixing vanes. The effect of the vanes decreased as a function of distance from the vanes, having the maximum value at the edge of the vanes (100 mm/s) and decreasing at an equivalent distance of four D_h from the grid's edge. It should be noted that the vane orientation changes with position, or in other words, the orientation of the vanes affecting each sub channel is not the same (please refer to the grid description for more details.) In addition to the inflection in the flow direction caused by the mixing vanes there is a wake created downstream from the vane tips which contributes to the increment in the normal component of the velocity vector.

The velocity measurements resulted from plane B2 are shown in figures 46 and

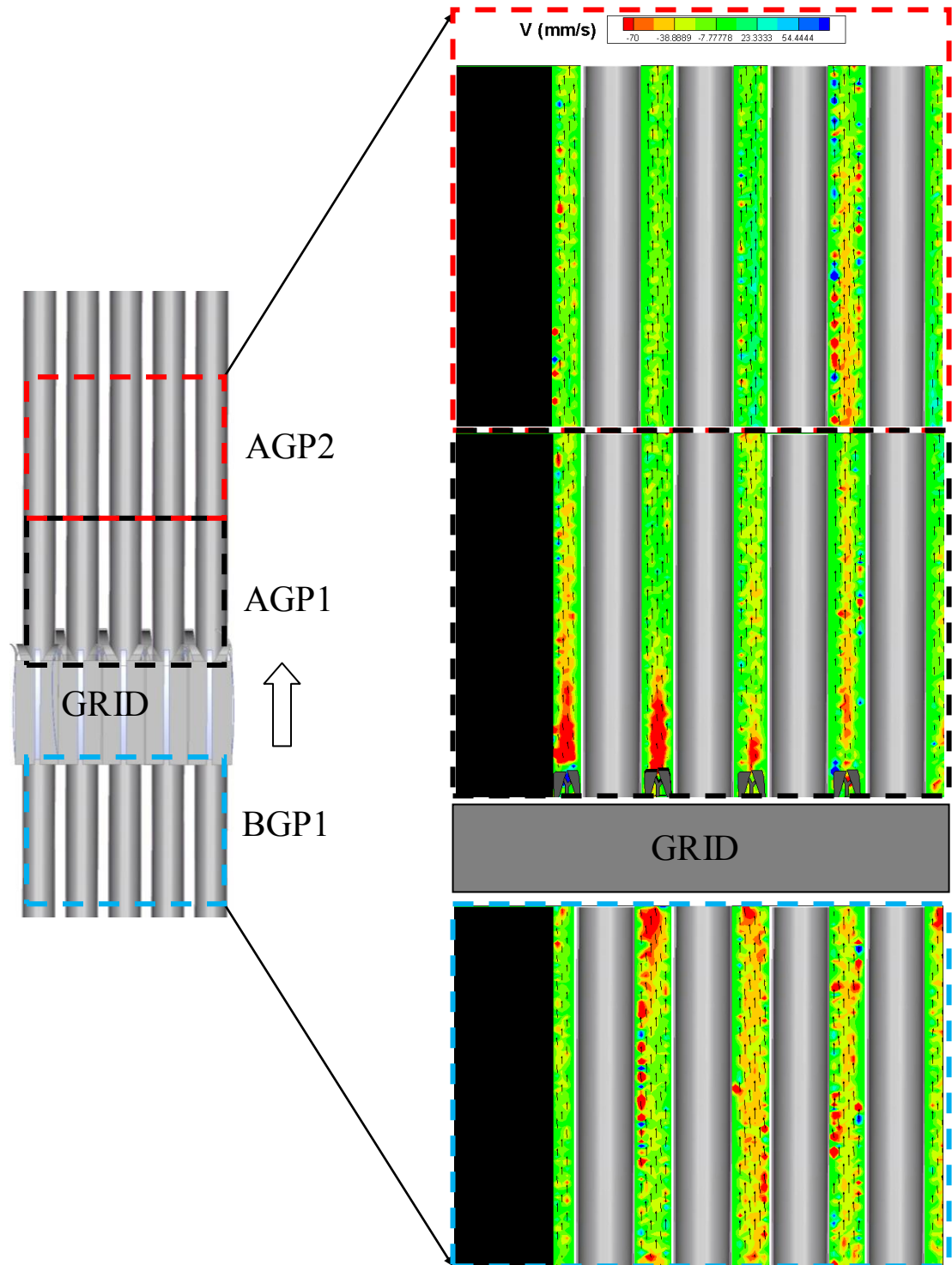


FIGURE 45. Average normal component of the velocity vector (V) for the three positions measured in the inter-channel scale, Plane C, $Re=15000$.

47. This plane does not have a physical obstruction of the fuel rods and have a direct influence from the swirl vanes. Since the cylindrical rods are not present in this plane, a full velocity vector can be obtained and the cylindrical rods are not represented in the figures. Figure 47 shows the contour plot for the averaged streamwise component of velocity vector for plane B2 for the three measured positions. There is a decrease in the streamwise component of 50% at position AGP1 with respect to position BGP1. The regions located nearby the mixing vanes are the ones with a higher decrease in velocity. The change is compensated by an increase in the normal component of the velocity vector as denoted in Figure 47. This figure presents strong red and blue colors distributed for position AGP1, especially in the region where the vanes are located. This plot shows the average change in flow direction caused by the mixing vanes. In both figures there is an empty space (no velocity vectors) for position BGP1. The former space was caused by the growth of a fungus inside one of the cylindrical rods. This situation does not affect in any way the obtained results since the fungus was located inside the rod. However, the fungus caused an optical obstruction for the particle detection. Therefore no vectors are present in these regions. The vectors surrounding the optical obstacle are considered as real vectors with a similar error value as the rest of the vector field. The changes in the normal component of the velocity vector decrease their value in area AGP2 but did not decrease back to the relative low values found in position BGP1. The results indicate that the flow attained a better mixing for the two positions located after the grid as indicated by the increase in the normal component of the velocity vector.

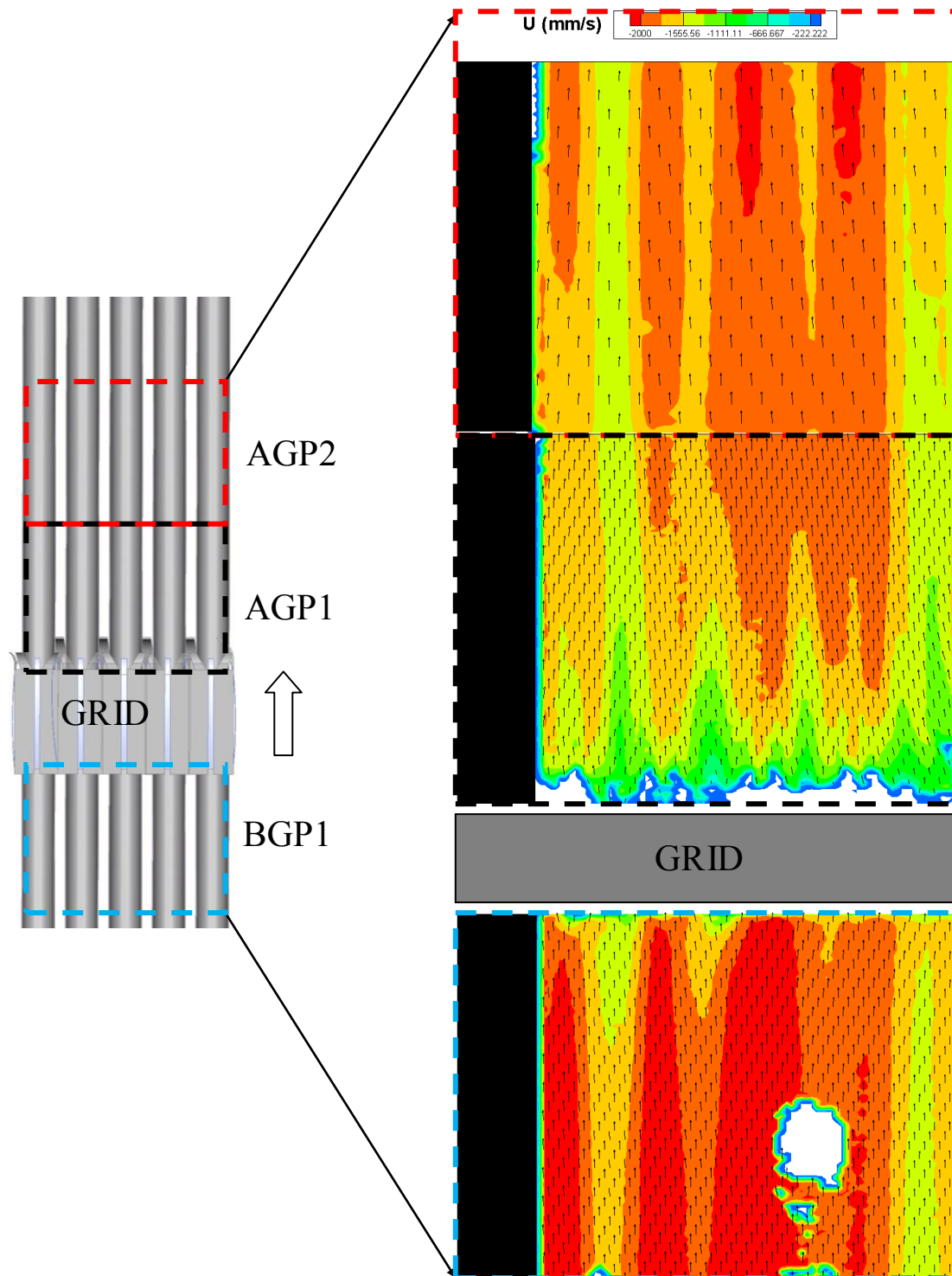


FIGURE 46. Average streamwise component of the velocity vector (U) for the three positions measured in the inter-channel scale, Plane B2, $Re=15000$.

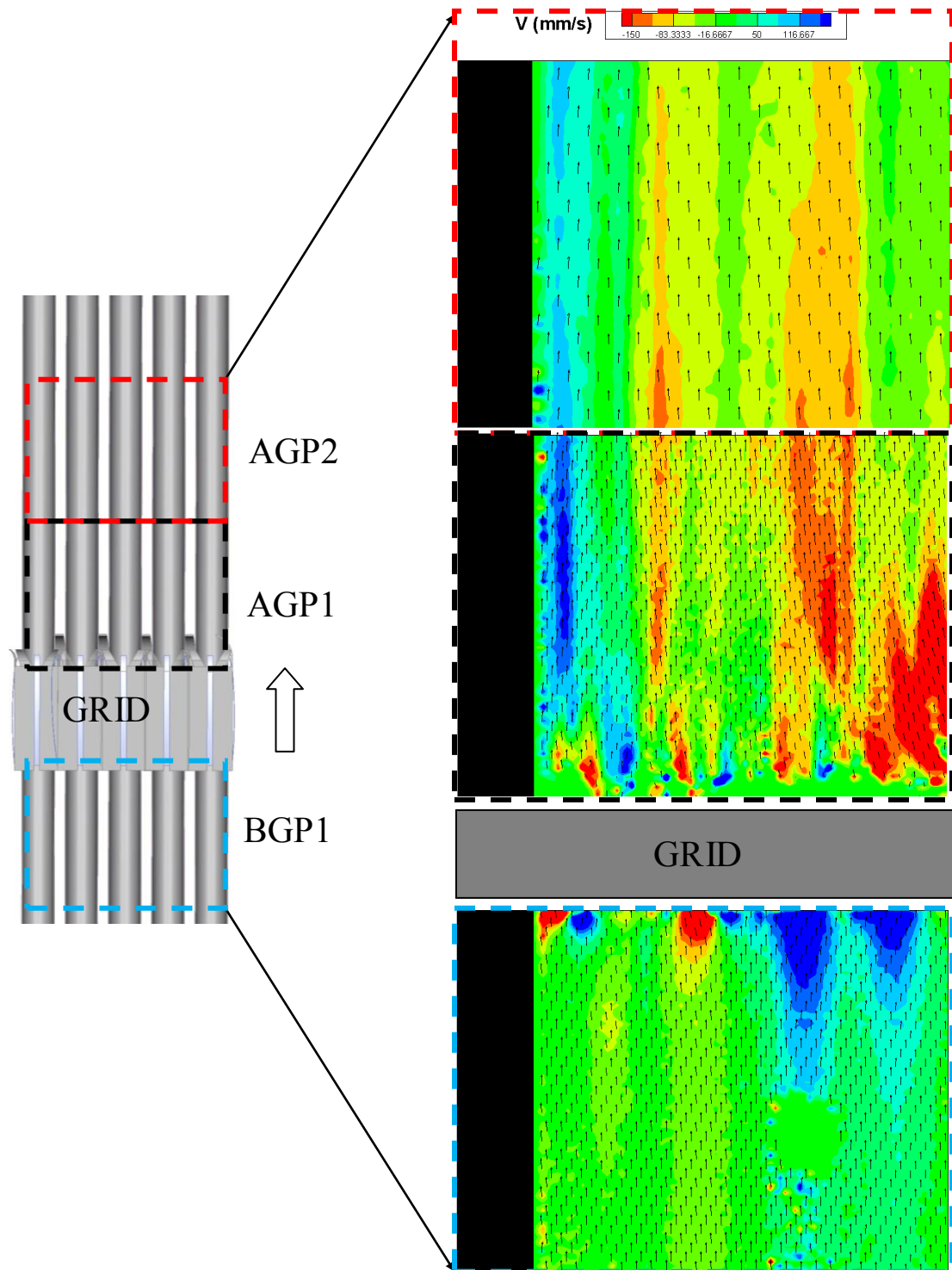


FIGURE 47. Average normal component of the velocity vector (V) for the three positions measured in the inter-channel scale, Plane B2, $Re=15000$.

The velocity statistics are determined from the PTV measurements by ensemble averaging the number of images using equation (7). Where A is the quantity being averaged (i.e. streamwise velocity or square of the velocity fluctuations), X is the position vector and N is the number of realizations. The result of equation(7) is a two-dimensional average flow field. Further averaging can be done in the X or Y direction when the flow is assumed to be fully-developed. This results in a one-dimensional average profile which is a function of x or y (depending on the direction of the averaging) only. For this case, the flow can not be considered as fully-developed since the measurements were made at various zones where the flow is not developed. However, the averaging was performed in a preferential direction (x or y) to obtain the 1-D profile for each quantity of interest. The profiles give a simple and efficient way to compare the averaged behaviour of the flow for various measured positions or under different conditions.

The one-dimensional velocity profile (averaged over the y -axis direction) comparing the three measured positions in the inter-channel scale (BGP1, AGP1 and AGP2) are shown in figure 48 for a $Re=15000$. This figure shows the one-dimensional averaged streamwise component of the velocity vector upstream of the grid is shown in blue color. The two positions downstream the grid under the same conditions are presented in red color (AGP1) and green color (AGP2). The velocity profile exhibits a distorted parabolic shape in the gap formed by two adjacent rods. The average maximum velocity shows a decrease in magnitude of 30 % for the position located immediately above the mixing vanes (red line) with respect to the profile measured before (upstream)

the grid (blue line). The gray color rectangular shape in the figure represents the position of the square channel.

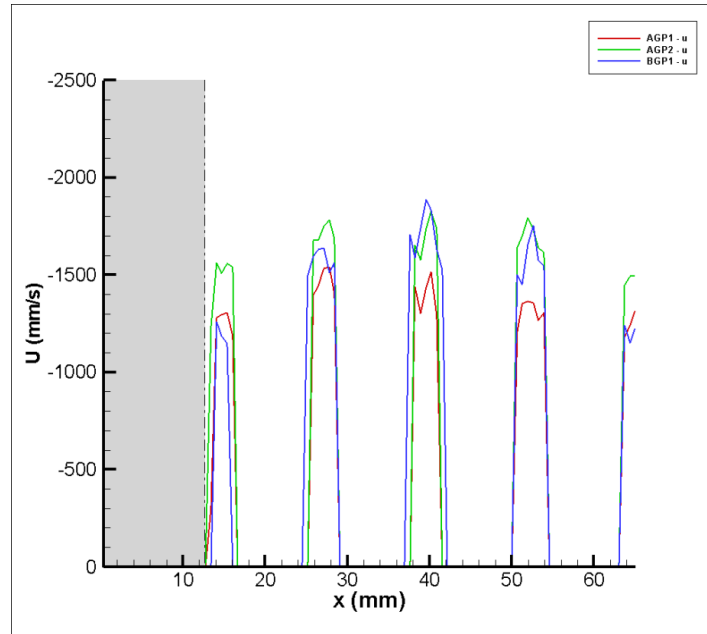


FIGURE 48. Averaged streamwise component (U) velocity profile for the three measured positions at the interchannel scale, Plane C , Re=15000.

Figure 49 shows the normal component of the velocity vector for the three measured positions in the interchannel scale. The profile shows a maximum value of about 120 mm/s for an x-direction position of 11.5 mm which is located contiguous to the square channel edge. However, the average magnitude for the normal component is of 40 mm/s.

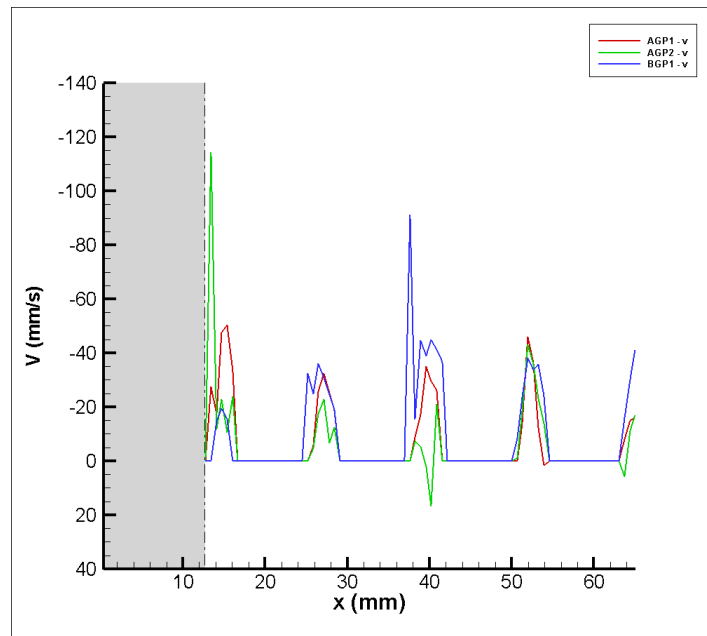


FIGURE 49. Averaged normal component (V) velocity profile for the three measured positions at the interchannel scale, Plane C , Re=15000.

The turbulence intensities for both components of the measured velocity vector are shown in figure 50 and figure 51. The streamwise component (u_{rms}) show a similar behavior to the typical intensities in a channel flow with non-slip conditions for the position upstream the grid (before grid). The highest values are reached at the vicinity of the rods walls and the minimum at the center of the gap. The results for Reynolds stresses in plane C are shown in figure 52.

The results show similitude with the results obtained from a channel flow with non-slip condition for the position located upstream the grid (BGP1). The behavior of the stresses is completely modified after passing through the mixing vanes. Since there is a change of flow direction caused by the vanes and the wake at the tip of the vanes make the stresses to redistribute in the channel.

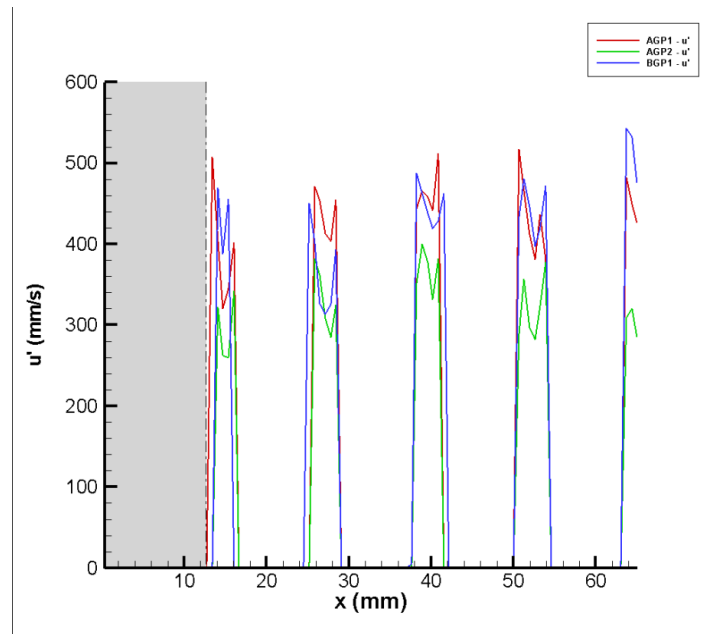


FIGURE 50. Averaged turbulence intensity for the streamwise component (u_{rms}) for the three measured positions at the interchannel scale, Plane C, $Re=15000$.

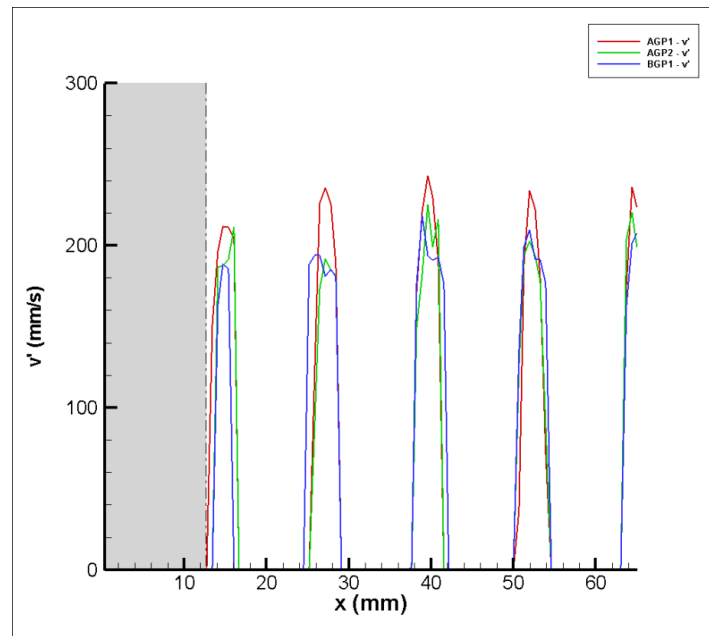


FIGURE 51. Averaged turbulence intensity for the normal component (v_{rms}) for the three measured positions at the interchannel scale, Plane C , $Re=15000$.

The results obtained from the measurements performed in plane B2 are shown in figures 53 to 57. It should be noted that plane B2 lies in the region where there are no rod obstacles. In other words, this plane does not present zero values of the vector since the vectors can be calculated in the whole image due to the optical transparency achieved without any solid obstacles. The maximum magnitude velocities for each component remain in the same range as for plane C. However, for the normal component the changes in sign show a considerable difference with respect to the previous case. The value of the turbulence intensities is comparable to the ones of plane C. The Reynolds stresses for position AGP2 show a considerable increase of 4 times with respect to the

plane C results. The positions immediately before and after grid show similar values to its counterpart in plane C.

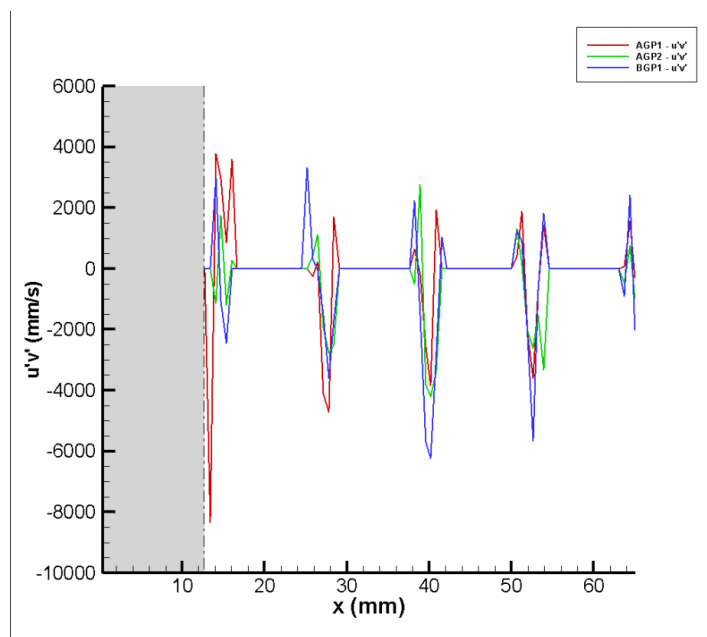


FIGURE 52. Averaged Reynolds stress ($u'v'$) for the three measured positions at the interchannel scale, Plane C , $Re=15000$.

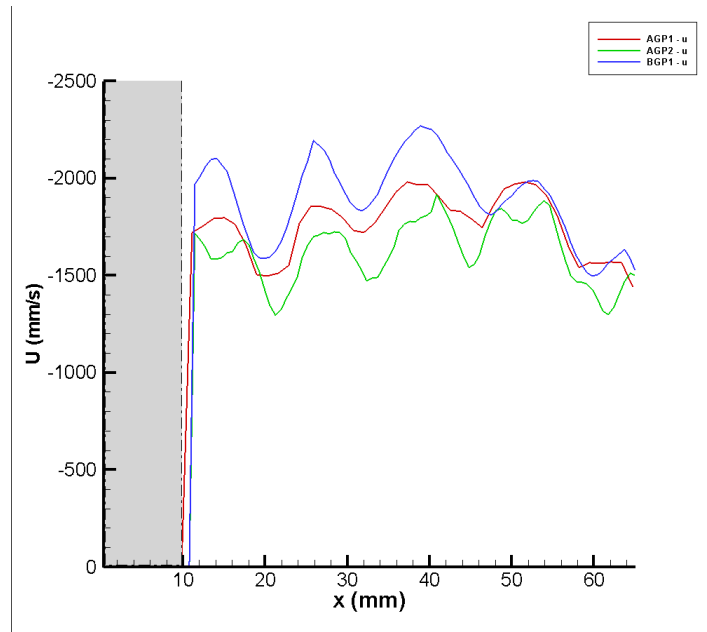


FIGURE 53. Averaged streamwise component (U) velocity profile for the three measured positions at the interchannel scale, Plane B2 , Re=15000.

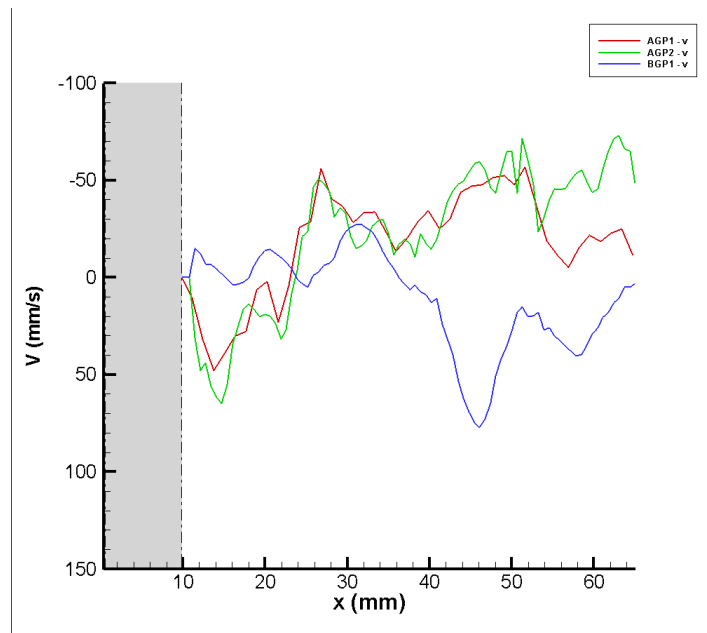


FIGURE 54. Averaged normal component (V) velocity profile for the three measured positions at the interchannel scale, Plane B2 , Re=15000.

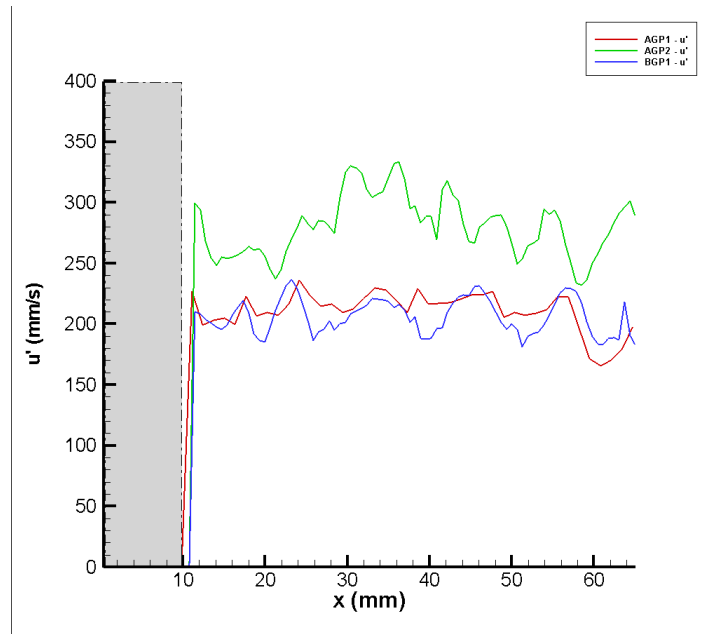


FIGURE 55. Averaged turbulence intensity for the streamwise component (u_{rms}) for the three measured positions at the interchannel scale, Plane B2 , Re=15000.

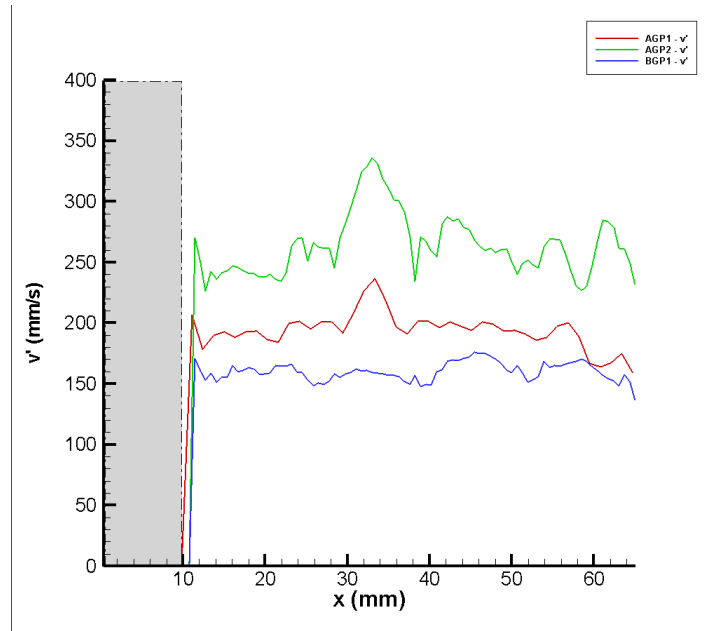


FIGURE 56. Averaged turbulence intensity for the normal component (v_{rms}) for the three measured positions at the interchannel scale, Plane B2 , Re=15000.

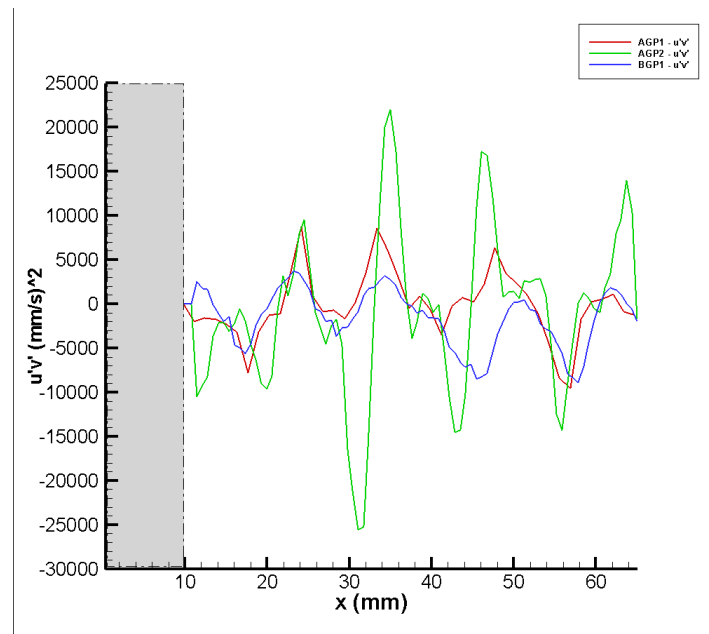


FIGURE 57. Averaged Reynolds stress ($u'v'$) for the three measured positions at the interchannel scale, Plane B2, $Re=15000$.

4.1.2 Sub-channel scale

Figure 58 shows a pictorial of the five positions measured using the viewing area covering the sub-channel scale. Each of the black rectangles represents one measured position. Each position was assigned with a representative name using the following logic. All measured positions upstream the grid were denominated as “Before Grid” (BG) and the positions downstream the grid were denominated as “After Grid” (AG). The corresponding nomenclature for each position was included in the name by using the abbreviation and the corresponding number. i.e., AGP1 represents the After Grid position 1 measurement zone. The distance covered by each measurement volume was measured from the edge of the grid without including the mixing vanes. Figure 58 shows the three measurement volumes used for the sub-channel scale and its corresponding

distance (H) from the grid in length units (mm) and the same distance is shown in equivalent hydraulic diameters (H/D_h). The distance range for positions after the grid varied from 0 (grid edge) to 9.15 H/D_h . For the before grid case (upstream grid) only two positions were measured and its corresponding distance from the grid edge to the tip of the viewing area was 4.5 H/D_h . The flow direction with respect to the measured positions is indicated in the figure by a white arrow pointing upwards. The five measured positions for this scale (BGP1, BGP2, AGP1, AGP4 and AGP8) have an equivalent viewing area of 12 mm x 16 mm. The correspondent scale for the results was 1 pix = 0.02519 mm for this sub-scale. The red dotted line in figure 58 shows the total area covered by the measurement positions. Measurements at this scale were performed following a similar procedure as the one used for the inter-channel scale.

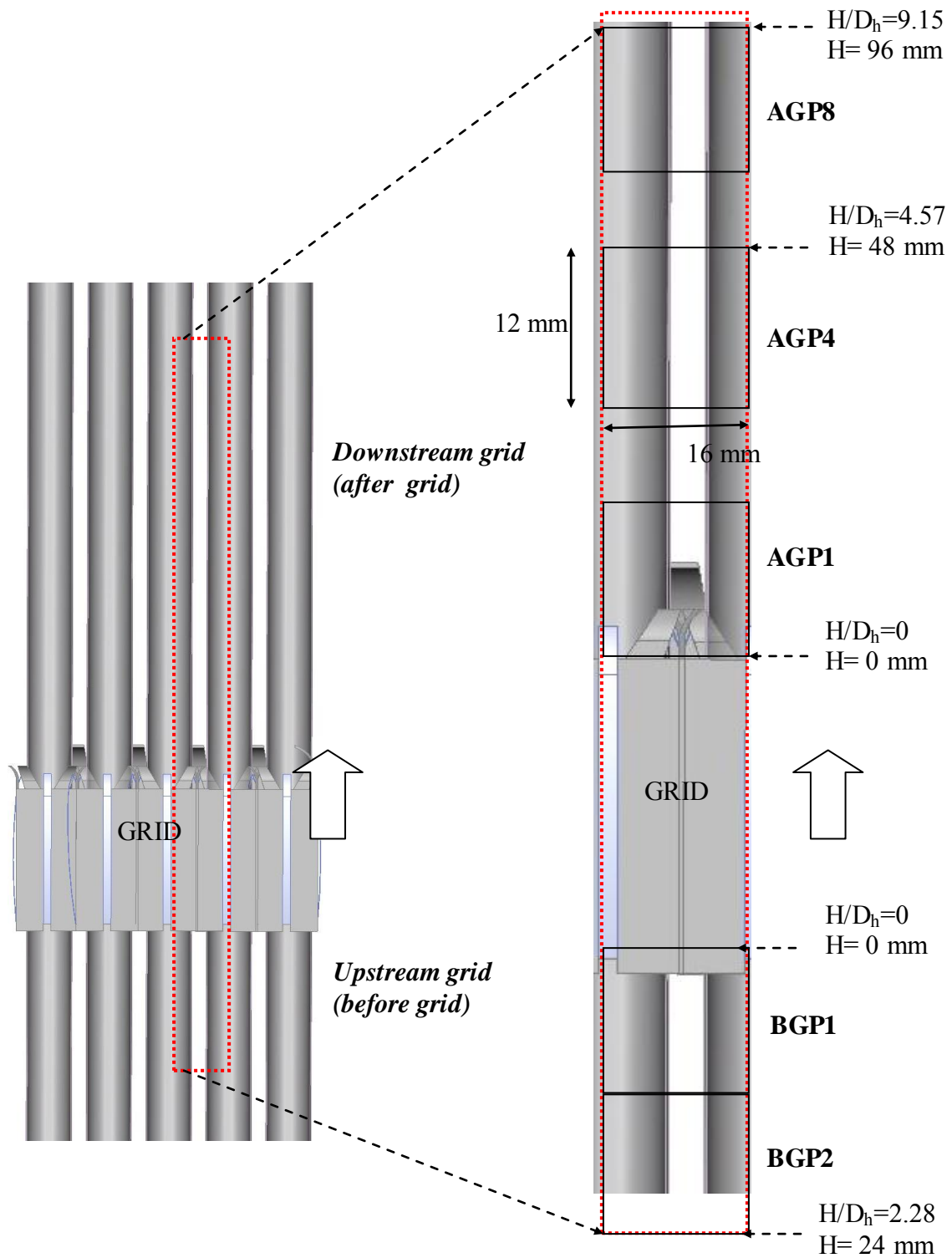


FIGURE 58. Sub-channel scale measurement viewing areas (zoom) for test grid 1.

The averaged velocity profile for the streamwise component of the velocity vector (U) for each measured position at the sub-channel can be seen in figure 59. The figure on the left side presents in a pictorial the position of the grid with respect to measured positions. Each position is framed by a rectangle with dotted line and different color code. The correspondent velocity field for each position is also framed by a rectangle following the same color code for easy identification of the position measured. The right side of figure 59 shows the evolution of the velocity field starting at position BGP2 (dark blue color) and following an upward path to position AGP8 (red color).

The velocity fields show a well delineated average field with a maximum velocity at the center of the field of 1700 mm/s. The maximum velocity is consistent at position BGP1; however there is an important decrease in the magnitude of the streamwise component of about 30% for position AGP1. The magnitude starts recovering its maximum value of 1700 mm/s at position AGP4 and AGP8. However, the profile exhibits a non-symmetric profile for these positions where the velocity is higher on the right side of the channel. Figure 60 shows the normal component of the velocity vector for the various positions. It is observed that the region immediately above the mixing vanes (position AGP1) shows the effect of the mixing vanes by a strong red color denoting magnitudes over 70 mm/s in the whole field. These magnitudes indicate the change in flow direction caused by the vanes and the effect of a wake after the tip of the vanes.

It should be noticed that the change in the flow is unidirectional as noted by the color plot where there is mostly red color denoting negative values of the normal velocity.

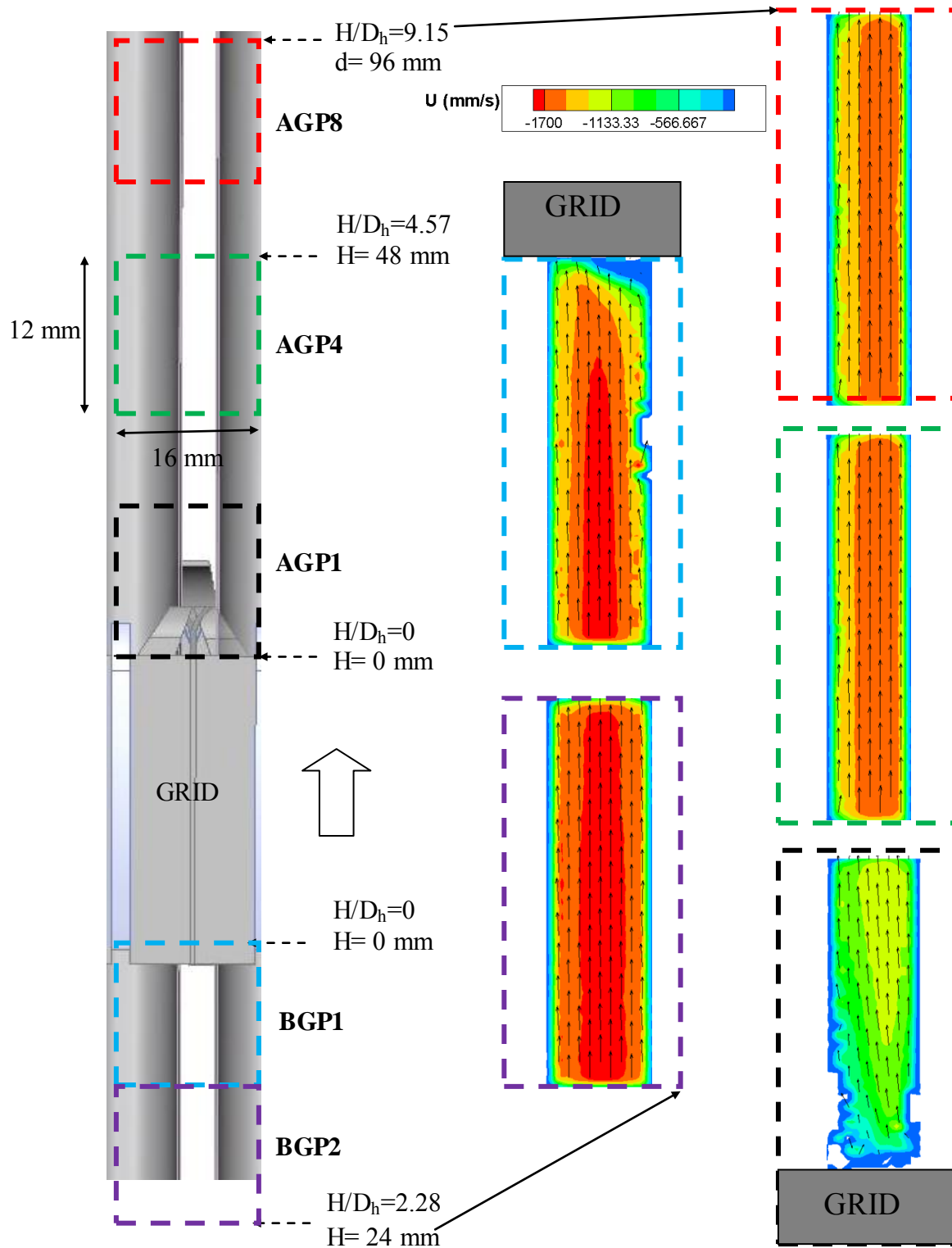


FIGURE 59. Average streamwise component of the velocity vector (U) for the three positions measured in the sub-channel scale, Plane C, $Re=15000$.

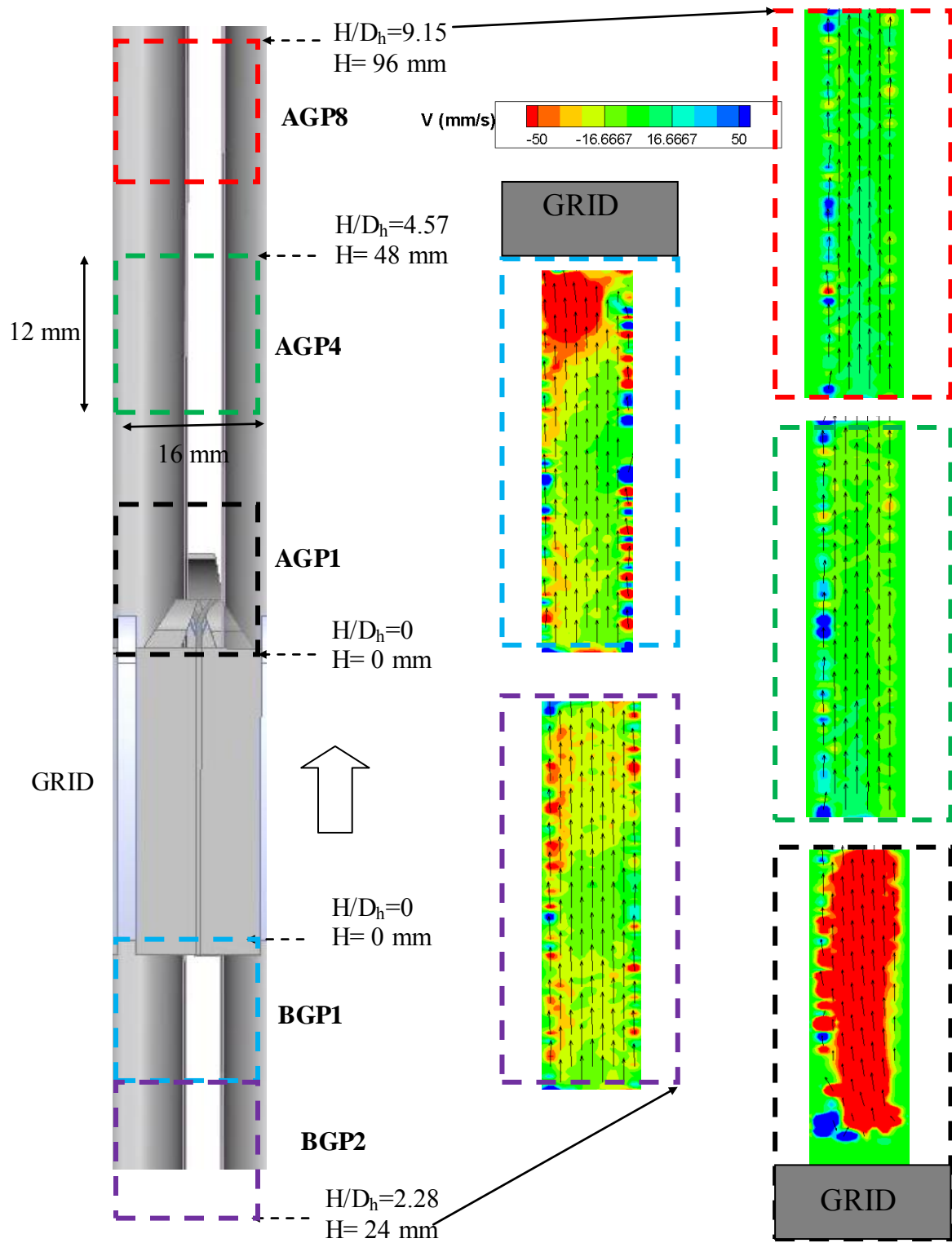


FIGURE 60. Average normal component of the velocity vector (V) for the three positions measured in the sub-channel scale, Plane C, $Re=15000$.

The sub-channels scale allowed the direct observation of the measured velocity vectors in the small gaps formed by adjacent rods. One of the advantages of the present measurements was the acquisition of velocity fields with a high temporal resolution (typical 125 μ s) which allows the study of the evolution of turbulence structures in the flow. In addition, the instantaneous fields can be used for comparison with CFD simulations. The comparison can be made using similar temporal and spatial scales. Figure 61 shows a typical instantaneous velocity field obtained under a condition of $Re=6400$ for positions BGP1 and AGP1. Each vector in figure 61 is color coded using the scale on the right side of the image. It is observed that most of the vectors upstream the grid have a magnitude of the streamwise component of the velocity vector (U) between 350 and 500 mm/s. However, the vectors downstream the grid presents a magnitude that ranges from 250 to 300 mm/s. In addition, the direction of the vectors oscillates as a function of distance from the grid as noted by the dotted black arrow in figure 61. This oscillatory behavior is observed in several fields among various data sets. Nevertheless, the averaged velocity field of 10,000 images does not give indication of the oscillatory behavior as shown in figure 62. The magnitude of the average velocity field closely follows the one presented in figure 61. However, the calculated streamlines overlapped in figure 62 shows a deflection in the flow downstream of the grid but does not give indication of the oscillatory behavior. The effect of averaging is shown in figure 63 which shows the averaged vector field of 5000 instantaneous velocity vectors. It is evident that there is a change in flow direction and magnitude but the details about those changes have been obscured during the averaging process.

FIGURE 61. Typical instantaneous velocity field for subchannel scale. Positions BGP1 and AGP1, plane C, $Re=6400$.

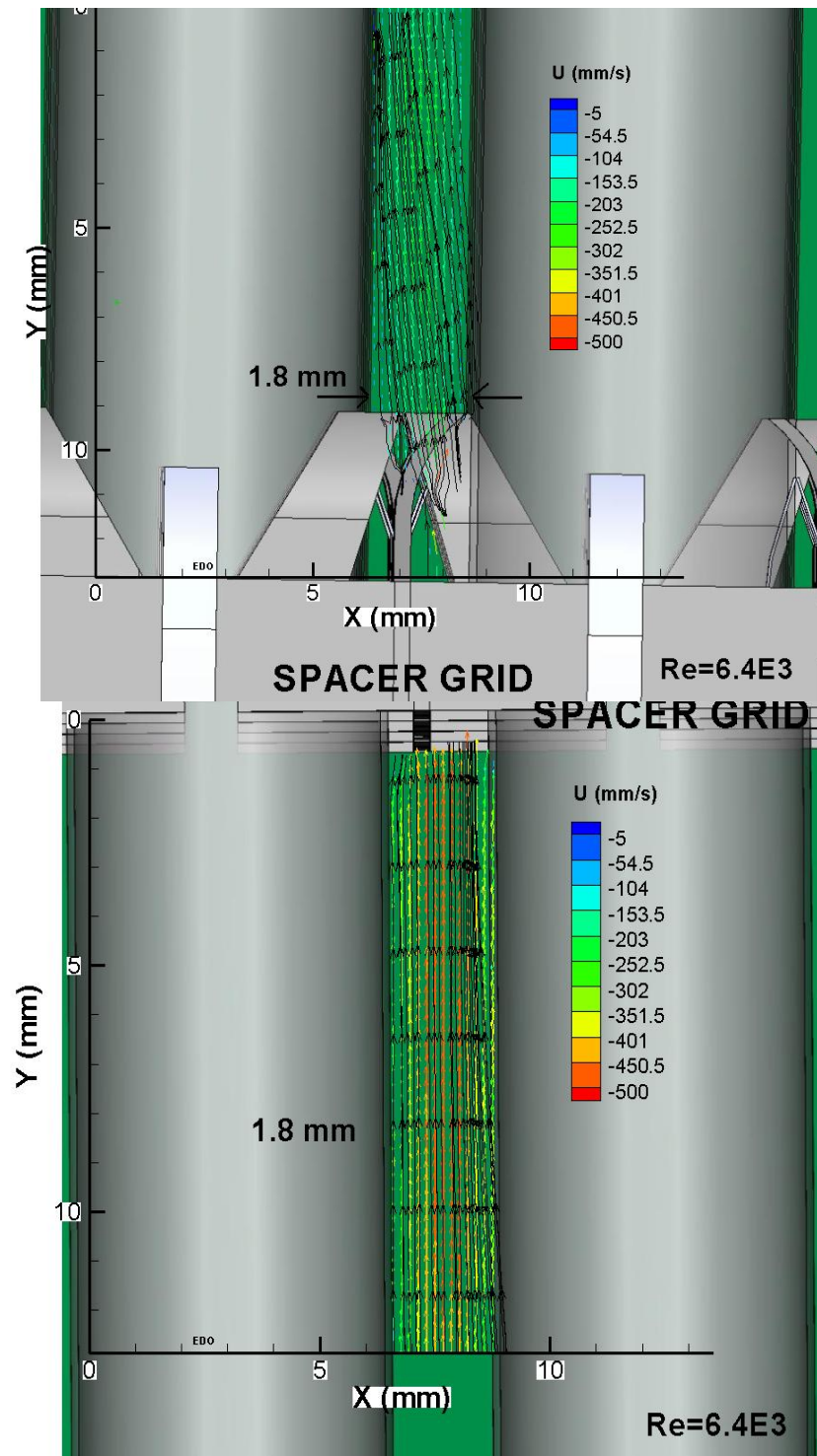


FIGURE 62. Averaged velocity field with overlapped streamlines for subchannel scale . Positions BGP1 and AGP1, plane C, $Re= 6400$.

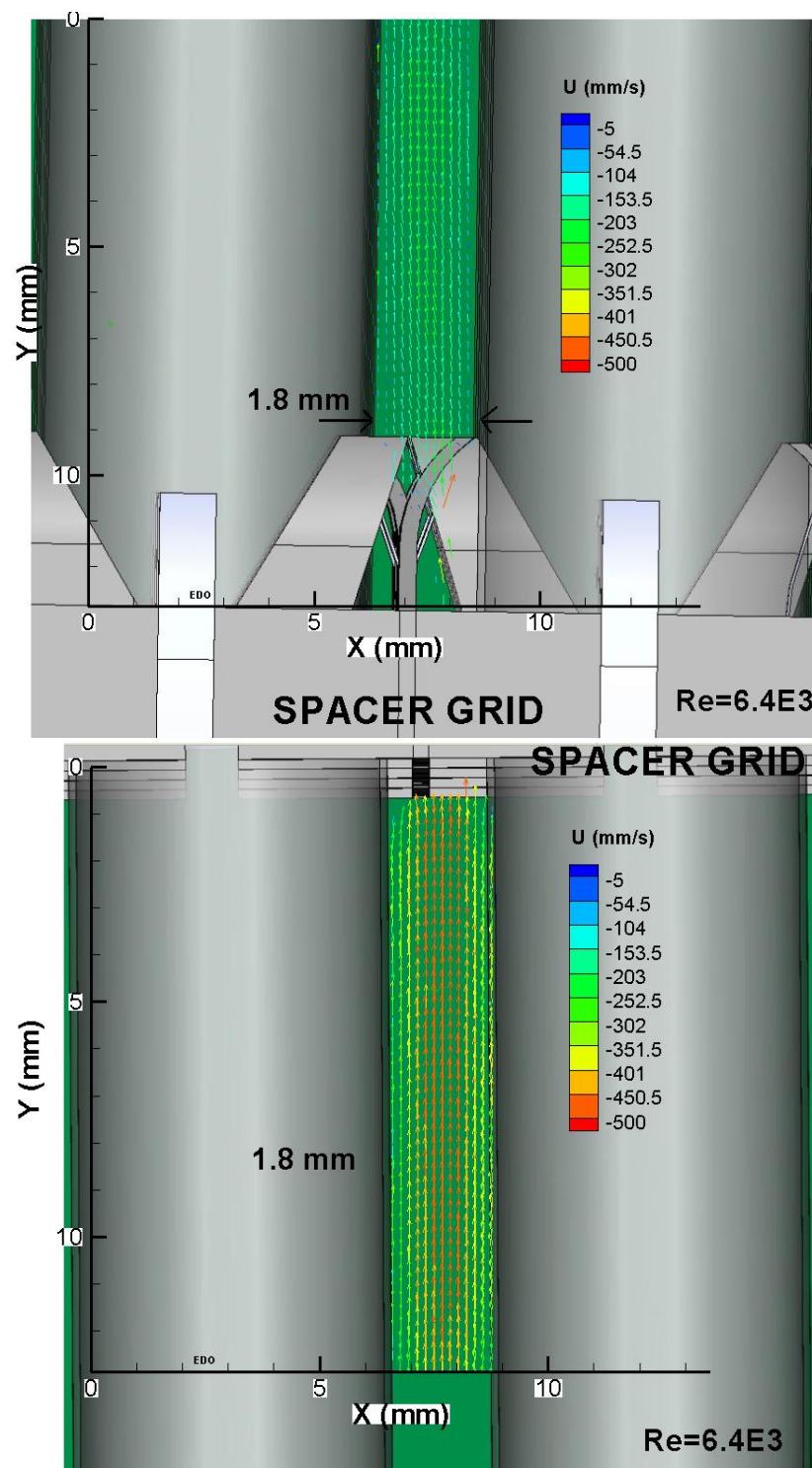


FIGURE 63. Averaged velocity field for subchannel scale . Positions BGP1 and AGP1, plane C, $Re = 6400$.

The results in plane B2 for the sub-channel scale at positions BGP1 and AGP1 are shown in the following plots. Figure 64 shows a typical instantaneous velocity field with color coded vectors. The color represents the value of the streamwise component of the velocity vector (U) for each vector plotted in the image. The color scale is indicated on the right side of the image with its correspondent label. It can be observed in figure 64 that the velocity vectors for position BGP1 follow a straight path toward the lower part of the grid. Its magnitude is in the 450 to 500 mm/s range for a $Re=6400$. Once the fluid passes through the grid the flow behavior changes and the vectors follow curved paths as indicated by thick black dotted lines denoting the fluid paths at position AGP1. Plane B2 does not have solid obstacles (rods) contained in the measurement volume, therefore vector are found in the whole image. There is an empty vector zone for position AGP1 (downstream grid) in the region of $y=0$ to $y=13$ mm. This zone denotes a region with no illumination from the laser light sheet since the light is blocked by one of the mixing vanes located at the right side of the grid. Therefore, no velocity vector can be found since no particles are illuminated in this particular region. The issue is not present at plane C due to the location of the vane obstacle. Figure 65 and 66 show the averaged velocity field of 10000 images for both positions and its calculated streamtraces respectively. The effect of averaging is visible in both figures where no curved paths are identified after the averaging process. This kind of comparison may help in the understanding of the physics at various temporal-spatial scales by means of CFD validation. Since the comparison may validate the results then the solved equations of motion in the CFD codes may bring a better insight of the phenomena at hand.

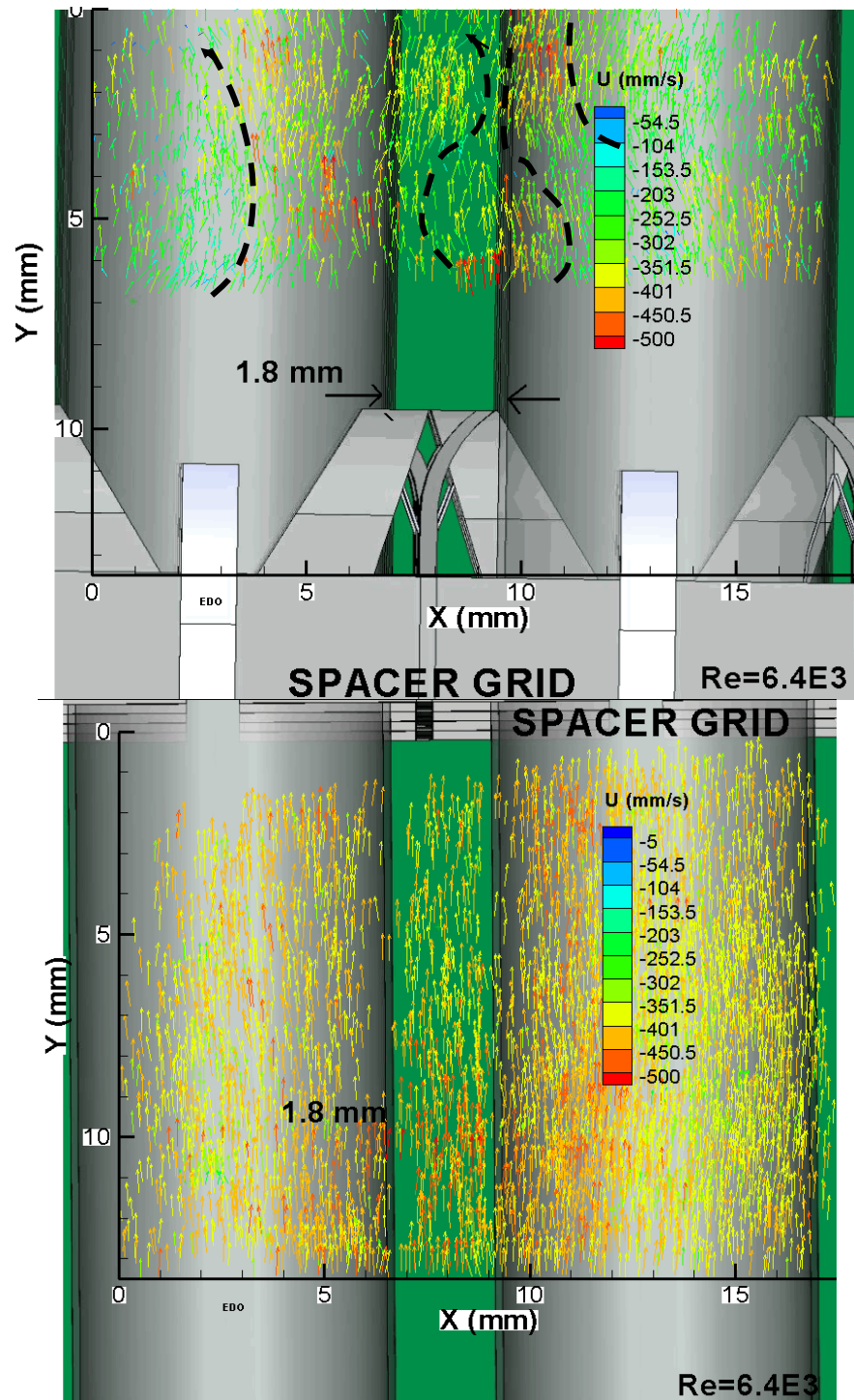


FIGURE 64. Typical instantaneous velocity field for subchannel scale. Positions BGP1 and AGP1, plane B2, $Re=6400$.

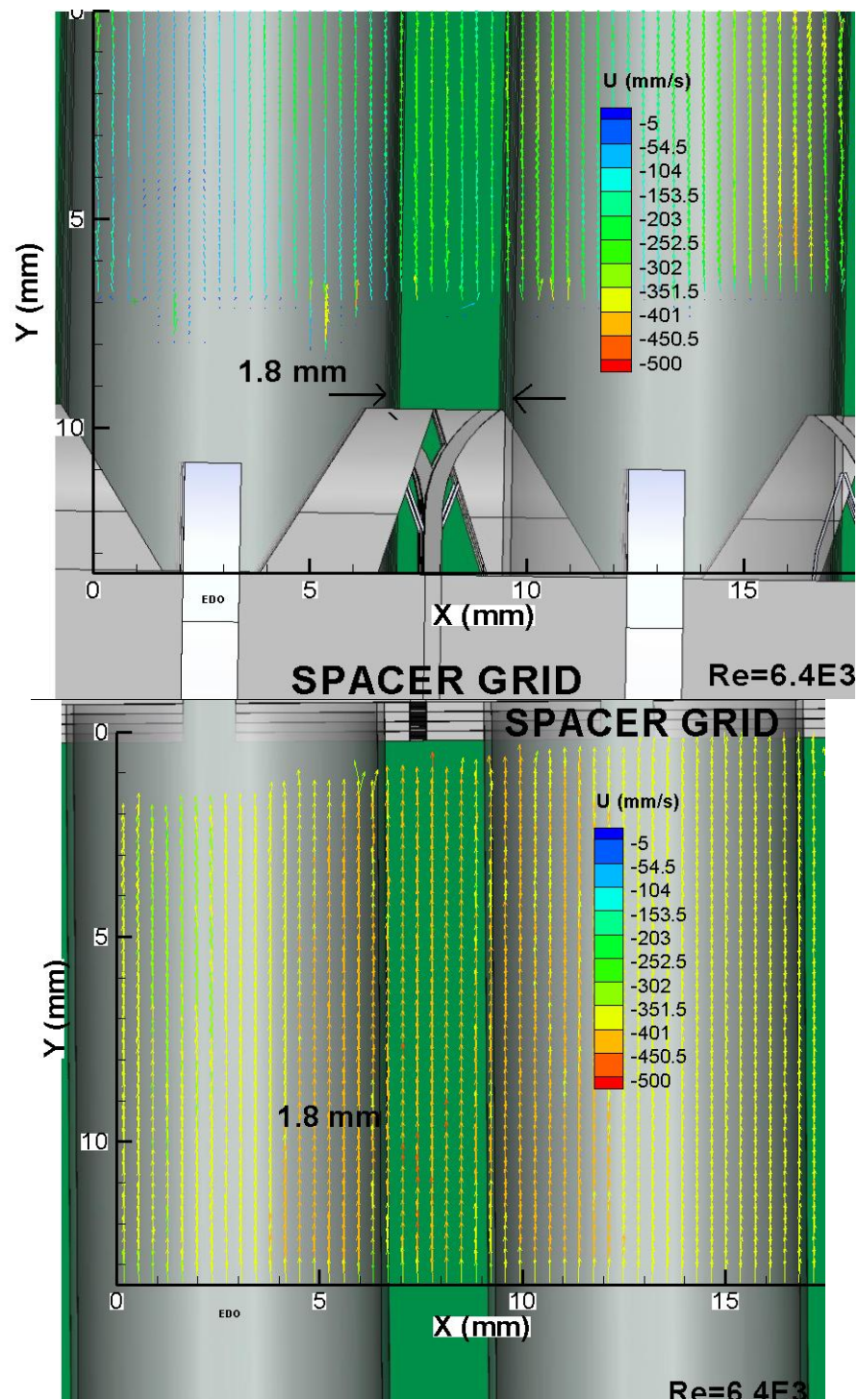


FIGURE 65. Averaged velocity field for subchannel scale . Positions BGP1 and AGP1, planeB2, Re= 6400.

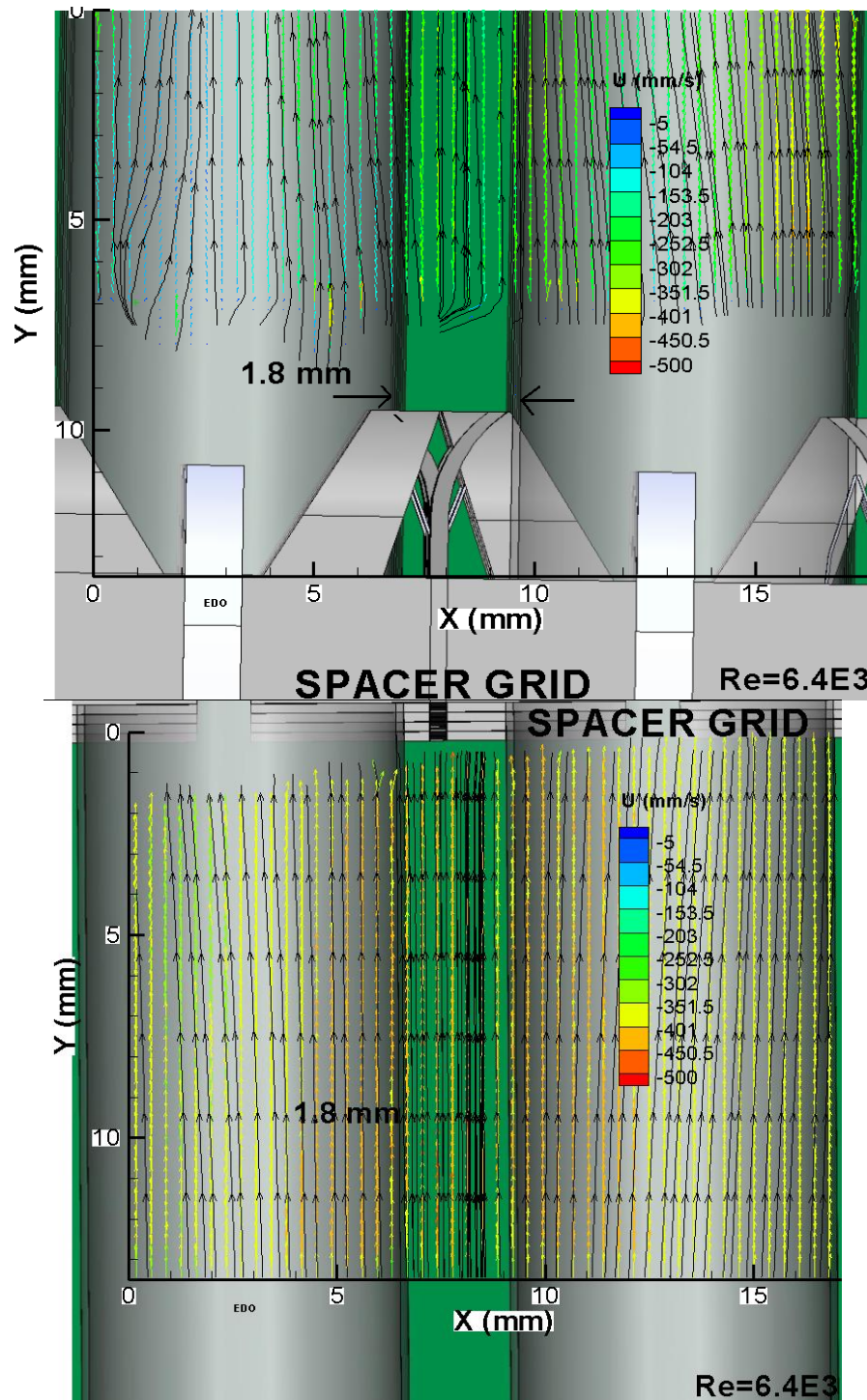


FIGURE 66. Averaged velocity field with overlapped streamlines for subchannel scale . Positions BGP1 and AGP1, plane B2, $Re= 6400$.

The velocity statistics are determined from the PIV measurements by ensemble averaging the number of images using equation (7). Where A is the quantity being averaged (i.e. streamwise velocity or square of the velocity fluctuations), X is the position vector and N is the number of realizations. The result of equation(7) is a two-dimensional average flow field. Further averaging can be done in the X or Y direction when the flow is assumed to be fully-developed. This results in a one-dimensional averaged profile which is a function of x or y (depending on the direction of the averaging) only. For this case, the flow can not be considered as fully-developed since the measurements were made at various zones where the flow is not developed. However, the averaging was performed in a preferential direction (x or y)to obtain the 1-D profile for each quantity of interest. The profiles give a simple and efficient way to compare the averaged behaviour of the flow at various of the measured positions or under different conditions.

The one-dimensional velocity profile (averaged over the y -axis direction) comparing two of the measured positions at the sub-channel scale (BGP1 and AGP1) are shown in figure 67 for various Re number ranging from 3250 to 15000. This figure shows the one-dimensional averaged streamwise component of the velocity vector upstream and downstream of the grid for the three Re conditions. Each case is presented using a red color line for $Re=3250$, a green color line for $Re= 9700$ and a blue color line for $Re=15000$. The velocity profile exhibits a parabolic shape in the gap formed by two adjacent rods. The averaged maximum velocity shows a decrease in magnitude of 30 % for the position located immediately above the mixing vanes with respect to the profile

measured before (upstream) of the grid. Figure 68 shows the normal component of the velocity vector for the three measured Re conditions in the sub-channel scale. The profile shows a maximum value for a x-direction position of 7.5 mm which is located at the center of the gap. There is a decrease in the normal velocity of about 50% in the three Re number tested at the position downstream of the grid with respect to the same cases at the upstream of the grid.

The turbulence intensities for both components of the measured velocity vector are shown in figure 69 and figure 70. The streamwise component (u') show a similar behavior to the typical intensities in a channel flow with non-slip conditions for the position upstream of the grid (before grid). The highest values are reached at the vicinity of the rod wall and the minimum at the center of the gap. The results for Reynolds stresses in plane C at the subchannel scale are shown in figure 71.

The results show similitude with the results obtained from a channel flow with non-slip condition for the position located upstream the grid (BGP1). The behavior of the stresses is completely modified after passing through the mixing vanes. Since there is a change of flow direction caused by the vanes and the wake at the tip of the vanes make the stresses to redistribute in the channel.

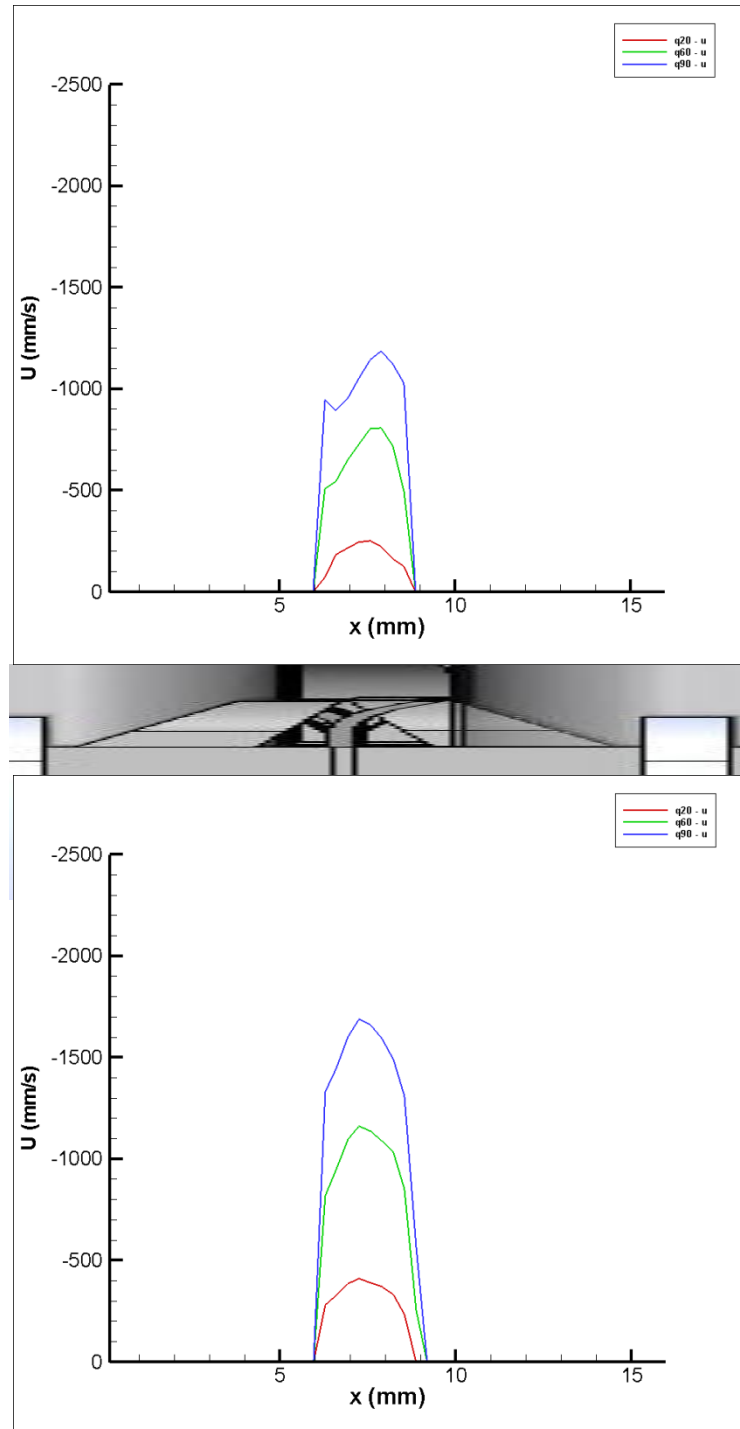


FIGURE 67. Averaged streamwise component (U) velocity profile for subchannel scale, positions BGP1 (down) and AGP1 (up), Plane C , Re=3250 (q20), Re= 9700 (q60) and Re=15000 (q90).

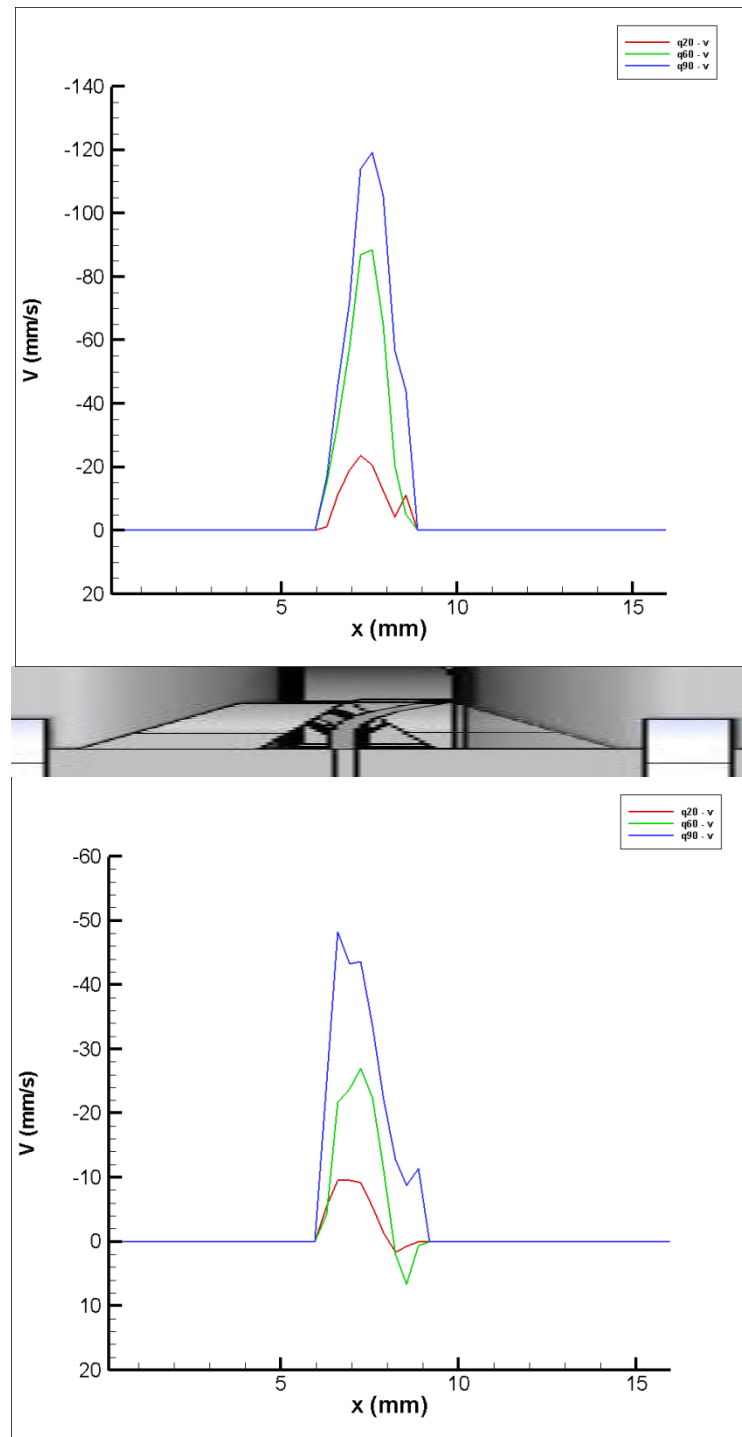


FIGURE 68. Averaged normal component (V) velocity profile for subchannel scale, positions BGP1 (down) and AGP1 (up), Plane C , Re=3250 (q20), Re= 9700 (q60) and Re=15000 (q90).

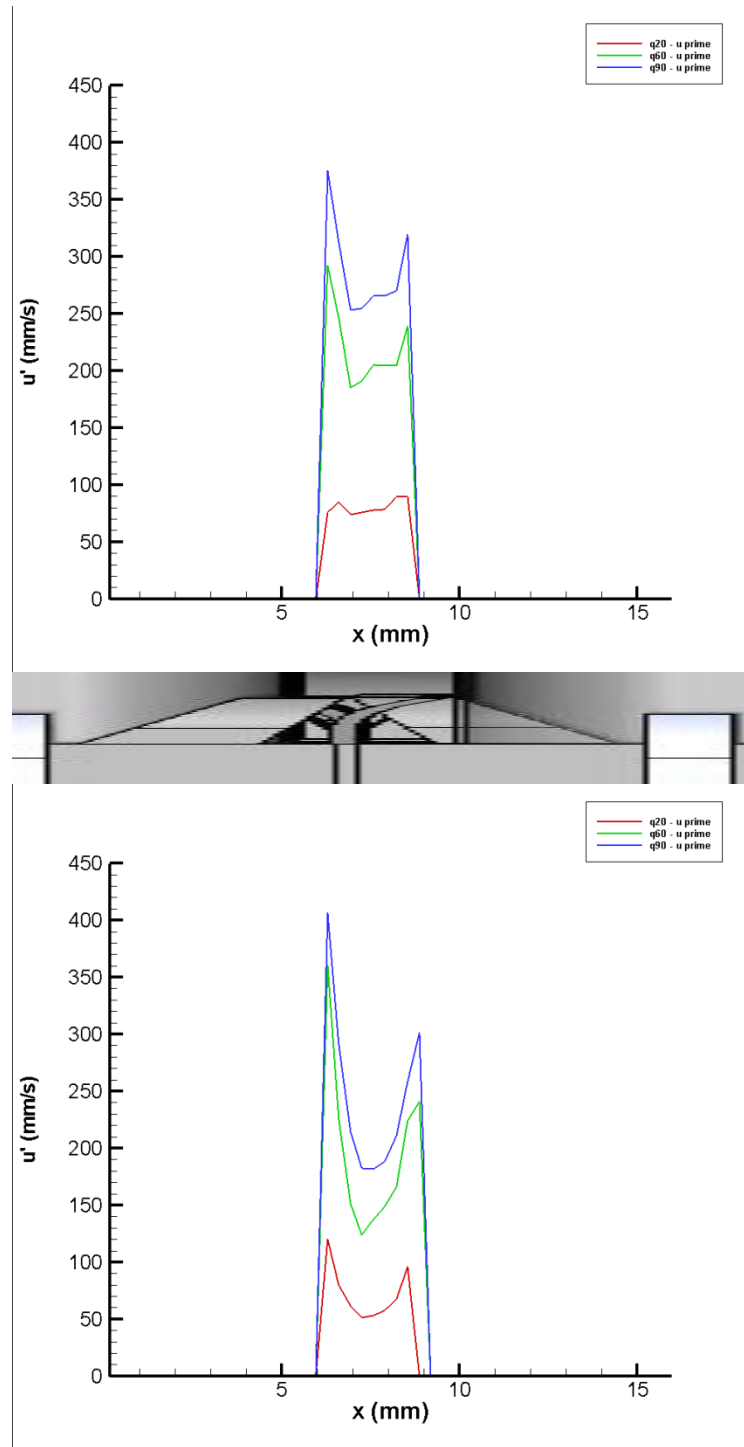


FIGURE 69. Averaged turbulence intensity for the streamwise component (u_{rms}) velocity profile for subchannel scale, positions BGP1 (down) and AGP1 (up), Plane C, $Re=3250$ ($q20$), $Re= 9700$ ($q60$) and $Re=15000$ ($q90$).

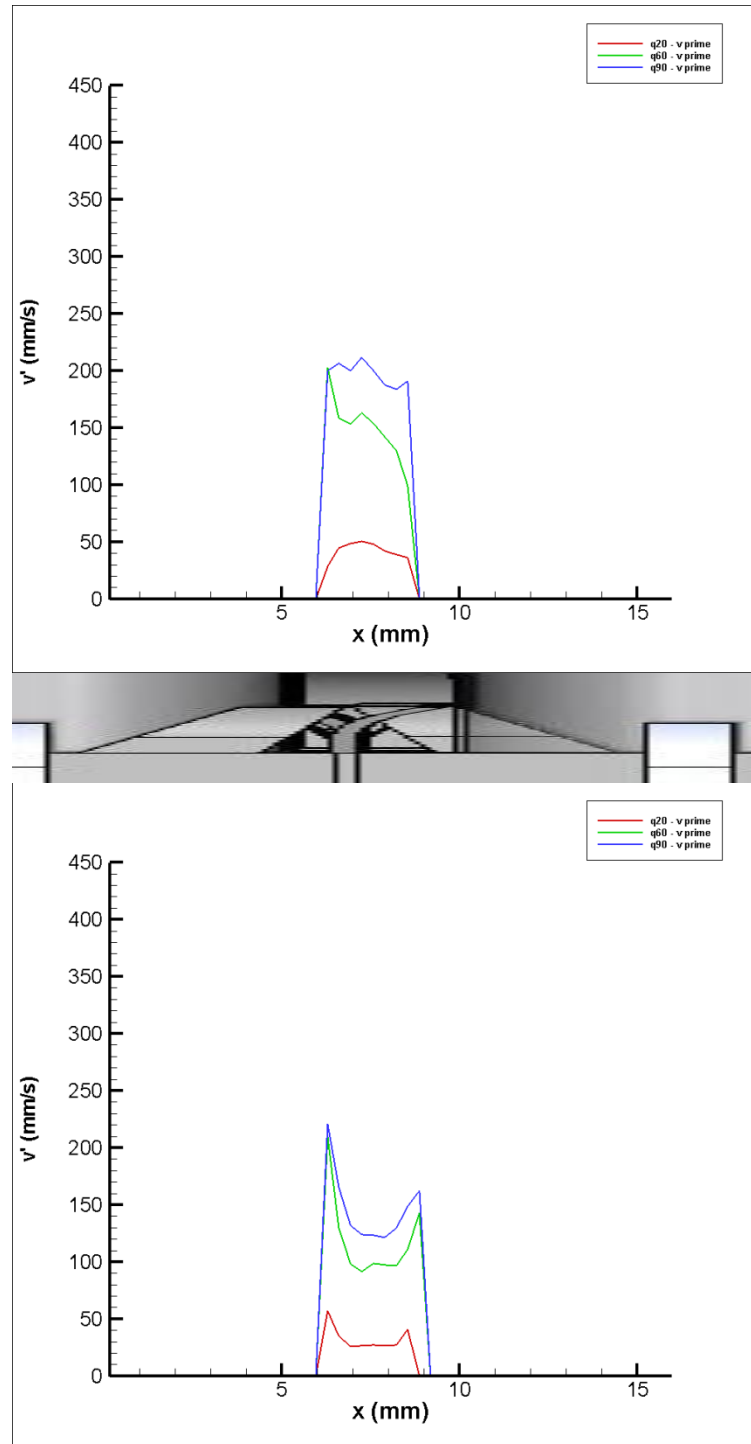


FIGURE 70. Averaged turbulence intensity for the normal component (v_{rms}) velocity profile for subchannel scale, positions BGP1 (down) and AGP1 (up), Plane C, $Re=3250$ ($q20$), $Re=9700$ ($q60$) and $Re=15000$ ($q90$).

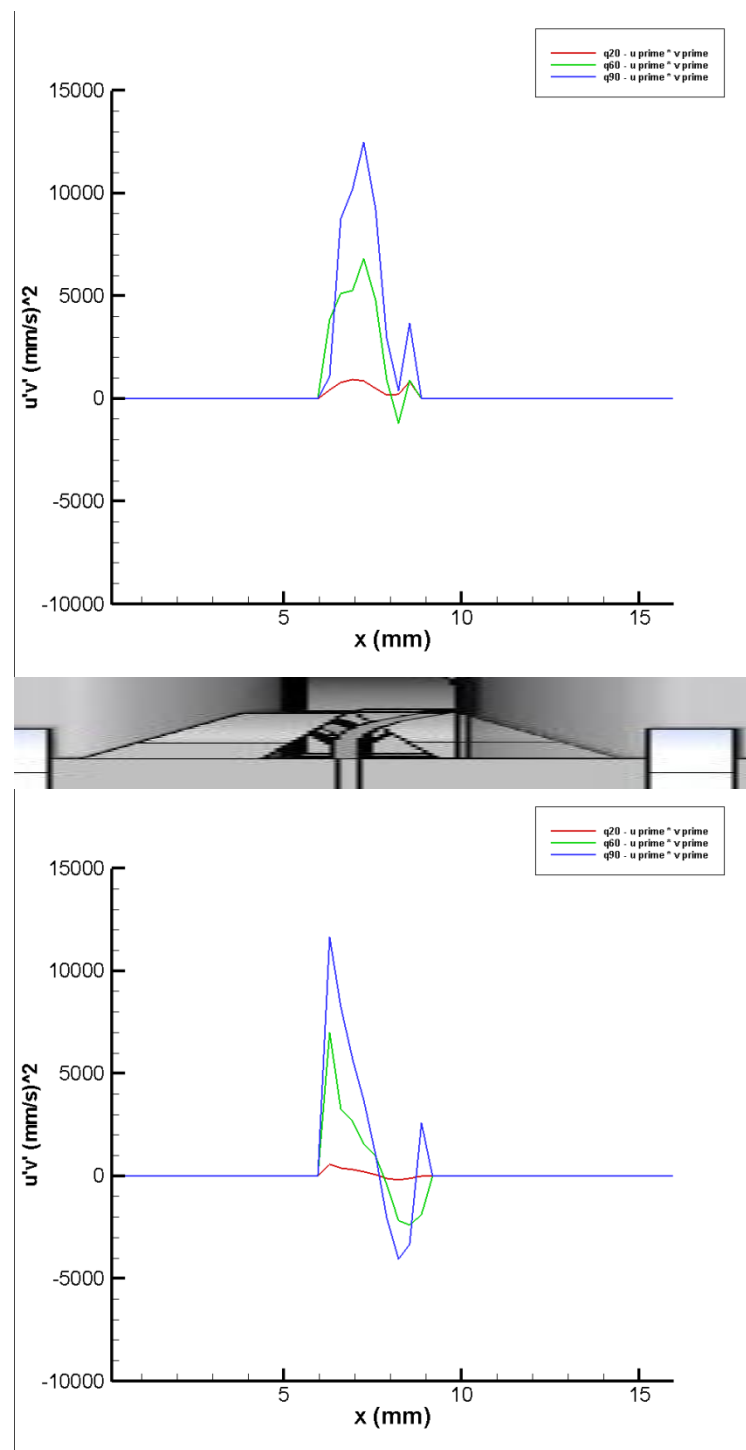


FIGURE 71. Averaged Reynolds stress ($u'v'$) for subchannel scale, positions BGP1 (down) and AGP1 (up), Plane C, $Re=3250$ ($q20$), $Re=9700$ ($q60$) and $Re=15000$ ($q90$).

4.1.3 Micro-scale

The micro-scale measurements were implemented in an effort to further resolve the flow characteristics in the gap formed by adjacent rods. The approximate width of the gap formed by adjacent rods depends on the specific grid design. For the cases tested in this work the width of the gap is about 2 mm. Using this dimension as a reference for the maximum length scale of the structures in the fluid, the appropriate viewing area can be selected. The selected measurement volume at this scale had the following dimensions: 6 mm in wide, 4 mm height and 1 mm thickness as shown in figure 72. This viewing area was achieved by the use of high resolution telecentric lenses with a 3X magnification factor. This kind of lens produced a sharp image of the objective and reduced to a minimum the aberration caused by normal lenses. The average velocity field of 5000 images under a $Re = 6400$ is shown in figure 73 for positions BGP1 and AGP1. Each vector is color coded with the color scale placed on the left side of the image. The vectors are overlapped on a black and white image taken with the camera in order to have a better appreciation of the mixing vanes size with respect to the whole measured viewing area. The results show that there is a well delineated color profile for the position BGP1 (upstream grid) starting with vectors of blue color nearby the rod wall transitioning to green color, yellow color and orange-red color at the center of the gap. The profile is symmetric for this position and repeated this pattern towards the second wall. In contrast, position AGP1 (downstream grid) shows a transition of colors denoting the streamwise component of the velocity vector starting with blue color at the

wall (right side of the image) , yellow color , green color and finishing with blue color at the second wall (left side of the image). The vectors show an inclined orientation towards the rod wall on the left part of the image. The profile is not symmetric for this position and denotes a velocity reduction of 30% with respect to position BGP1. The average thickness of the boundary layer for this case is estimated to be about $\delta_{99} = 400 \mu\text{m}$ based on the position where the velocity is 99% of the centerline velocity. Figure 74 shows the averaged velocity profile with the calculated streamtraces showed in white color. The streamtraces show a straight pattern for the measured position upstream of the grid (BGP1) and a deflected flow pattern for the position upstream of the grid (AGP1). The inclination of the deflected pattern is proportional to the angle of the mixing vanes.

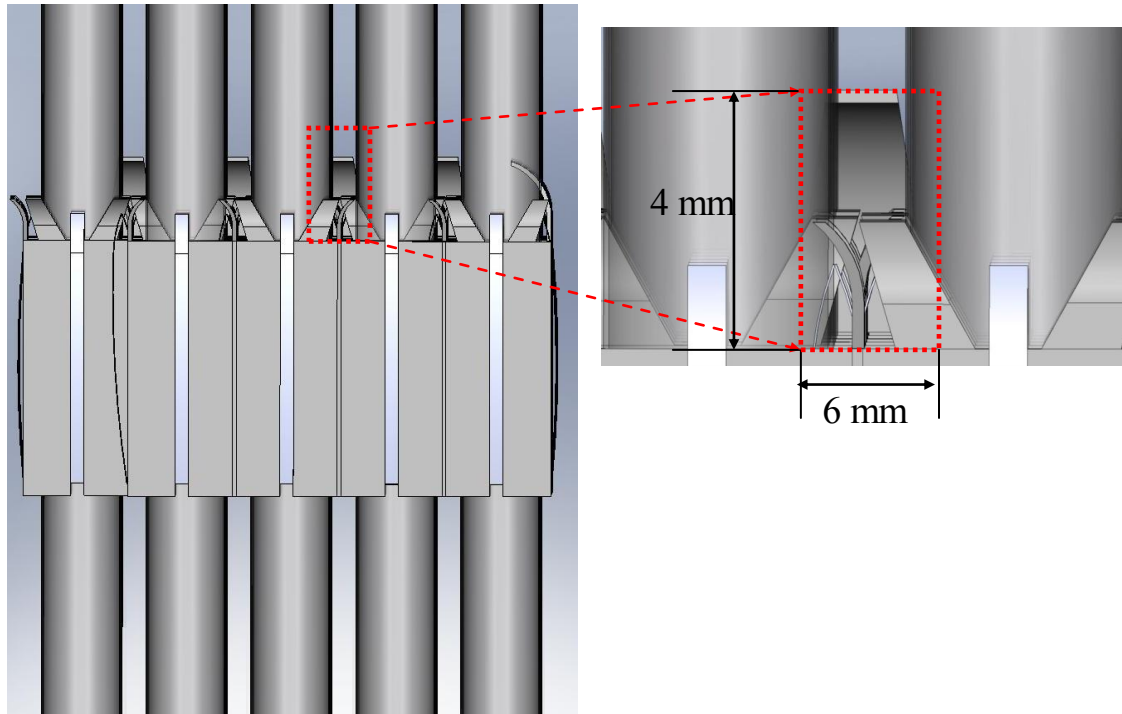


FIGURE 72. Micro scale viewing area

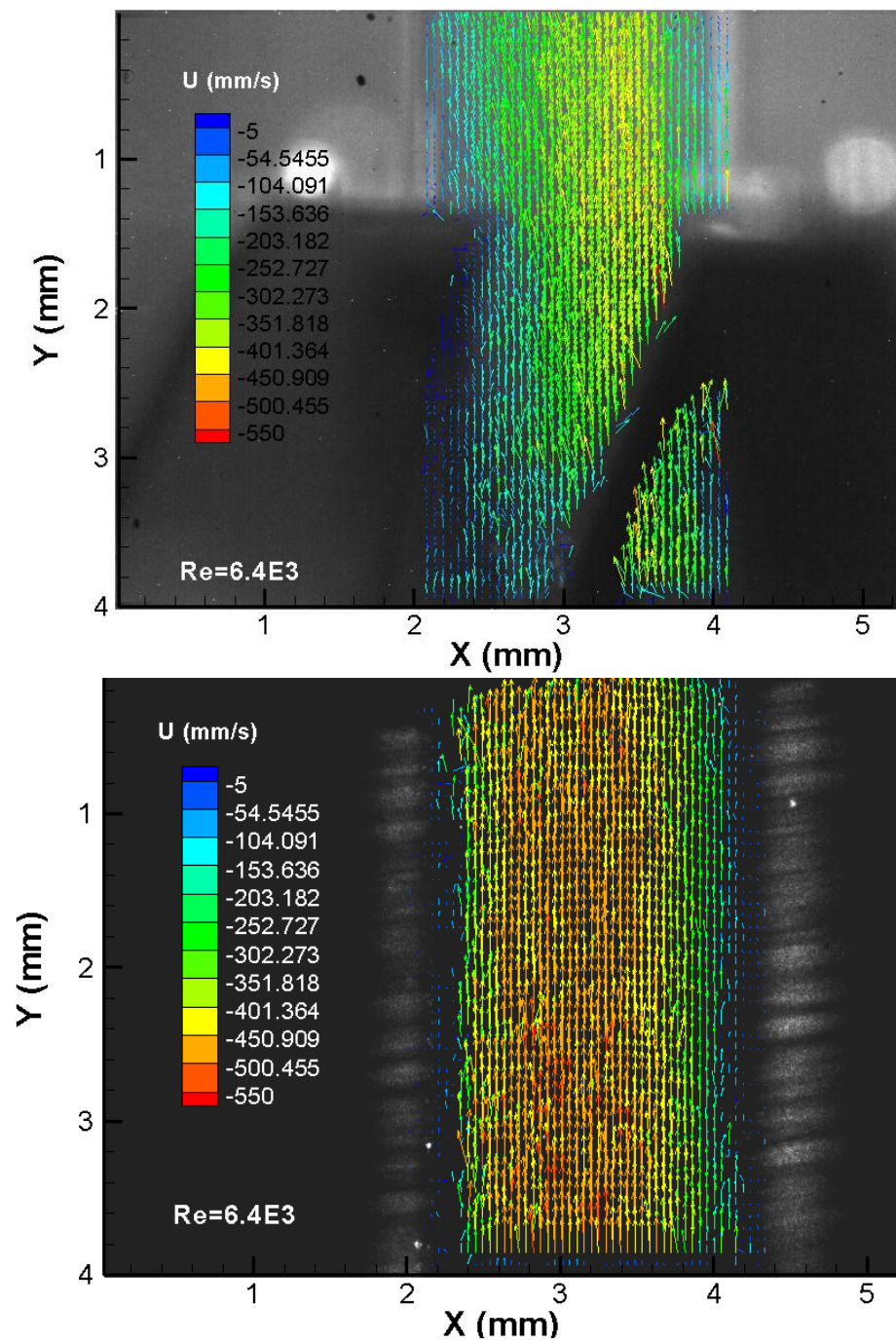


FIGURE 73. Typical instantaneous velocity field for micro scale. Positions BGP1 (down) and AGP1 (up), plane C, $Re=6400$.

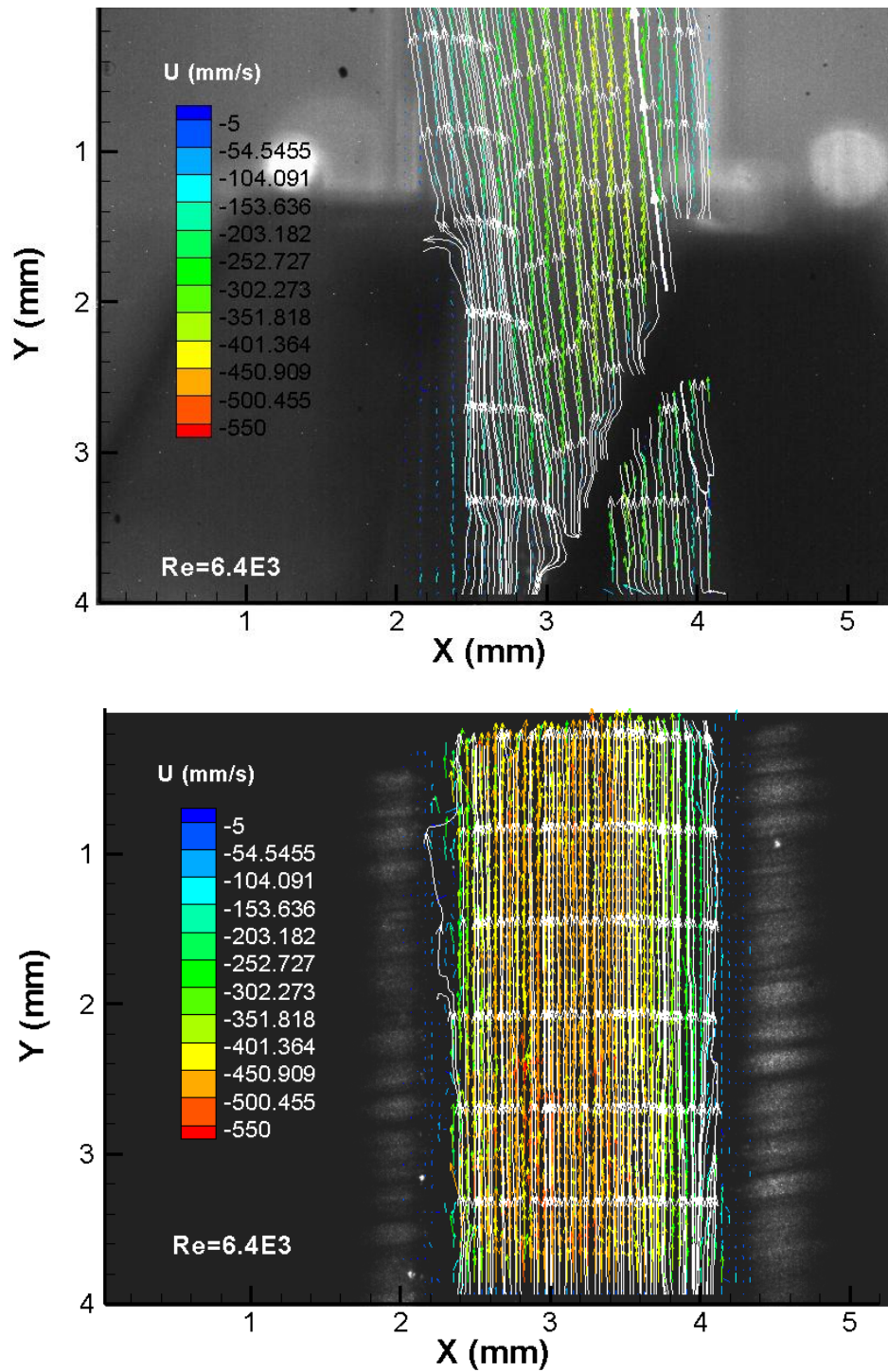


FIGURE 74. Typical instantaneous velocity field with overlapped streamlines for micro scale. Positions BGP1 (down) and AGP1 (up), plane C, $Re= 6400$.

4.2 Grid 2

The measurements for axial and lateral velocity at the investigated region were performed at several planes using a multi-scale approach. This approach consisted of performing measurements on various viewing areas of the test section. The scales were selected based on the physical constrictions and the desired resolution of the velocity fields. The measured planes for grid2 are shown in figure 75. Nine planes were measured for grid 2 which are represented by different color lines in the figure. The planes were formed by the laser light where the light passes through the test section. The planes were identified using the number assigned to each of them or by the corresponding notation using the first four letters from the alphabet. For this case plane A was the closest plane to the by-pass flow plane explained in chapter II. Figure 42 in the previous section shows the different scales used in this work. The first scale examined the flow behavior in the planes that cover the five rods and its respective sub-channels. At this scale the interaction between sub-channels and general characteristics of the flow were captured. The equivalent viewing area of the cameras for this scale was 71.1 x 52.5 mm. The second scale is denoted by the area marked with a solid red line in Figure 42. This scale captured the flow characteristics of a central sub-channel with an equivalent camera viewing area of 17 x 12.5 mm. At this scale the flow evolution in the sub-channel could be observed.

The planes position was changed using a two-dimensional (Y-Z) positioning system. Figure 75 shows a schematic of the grid and the position of the measured planes. Each plane is represented by a horizontal line with a solid or dashed pattern. The

measurements were performed upstream (before grid) and downstream (after grid) of the spacer using the various planes presented in figure 75.

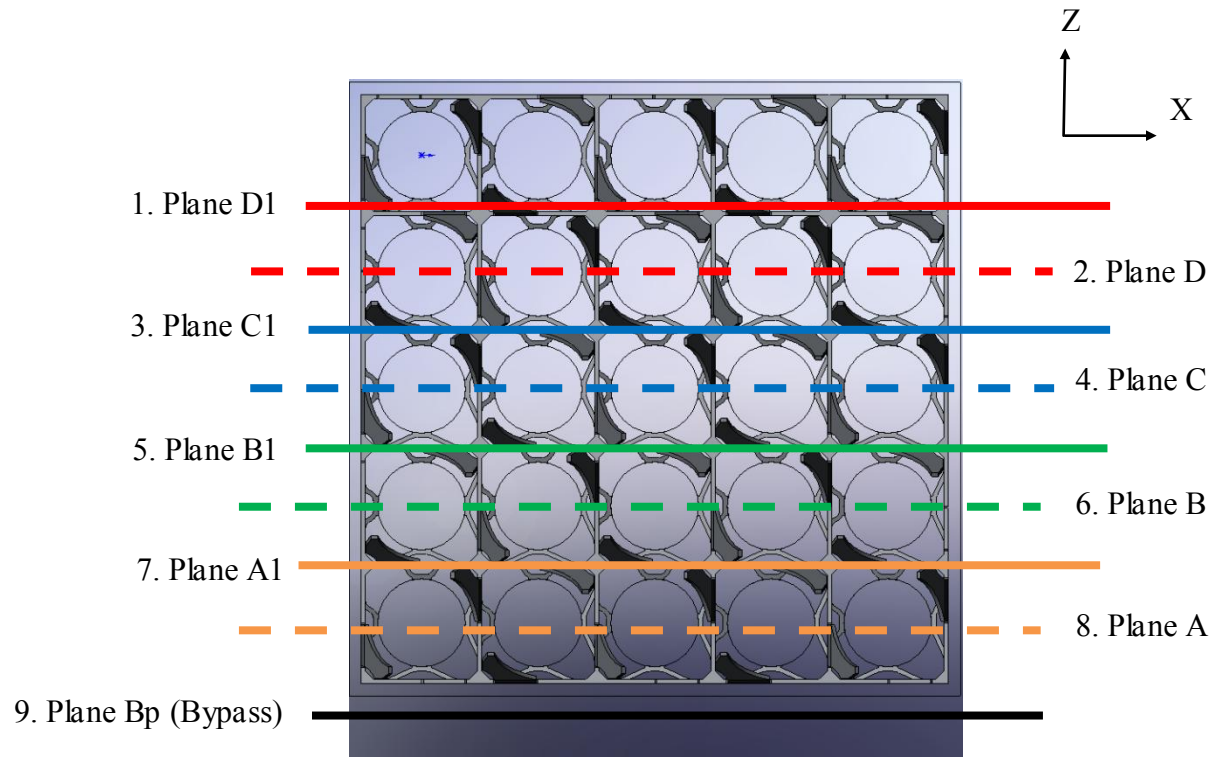


FIGURE 75. Location of the various 2D PIV measurement planes.

Figure 76 shows a side view of the test section. The measured planes are presented from a different perspective in order to appreciate plane 9 which measures the bypass flow. The gap formed between the edge of the spacer grid and the boundary of the plastic u-shaped internal channel allows a higher flow rate to pass through it. Therefore, measurement of the velocity profile will give an accurate estimation of the percentage of flow that flows through the gap.

The colored lines in figure 76 show the different measured planes. The line pattern denotes the type of plane being measured which can be a plane where the laser light lies in the middle of a cylindrical rod such as planes 2, 4, 6 and 8 denoted by dotted lines of different color. The solid lines represent those planes where the laser light has no obstruction inside the grid such as planes 1,3,5,7 and 9. It can be observed in the figure that no measurements were performed in the rod section closest to the left wall. The cause for this omission in the measurements is the wall itself from the observation window (not showed in figure 76), since the wall thickness obstructs the laser light path. Therefore, the first measurement plane was located at the edge of the geometric constriction which is plane 1. The color code was selected in such a way that contiguous planes have the same color, therefore there are four different colors and the bypass plane is represented by a black colored line.

The position of the camera is perpendicular to the planes as shown in figure 76. The PIV measurements were performed in the X-Y plane. The third axis denoted as the z direction in Cartesian coordinates runs along the planes 1 through 9.

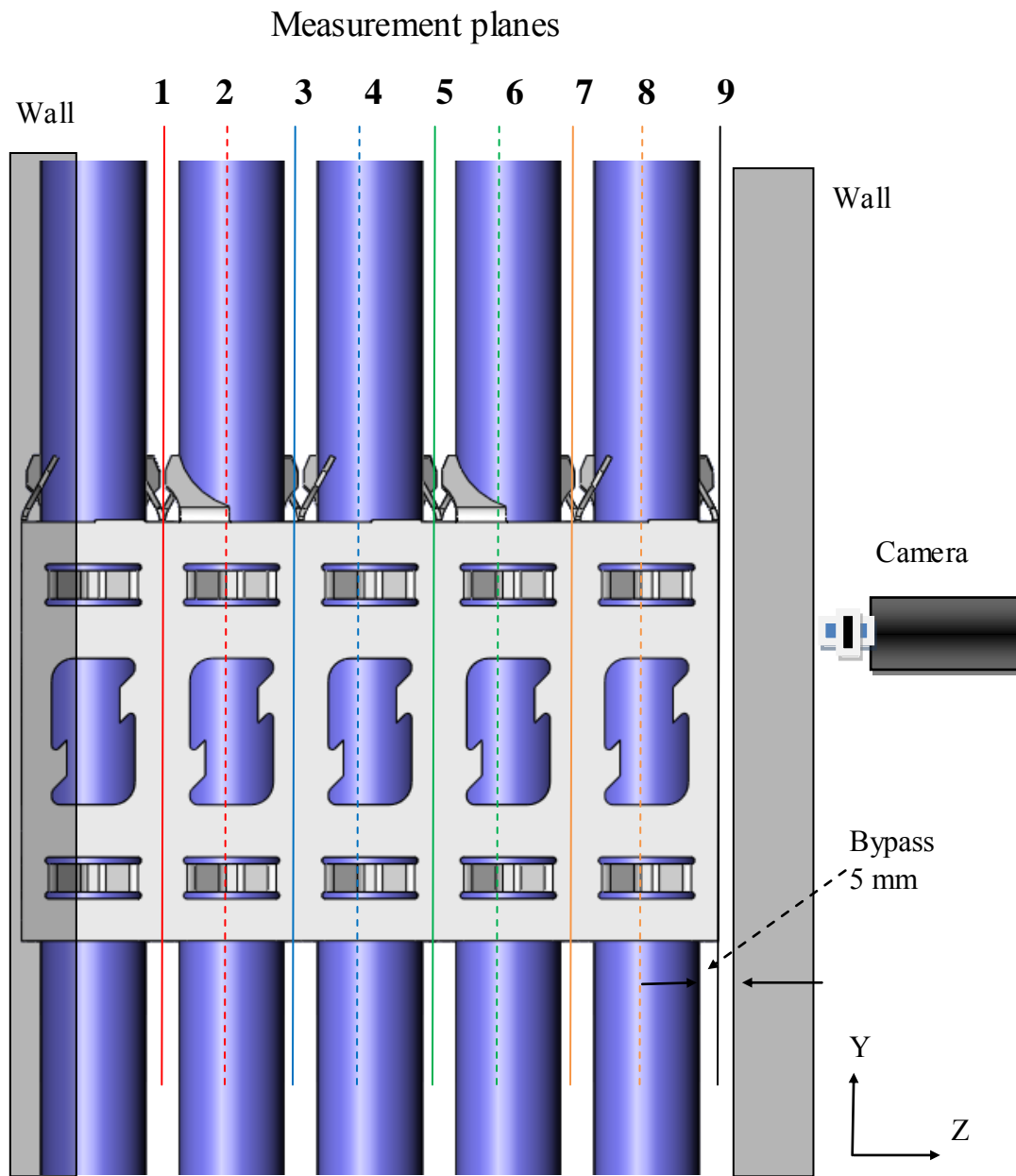


FIGURE 76.Side view of test section showing position of measurement planes.

4.2.1 Inter-channel scale

Figure 77 shows a pictorial of the two positions measured using the viewing area covering the inter-channel scale. Each of the black dotted rectangles represents one measured position. Each position was assigned with a representative name using the following logic. All measured positions upstream from the grid were denominated as “Before Grid” (BG) and the positions downstream from the grid were denominated as “After Grid” (AG). The corresponding nomenclature for each position was included in the name by using the abbreviation and the corresponding number. i.e., AGP1 represents the After Grid position 1 measurement zone. The distance covered by each measurement volume was measured from the edge of the grid without including the mixing vanes. Figure 43 shows the three measurement volumes used for the inter-channel scale and its corresponding distance from the grid in length units (mm) and equivalent hydraulic diameters (D_h). The distance range for positions after the grid varied from 0 (grid edge) to $9.3 D_h$ (tip of measured volume 2, AGP2). From the before grid case (upstream grid) only one position was measured and its corresponding distance from the grid edge to the tip of the viewing area was $4.5 D_h$. The flow direction with respect to the measured positions is indicated in the figure by a white arrow pointing upwards.

The first step for the PIV analysis was the acquisition of 2D images of the seeded flow using high speed cameras which have the equivalent viewing areas 1 (inter-channel scale) and 2 (sub-channel scale) mentioned previously in this document.

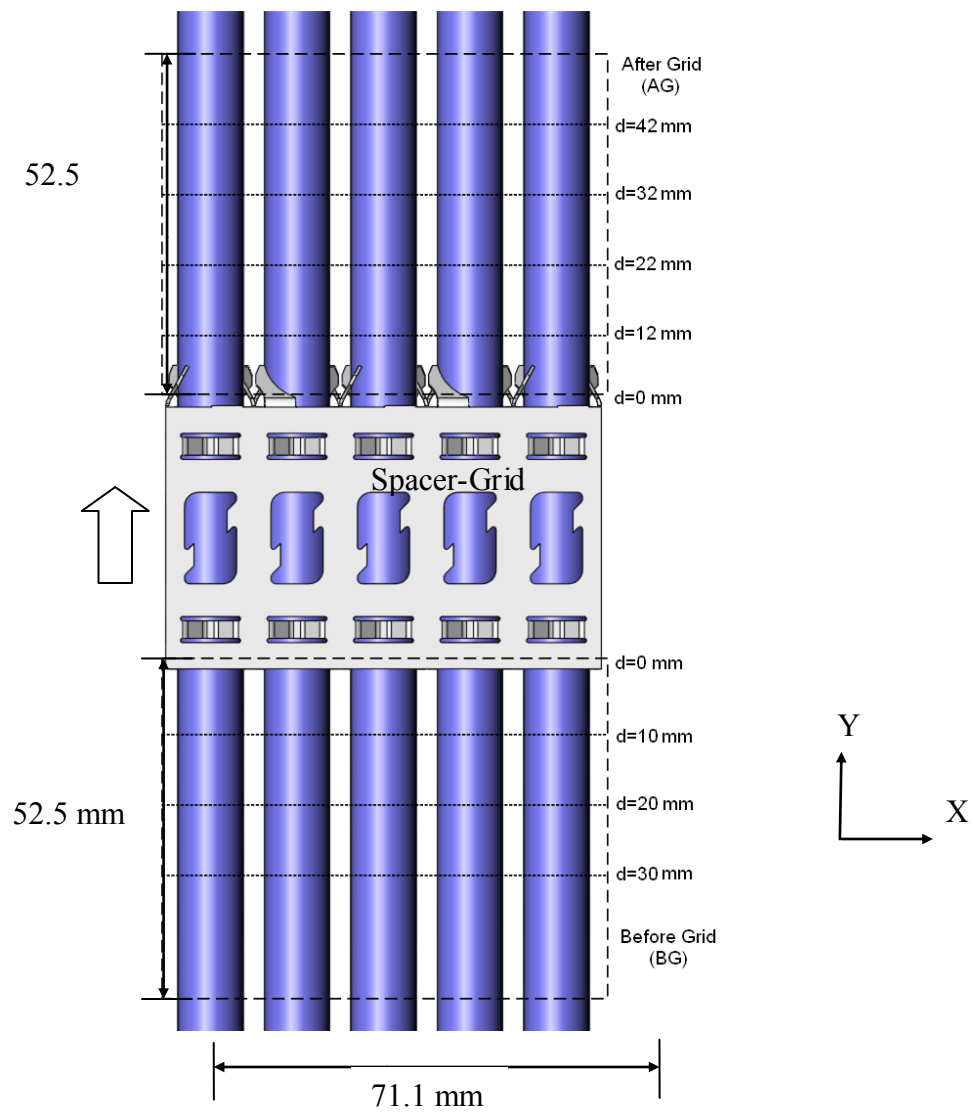


FIGURE 77. Equivalent view wing area #1 (all channels).

Typical obtained images for the inter-channel scale PIV viewing areas at portions BGP1 and AGP1 for plane C are shown in figure 78. The figure shows the position of the spacer grid with respect to the two measured viewing areas. Since the flow was seeded with the PIV particles, the light scattered by the particles is the only light captured in the PIV images. Therefore, for this particular measured plane the flow geometry constraints are represented by the brighter zones in the picture. The edges of the rods are well delineated and the particles can be easily identified. The measurements capture two components of the velocity vector: 1) X-axis direction and 2) Y-axis direction. The results presented in this work utilized a common name code to identify each of the components measured using two-dimensional PIV. The velocity component in the Y-axis direction was designated as “streamwise” component since in points in the direction of the main stream. The component in the X-axis direction was designated as the “normal” component of the velocity vector. The sign convention utilized in this work for each component was designated based on the logic followed by the particle identification and vector calculation software. In which any component in the Y-axis direction will be positive when pointing downwards the page and negative when pointing upward the page. The X-axis direction is positive when pointing towards the right side of this page and negative when pointing towards the left edge. The sign coding utilized during this work it may be different from other results and the reader is advised to recognize this detail. However, a change in signs in the plots may be made later for future publications.

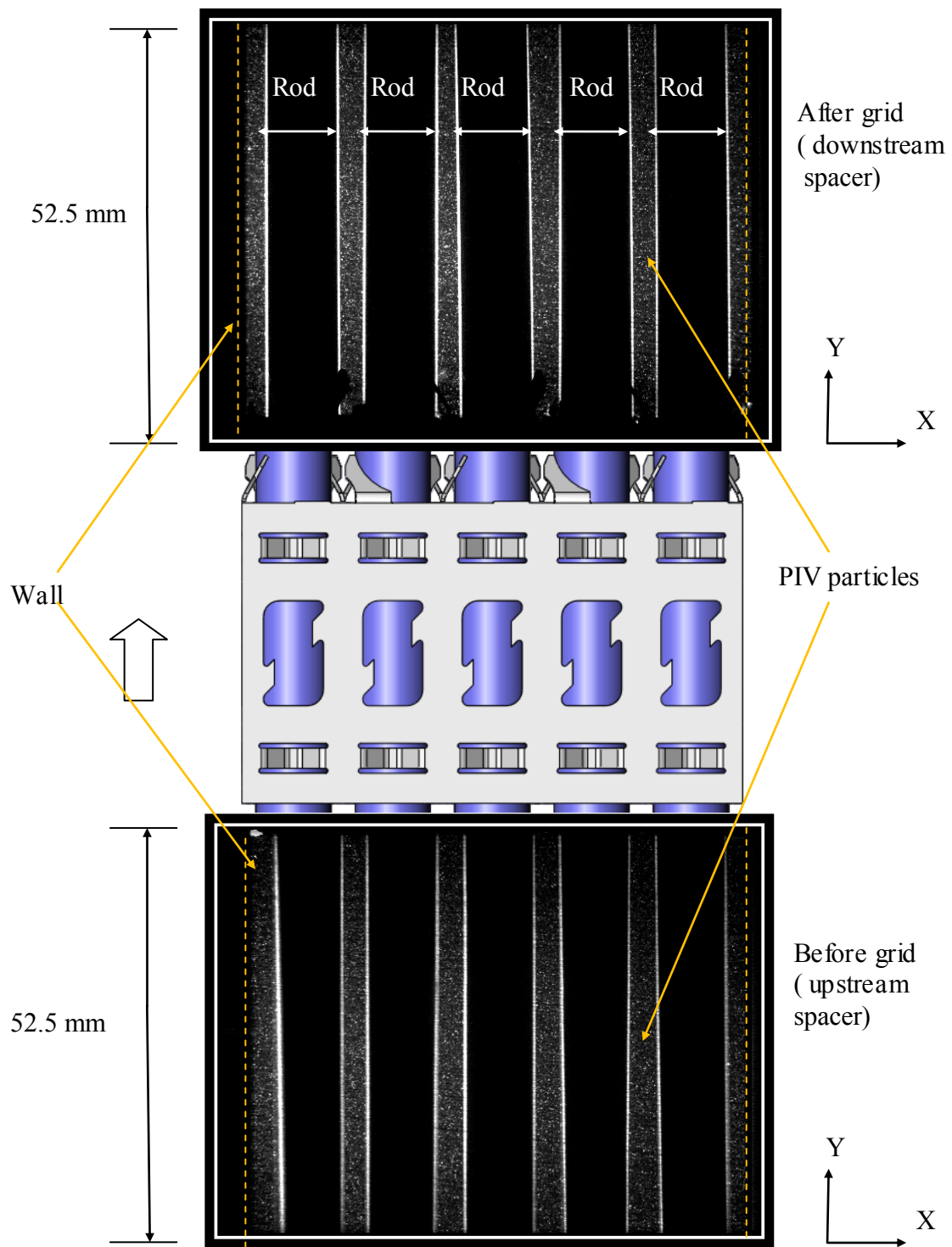


FIGURE 78. Typical PIV image for equivalent viewing area #1 (all channel).

The PIV images are processed using an in-house developed computer code which detects the centroid location of each particle in the picture and calculates its displacement in consecutive images. In this way, velocity vector fields can be obtained using a pair of consecutive images. The obtained velocity fields were used to obtain averaged quantities of the parameters of importance for the investigation. Some of the most important averaged parameters are presented in the following sections. Figure 79 shows the obtained velocity fields for each measured plane upstream and downstream the spacer-grid. The 18 planes measured are compacted into a single plot with the grid position scaled. The first plane show in figure 79 from left to right correspond to the bypass (Bp) plane. The rod position was omitted intentionally for better appreciation of the different planes position and its corresponding velocity fields. The white arrow on the left side of the image represent the main flow direction going from the bottom of the page , passing through the spacer and going upwards. The two positions measured: BGP1 and AGP1 are presented next to its correspondent results. The planes were measured independently at steady state conditions for this part of the work.

The various planes presented in Figure 79 are presented separately in figures 80 and 81 for better appreciation. These figures show the average velocity fields for each plane for the two components of the velocity vectors coded by color with its calculated streamtraces overlapped on the contour plots. A more detailed description for each plane can be found in Appendix B of this document.

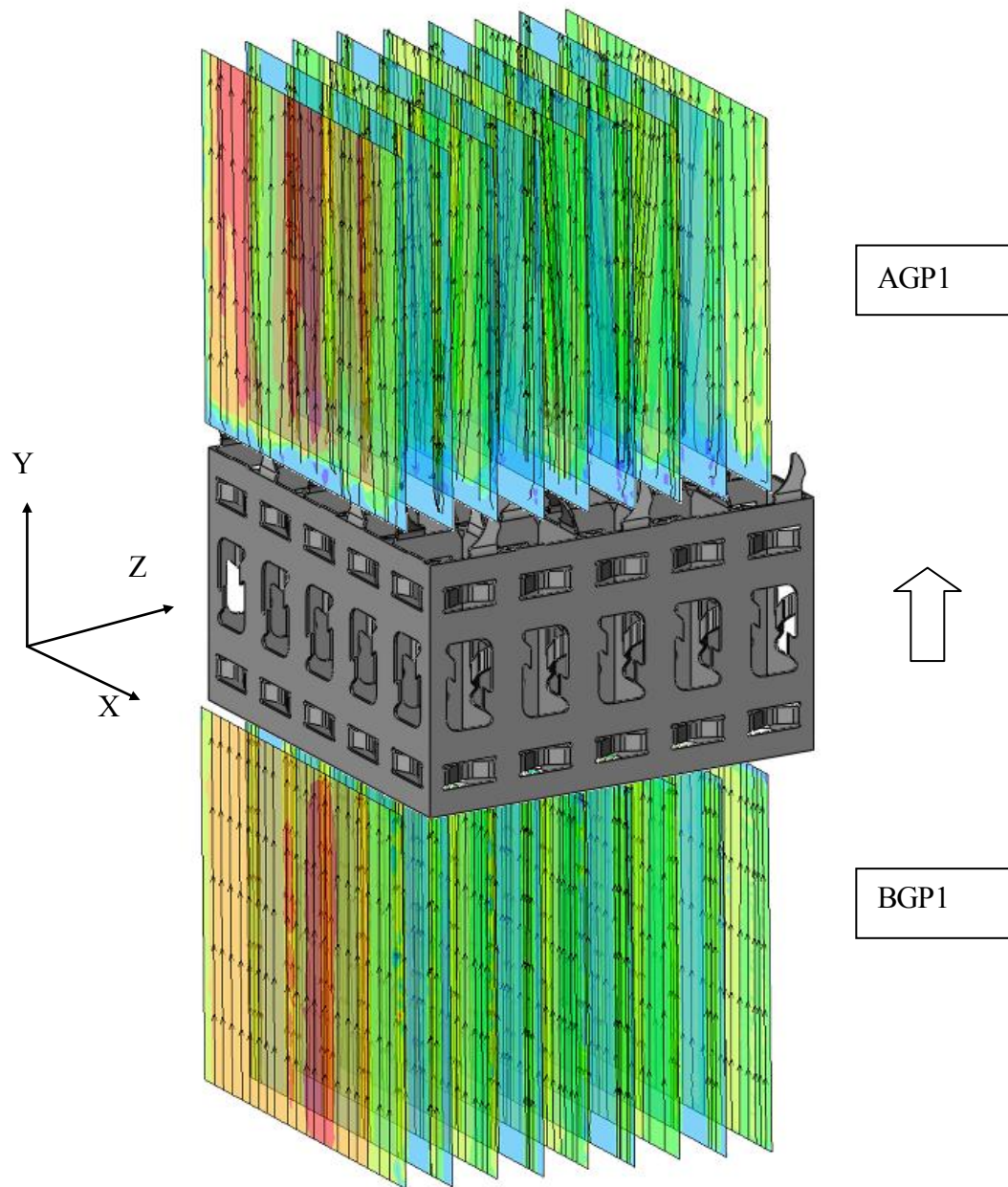


FIGURE 79. Average velocity fields before and after grid. Color code represents streamwise component of velocity vector (U) with red color = 2500 mm/s dark blue = 0 mm/s. $Re = 16300$.

The following results present the velocity profiles of 10,000 images using the assembled averaged process indicated in chapter III of this work. The average number of vectors per image depends on the plane position. In general, planes that lie between rods had an average of 1000 vectors per image. The planes with no rods had an average of 4000 vectors per image.

The effect of the bypass flow is shown in figure 80 where the red color for the first plane from left to right exhibits zones with velocity magnitudes in the streamwise component of up to 2500 mm/s. This velocity range is constrained to the bypass flow and caused by the increase in cross sectional area formed by the gap between the flow casing (u-shaped channel) and the edge of the grid. The effect of the bypass flow is diminished as a function of distance from the wall (z-direction of figure 80). The streamlines denote a strong change in flow direction for all planes but plane Bp for position AGP1. The deflection is caused by the spacer split vanes. In contrast, figure 81 shows the averaged results for the streamwise component of the velocity for all the measured planes in position BGP1. The flow at this position does not have the direct influence of the spacer. The flow follows straight paths as indicated by the streamtraces shown for each plane in figure 81. The influence of the bypass flow is noticeable exhibiting velocity magnitudes of 2500 mm/s. Averaged velocities show influence of the bypass flow in the streamwise component of the velocity vector for planes 9, 8 and 7.

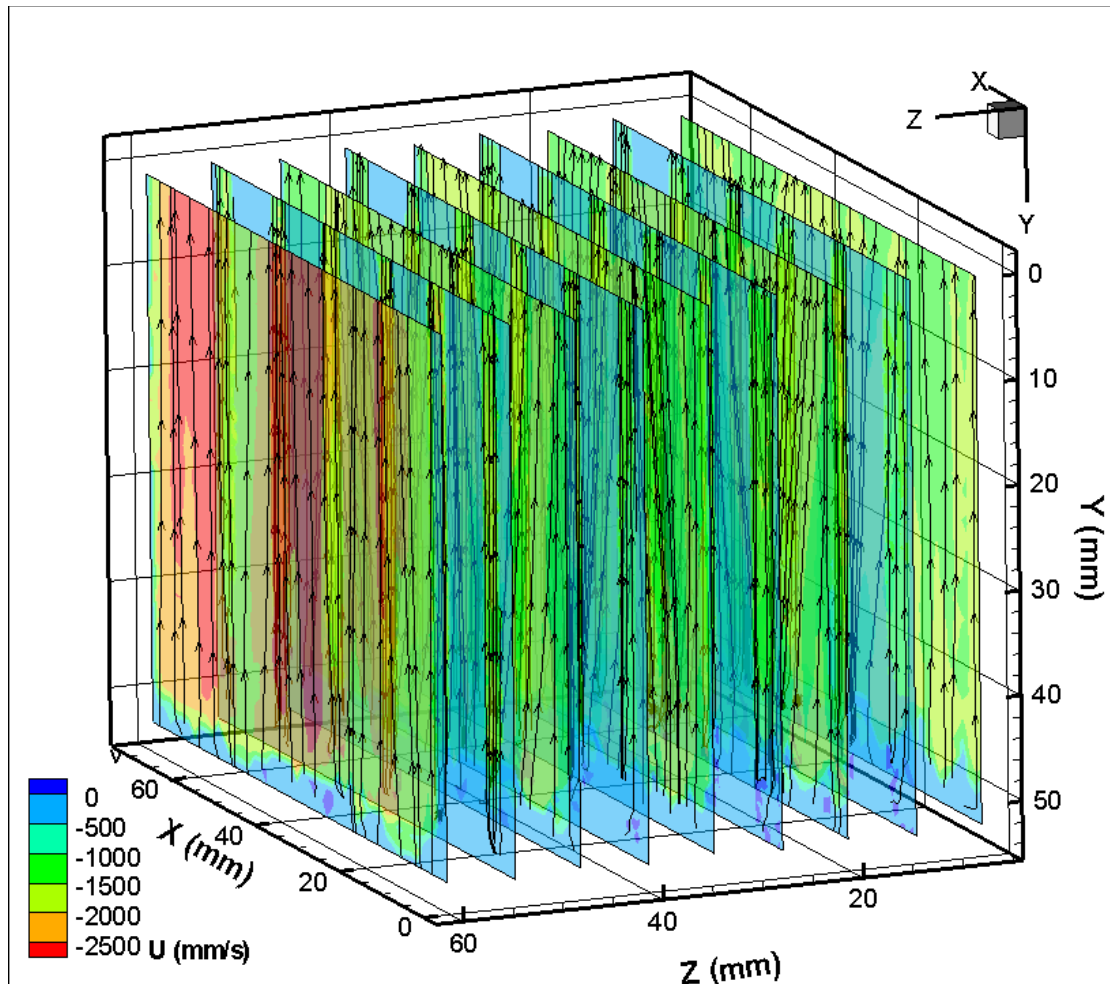


FIGURE 80. Average velocity fields and overlapped streamtraces for the downstream grid case. Color code represents streamwise component of velocity vector (U) with red color = 2500 mm/s dark blue = 0 mm/s. $Re = 16300$.

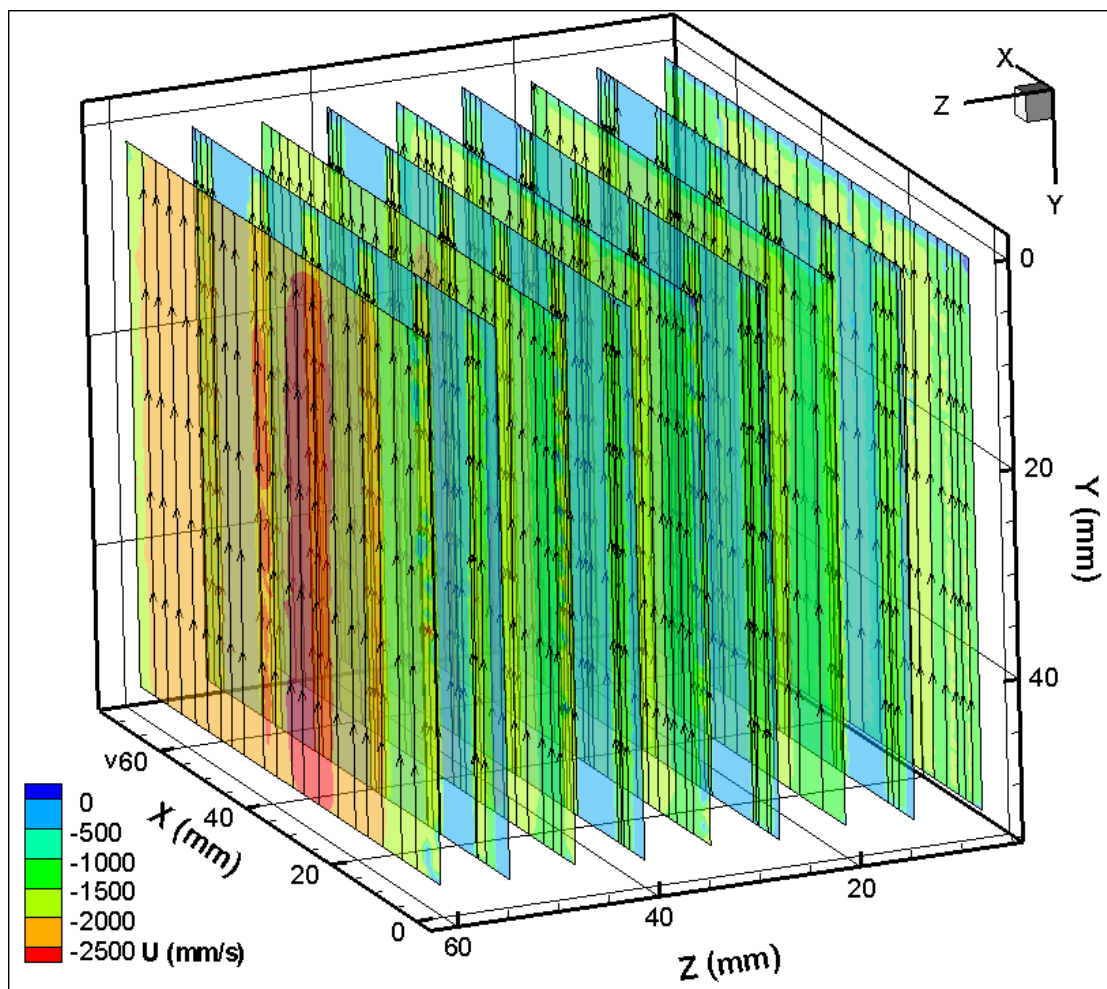


FIGURE 81. Average velocity fields and overlapped streamtraces for the upstream grid case. Color code represents streamwise component of velocity vector (U) with red color = 2500 mm/s dark blue = 0 mm/s. $Re = 16300$.

The averaged velocity field for the normal component of the velocity vector at position AGP1 for all planes is shown in figure 82. There is a strong deflection in the fluid direction caused by the split vanes of the grid. The magnitude of the normal component is denoted by large zones of red and blue color. The color denotes the sign change of the normal component of the velocity vector. It is observed in figure 82 that there is a consistent pattern in the sign change for planes 1, 3 5 and 7. The vanes caused the flow “to split” into two streams with opposite directions. This effect is attenuated in the planes that lie between rods. This behavior is due to the presence of the rods where the fluid splits but keep going along the surface of the rod.

Figure 83 shows the averaged velocity field for the normal component of the velocity vector at positionBGP1. This position is not affected by the grid vanes of the spacer nearby. However, the conditioning grid located 500 mm downstream position BGP1 still affects these results. However, the results exhibit straight paths as denoted by the streamtraces plotted in figure 83. The magnitude of this component has an n average value five times smaller than its counterpart in position AGP1 for most of the planes but the bypass flow.

The velocity statistics are determined from the PTV measurements by esemble averaging the number of images using equation (7). Further averaging can be done in the X or Y direction when the flow is assumed to be fully-developed. This results in a one-dimensional averaged profile which is a function of x or y (depending on the direction of the averaging) only. For this case, the flow can not be considered as fully-developed since the measurements were made at various zones where the flow is not developed.

However, the averaging was performed in a preferential direction (x or y) to obtain the 1-D profile for each quantity of interest. The profiles give a simple and efficient way to compare the averaged behaviour of the flow at various of the measured positions or under different conditions.

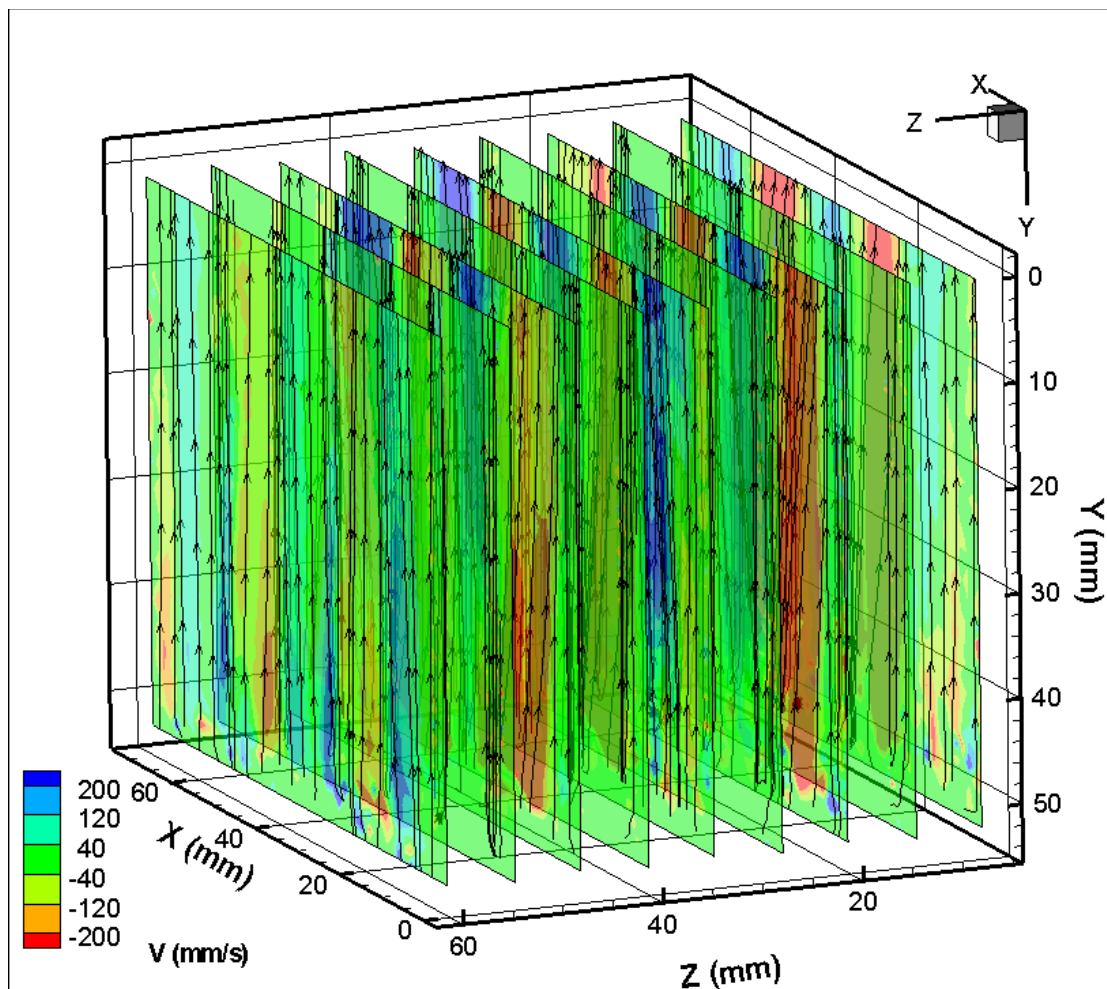


FIGURE 82. Average velocity fields and overlapped streamtraces for the upstream grid case. Color code represents spanwise component of velocity vector (V) with red color = -200 mm/s dark blue = 200 mm/s. $Re = 16300$.

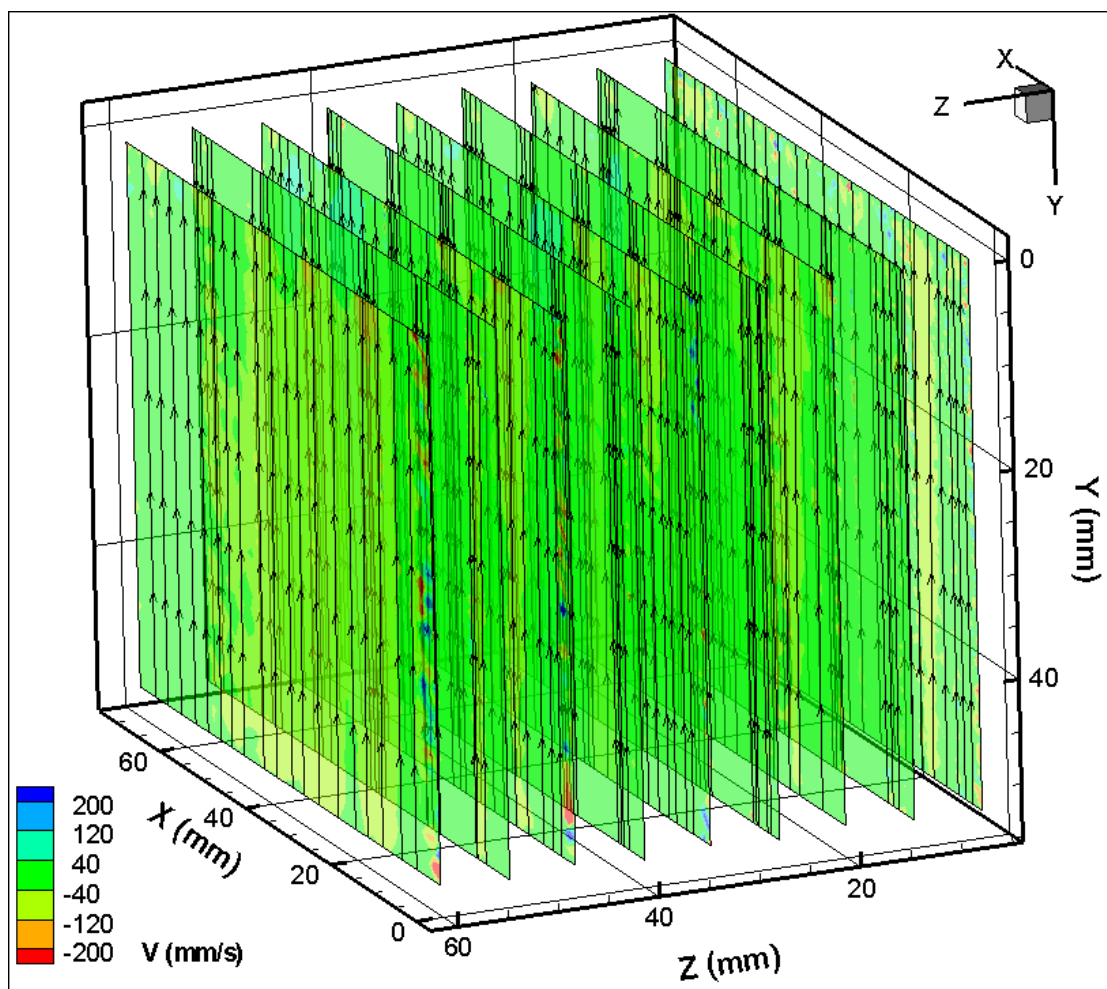


FIGURE 83. Average velocity fields and overlapped streamtraces for the downstream grid case. Color code represents spanwise component of velocity vector (V) with red color = -200 mm/s dark blue = 200 mm/s. $Re = 16300$.

The following figures show the main averaged turbulence parameters for each plane and each position (upstream and downstream of the spacer) in a one-dimensional profile. The plots for each quantity have been separated into two different plots: 1) planes A, B, C, and D and 2) planes A1, B1, C1, D1 and Bypass for better appreciation of the grid effects. The profiles are color coded and line pattern coded. Similar colors are used for

contiguous planes for easy identification in the plot. The line pattern denoting each profile is coded as solid line for all profiles measured at position BGP1 (upstream the grid) and dotted lines for all profiles measured at position AGP1 (upstream the grid).

Figure 84 presents the streamwise component averaged profile for planes with rods under a Re number condition of 15000. The profiles exhibit a parabolic shape for the central rods downstream the grid. The profiles have a velocity decrease of 30 % for the position upstream of the grid. The profiles nearby the containing walls exhibits lower velocities than the central channels.

Figure 85 shows the profiles for both measured positions under similar conditions for planes without rods. The effect of the bypass flow is denoted by a higher velocity magnitude for the Bp plane. The plane A1, located nearby the Bp plane, shows a higher velocity than the central planes. There is a decrease in velocity for all planes but for the bypass flow for the position AGP1 with respect to the BGP1 measurements. The analysis of the bypass flow profiles is of particular interest in this investigation since the flow is affected by the vanes only and not the grid itself which can be treated as a reduction in cross sectional area. In other words, the flow bypasses the grid, but the zone where AGP1 is located exhibits modification on its velocity profile. The former modification can be only due to the vanes.

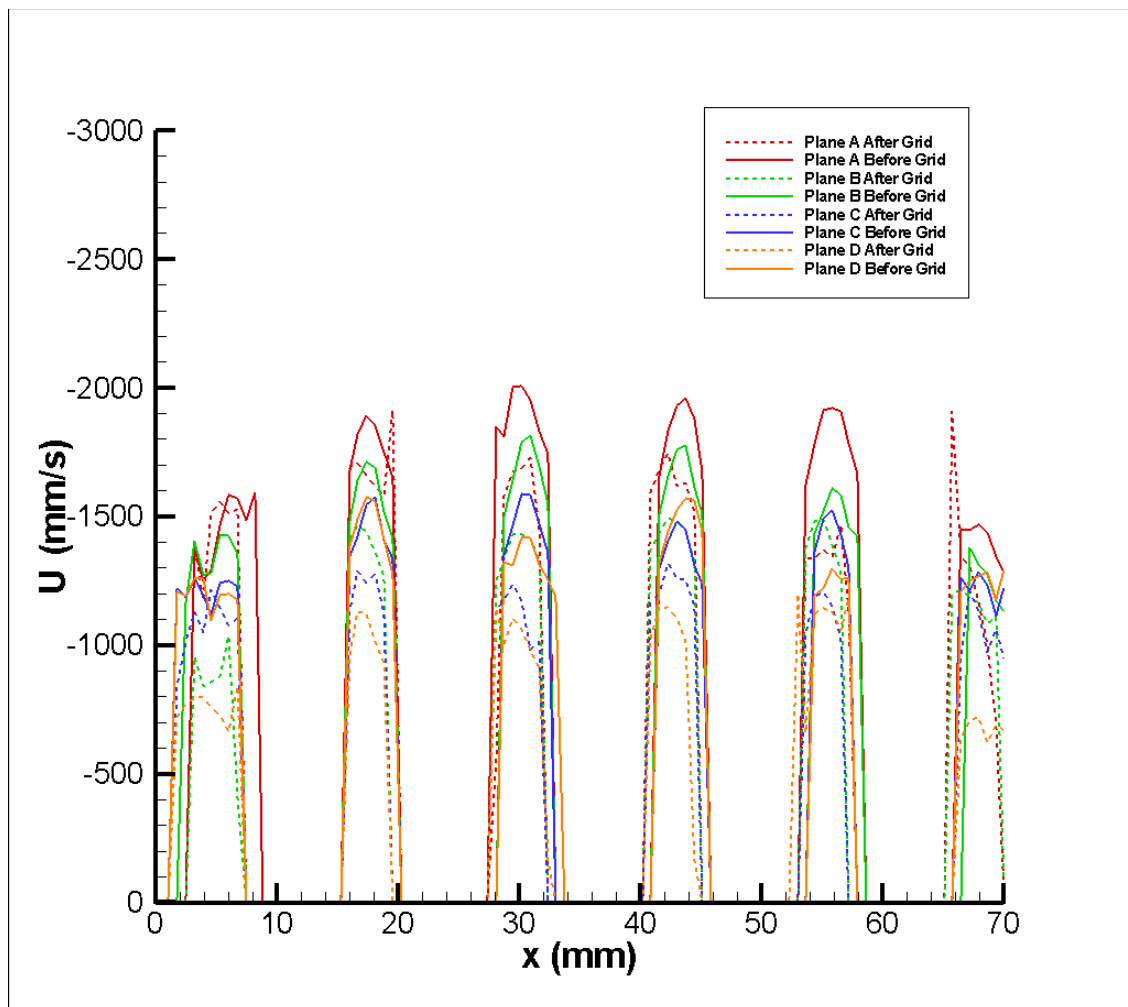


FIGURE 84. Averaged streamwise component of the velocity vector (U) for the A,B, and C, D planes downstream and upstream of the grid. $Re= 16300$.

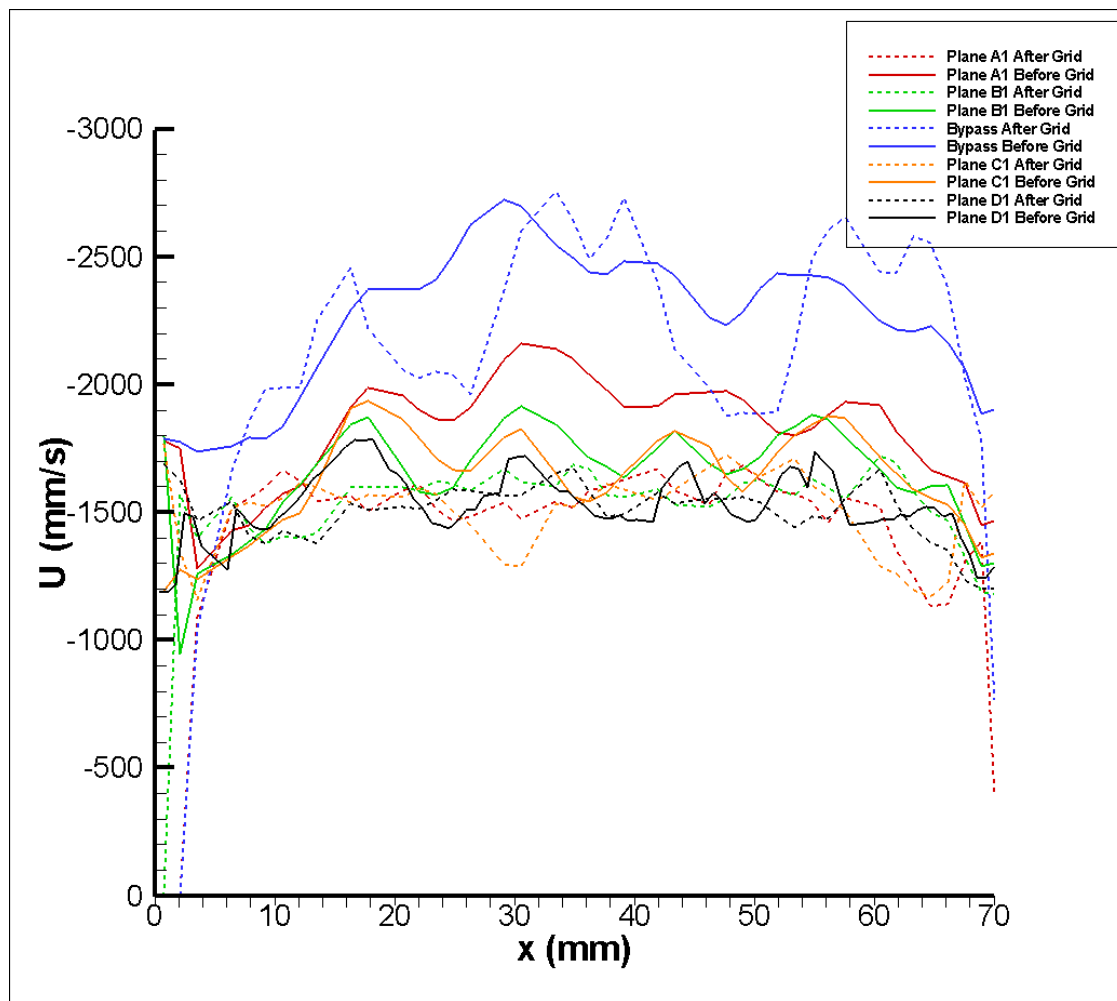


FIGURE 85. Averaged streamwise component of the velocity vector (U) for the A1, B1, C1, D1, Bypass planes downstream and upstream of the grid. $Re = 16300$.

The one-dimensional profiles for the normal component of the velocity vector is shown in figure 86 for the planes with rods and figure 87 for planes without rods. The results show mostly a unidirectional change in flow direction for all planes with rods upstream the grid as shown in figure 86. The magnitude of the normal component shows an increase of about 50% for position AGP1 (upstream of the grid) with respect to position BGP1 (downstream of the grid). Figure 87 show the profiles for both measured positions for the planes without rods. The increase in the normal component at position AGP1 is noticeable with an increment of up to four times the magnitude found at position BGP1. The increment is observed in both directions of the normal component as denoted in figure by the change in sign.

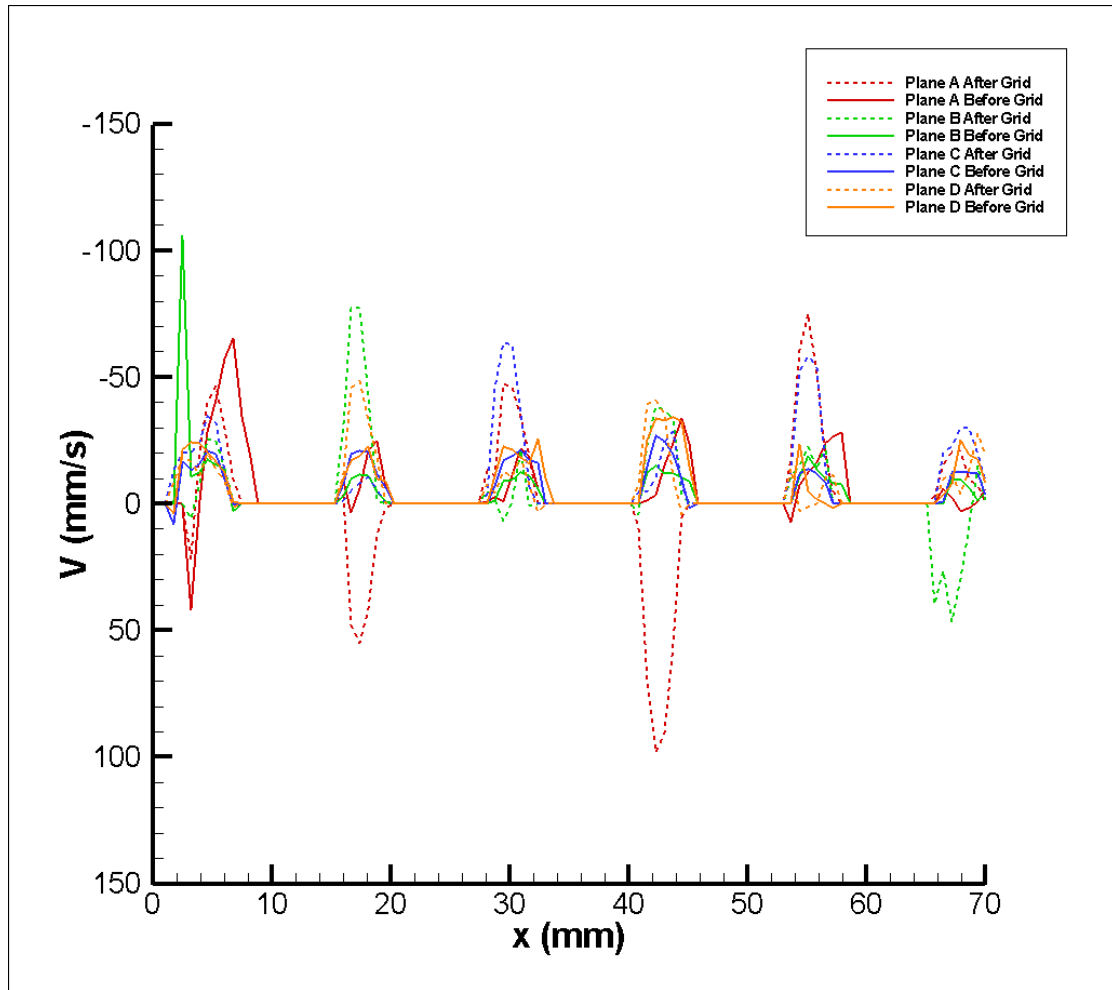


FIGURE 86. Averaged spanwise component of the velocity vector (V) for the A, B, and C, D planes downstream and upstream of the grid. $Re = 16300$.

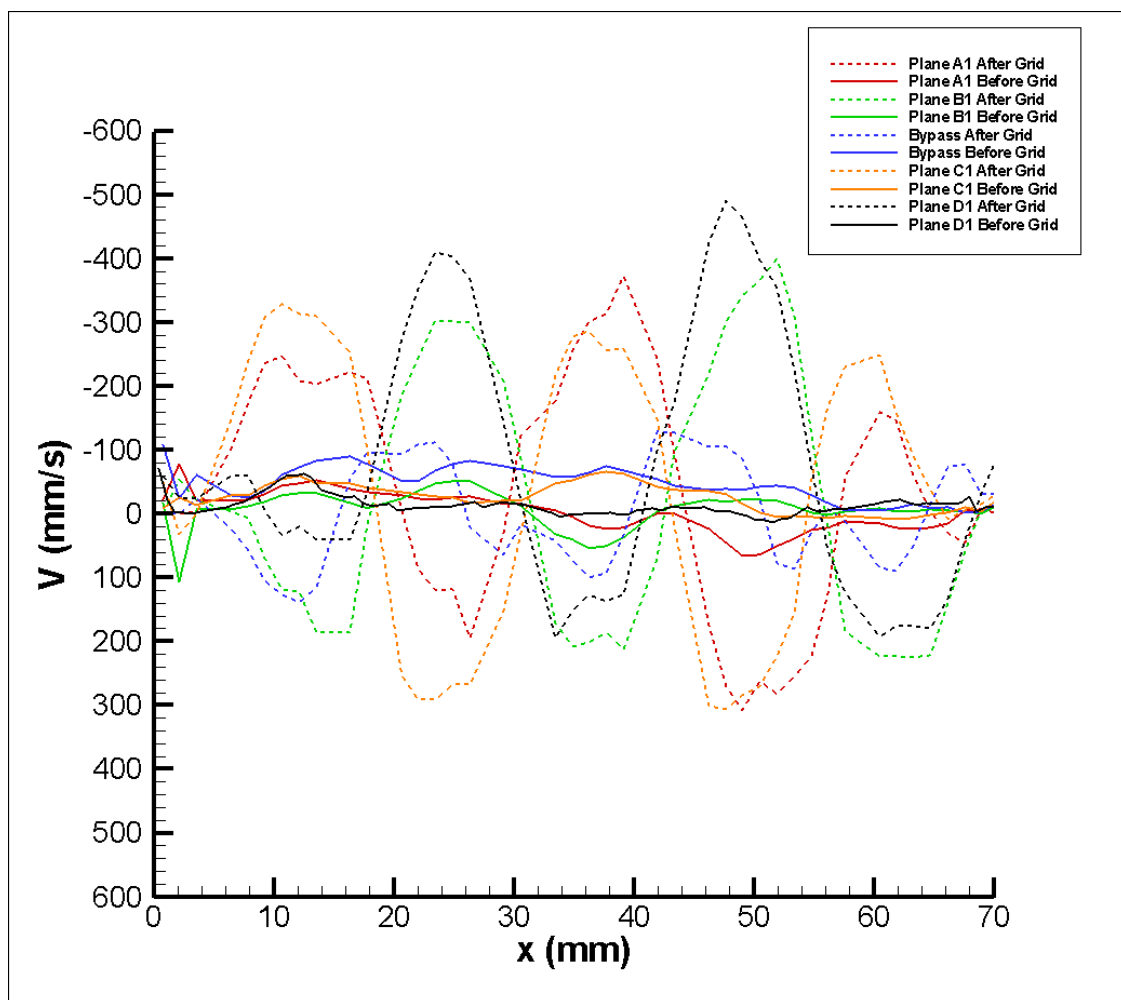


FIGURE 87.. Averaged spanwise component of the velocity vector (V) for the A1, B1, C1, D1, Bypass planes downstream and upstream of the grid. $Re=16300$.

The turbulence intensities in the streamwise direction (u_{rms}) and normal direction (v_{rms}) of the velocity vector are presented in the following section. Figure 88 shows the streamwise direction velocity fluctuation field for planes with rods. The fluctuations exhibit a behavior similar to the one found in channel flow with solid boundaries where non-slip conditions is enforced for the measured position downstream of the grid. However, this behavior is not persistent upstream of the grid. The fluctuation profile is modified and its magnitude increase by 40 % for position AGP1. The profiles upstream of the grid have a preferential peak direction for several channels caused by the flow change in direction caused by the vanes. The three central channels located in the X-axis at positions 18 mm, 30 mm and 43 mm have a similar behavior for position BGP1. This fact elucidates that these three channels can be considered as not affected by the containing walls. Figure 89 shows the streamwise turbulence intensities profiles for the planes without rods. The main difference between profiles measured upstream and downstream of the grid is the increase of the intensities by 40 % for the upstream case. Figure 90 shows the averaged profiles for the normal component of the velocity vector for planes with rods. The increment in the turbulence intensities for the normal component at position AGP1 is of 40% with respect to the profiles downstream of the grid. The profiles for the normal component corresponding to planes without rods are won in figure 91. For this case, the increment in the normal turbulence intensities is of 45% at the upstream position with respect to position BGP1. The normal direction fluctuations for plane Bp (bypass) showed in figure 91 exhibit a clear increment (blue

dotted and solid lines). The increment indicates the influence of the vanes located at the edge of the grid over the bypass flow.

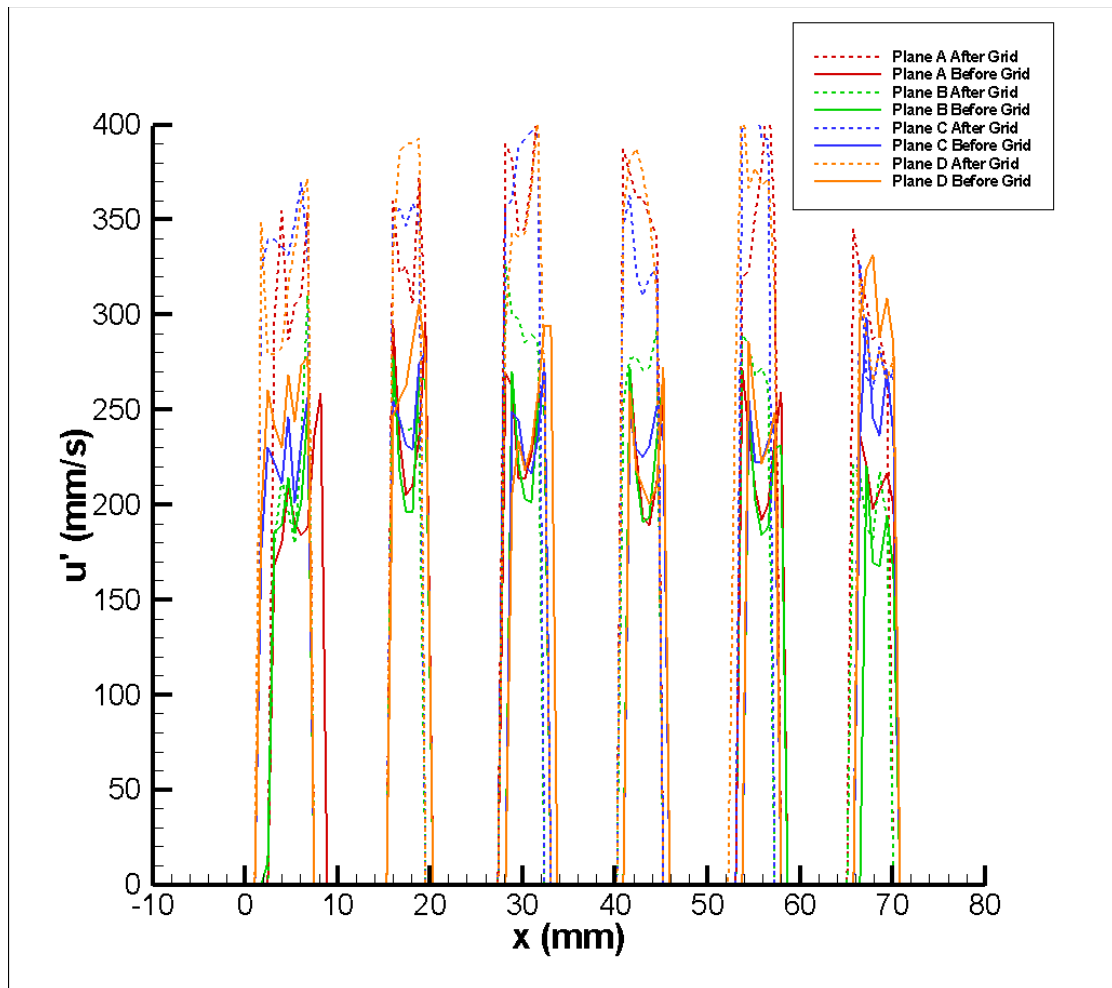


FIGURE 88. Averaged turbulence intensities for the streamwise component of the velocity vector (u') for the A, B, and C, D planes downstream and upstream of the grid. $Re = 16300$.

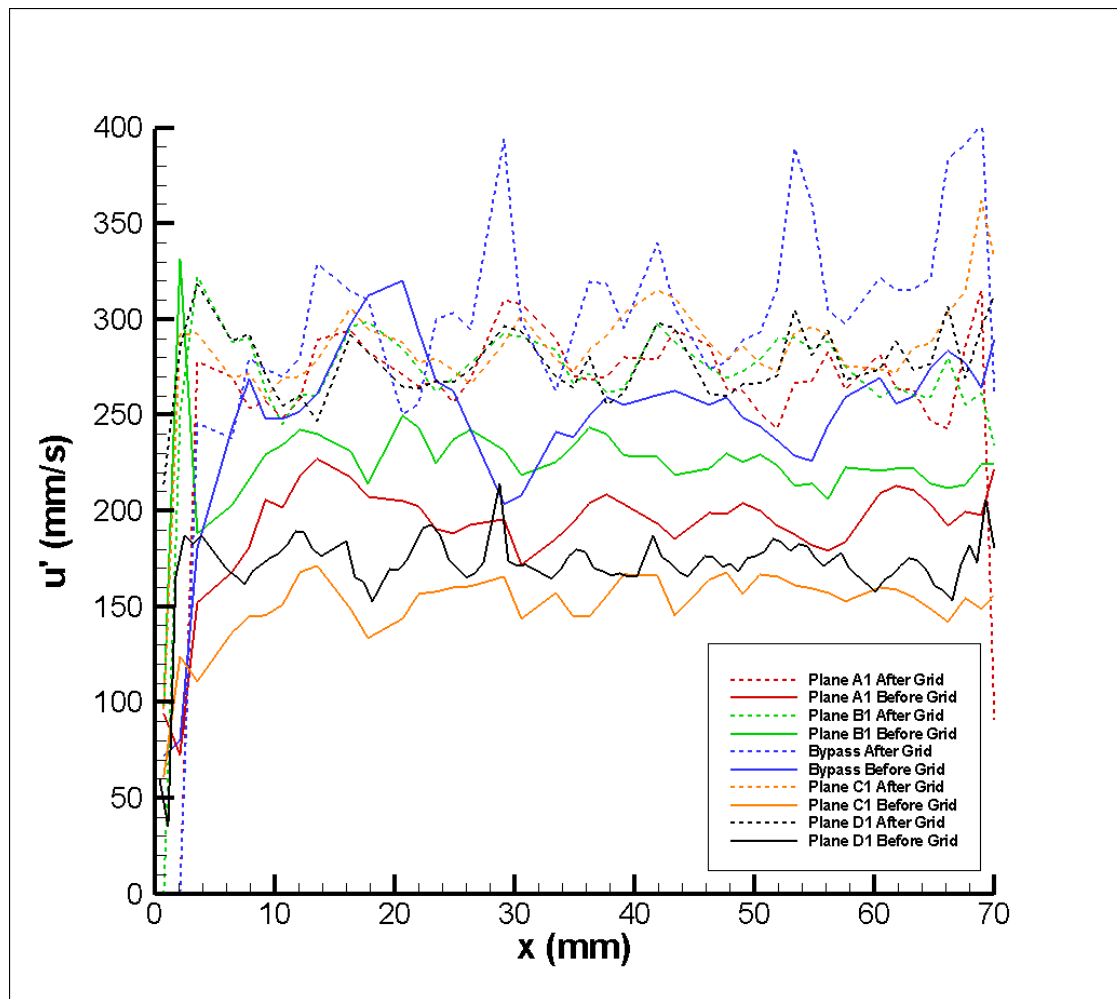


FIGURE 89. Averaged turbulence intensities for the streamwise component of the velocity vector (u') for the A1, B1, C1, D1, Bypass planes downstream and upstream of the grid. $Re = 16300$.

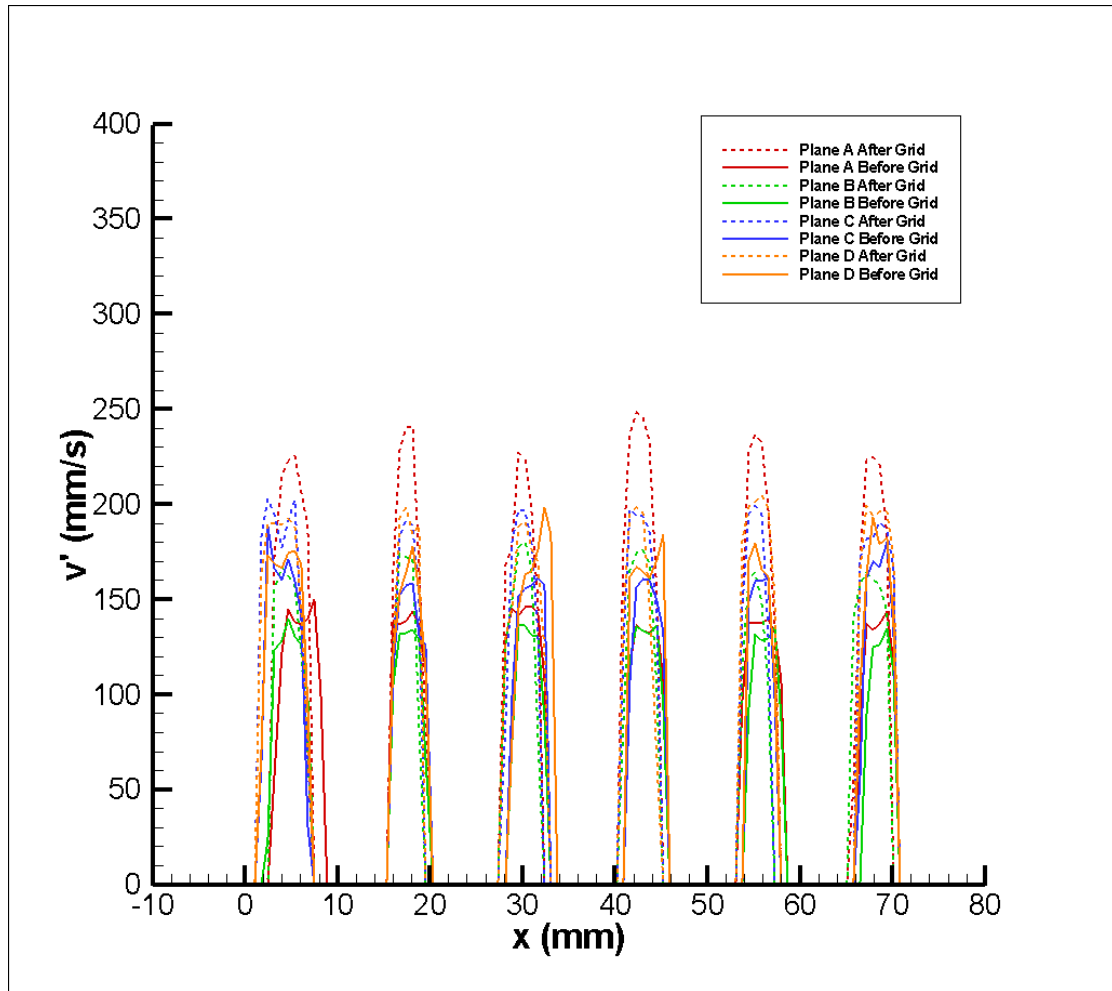


FIGURE 90. Averaged turbulence intensities for the spanwise component of the velocity vector (v') for the A, B, and C, D planes downstream and upstream of the grid. $Re=16300$.

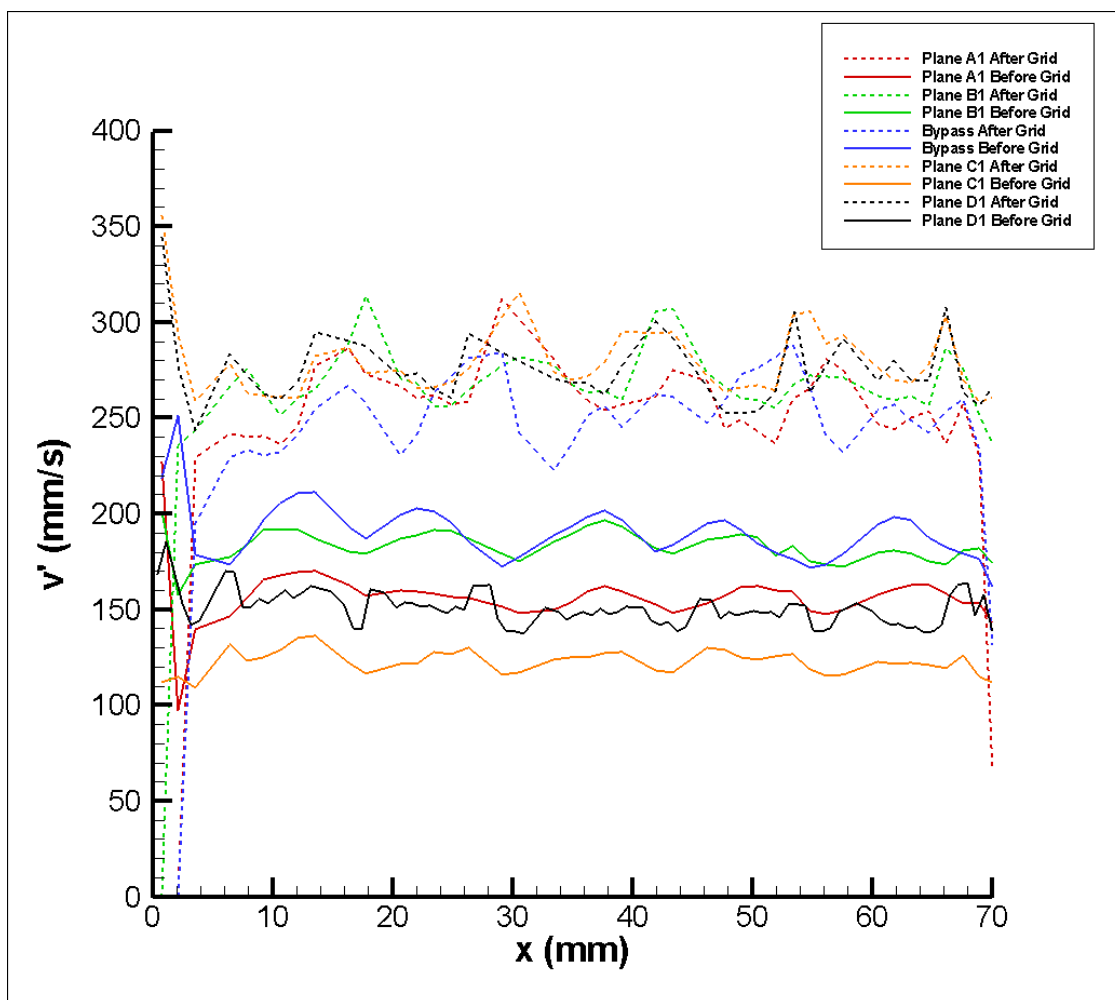


FIGURE 91. Averaged turbulence intensities for the spanwise component of the velocity vector (v') for the A1, B1, C1, D1, Bypass planes downstream and upstream of the grid. $Re=16300$.

Reynolds stresses, for single phase flows, can be obtained from the velocity fields. The viscous stress can be obtained from the measured streamwise mean velocity profile. Figure 92 shows the averaged Reynolds stresses profiles for planes with rods. The profiles exhibit a similar behavior than the one found in a channel flow with solid boundaries at position BGP1. The stresses are higher near the walls and zero at the center of the channels. In contrast, the stresses show a completely different shape for the position upstream of the grid. Figure 93 shows the Reynolds stresses profiles for the planes without rods. There is a decrease in the profiles at positions downstream of the grid with respect to the position upstream of the grid. This reduction in the value of the Reynolds stresses is a function position, as the position increases, the Reynolds stresses decrease. A de-correlation between the streamwise (u') and the normal (v') velocity fluctuating components is the source of these decrease of the Reynolds stresses. This phenomenon may be explained due to a modification in the organized structures in the boundary layer.

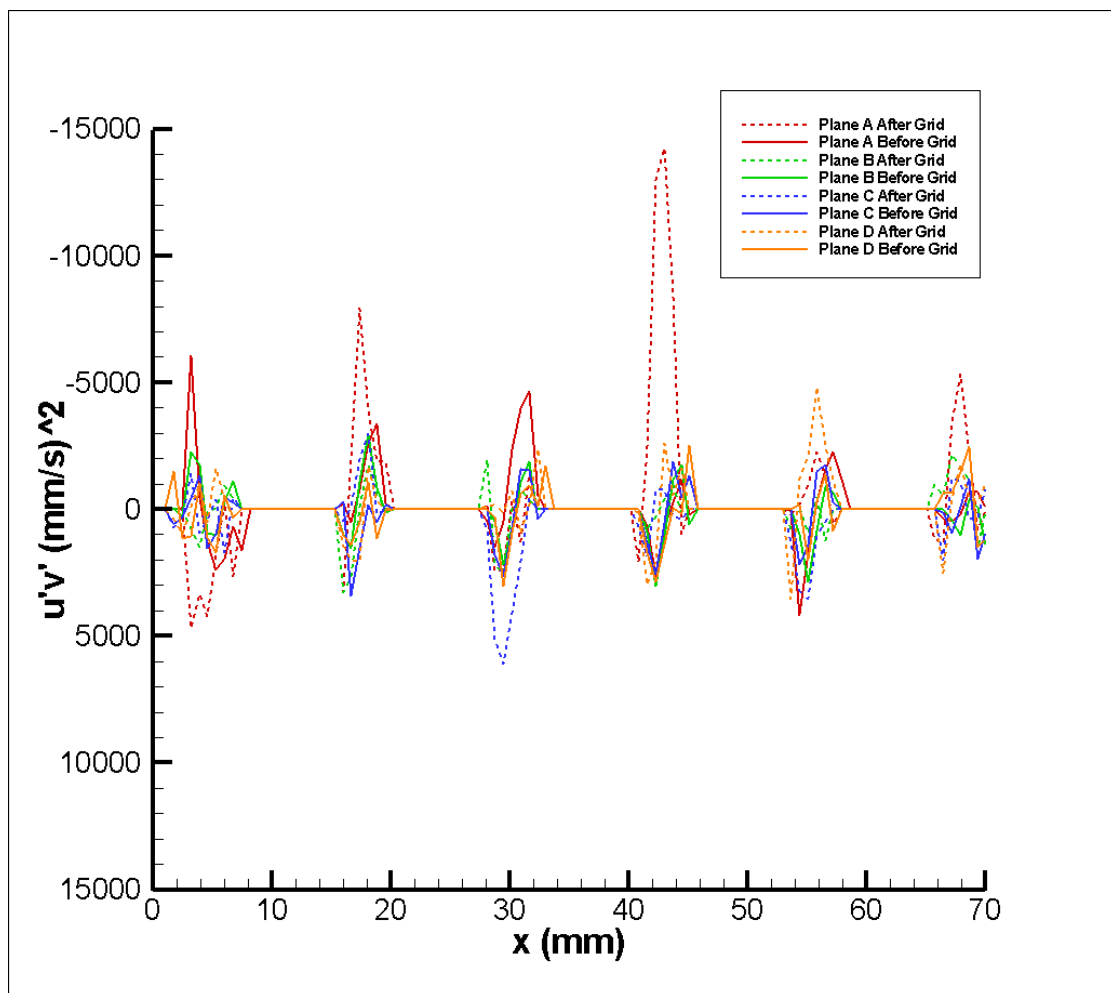


FIGURE 92. Averaged Reynolds stresses ($u'v'$) for the A, B, C, D planes downstream and upstream of the grid. $Re=16300$.

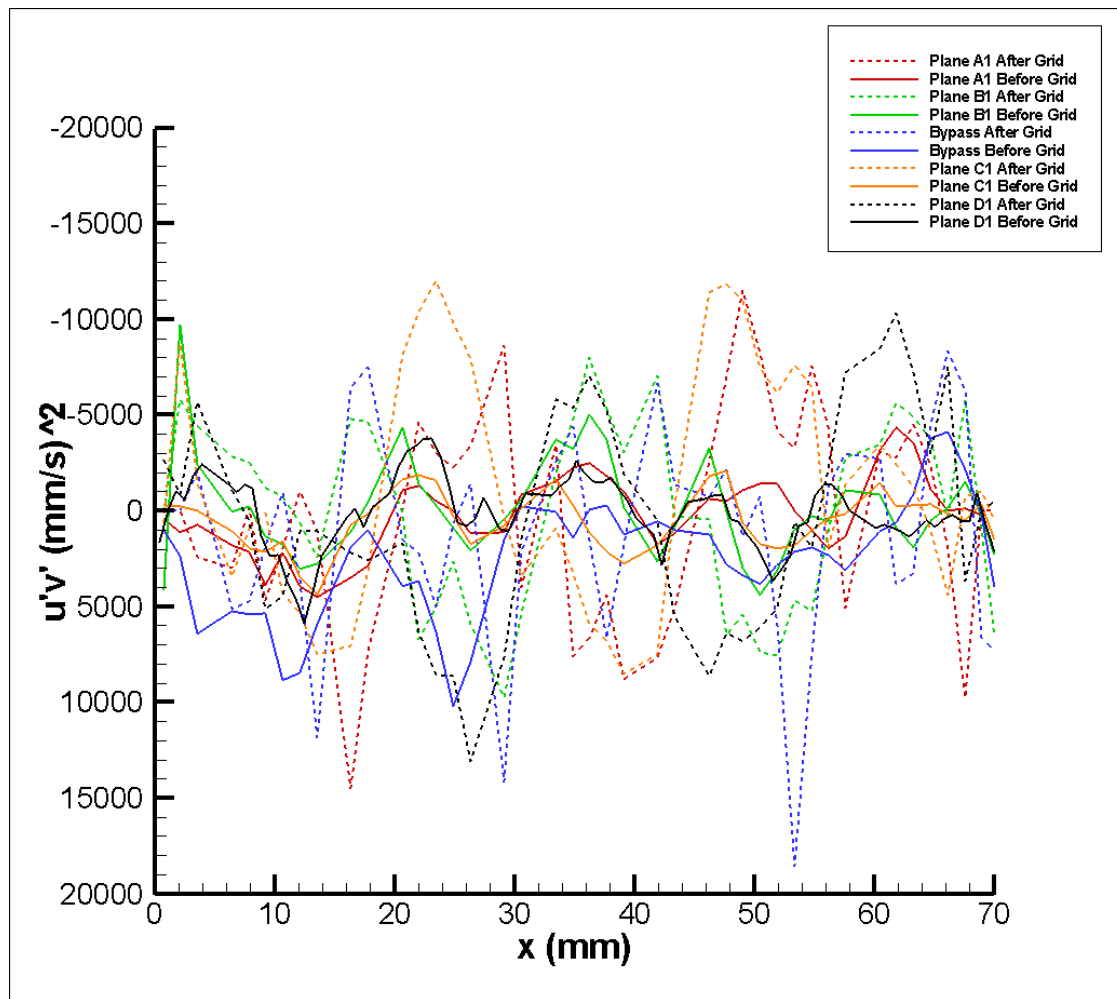


FIGURE 93. Averaged Reynolds stresses ($u'v'$) for the A1, B1, C1, D1, Bypass planes downstream and upstream of the grid. $Re = 16300$.

4.2.2 Sub-channel scale

Measurements were performed at a second viewing area (12.5 mm x 17 mm) in order to increase the resolution and the accuracy of the measurements at the sub-channel level. A similar procedure to the one described previously for the inter-channel scale was performed.

Figure 94 shows a pictorial of the two positions measured using the viewing area covering the sub-channel scale. Each of the black dotted rectangles represents one measured position. Each position was assigned with a representative name using the following logic. All measured positions upstream from the grid were denominated as “Before Grid” (BG) and the positions downstream from the grid were denominated as “After Grid” (AG). The corresponding nomenclature for each position was included in the name by using the abbreviation and the corresponding number. i.e., AGP1 represents the After Grid position 1 measurement zone. The distance covered by each measurement volume was measured from the edge of the grid without including the mixing vanes. Figure 43 shows the three measurement volumes used for the sub-channel scale and its corresponding distance from the grid in length units (mm). The distance range for positions after the grid varied from 0 (grid edge) to 12.5 mm (tip of measured volume, AGP1). From the before grid case (upstream grid) only one position was measured and its corresponding distance from the grid edge to the tip of the viewing area was 12.5 mm. The flow direction with respect to the measured positions is indicated in the figure by a white arrow pointing upwards.

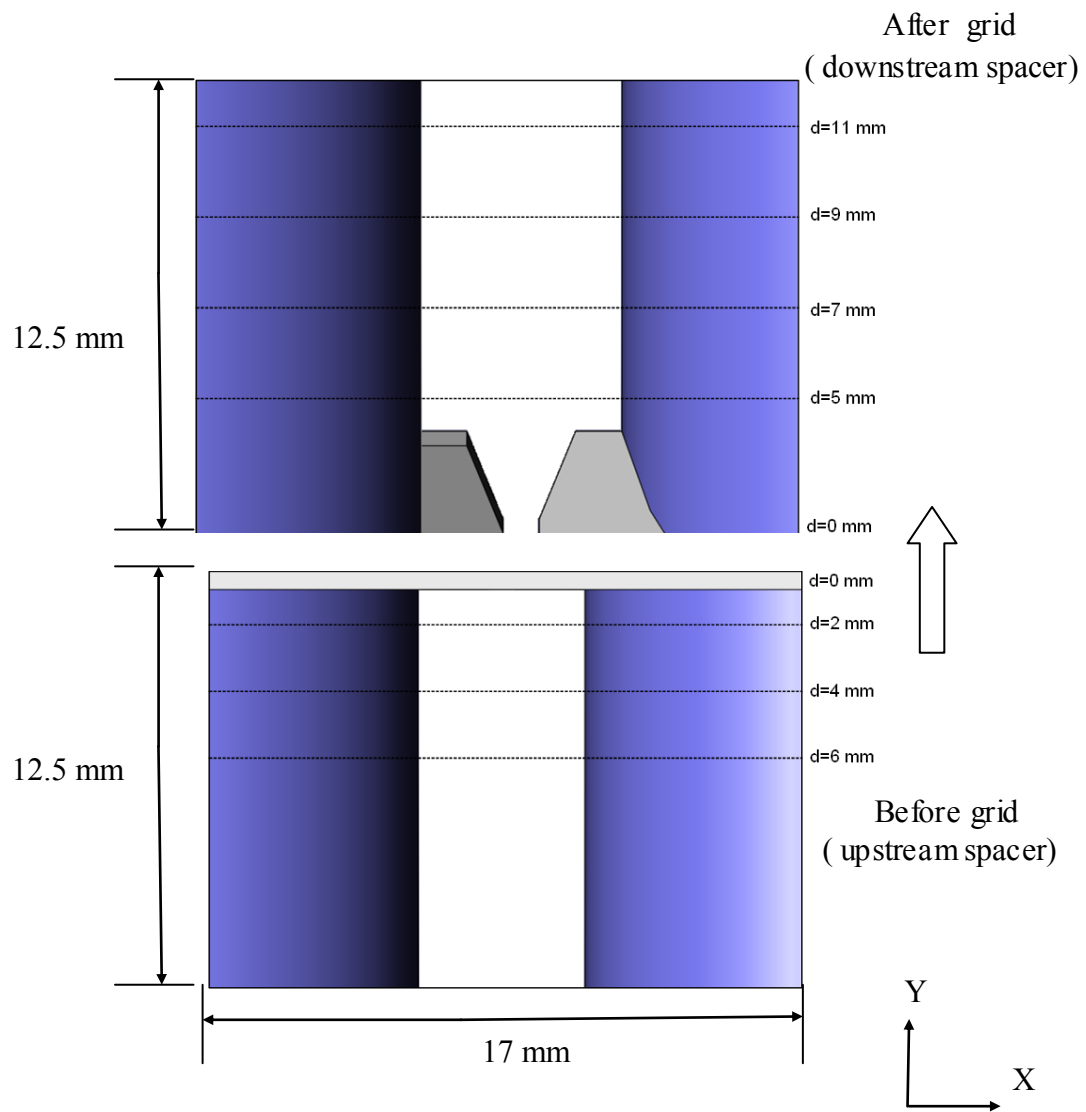


FIGURE 94.. Equivalent viewing area #2 (sub-channel scale) for positions BGP1 (down) and AGP1 (up).

Typical obtained images for the sub-channel scale PIV viewing areas at positions BGP1 and AGP1 for plane C are shown in figure 95. The figure shows the position of the spacer grid with respect to the two measured viewing areas. Since the flow was seeded with the PIV particles, the light scattered by the particles is the only light captured in the PIV images. Therefore, for this particular measured plane the flow geometry constraints are represented by the brighter zones in the picture. The edges of the rods are well delineated and the particles can be easily identified. The measurements capture two components of the velocity vector: 1) X-axis direction and 2) Y-axis direction. The sub-channel scale has an equivalent viewing area of 12.5 mm x 17 mm.

Figure 96 shows the obtained velocity fields for each measured plane upstream and downstream of the spacer-grid. The 18 planes measured are compacted into a single plot with the grid position scaled. The first plane shown in figure 96 from left to right corresponds to the bypass (Bp) plane. The rod position was omitted intentionally for better appreciation of the different planes position and its corresponding velocity fields. The white arrow on the left side of the image represents the main flow direction going from the bottom of the page, passing through the spacer and going upwards. The two positions measured: BGP1 and AGP1 are presented next to its correspondent results. The planes were measured independently at steady state conditions for this part of the work. The various planes presented in Figure 96 are presented separately in figures 97 and 98 for better appreciation. These figures show the average velocity fields for each plane for the two components of the velocity vectors coded by color with its calculated

streamtraces overlapped on the contour plots. A more detailed description for each plane can be found in Appendix C of this document.

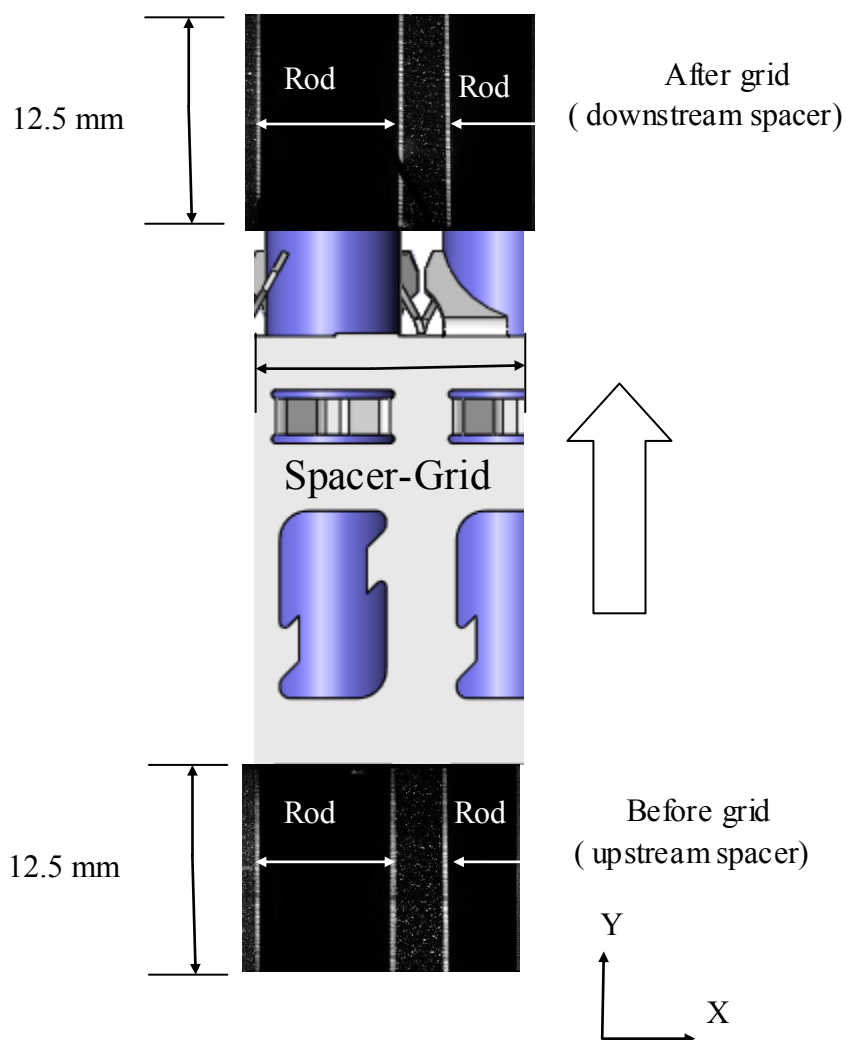


FIGURE 95. Typical PIV image for equivalent viewing area #1 (zoom) for positions BGP1 (down) and AGP1 (up).

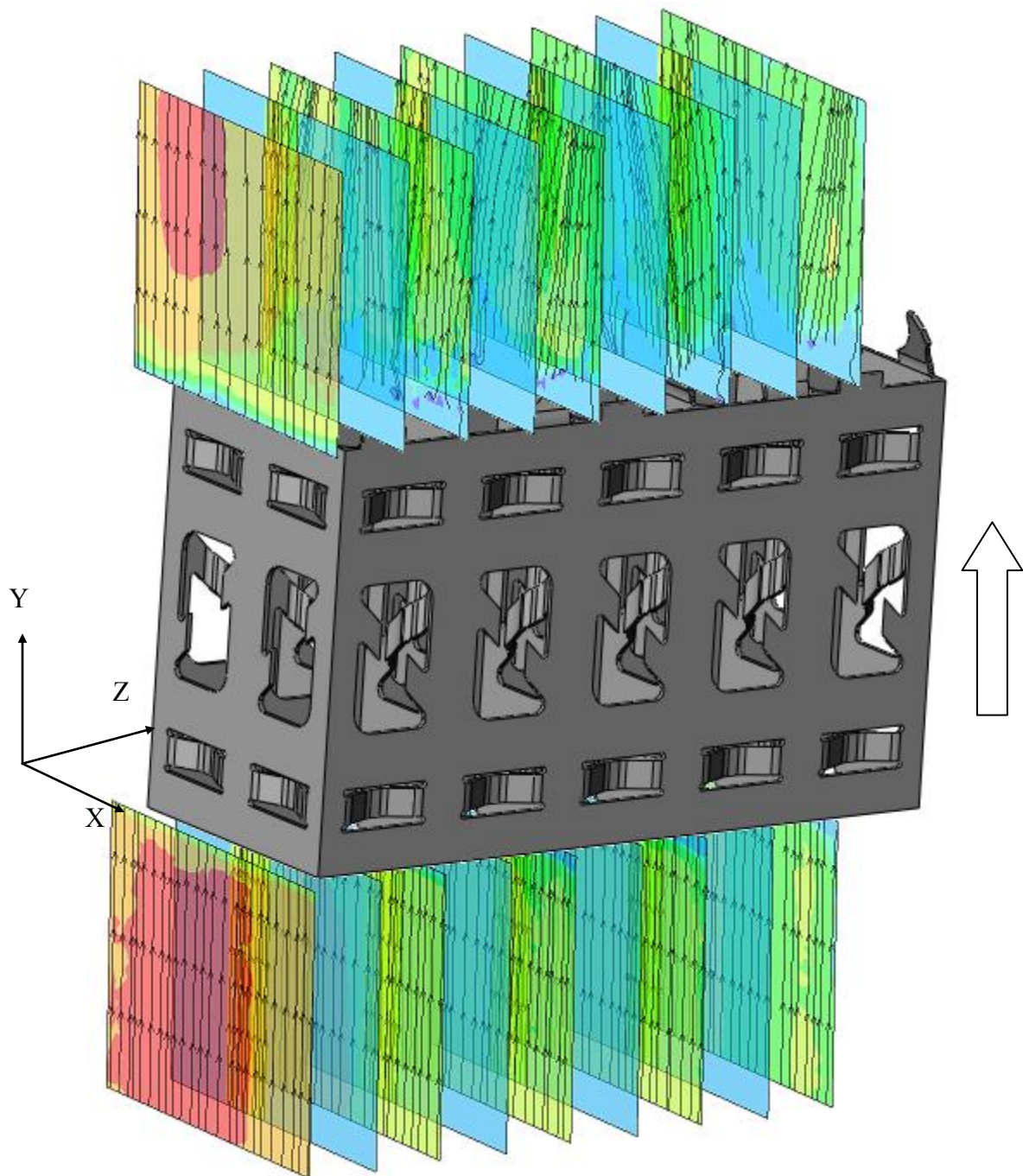


FIGURE 96. Average velocity fields before and after grid for the sub-channel scale cases. Color code represents streamwise component of velocity vector (U) with red color = 2500 mm/s dark blue = 0 mm/s. $Re = 16300$.

The streamwise component averaged velocity profile for position AGP1 (downstream of the grid) is shown in figure 97. The first plane from left to right represents the bypass plane which exhibits a red color zone denoting a magnitude of 2200 mm/s under a $Re=16300$ condition. The planes show a flow deflection caused by the split vanes for position AGP1. The position downstream the grid (BGP1) is shown in figure 98. The flow paths follow straight lines as denoted by the streamtraces overlapped on the contour velocity plots.

The averaged velocity fields for the normal component of the velocity vector are shown in figures 99 and 100. The increase in the average magnitude for this component is obvious for the position upstream of the grid. There are big areas covered by red and blue color in figure 99 for all the planes. The red color denotes a change in the flow direction towards the negative direction of the component and the blue color shows positive values. The magnitude of these changes is over 100 mm/s which account for about 10% of the axial averaged velocity in central channel without considering the velocities at the bypass flow plane.

Figure 100 shows the averaged velocity profile of the normal component of the velocity vector for the measured position downstream of the grid. There are zones denoting variation in the flow direction in the 100 mm/s range. However, the intensity and area range is greatly diminished with respect to the AGP1 (upstream) position. It should be noted that planes 1, 3, 5 and 7 are the planes without rods and the change in direction has higher values than for the planes with rods. The direction of the normal component alternates in direction according to the plane number i.e. plane number 1 start with a

positive direction at $x=15$ mm (blue color) and positive direction at $x=5$ mm. In contrast, plane 3 has a red color at $x=15$ mm and a blue color at $x=5$ mm. This alternate pattern coincides with the orientation of the split vanes of the grid.

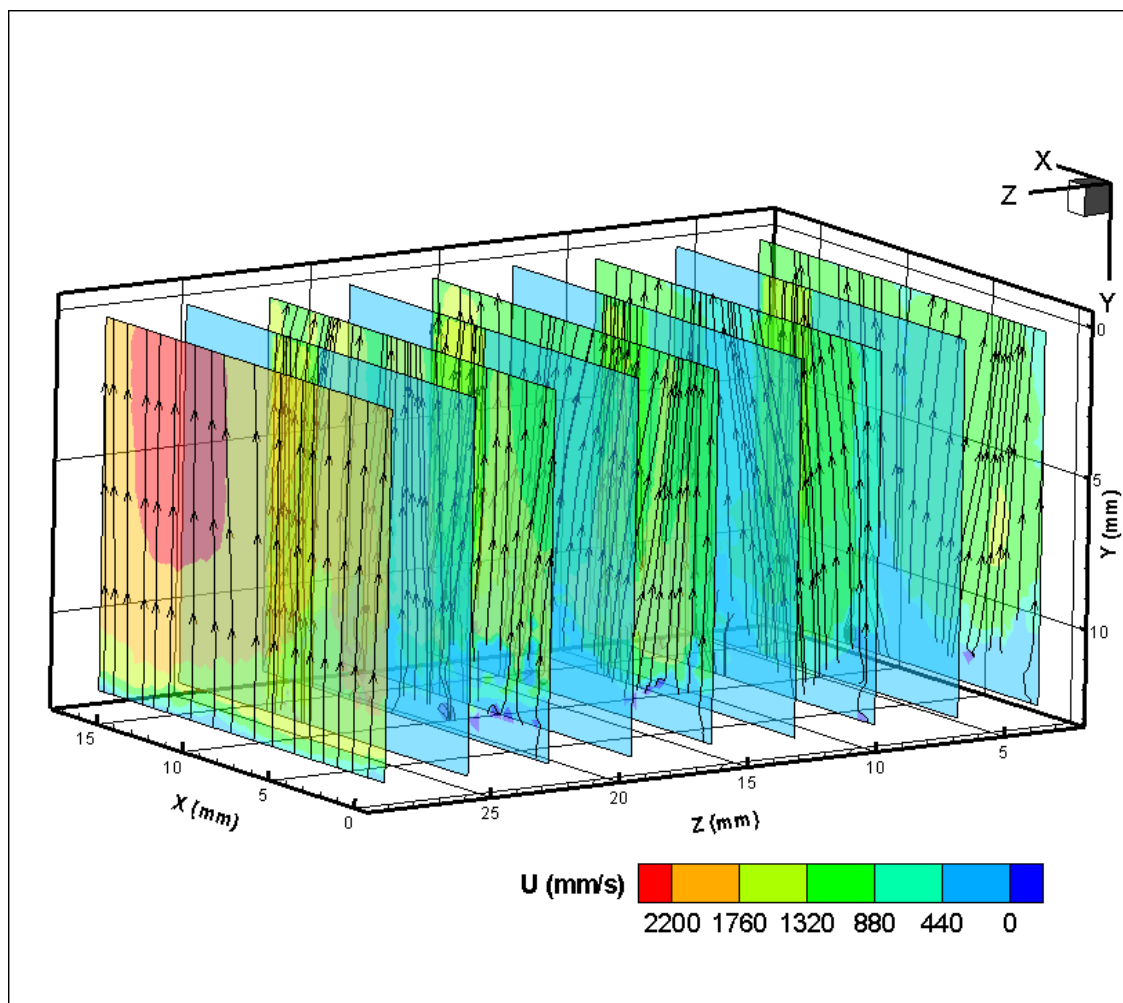


FIGURE 97. Average velocity fields and overlapped streamtraces for the downstream grid sub-channel scale case. Color code represents streamwise component of velocity vector (U) with red color = 2500 mm/s dark blue = 0 mm/s. $Re=16300$.

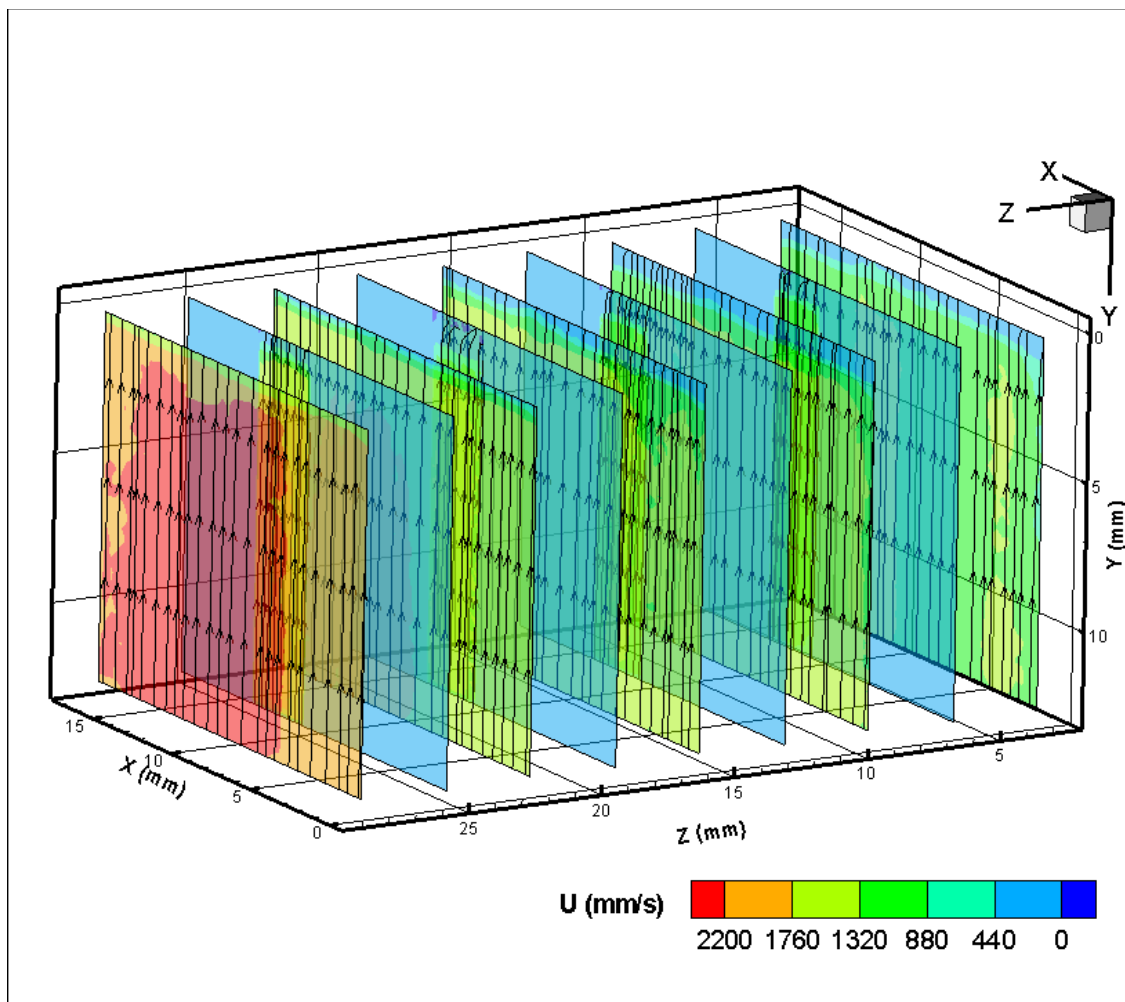


FIGURE 98. Average velocity fields and overlapped streamtraces for the upstream grid sub-channel scale case. Color code represents streamwise component of velocity vector (U) with red color = 2500 mm/s dark blue = 0 mm/s. $Re = 16300$.

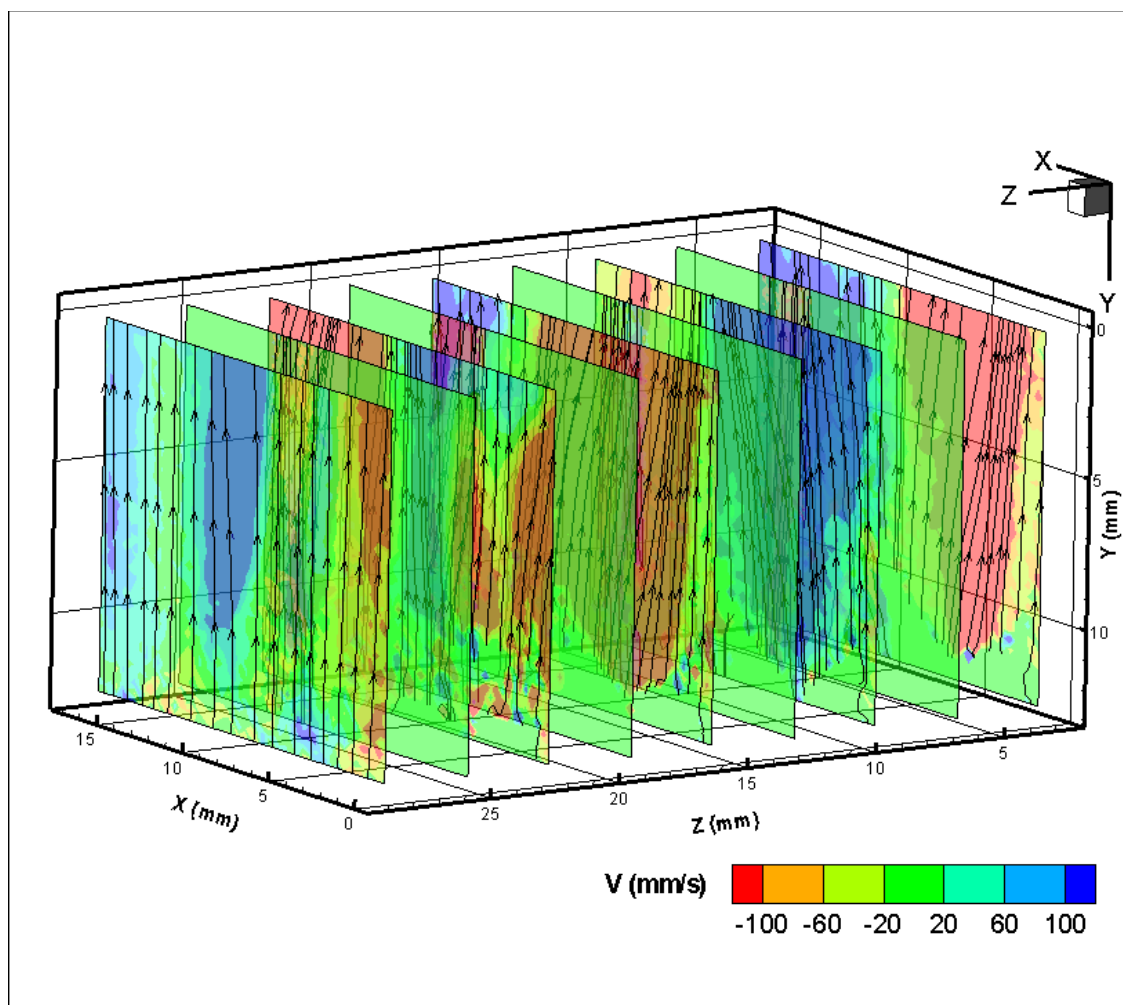


FIGURE 99. Average velocity fields and overlapped streamtraces for the downstream grid sub-channel scale case. Color code represents spanwise component of velocity vector (V) with red color = 2500 mm/s dark blue = 0 mm/s. $Re = 16300$.

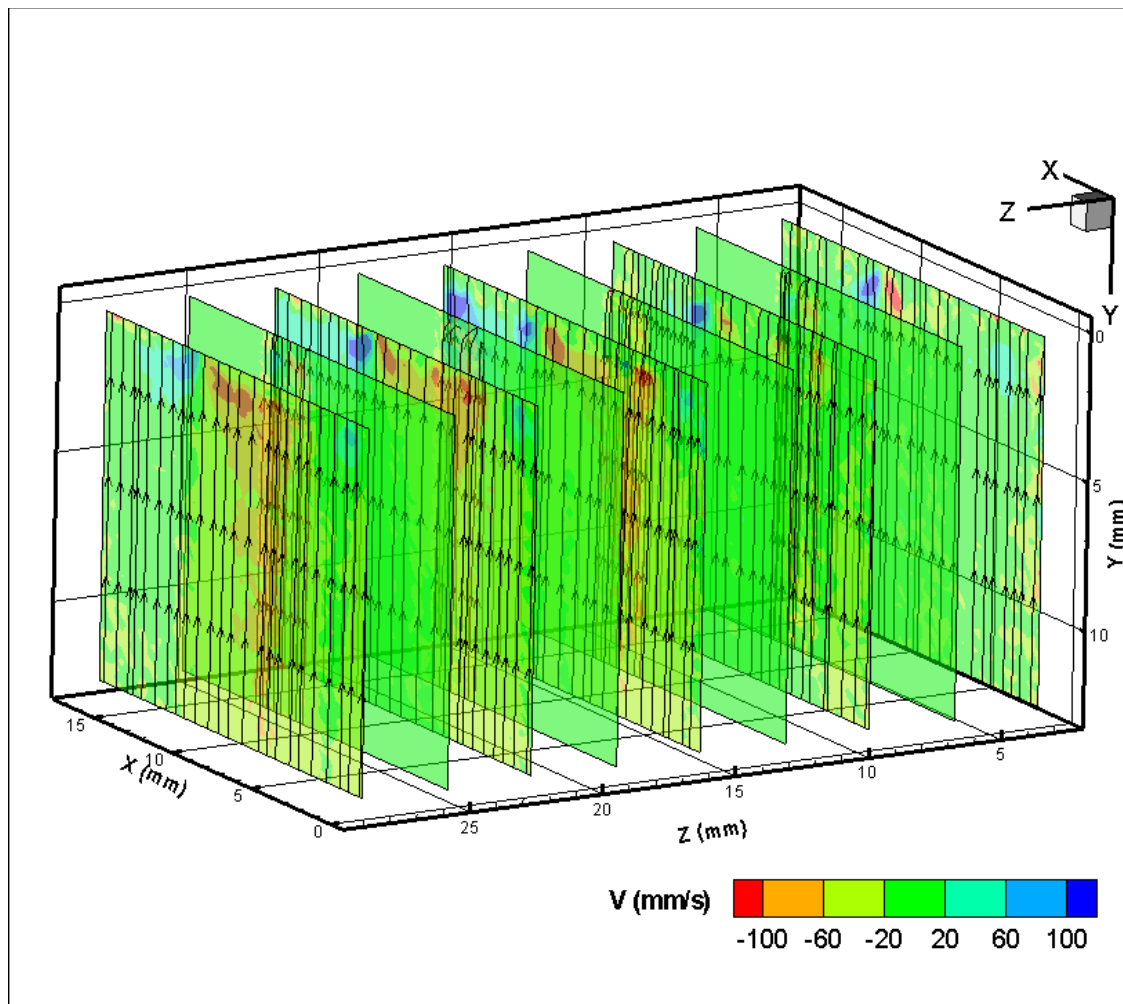


FIGURE 100. Average velocity fields and overlapped streamtraces for the upstream grid sub-channel scale case. Color code represents spanwise component of velocity vector (V) with red color = 2500 mm/s dark blue = 0 mm/s. $Re = 16300$.

The following figures show the main averaged turbulence parameters for each plane and each position (upstream and downstream of the spacer) in a one-dimensional profile. These measurements used viewing area 2 in order to increase the resolution and accuracy in specific locations near the spacer. The plots for each quantity have been separated into two different plots: 1) planes A, B, C, and D and 2) planes A1, B1, C1, D1 and Bypass for better appreciation of the grid effects. The effects of the grid spacer are noticeable for all quantities after grid. Figure 101 shows the averaged velocity profile for the streamwise direction of the velocity vector. The profiles at position BGP1 show a parabolic shape which contrast the results of position AGP1 which are inclined towards the left for planes and B and D and towards the right for planes A and C. Figure 102 shows the streamwise direction averaged velocity profiles for the planes without rods. The streamwise direction shows a similar magnitude for upstream and downstream positions. However, the shape of the profile changed. Figure 103 shows the normal direction of the averaged velocity profile for upstream and downstream of the grid. In the case of planes with rods, the measurements downstream of the grid show a close behavior in all cases. However, after the grid (AGP1) position exhibits a different behavior. These planes show an increase in the normal direction magnitude of up to five times the magnitude of the same plane downstream the grid. Planes D and B have a negative value. On the other hand planes A and C have a positive value for position AGP1. Figure 104 show the normal component of the velocity vector at planes without rods. It is observed that the change in magnitude is as large as 4 times the magnitude

found at position BGP1. This indicates the strong change in flow direction after the grid caused by the split vanes downstream the grid.

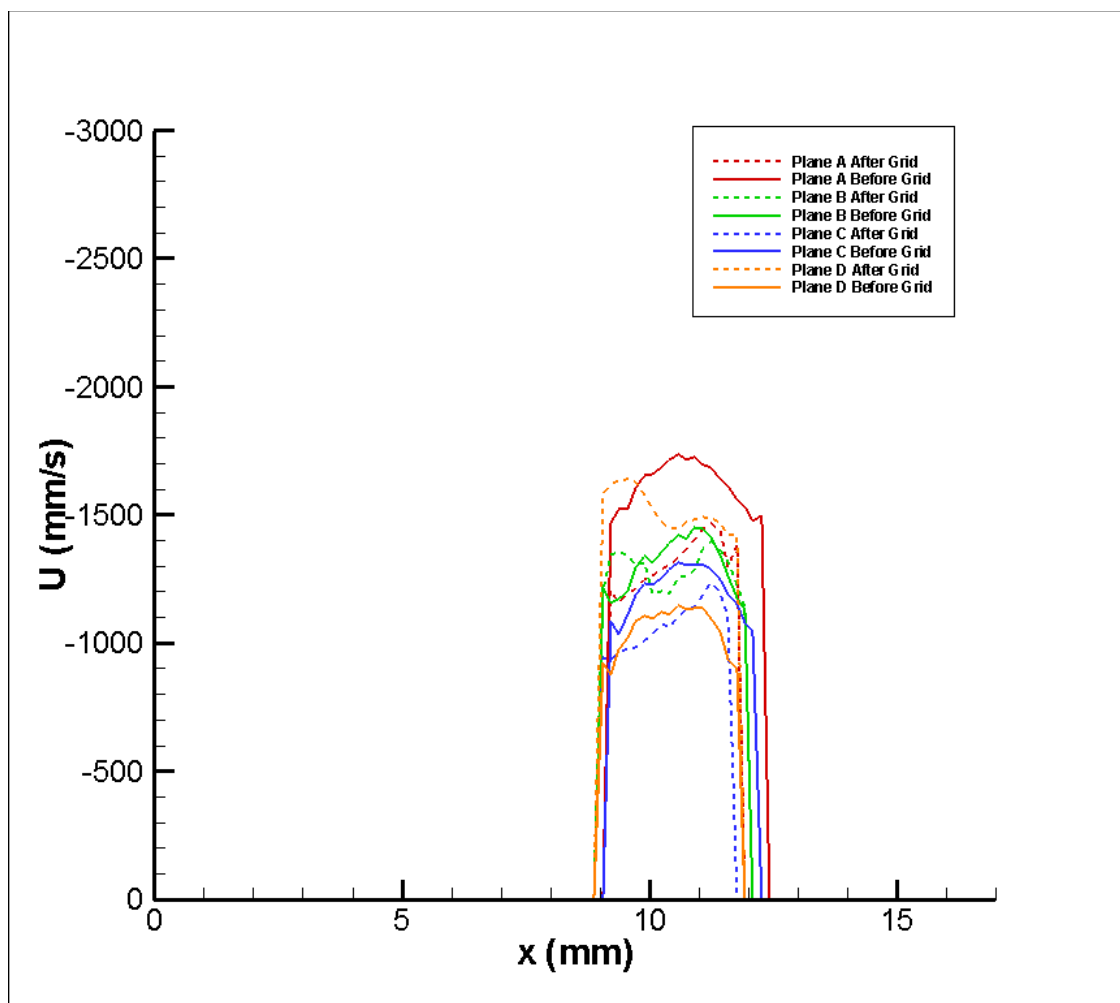


FIGURE 101. Averaged streamwise component of the velocity vector (U) for the A, B, C, D (sub-channel scale) planes downstream and upstream of the grid. $Re=16300$.

65

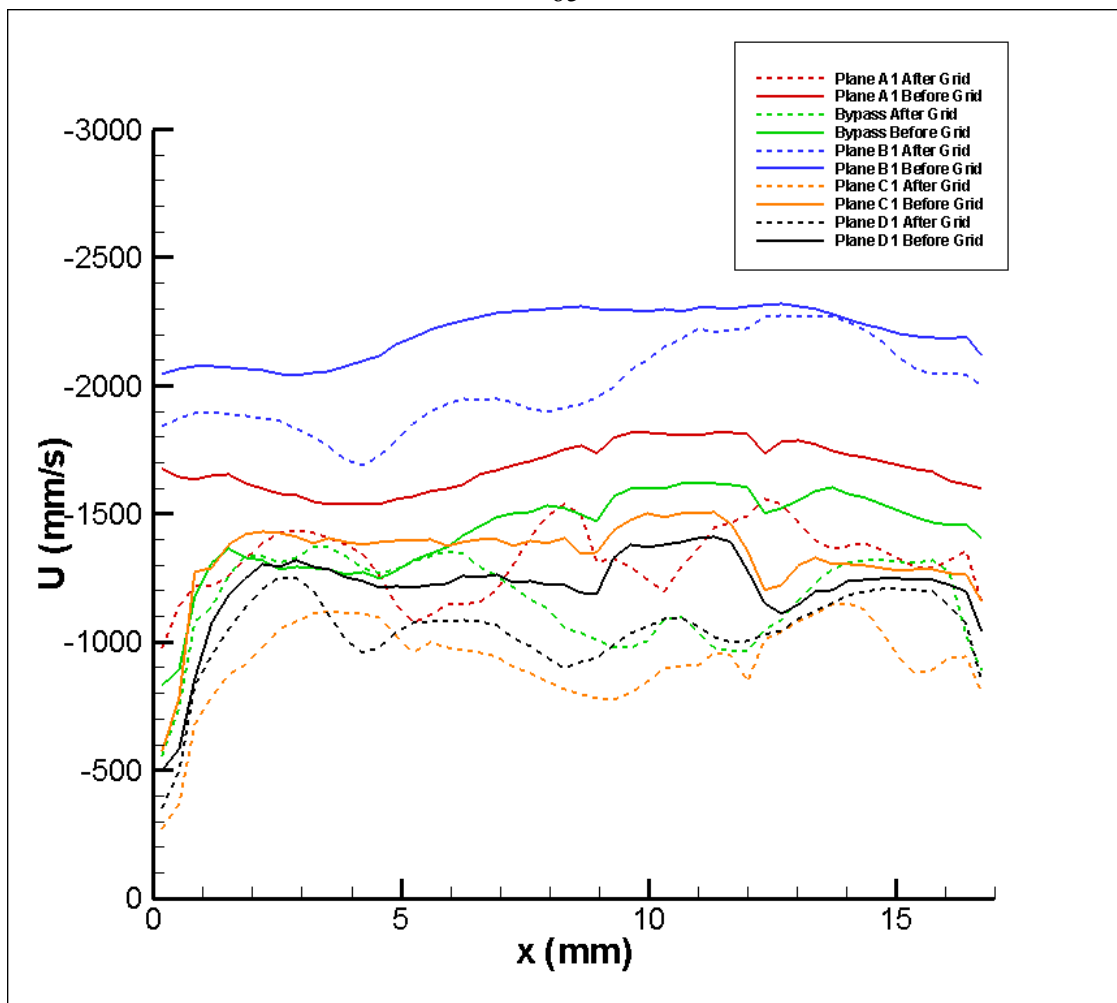


FIGURE 102. Averaged streamwise component of the velocity vector (U) for the A1, B1, C1, D1, Bypass (sub-channel scale) planes downstream and upstream of the grid. $Re=16300$.

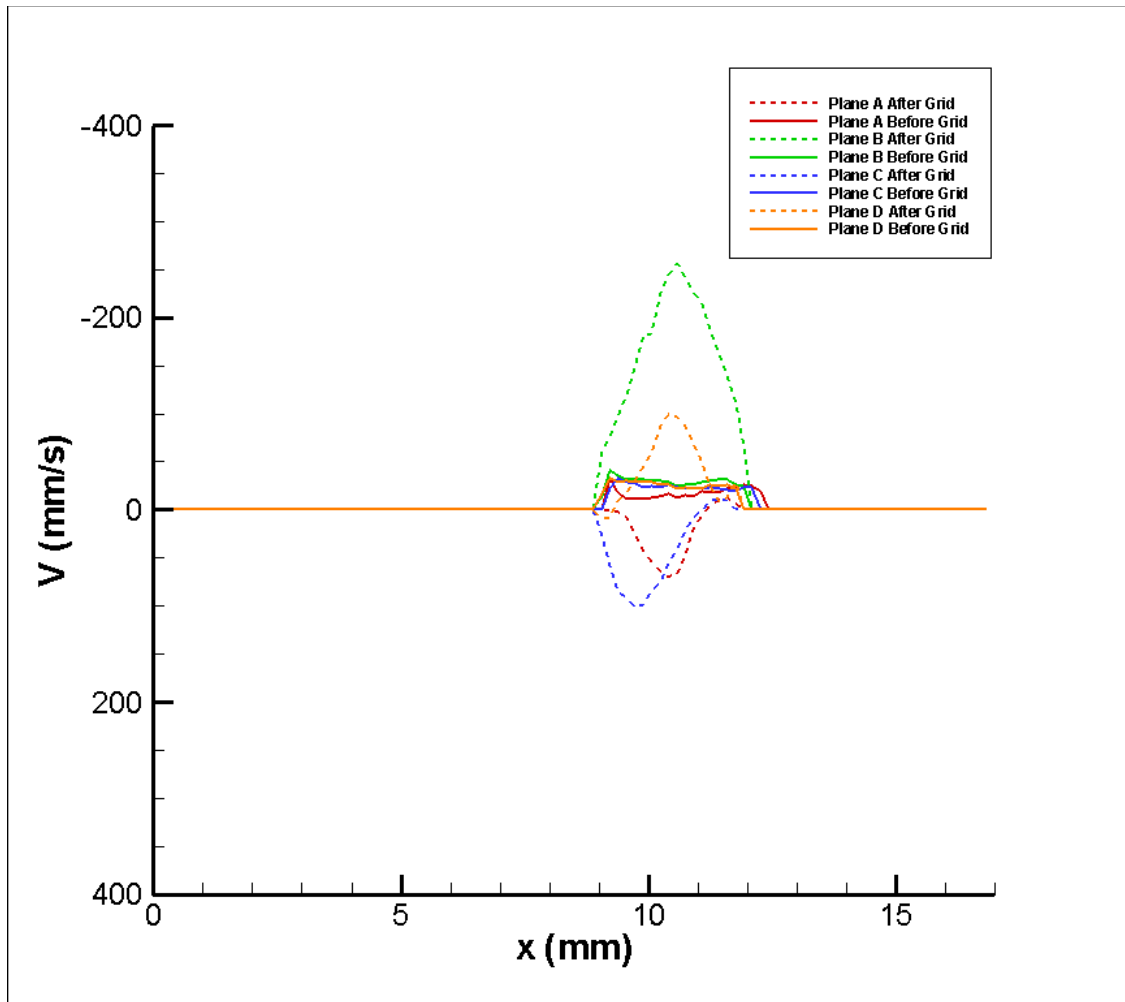


FIGURE 103. Averaged spanwise component of the velocity vector (V) for the A, B, C, D (sub-channel scale) planes downstream and upstream of the grid. $Re = 16300$.

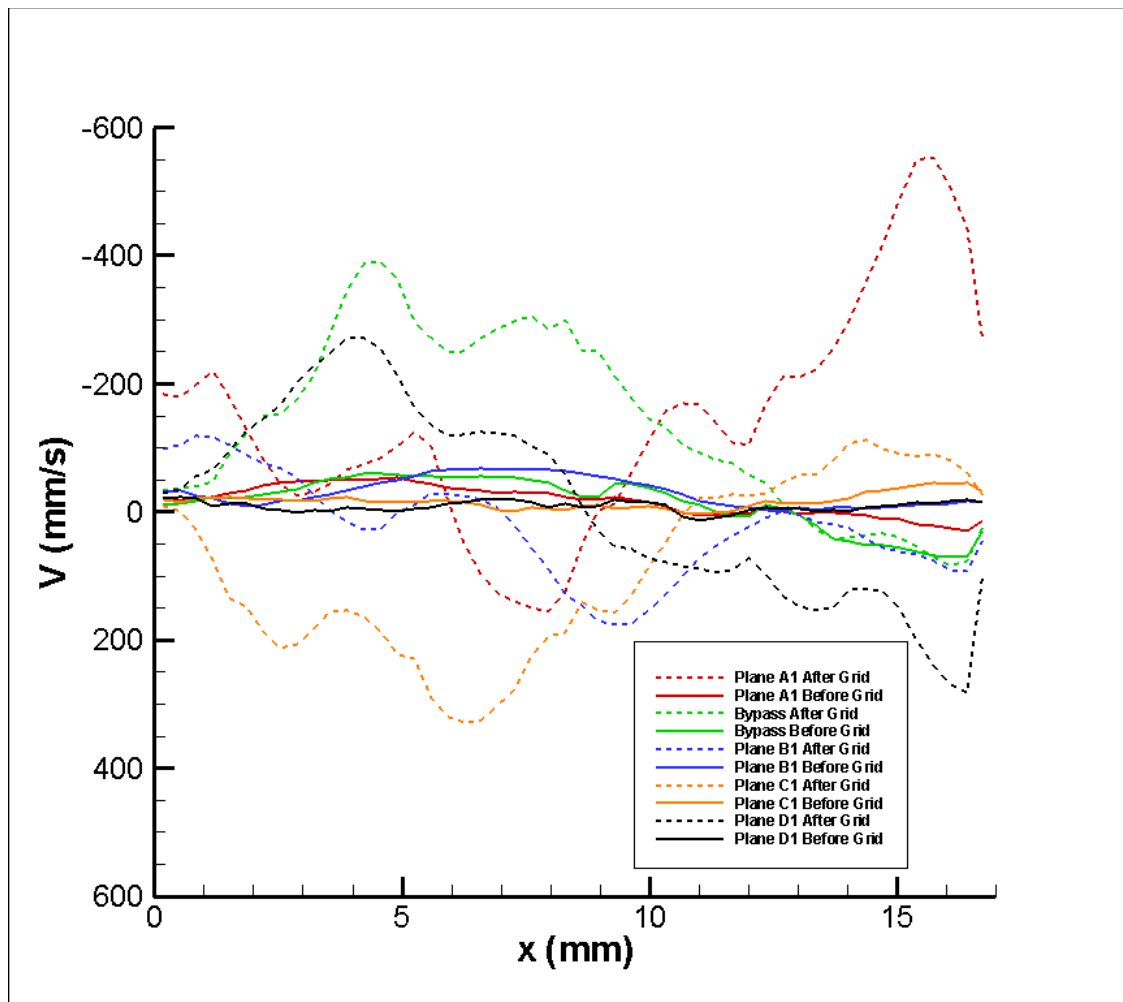


FIGURE 104. . Averaged spanwise component of the velocity vector (V) for the A1, B1, C1, D1, Bypass (sub-channel scale) planes downstream and upstream of the grid. $Re = 16300$.

Figures 105 and 106 show the averaged turbulence intensities profiles for the streamwise component of the velocity vector (u_{rms}) at planes with rods and without rods respectively. The results shown in figure 105 for the planes with rods exhibit a profile shape similar to a channel flow with non-slip boundaries for the profiles measured upstream of the spacer where the peaks of the profiles are located nearby the rod wall. In contrast, the profiles measured downstream of the spacer show a peak located at $x = 11$ mm of the X-axis on figure 105. The peak is 50 % higher for planes B and C (blue and green dotted lines) than planes A and D (red and orange dotted lines). This increase is attributed to the proximity of channels A and D to the walls of the containing vessel, while planes B and C are located at the center of the bundle therefore are not affected by external phenomena created by the experimental set-up such as the bypass flow.

Figures 107 and 108 show the averaged turbulence intensity profiles for the normal component of the velocity vector (v_{rms}) at planes with rods and without rods respectively. There is an increase in the average value of the normal fluctuations of 30 % for the position downstream the grid with respect to the position upstream the grid for all planes. For the planes with rods shown in figure 107 the normal turbulence intensity upstream of the grid show a shape similar to the one found at a wall-bounded turbulent channel flow. Figure 108 shows same increment of 30% for the position downstream of the grid with respect to the upstream one. The increase in the normal intensities is observed in the Bp plane at the after grid position. This fact elucidates the influence of the split vanes on the increment.

\

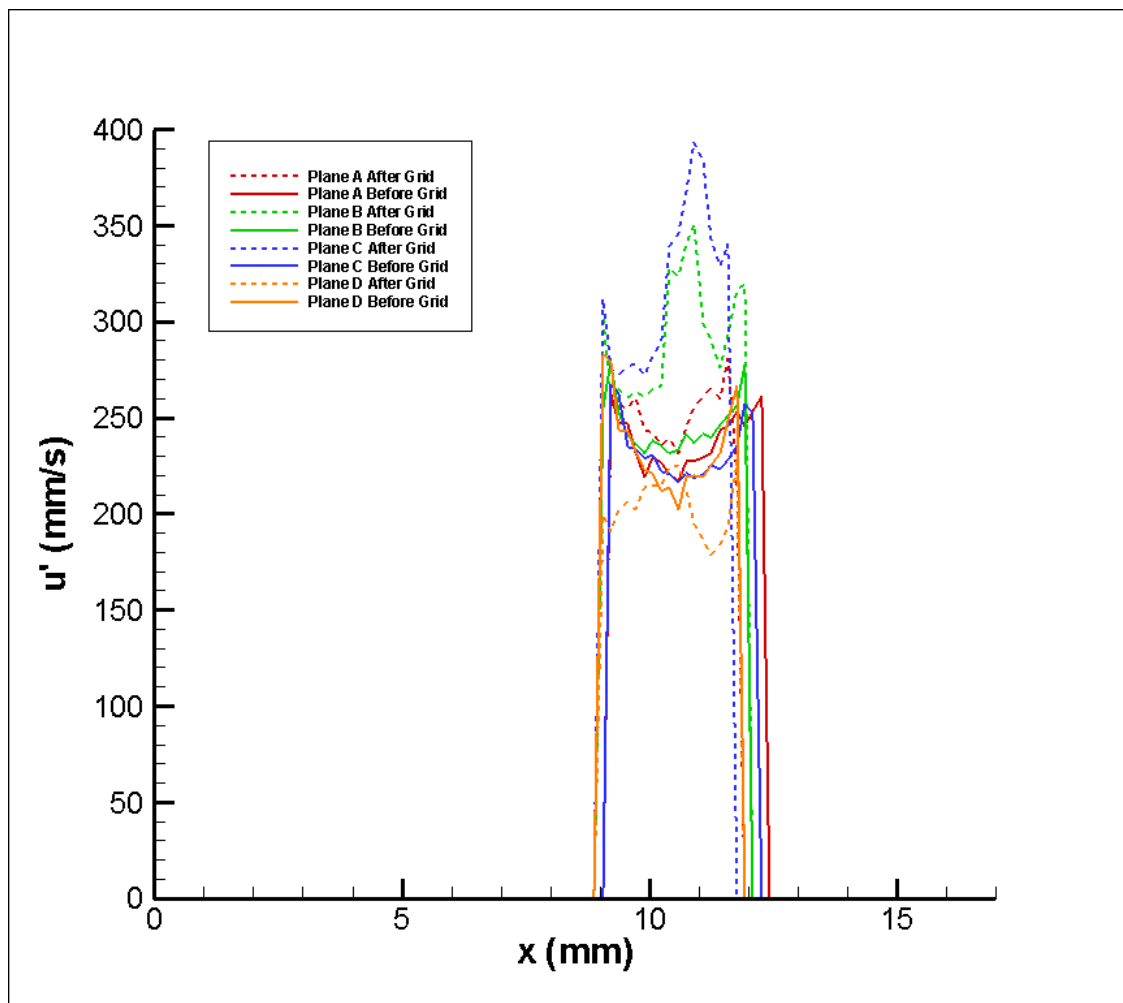


FIGURE 105. Averaged turbulence intensities for the streamwise component of the velocity vector (u') for the A, B, C, D (sub-channel scale) plane downstream and upstream of the grid. $Re = 16300$.

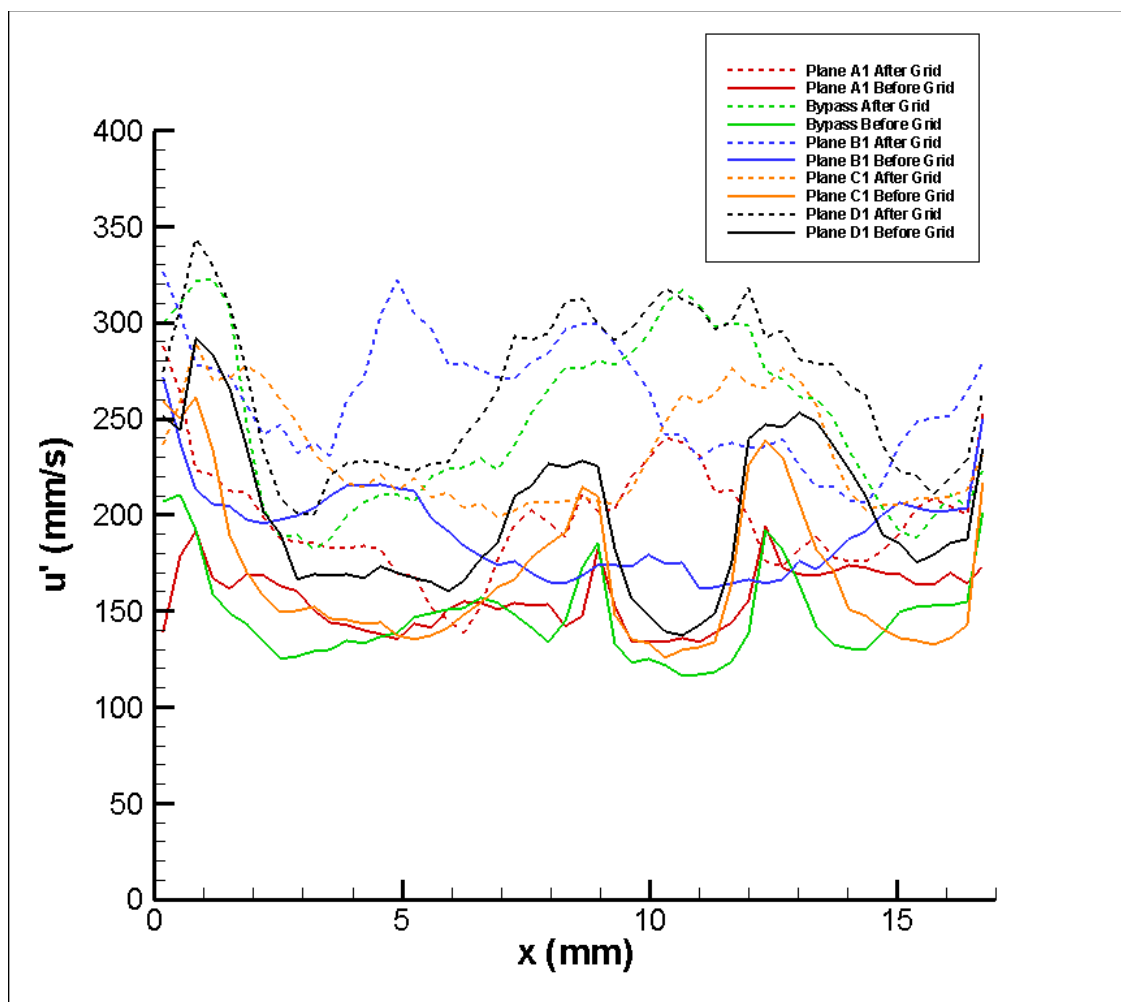


FIGURE 106. . Averaged turbulence intensities for the streamwise component of the velocity vector (u') for the A1, B1, C1, D1, Bypass (sub-channel scale) plane downstream and upstream of the grid. $Re= 16300$.

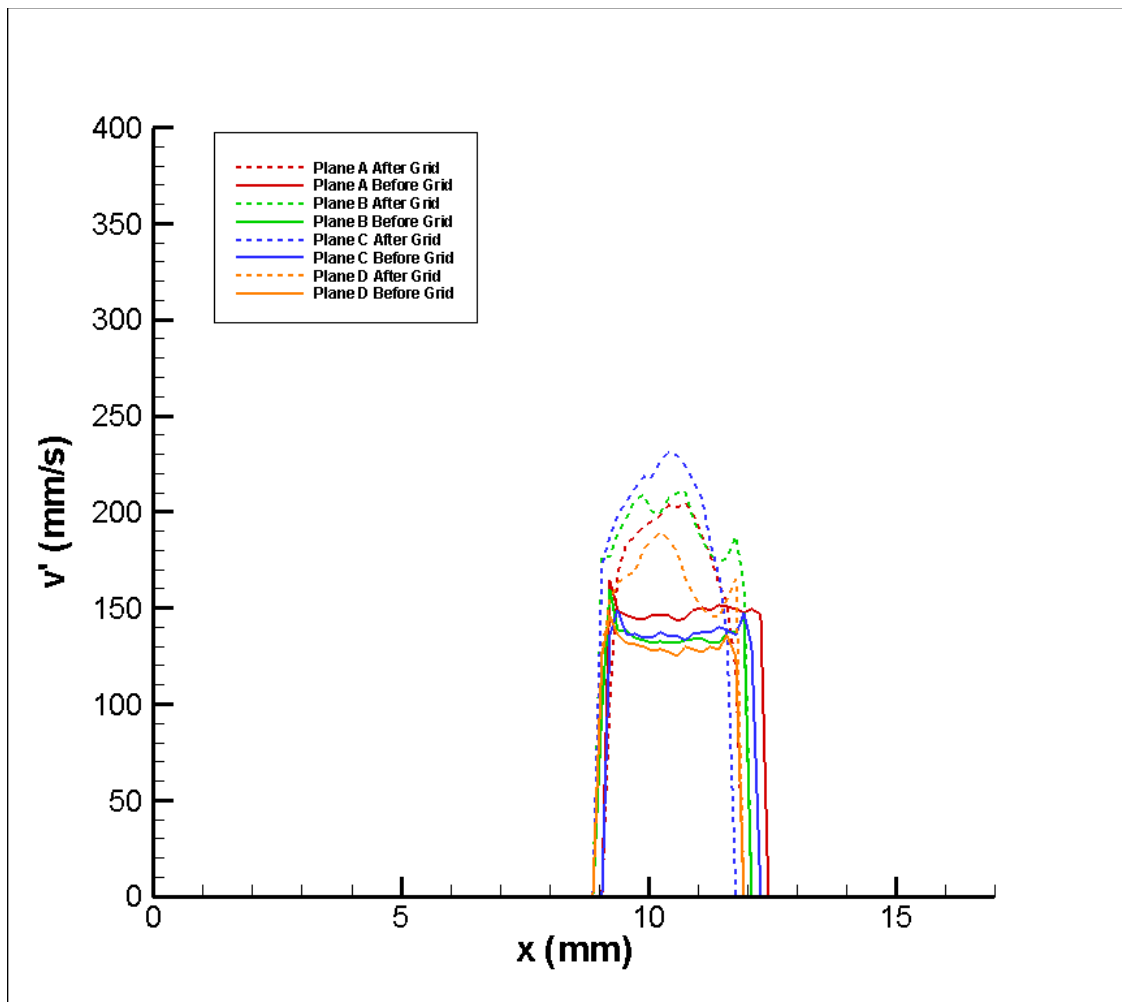


FIGURE 107. Averaged turbulence intensities for the spanwise component of the velocity vector (v') for the A, B, C, D (sub-channel scale) plane downstream and upstream of the grid. $Re = 16300$.

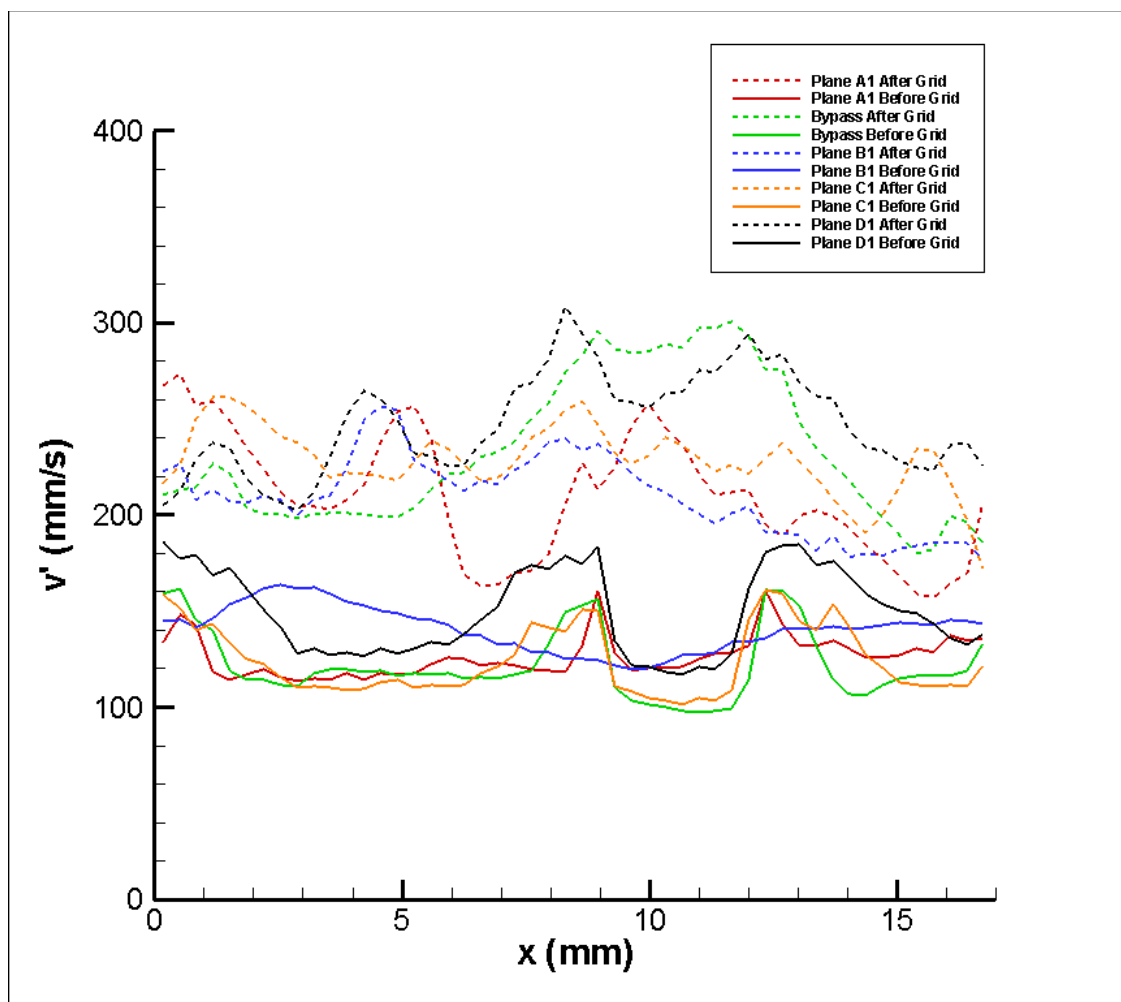


FIGURE 108. Averaged turbulence intensities for the spanwise component of the velocity vector (v') for the A1, B1, C1, D1, Bypass (sub-channel scale) plane downstream and upstream of the grid. $Re=16300$.

Reynolds stresses, for single phase flows, can be obtained from the velocity fields. The viscous stress can be obtained from the measured streamwise mean velocity profile. Experimental results of Reynolds stresses for various cases are shown in figure 109 and figure 110. The typical Reynolds stress calculation includes the following terms $-\rho \overline{u'v'}$. The results showed in figures 109 and 110 does not consider the fluid density and negative sign, therefore the plots shows the values of $\overline{u'v'}$ product in the Y-axis and the distance in the X-direction in the abscissa axis.

Figure 109 show the Reynolds stress results for planes with rods. The shape of the stresses is consistent to the one obtained in wall-bounded turbulent channel flow for the position before the grid (BGP1) denoted by solid lines in the picture. The four planes presented in this picture show a close similitude in shape and value. However, the results of the position after the grid (AGP1) show a different behavior. There is a noticeable change in the distribution of the stresses. The value of the Reynolds stress is opposite at the position downstream the grid with respect to the position upstream the grid. All the profile have a value near zero at the center of the gap formed by adjacent rods which is located at $x = 10.3$ mm in figure 109. A de-correlation between the streamwise (u') and the normal (v') velocity fluctuating components is the source of these discrepancies of the Reynolds stresses. This phenomenon may be explained due to a modification in the organized structures in the flow which are forced to change when the fluid passes through and near the split vanes.

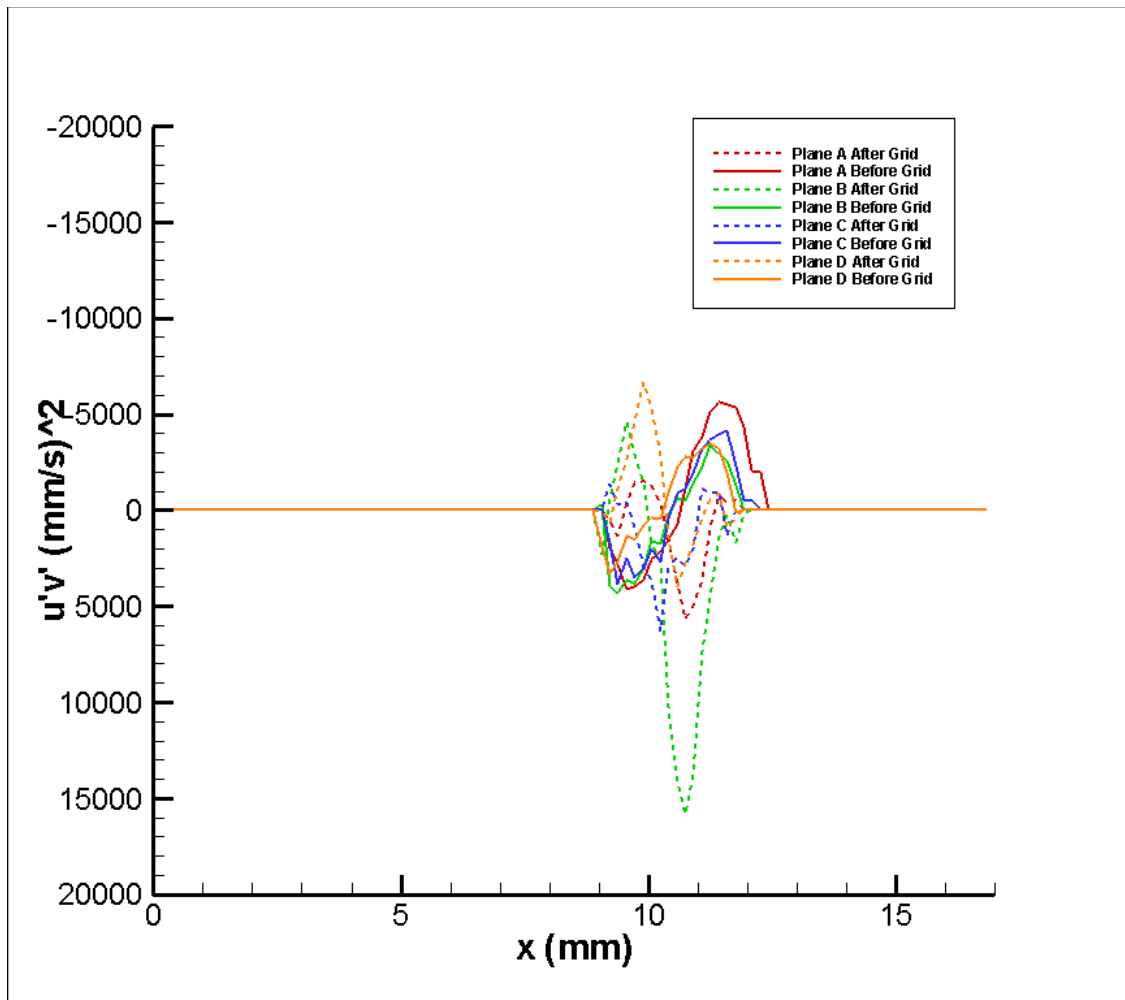


FIGURE 109. Averaged Reynolds stresses ($u'v'$) for the A, B, C, D (sub-channel scale) planes downstream and upstream of the grid. $Re=16300$.

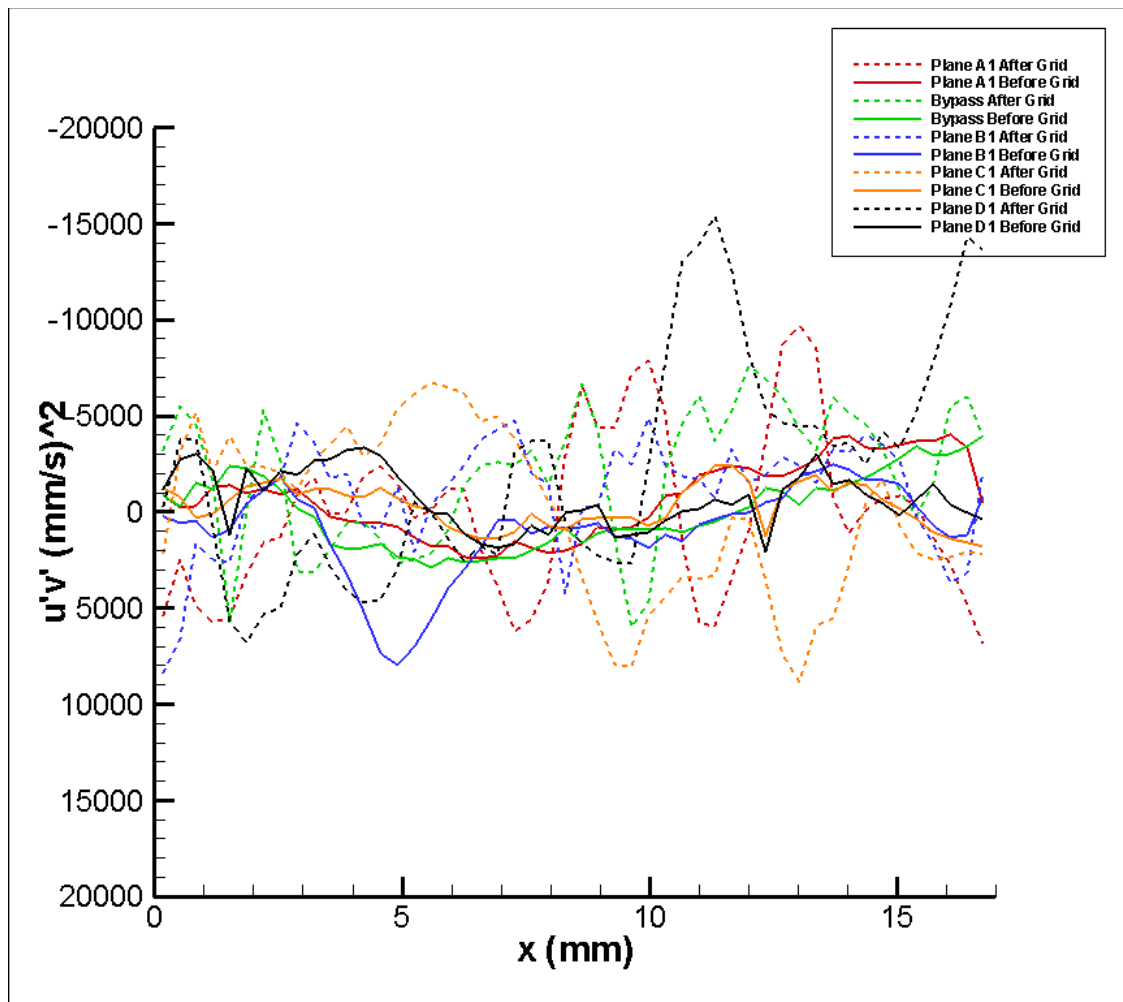


FIGURE 110. Averaged Reynolds stresses ($u'v'$) for the A1, B1, C1, D1, Bypass (sub-channel scale) planes downstream and upstream of the grid. $Re=16300$.

The calculation procedure of strain rate was presented in chapter III of this work. The strain was calculated for every instantaneous velocity field and then averaged over the number of realizations. The averaged strain rate obtained from the PIV measurements is shown in figures 111 and 112 for a plane without rods and a plane with rods respectively. The energy dissipation process is directly associated with strain, not with vorticity. The so named “vortex stretching” process has been regarded as the cause of the high rate of dissipation associated with turbulent motions. The two-dimensional average strain rates are shown in figures 111 and 112 in an effort to visualize the energy dissipation process. Since, in this research just the plane x-y was studied, just one term of the dissipation ($\epsilon = 2 \nu \overline{s_{1j} s_{1j}}$) can be calculated. However, from the calculated term of the rate of strain tensor, it can be observed that a decrease in the turbulent dissipation is expected at the position immediately above the grid (upstream). The split vanes are turbulence promoters; therefore the strain rate after the grid shows a decrease with respect to the position before the grid.

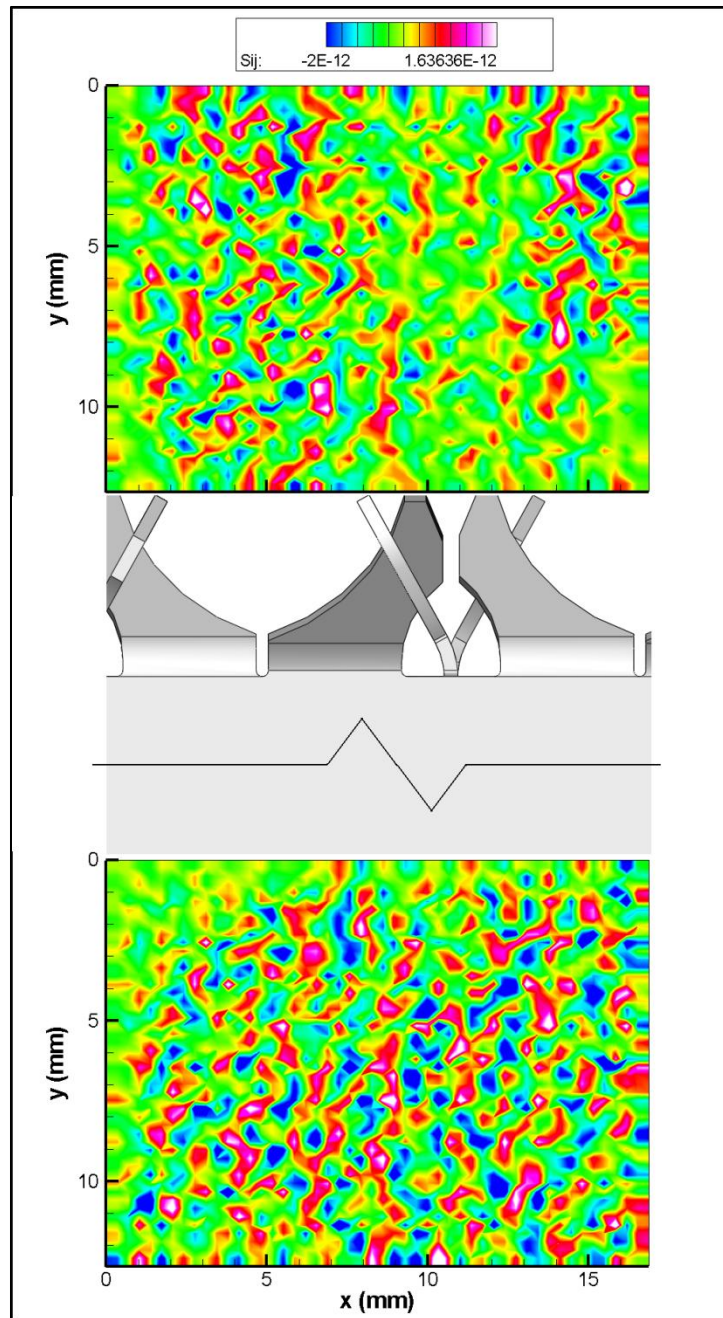


FIGURE 111. Average strain rate for sub-cahnnel scale , plane B1.

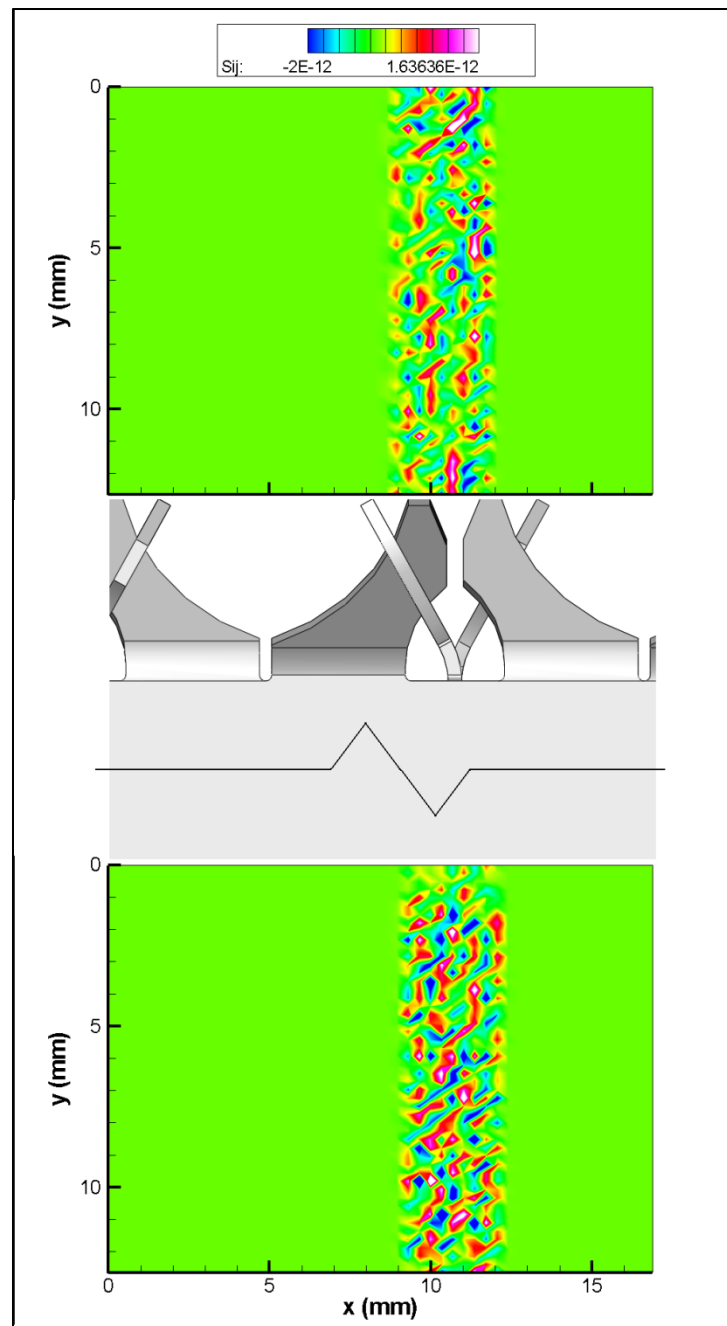


FIGURE 112. Average strain rate for sub-channel scale , plane C.

The swirl strength was calculated for plane C and plane B1. These planes are located at the middle of the rod bundle and the main difference between them is the presence of rods for plane C and the lack of them for plane B1. The swirl strength gives an indication for vortex identification and its strength. The frequency of rotation is associated with the swirl strength. Figure 113 shows the calculated averaged strength from 500 instantaneous fields. The figure shows positions BGP1 (upstream of the grid) and AGP1 (downstream of the grid). For this case, the plane B1 does not have the presence of rods. A pictorial of the spacer-grid is located between the two measured positions for better understanding. The strength is increased at various zones at position AGP1 which denotes several red spots in the picture. The strength was expected to increase at the position upstream since the split vanes deflect the flow direction and promote the formation of new flow structures.

Figure 114 shows the averaged strength results for plane C. This is the central plane of the rod bundle, therefore the measurements were focused at the gap formed by adjacent rods. The results show a strong increase of the swirl strength in the fluid for position AGP1. This is a similar behaviour than the one found for plane B1. It is noted that the strength distribution before the grid (BGP1) is located at the rods walls, indicating the presence of vortex near by the solids. In contrast, the position after the grid (AGP1) shows a distribution of the strength values all over the entire domain. This fact shows the formation of new structures in the flow induced by the grid geometry. The orientation of the split vanes have a direct correlation with the formation of these new structures.

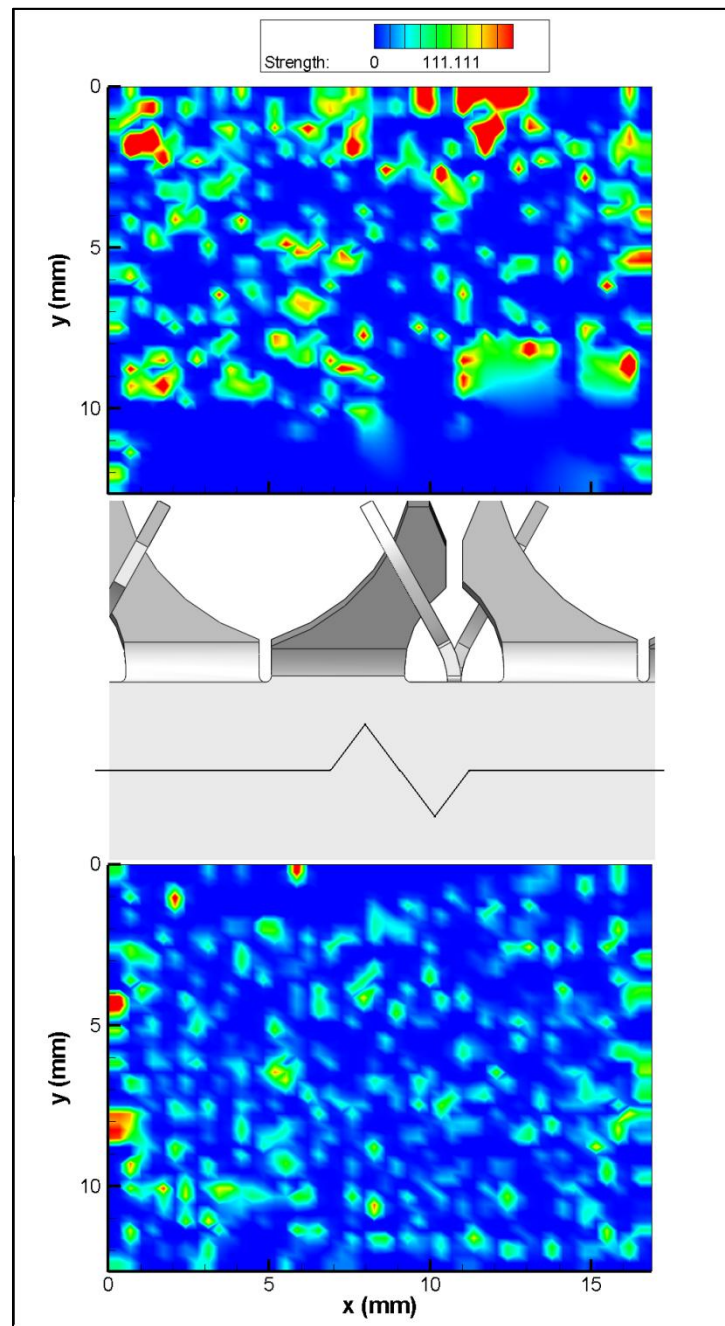


FIGURE 113. Swirl strength sub-channel scale, plane B1.

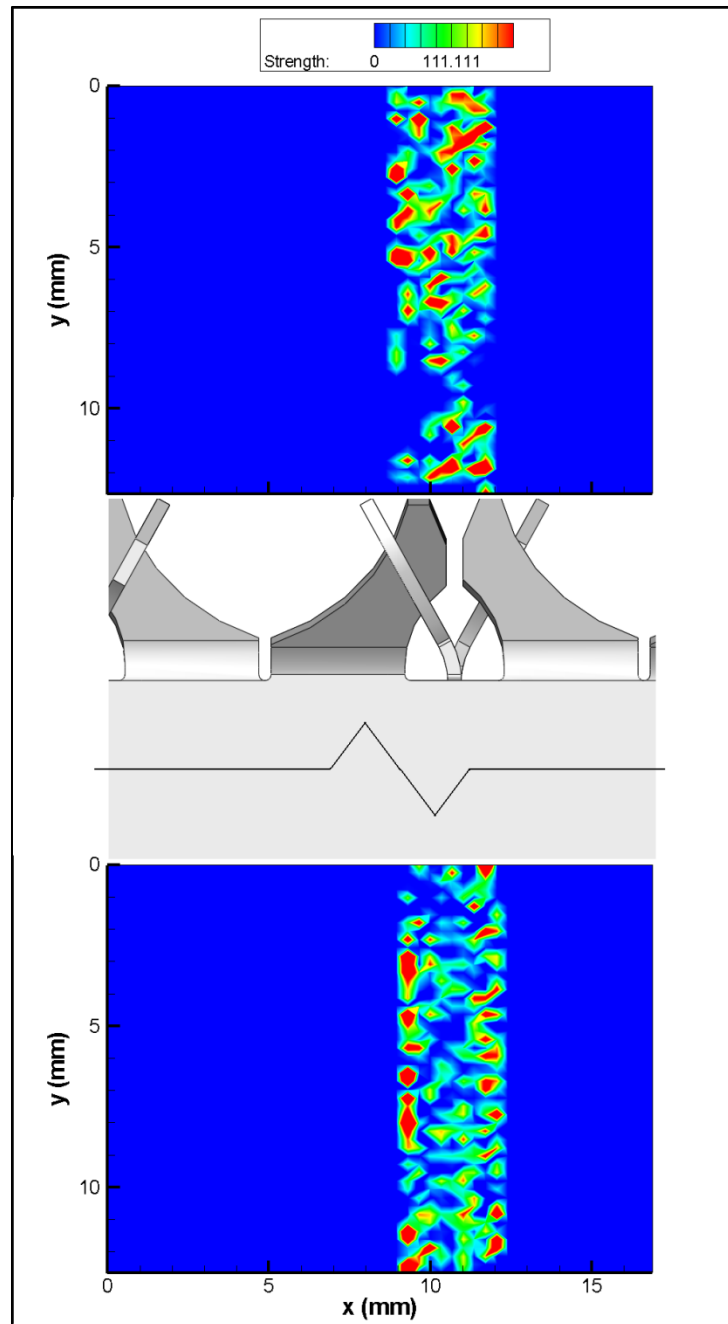


FIGURE 114. Swirl strength for sub-channel scale , plane C.

Two-dimensional correlation calculations were obtained in the x-y plane at two different (x,y) locations for u' and v' . The locations were selected in such a way that the center of the correlation point lie exactly in the middle of the gap formed by adjacent rods. The correlation results are shown for planes with rods and planes without rods. Figures 115 to 118 show the changes produced by the spacer grid in the correlation results. The averaged change of the streamwise and the normal length scales, which are associated with the maximum widths (along the x- and y-directions, respectively) of the contours R_{uu} and R_{vv} obtained from the averaged fluctuating velocity fields can be observed in these figures by noticing the increase in the correlation value denoted by the color change in the plots. It is observed that for the streamwise fluctuating velocity, the length scales in X- and Y- direction increases for position AGP1 which is located upstream of the grid. Figures 117 and 118 show the correlation result for plane C which is located at the center of the 5 x 5 rod bundle. The results of the correlation show an increase in correlation for the both directions, along the x- and y-directions, respectively.

The increase in correlation denotes the effect of the grid on the flow by forming new similar structures in the region immediately above the split vanes. The structures, in average, have a bigger length scale. Table 5 shows a summary of the obtained length scales from the two planes shown in figures 115 to 118.

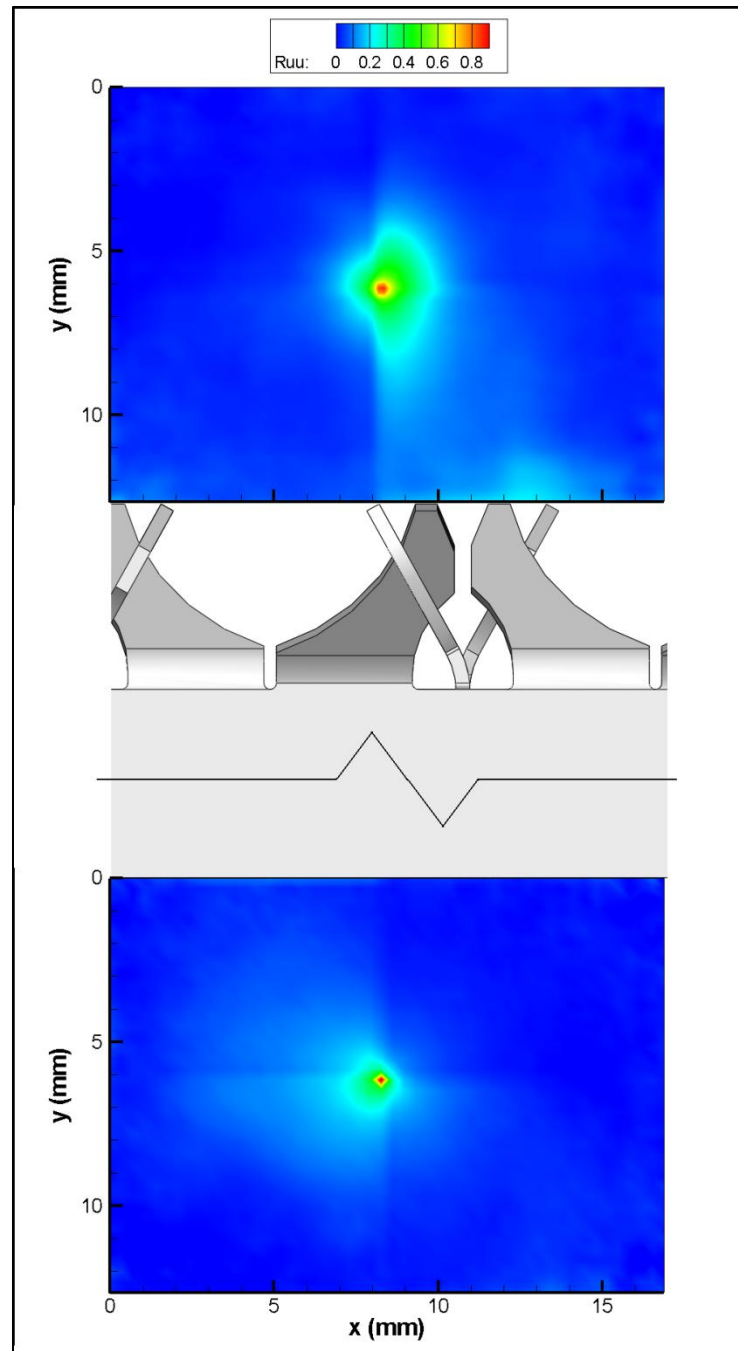


FIGURE 115. R_{uu} correlation for sub-channel scale, plane B1.

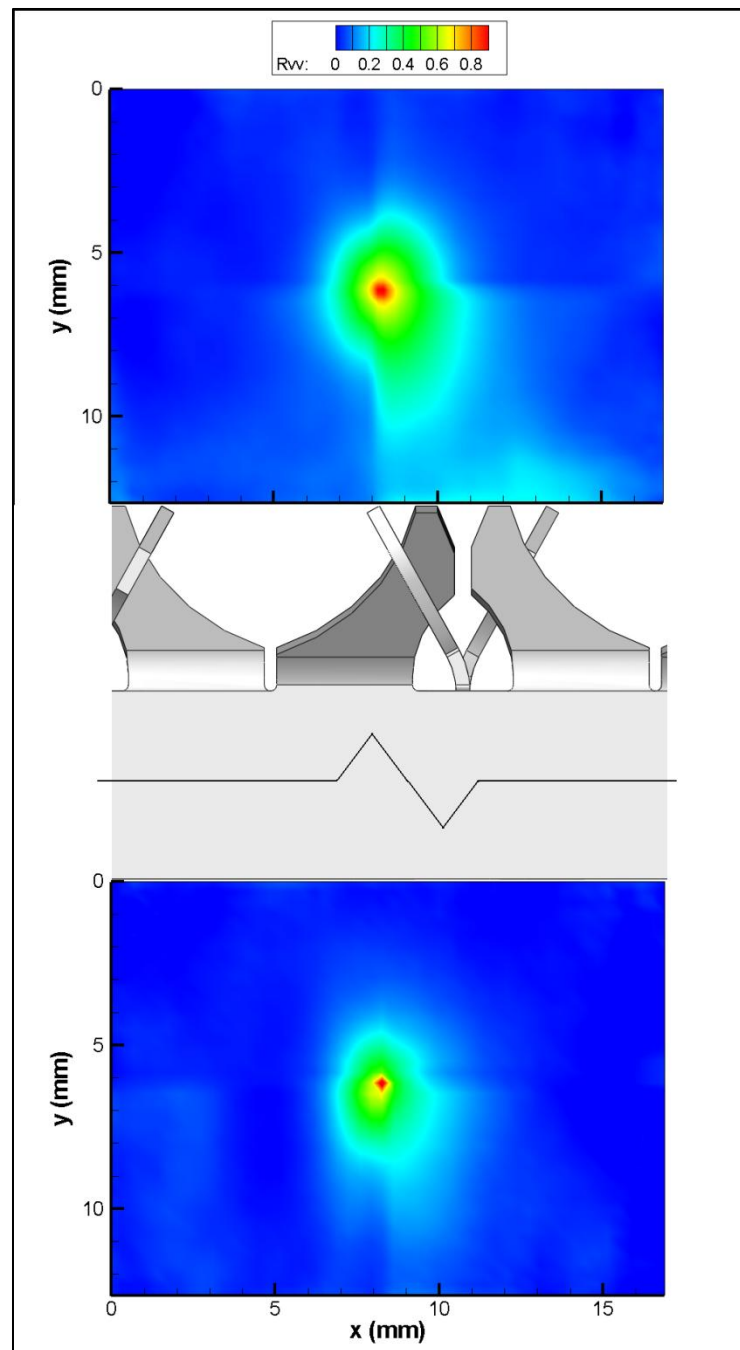


FIGURE 116. R_{vv} correlation for sub-channel scale, plane B1.

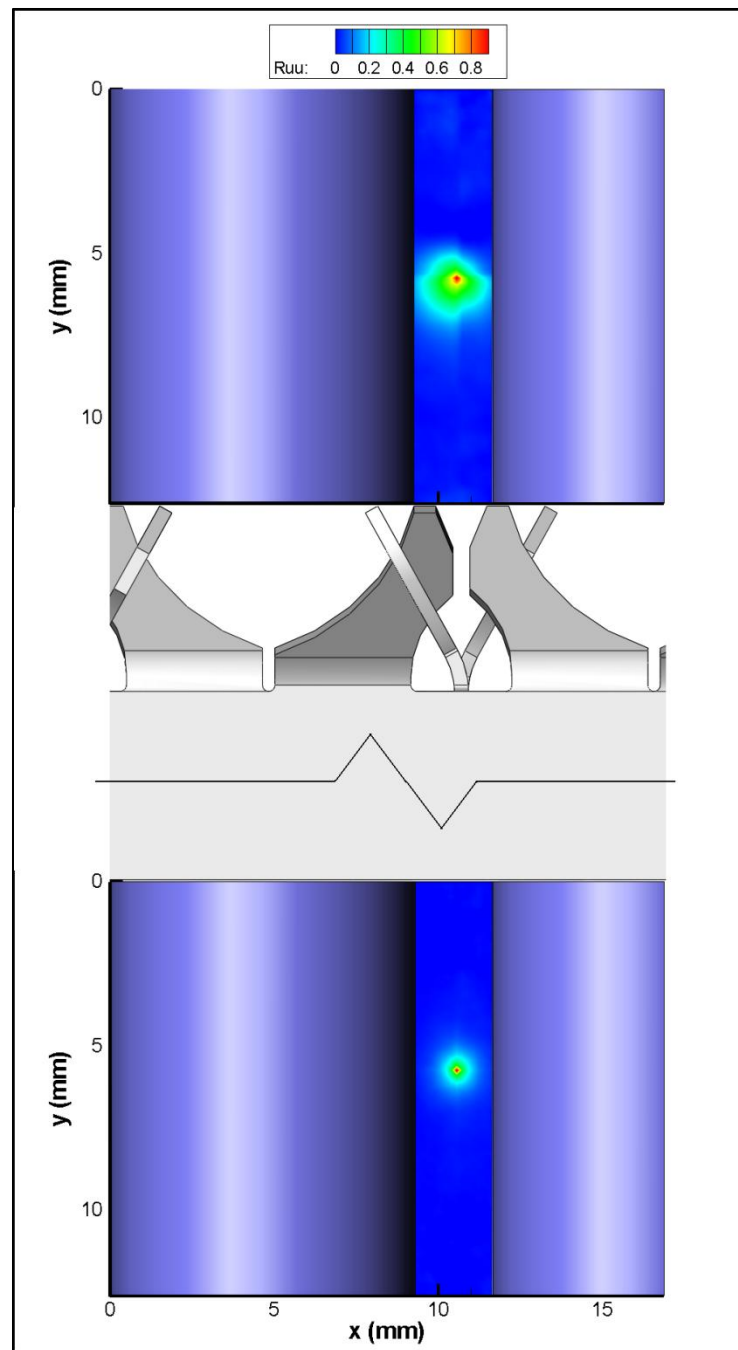


FIGURE 117. R_{uu} correlation for sub-channel scale, plane C.

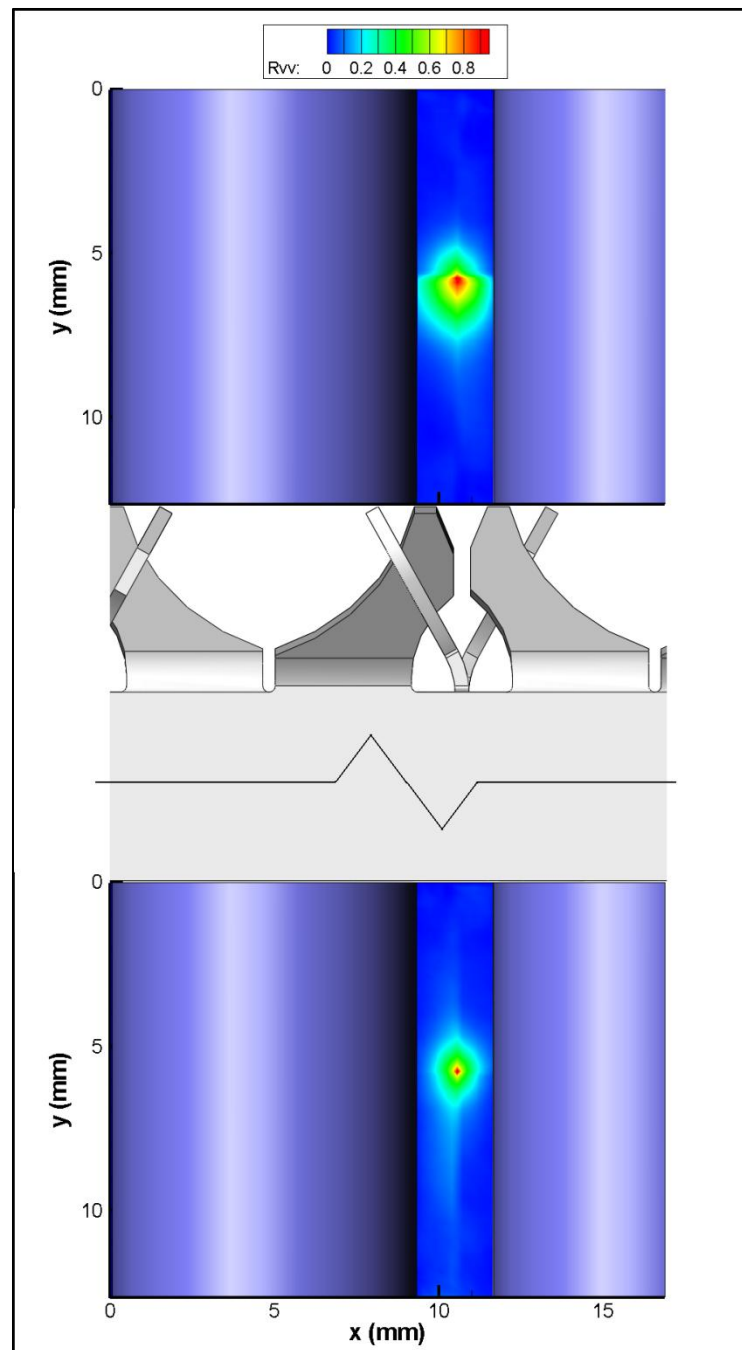


FIGURE 118. R_{vv} correlation for sub-channel scale, plane C.

Before Grid / After Grid	Plane	Ruu / Rvv	Lx-Width (mm)	Ly-Height (mm)
After Grid	B1	Ruu	2.73731	3.88003
After Grid	B1	Rvv	4.22192	6.65322
Before Grid	B1	Ruu	1.85636	1.72638
Before Grid	B1	Rvv	3.69966	5.23426
After Grid	C	Ruu	2.01061	1.86679
After Grid	C	Rvv	2.2463	2.74628
Before Grid	C	Ruu	0.732199	0.850409
Before Grid	C	Rvv	1.34319	2.04116

Table 4. Measurements of areas with high 2D correlation for sub-channel scale.

CHAPTER V

CONCLUSIONS

Successful use of PIV in addition to Matched Index of Refraction was used for full field velocity fields in a complex geometry without flow disturbance. The results showed that turbulence evolution can be observed using the DPIV technique. Good quality data with high spatial and temporal resolution open the possibility of CFD benchmarking and validation among important quantification of the turbulent structures present in the flow above spacer grids. The experimental results from this work may be useful for the development of a turbulence model for applications such as sub-channel geometries, where the flow is highly non-isotropic.

Measurements were performed using two different grid designs. One typical of BWR's with swirl type mixing vanes and the other typical of PWR's with split type mixing vanes. The results for both cases included the measurement of regions that cover the flow behavior upstream and downstream of the tested grid under various conditions. High quality data was obtained in the vicinity of the grid using the multi-scale approach. Turbulence parameters were calculated from the results obtained from PIV

5.1 Grid 1

The streamwise component of the velocity vector showed a decrease of up to 30% in the regions immediately above the mixing vanes (downstream) with respect to

the results obtained in the regions immediately below the spacer (upstream). The normal component of the velocity vector showed an increase in magnitude for regions nearby the mixing vanes due to the inflection caused in flow direction by the mixing vanes. Turbulence intensities in the streamwise direction had an average value of 25% of the maximum velocity attained in the regions between adjacent rods. On the other hand the normal turbulent intensity had a value of 12 % of maximum velocity attained in the regions between adjacent rods. For measurements including regions where the rods are not present, i.e. plane B2, the turbulent intensities in both directions, streamwise and normal had a similar value of 12% of the maximum velocity. The Reynolds stresses in the gap formed by adjacent rods showed a similar behavior to a channel flow with non-slip condition for measured positions upstream the grid. This behavior was considerably modified after the flow passed through the grid. The measured regions in the vicinity of the mixing vanes exhibited a considerable change in the behavior of Reynolds stresses. Although the magnitude of the stresses downstream from the grid remained similar to the magnitude upstream the grid the multiplied fluctuations forming the stresses exhibited only positive values which indicates the redistribution of the stresses in a preferential direction.

The effect of the spacer grid was a modification of the boundary layer caused by the mixing vanes which produced an attenuation of the vorticity magnitude. Although vorticity was always present in the flow, there seemed to be a counteracting phenomenon that suppressed the stretching in the flow. There is a change in the maximum velocity attained in the channel of 50% with respect to the maximum

measured downstream of the spacer. The averaged data showed a uniform direction profile of the velocity field after passing the spacer which elucidates the effect of averaging on the results. On the other hand, the velocity profile downstream of the spacer grid shows a similar profile to those found in shear flow along a no-slip wall.

One of the advantages of the DPIV obtained measurements is the direct comparison of instantaneous data with CFD which was previously done using an averaging approach. The results indicated that the flow field around the spacer included a large-scale unsteadiness and an undeveloped turbulent flow. The unsteadiness was caused by a separation above the mixing vane attached to the spacer. The undeveloped turbulence appeared in the inlet of the spacer, where the developed main flow in the sub-channel center was divided by the spacer edge. Turbulence models based on a developed turbulent flow are fundamentally inapplicable to these flows.

5.2 Grid 2

The results showed the effect of by-pass flow created by geometrical configurations of the test section. The central sub-channels exhibited no major changes denoting that by-pass flow did not considerably affect the central sub-channels.

The streamwise component of the velocity vector showed a decrease of up to 50% in the regions immediately above the mixing vanes (downstream) with respect to the results obtained in the regions immediately below the spacer (upstream). The normal component of the velocity vector showed an increase in magnitude for regions near the split vanes of 50 % due to the inflection caused in flow direction by the split vanes.

Turbulence intensities in the streamwise direction have an averaged value of 20% of the maximum velocity attained in the regions between adjacent rods for measured zones located downstream of the spacer grid. On the other hand, the intensities upstream the grid exhibited an averaged value of 10% of the maximum velocity. This behavior is the main difference between grid 1 and grid 2 results.

The averaged normal turbulent intensity had a value of 10 % of maximum velocity for planes including rods and the planes without the rods. However, the magnitude of the turbulence intensities upstream of the grid, in general, was 50 % smaller with respect to the magnitude of the intensities downstream of the grid which contrast with the results of grid 1.

The Reynolds stresses in the gap formed by adjacent rods showed a similar behavior to a channel flow with non-slip condition for measured positions upstream of the grid. This behavior was considerably modified after the flow passed through the grid. The measured regions in the vicinity of the mixing vanes exhibited a considerable change in the behavior of Reynolds stresses.

The turbulence analysis performed on the results obtained from grid 2 showed an increase in the degree of correlation for regions located immediately above the split vanes (downstream) with respect to the regions located immediately below the grid (downstream). The calculated length scales from the correlation fields showed an increase in the length scale of 20% for regions located upstream of the grid with respect to regions located downstream of the grid. This fact elucidates the modification of eddy size caused by the grid.

REFERENCES

ADRIAN, R. J., CHRISTENSEN, K. T. and LIU, Z. 2000 Analysis and interpretation of instantaneous turbulent velocity fields. *Experiments in Fluids* **29**, 275-290.

BUDWIG, R. 1994 Refractive index matching methods for liquid flow investigations. *Experiments in Fluids* **17**, 350-355.

CARAGHIAUR, D. and ANGLART, H. 2007 Measurements and CFD predictions of velocity, turbulence intensity and pressure development in BWR fuel rod assembly with spacers. In *Proceedings of the 12th International Meeting on Nuclear Reactor Thermal Hydraulics (NURETH12)*, Pittsburgh, Pennsylvania.

CARAJILESCOV, P. and TODREAS, N. E. 1976 Experimental and analytical study of axial turbulent flows in an interior subchannel of a bare rod bundle. In *Heat Transfer Division Winter Annual Meeting ASME*, Houston, Texas.

CARGILLE-SACHER LABORATORIES INC. 2010 <http://www.cargille.com>.

CHANG, S. K., MOON, S. K., BAEK, W. P. and CHOI, Y. D. 2008 Phenomenological investigations on the turbulent flow structures in a rod bundle array with mixing devices. *Nuclear Engineering and Design* **238**, 600-609.

CHEN, R. C. and FAN, L. S. 1992 Particle image velocimetry for characterizing the flow structure in three-dimensional gas-liquid-solid fluidized beds. *Chemical Engineering Science* **47**, 3615-3622.

CHONG, M. S., PERRY, A. E. and CANTWELL, B. J. 1990 A general classification of three-dimensional flow fields. *Physics of Fluids* **2**, 765-777.

CONNER, M. E., SMITH, L. D., HOLLOWAY, M. V. and BEASLEY, D. E. 2005 Heat transfer coefficient testing in nuclear fuel rod bundles with mixing vane grids. In *Water Reactor Fuel Performance Meeting*, Kyoto, Japan.

CUI, M. M. and ADRIAN, R. J. 1997 Refractive index matching and marking methods for highly concentrated solid-liquid flows. *Experiments in Fluids* **22**, 261-264.

DOMINGUEZ-ONTIVEROS, E. E., ESTRADA-PEREZ, C. E., ORTIZ-VILLAFUERTE, J. and HASSAN, Y. A. 2006 Development of a wall shear stress integral measurement and analysis system for two-phase flow boundary layers. *Review of Scientific Instruments* **77**, 10-32.

DYBBS, A. and EDWARDS, R. V. 1984 An index matched flow system for measurement of flow in complex geometries. In *Proceedings of International Symposium on the Application of Anemometry to Fluid Mechanics*, Lisbon, Portugal.

EIFLER, W. and NIJSING, R. 1967 Experimental investigation of velocity distribution and flow resistance in a triangular array of parallel rods. *Nuclear Engineering and Design* **5**, 22-42.

ESTRADA-PEREZ, C. 2004 Analysis, comparison and modification of various particle image velocimetry (PIV) algorithms. Thesis, Texas A&M University

FOX, R. W. and MCDONALD, A. T. 1998 *Introduction to Fluid Mechanics, 5th Ed.*, John Wiley and Sons.

HAAM, S. J., BRODKEY, R. S., FORT, I., KLABOCH, L., PLACNIK, M. and VANECEK, V. 2000 Laser doppler anemometry measurements in a index of refraction matched column in the presence of dispersed beads, part I. *International Journal of Multiphase Flow* **26**, 1401-1418.

HASSAN, Y., GUTIERREZ-TORRES, C. and JIMENEZ-BERNAL, J. 2005 Temporal correlation modification by microbubbles injection in a channel flow. *International Communications in Heat and Mass Transfer* **32**, 1009-1015.

HENDRIKS, F. and AVIRAM, A. 1982 Use of zinc iodide solutions in flow research. *Review of Scientific Instruments*. **53**, 75-78.

IBRAGIMOV, M. K., ISUPOV, A., KOBZAR, L. L. and SUBBOTIN, I. 1966 Calculation of the tangential stresses at the wall of a channel and the velocity distribution in a turbulent flow of liquid. *Atomnaya Energiya* **21**, 101-107.

IKEDA, K. and HOSHI, M. 2006 Development of rod-embedded fiber LDV to measure velocity in fuel rod bundles. *Journal of Nuclear Science and Technology* **43**, 150-158.

IKENO, T. and KAJISHIMA, T. 2006 Decay of swirling turbulent flow in rod-bundle. *Journal of Fluid Science and Technology* **1**, 36-47.

LEE, C. M. and CHOI, Y. D. 2007 Comparison of thermo-hydraulic performances of large scale vortex flow (LSVF) and small scale vortex flow (SSVF) mixing vanes in 17×17 nuclear rod bundle. *Nuclear Engineering and Design* **237**, 2322-2331.

LEIS, A. P., SCHLICHER, S. and FRANKE, H. 2005 Optically transparent porous medium for nondestructive studies of microbial biofilm architecture and transport dynamics. *Applied and Environmental Microbiology* **71**, 4801-4808.

LEVCHENKO, Y. D., SUBBOTIN, I. and USHAKOV, P. A. 1972 Experimental investigation of averaged characteristics of turbulent flow in cells of rod packs. *Atomnaya Energiya* **33**, 893-899.

NARROW, T. L., YODA, M. and ABDEL-KHALIK, S. I. 2000 A simple method for the refractive index of sodium iodide aqueous solutions. *Experiments in Fluids* **28**, 282-283.

NETI, S., EICHHORN, R. and HAHN, O. J. 1982 Laser doppler measurements of flow in a rod bundle. *Nuclear Engineering and Design* **74**, 105-116.

NGUYEN, T. T., BIADILLAH, Y., MONGRAIN, R., BRUNETTE, J., TARDIF, J. C. and BERTRAND, O. F. 2004 A method for match the refractive index and kinematic viscosity of a blood analog for flow visualization in hydraulic cardiovascular models. *Journal of Biomedical Engineering* **126**, 529-535.

NIJSING, R., GARGANTINI, I. and EIFLER, W. 1966 Analysis of fluid flow and heat transfer in a triangular array of parallel heat generating rods. *Nuclear Engineering and Design* **1966**, 375-398.

NORTHROP, M. A., KULP, T. J. and ANGEL, S. M. 1991 fluorescent particle image velocimetry: application to flow measurements in refractive index-matched porous media. *Applied Optics* **30**, 3034-3040.

PANTON, R. L. 1996 *Incompressible flow, 2nd. Ed.*, John Wiley and Sons.

PIIRTO, M., IHALAINEN, H., ELORANTA, H. and SAARENINNE, P. 2001 2D Spectral and turbulence length scale estimation with PIV. *Journal of Visualization* **4**, 39-49.

POPE, S. B. 2000 *Turbulent Flows*, Cambridge University Press.

REHME, K. 1978 The structure of turbulent flow through a wall subchannel of a rod bundle. *Nuclear Engineering and Design* **45**, 311-323.

REHME, K. 1987 The structure of turbulent flow through rod bundles. *Nuclear Engineering and Design* **74**, 105-154.

ROWE, D. S. 1973 Measurement of turbulent velocity, intensity and scale in rod bundle flow channels. Thesis, Oregon State University

SEALE, W. J. 1979 Turbulent diffusion of heat between connected flow passages. *Nuclear Engineering and Design* **54**, 197-209.

- SIMONIN, O. and BARCOUDA, M. 1988 Measurements and prediction of turbulent flow entering a staggered tube bundle. In *Proceedings of the 4th international symposium on applications of laser anemometry to fluid mechanics*, Denver, Colorado.
- SKINNER, V. R., FREEMAN, A. R. and LYALL, H. G. 1969 Gas mixing in rod clusters. *International Journal of Heat Mass Transfer* **12**, 265-278.
- STOHR, M., ROTH, K. and JAHNE, B. 2003 Measurement of 3d pore-scale flow in index-matched porous media. *Experiments in Fluids* **35**, 159-166.
- STOOTS, C., BECKER, S., CONDIE, K., DURST, F. and MCELIGOT, D. 2001 A large-scale matched index of refraction flow facility for lda studies around complex geometries. *Experiments in Fluids* **30**, 391-398.
- TACHIBANA, F., OYAMA, A., AKIYAMA, M. and KONDO, S. 1969 Measurement of heat transfer coefficient for axial air flow through eccentric annulus and seven-rod cluster. *Journal of Nuclear Science and Technology* **6**, 207-214.
- TAPUCU, A. and MERILO, M. 1977 Studies on diversion cross-flow between two parallel channels communicating by a lateral slot. II: axial pressure variations. *Nuclear Engineering and Design* **42**, 307-318.
- TAYLOR, G. I. 1935 Statistical theory of turbulence. In *Proc. Roy. Soc.* vol. 151A, pp. 421.
- TENNEKES, H. and LUMLEY, J. L. 1974 *A First Course in Turbulence*, MIT Press.
- TZANOS, C. 2004 Computational fluid dynamics for the analysis of light water reactor flows. *Nuclear Technology* **147**, 181-190.
- UZOL, O., BROZOWSKI, D., CHOW, Y.-C., KATZ, J. and MENEVEAU, C. 2007 A database of PIV measurements within a turbomachinery stage and sample comparisons with unsteady RANS *Journal of Turbulence* **8**, 19.
- VAN DER ROS, T. and BOGAARDT, M. 1970 Mass and heat exchange between adjacent channels in liquid-cooled rod bundles. *Nuclear Engineering and Design* **12**, 259-268.
- YANG, S. K. and CHUNG, M. K. 1998 Turbulent flow through spacer grids in rod bundles. *Journal of Fluids Engineering ASME* **120**, 786-791.
- ZDRAVKOVICH, M. M. 1987 The effects of interface between circular cylinders in cross flow. *Journal of Fluids and Structures* **1**, 239-261.

ZHOU, J., ADRIAN, R. J. and BALANCHANDAR, S. 1996 Autogeneration of near-wall vertical structures in channel flow. *Physics of Fluids* **8**, 288-290.

ZHOU, J., ADRIAN, R. J., BALANCHANDAR, S. and KENDALL, T. M. 1999 Mechanisms for generating coherent packets of hairpin vortices in channel flow. *Journal of Fluid Mechanics*. **387**, 353-396.

APPENDIX A

This appendix shows the uncertainty analysis performed for the flow rate, Reynolds number and Particle Image Velocimetry measurements.

The uncertainty of the measured variables in the test facility was determined based on the propagation of error approach (Kline and McClintock, 1953). In this approach a general result for the error can be obtained if the errors of the contributed variables are individually small and symmetric about zero. The general result is obtained for the expected error to be associated with any quantity that is calculated as a function of any number of independent variables. If x, y, z, \dots are directly measured variables for which the standard deviation is known $\sigma_x, \sigma_y, \sigma_z, \dots$ then the standard deviation for any quantity u derived from these measurements can be calculated from the following equation.

$$\sigma_u^2 = \left(\frac{\partial u}{\partial x}\right)^2 \sigma_x^2 + \left(\frac{\partial u}{\partial y}\right)^2 \sigma_y^2 + \left(\frac{\partial u}{\partial z}\right)^2 \sigma_z^2 + \dots$$

Where $u = u(x, y, z, \dots)$ represents the derived quantity. The variables x, y, z, \dots , however, must be chosen so that they are truly independent in order to avoid the effects of correlation.

Flow rate

The flow rate was measured using a turbine type sensor (SDI flow sensor model SDIOH1N))-0200. The error in the calibration was taken from the manufacturer specifications to be $\pm 1\%$ of the full scale. The meter counts with an internal analog to digital converter and a display reader. The integrated electronics inside the meter account for electronic noise and thermal compensation therefore no considerable error was considered regarding the electronic part. The calibration is NIST traceable which translates into a maximum error in the flow rate measurements of $\pm 63 \times 10^{-6} \frac{m^3}{s}$.

Reynolds number

The contribution to the Reynolds number calculation was estimated from three main sources: average velocity in the flow casing, diameter of the rods and the fluid properties change with temperature. The velocity uncertainty contribution was caused by the error in the flow rate measurement only, $\pm 63 \times 10^{-6} \frac{m^3}{s}$. The rod diameter error was associated with the manufacturing tolerances process which for this case was ± 0.12 mm. The changes in fluid temperature were due to the energy added by the pump to the system which were measured during each data acquisition process with a maximum increase in temperature of 5 C. This increase in temperature correspond to a change in the kinematic viscosity of the fluid of $\pm 1 \times 10^{-7} \frac{m^2}{s}$.

$$\sigma_{Re}^2 = \left(\frac{\partial Re}{\partial V_{avg}}\right)^2 \sigma_{V_{avg}}^2 + \left(\frac{\partial Re}{\partial D}\right)^2 \sigma_D^2 + \left(\frac{\partial Re}{\partial \vartheta}\right)^2 \sigma_{\vartheta}^2$$

Particle image velocimetry

The local velocity measurements obtained from the PIV technique have various sources of error. One source of error is the capability of the seed particles to follow the fluid flow. In order to quantify the response of a particle to changes in fluid motion, the stokes number can be calculated using the following expression.

$$St = \frac{\tau_p}{\tau_f}$$

Where τ_p is the relaxation time of the particle and τ_f is the characteristic time of the fluid. The particle relaxation time can be estimated using the following equation (Adrian *et. al.*, 1997)

$$\tau_p = \frac{\rho_p d_p^2}{18\mu}$$

For this case, the working fluid was water therefore the terms in the above equation were evaluated as $d_p = 10 \mu m$, $\rho_p = 1050 \frac{kg}{m^3}$ and $\mu = 1000 \times 10^{-6} \frac{Ns}{m^2}$. Therefore the particle relaxation time is $\tau_p = 5.8 \mu s$.

The fluid time scale can be estimated using a characteristic length D_h and the maximum bulk velocity attained in the test section using the following expression.

$$\tau_f = \frac{D_h}{U}$$

The maximum fluid velocity is 2500 mm/s, consequently $\tau_f = 4.7 \text{ ms}$. Performing the calculation of the Stokes number gives $St = 1.2 \times 10^{-3}$. As a result the $10 \text{ }\mu\text{m}$ particles closely follow the fluid motion.

The accuracy of the measurements is given by the following expression (Adrian 1986)

$$\sigma_U = \frac{\sigma_{\Delta x} + U\sigma_{\Delta t}}{\Delta t}$$

Where σ_U is the root mean square of the uncertainty of the velocity, $\sigma_{\Delta x}$ is the root mean square of the uncertainty in the separation of images, and $\sigma_{\Delta t}$ is the uncertainty in the time between pulses. The uncertainty in the separation $\sigma_{\Delta x}$ is proportional to the error in locating the centers of the particle images and depends on the algorithm used to determine the positions x_1 and x_2 . The algorithm used in this investigation has a maximum error of 0.1 pixels in centroid particle detection (Estrada-Perez, 2004) which was determined using artificial images. The final error in the particle center location has the effect of lenses and geometry used in the experiment. Therefore, for the case of real images it has an additional dependence on the particle spot diameter projected by the

imaging system. The spot diameter can be calculated using the following expression (Adrian 1986)

$$d_{\tau} = (M^2 d_p^2 + d_s^2 + d_r^2)^{\frac{1}{2}}$$

Where M is the magnification factor of the imaging system, d_p is the particle diameter, d_s is the diffraction limited spot diameter of the optical system, and d_r is the resolution of the recording medium. For the particular configuration of this investigation, $M = 0.75\times$, $d_p = 10\ \mu m$, and the resolution of the CMOS array, d_r , is $6\ \frac{\mu m}{pixel}$. The d_s value depends on the optical system parameters, including focal length of the lens, magnification, and the wavelength of the laser. For this investigation d_s was computed to be $12\ \mu m$. The uncertainty in the time separation is consider small having a maximum value of $10\ \mu s$. This value corresponds to the maximum exposure time of the camera, since the laser pulse duration is in the order of 200 ns, the maximum possible error in time separation to acquire an image corresponds to the exposure time. Otherwise, there will not be a valid image.

The accuracy of the measurement due solely to the PIV algorithm and associated optical system is of 6 %.

In this investigation there is an additional source of error due to the geometrical configuration of the test section and the imperfections of the matched refractive index technique. This error depends on the specific location of the measurements in the velocity field. The main contribution to this error is the optical aberrations caused by the

rods edge caused by a dissimilar refractive index of the plastic rods. The following figure illustrates the optical distortion caused by the edge of the rods in the PIV measurement plane.

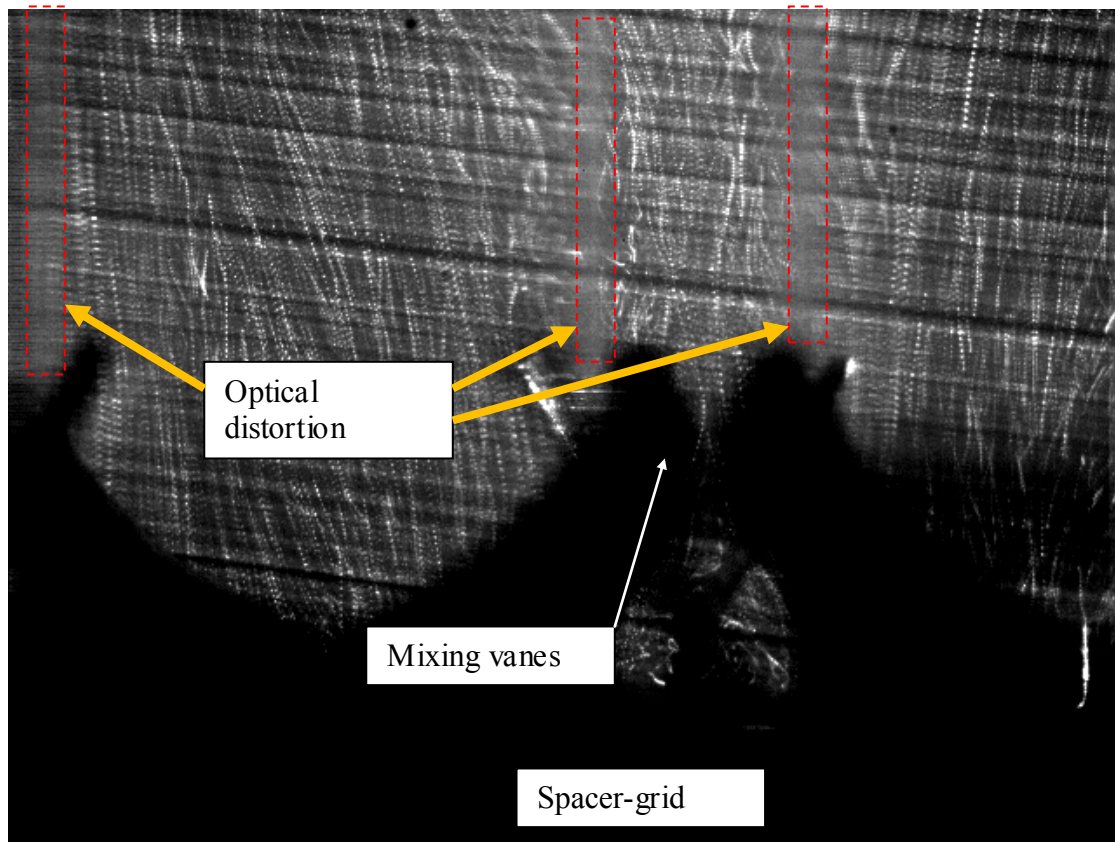


Figure A1. Optical distortion caused by not perfect matching index of refraction between the plastic rods. and the working fluid.

The center particle detection using the PIV algorithm is affected by the optical distortion causing an increased error for specific locations. The following figure illustrates a typical PIV image (sub-channel scale) obtained and the localized optical distortion caused by the rods edge.

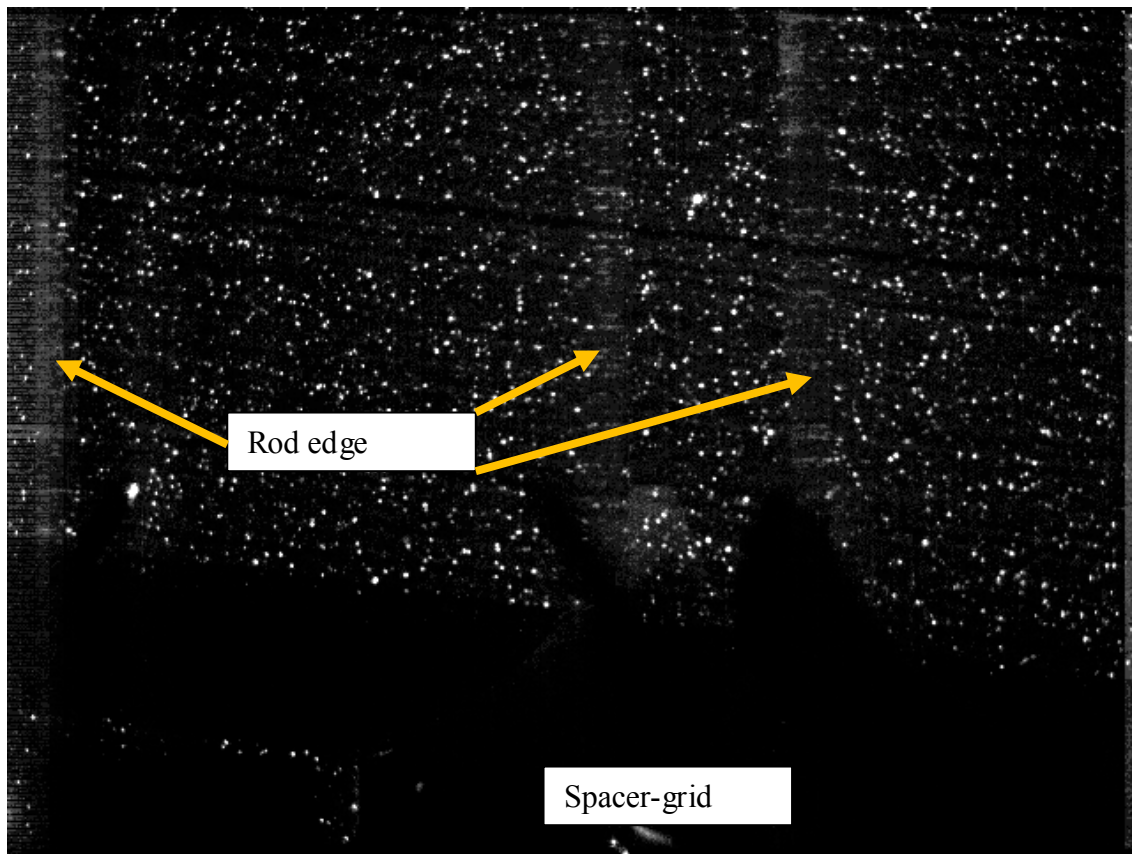


Figure A2. Typical PIV image (sub-channel scale) showing the optical distortion caused by not perfect matching index of refraction between the plastic rods.

The error due to the optical distortion is associated to specific locations in the image and depends on the image itself. Therefore, quantification of the error for each location was calculated using the number of valid vector located at each position as shown in figure C3. The error in the optical distortion zones has increased values of up to 60% of the maximum velocity.

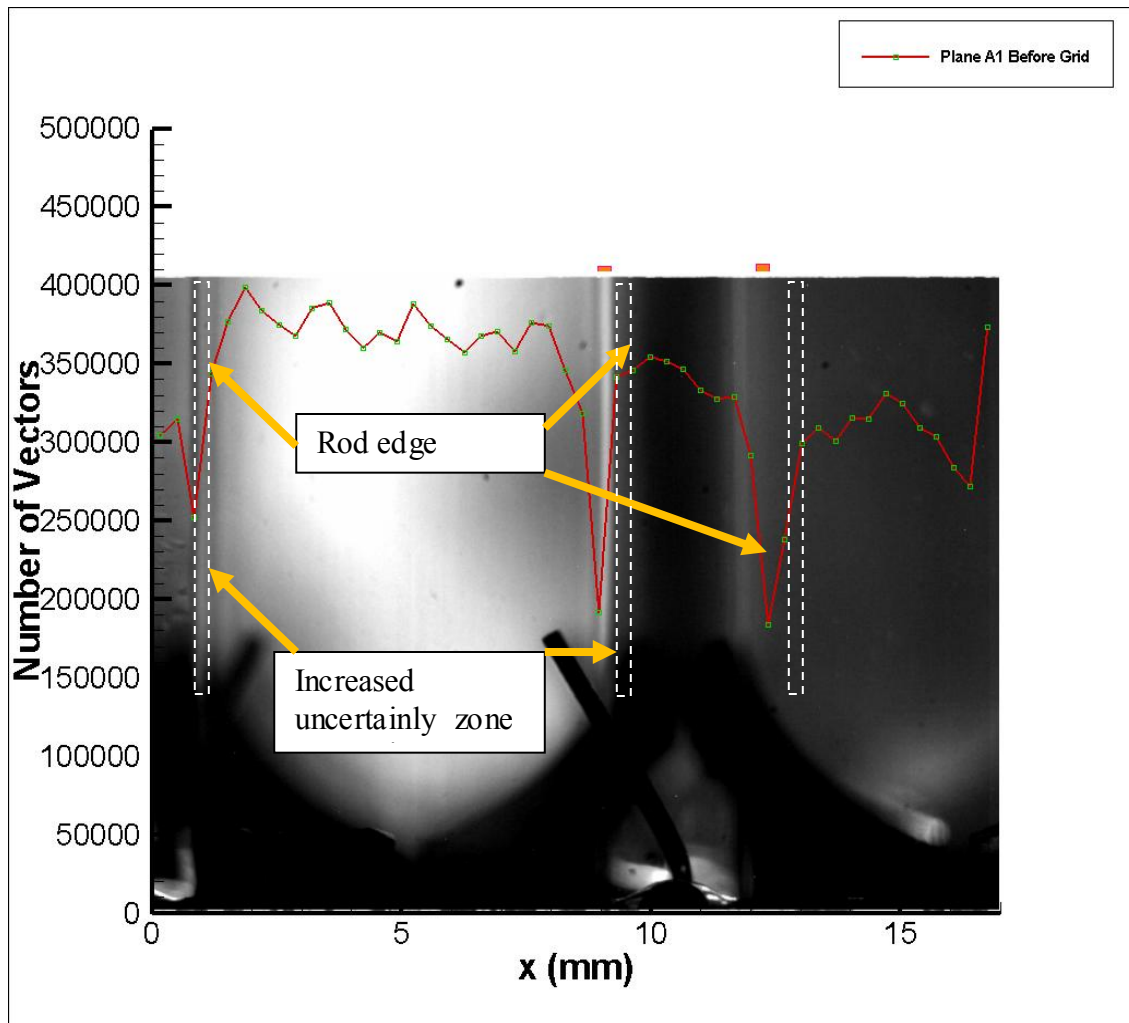


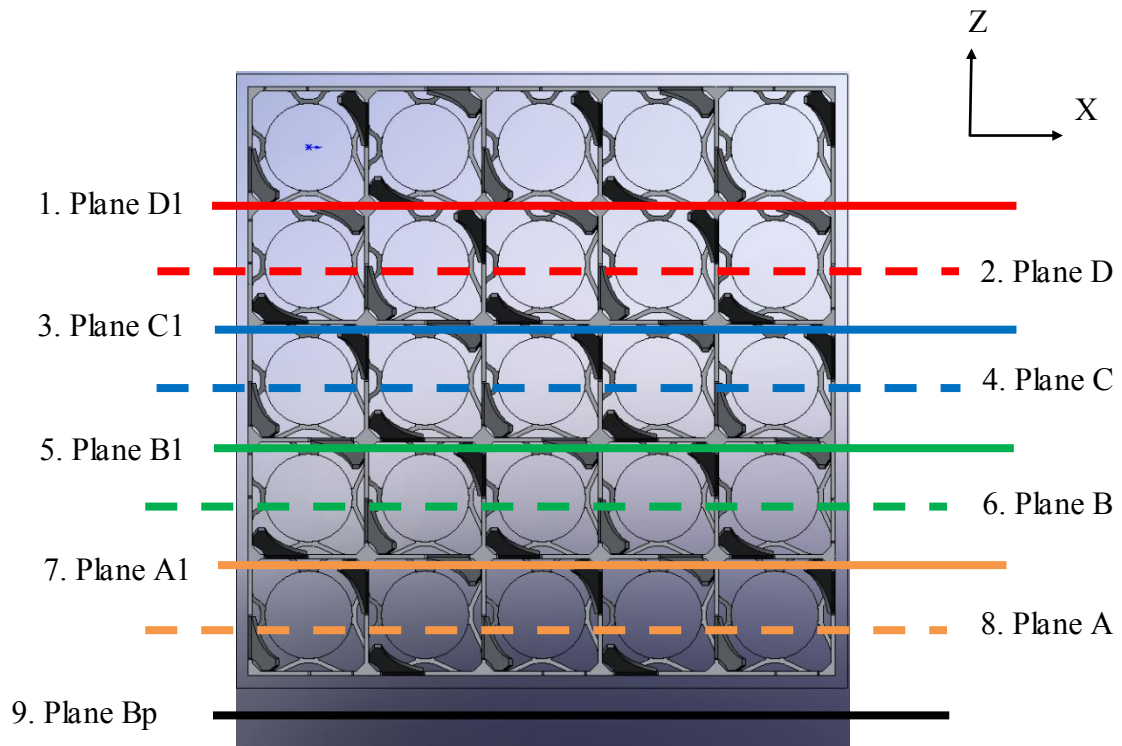
Figure A3. Typical averaged vector number profile (sub-channel scale) showing a decrease in the valid number of vectors found nearby the edge of the rods edge.

The total error due to optical distortion in the velocity measurements was quantified using the valid number of vectors found at each position and the associated error from PIV using the error propagation approach. Since the error is location specific, the results shown in profiles in chapter IV have been corrected by omitting the points falling in the

high uncertainty zones. This procedure was considered necessary to avoid confusion or misinterpretation of results by the reader.

APPENDIX B

This appendix shows the velocity fields for each measured plane using test grid 2 for the inter-channel scale. The measurements were performed under a Reynolds number condition of 16300. The color code represents the magnitude of the streamwise component of the velocity vector (Y-axis direction) or the magnitude of the normal component of the velocity vector (X-axis direction) respectively. The following figure shows the position of each measured plane with respect to the bundle.



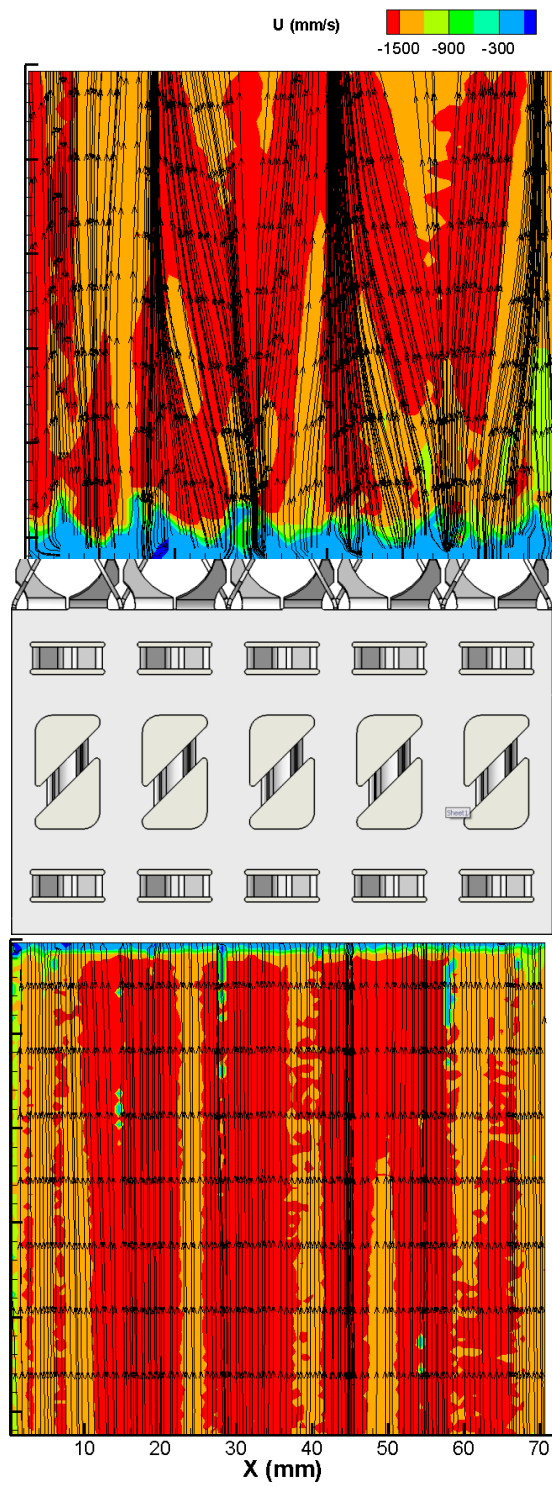


Figure B1. Streamwise average velocity before and after grid. Plane 1. $Re=16,300$

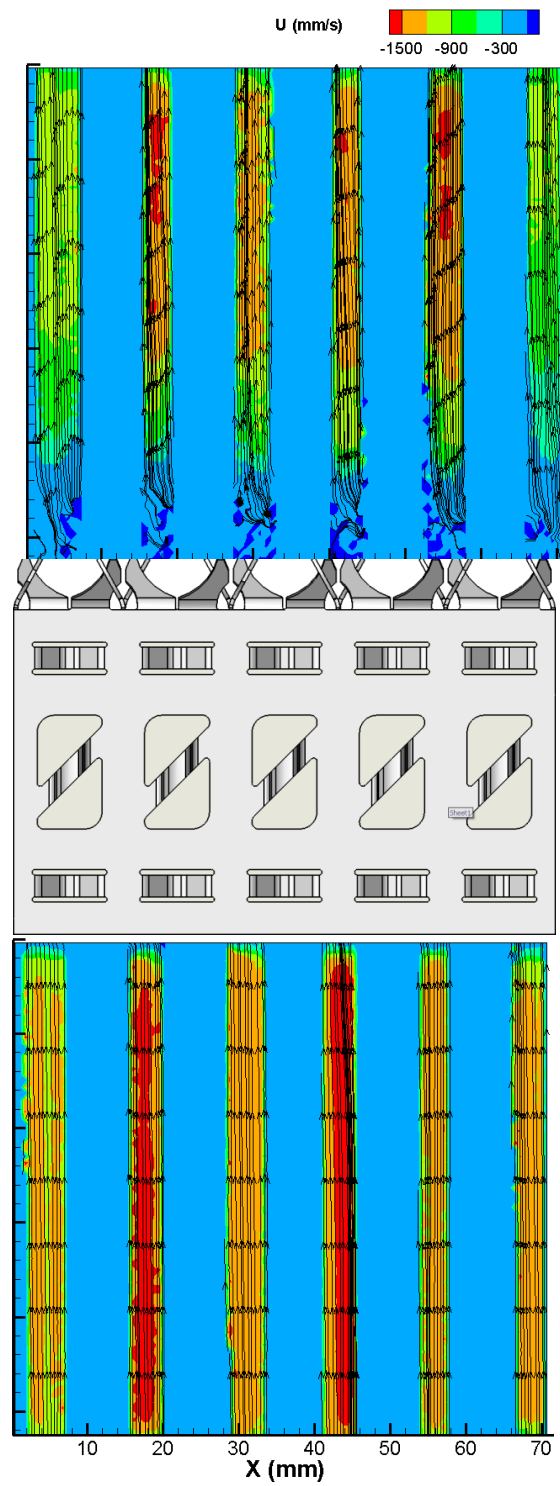


Figure B2. Streamwise average velocity before and after grid. Plane 2. $Re=16,300$

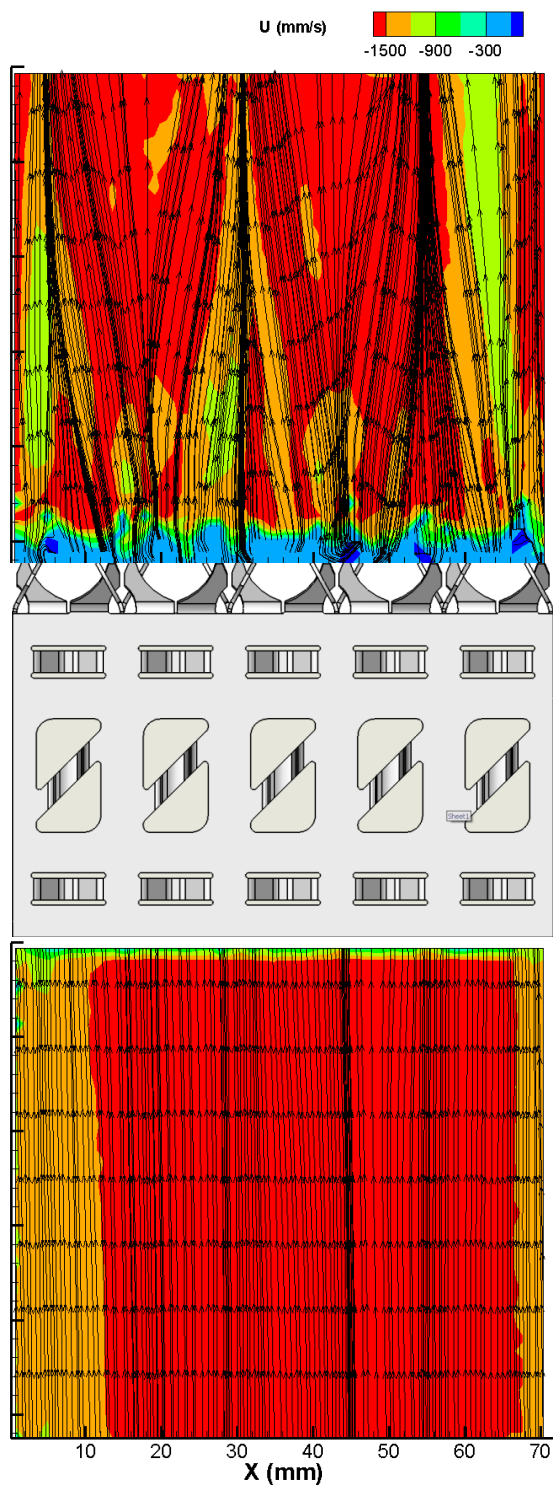


Figure B3. Streamwise average velocity before and after grid. Plane 3. $Re=16,300$

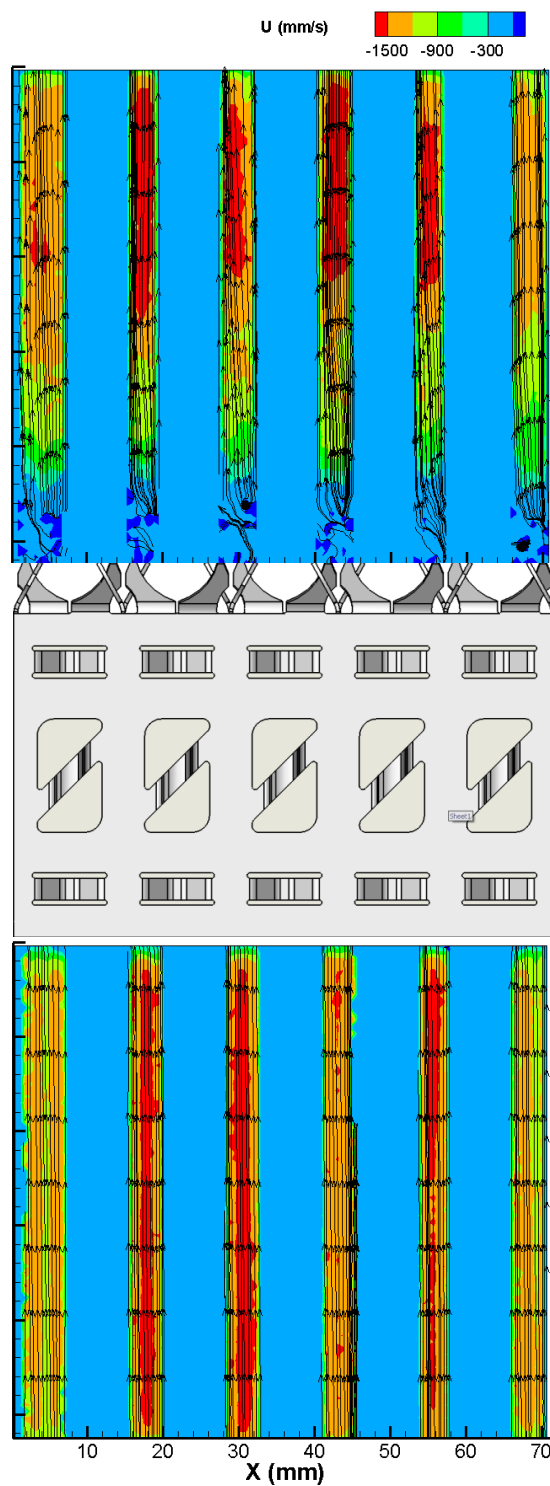


Figure B4. Streamwise average velocity before and after grid. Plane 4. $Re=16,300$

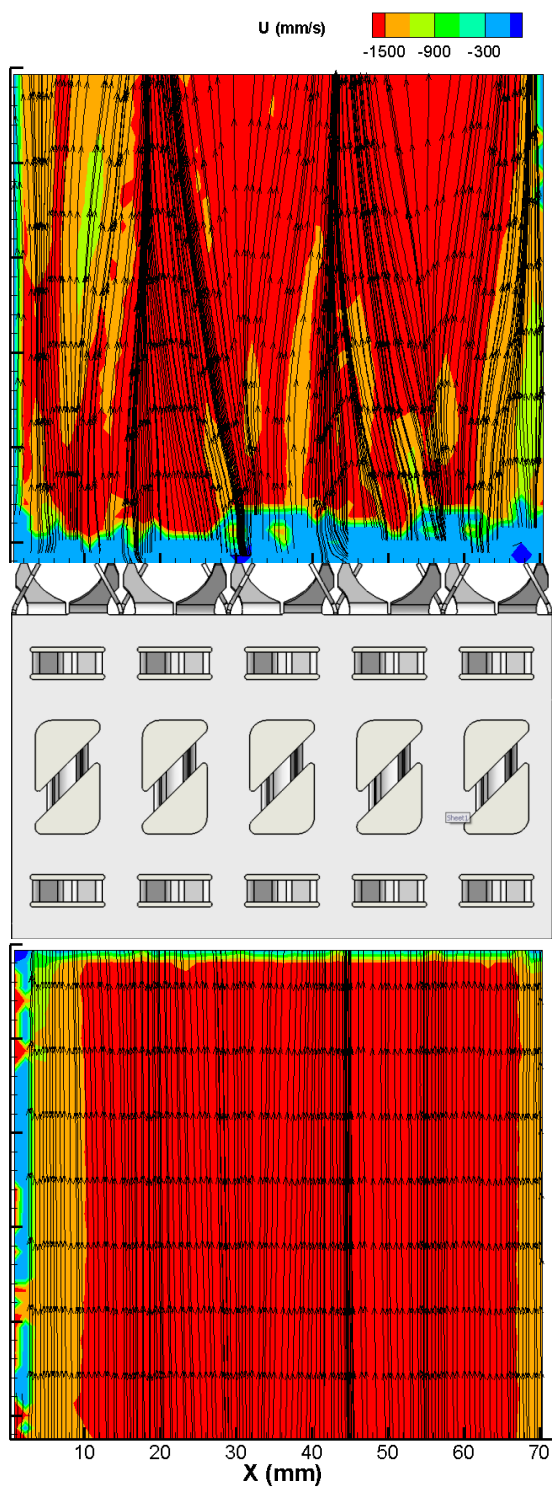


Figure B5. Streamwise average velocity before and after grid. Plane 5. $Re=16,300$

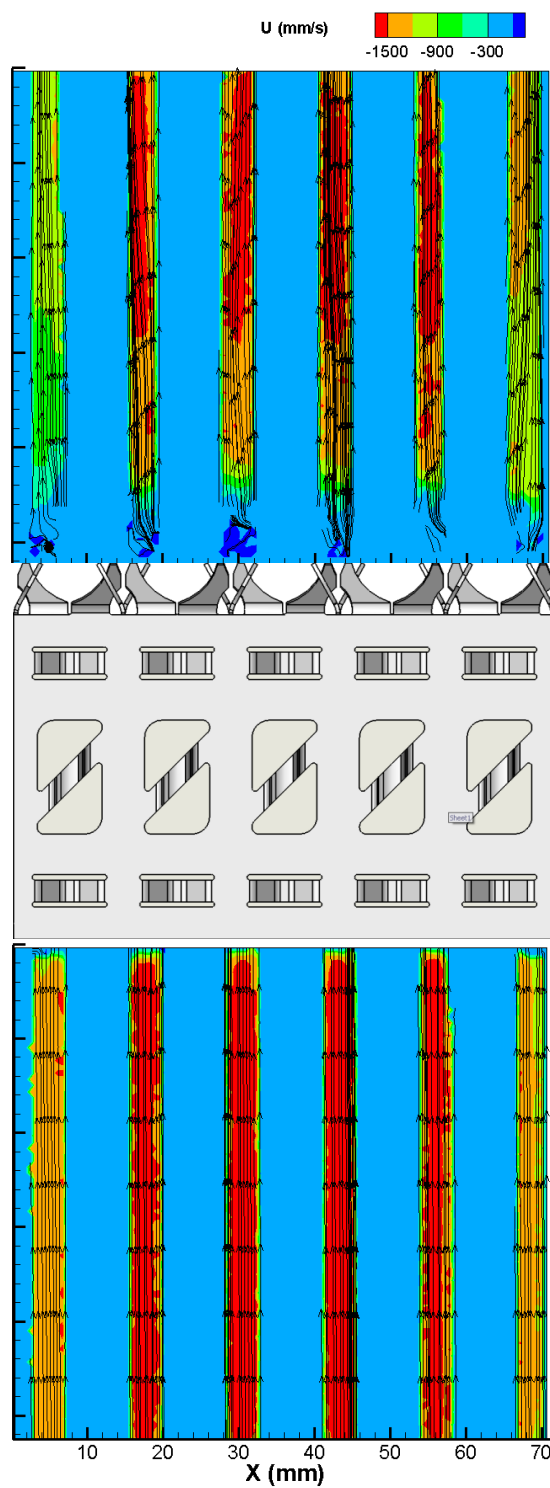


Figure B6. Streamwise average velocity before and after grid. Plane 6. $Re=16,300$

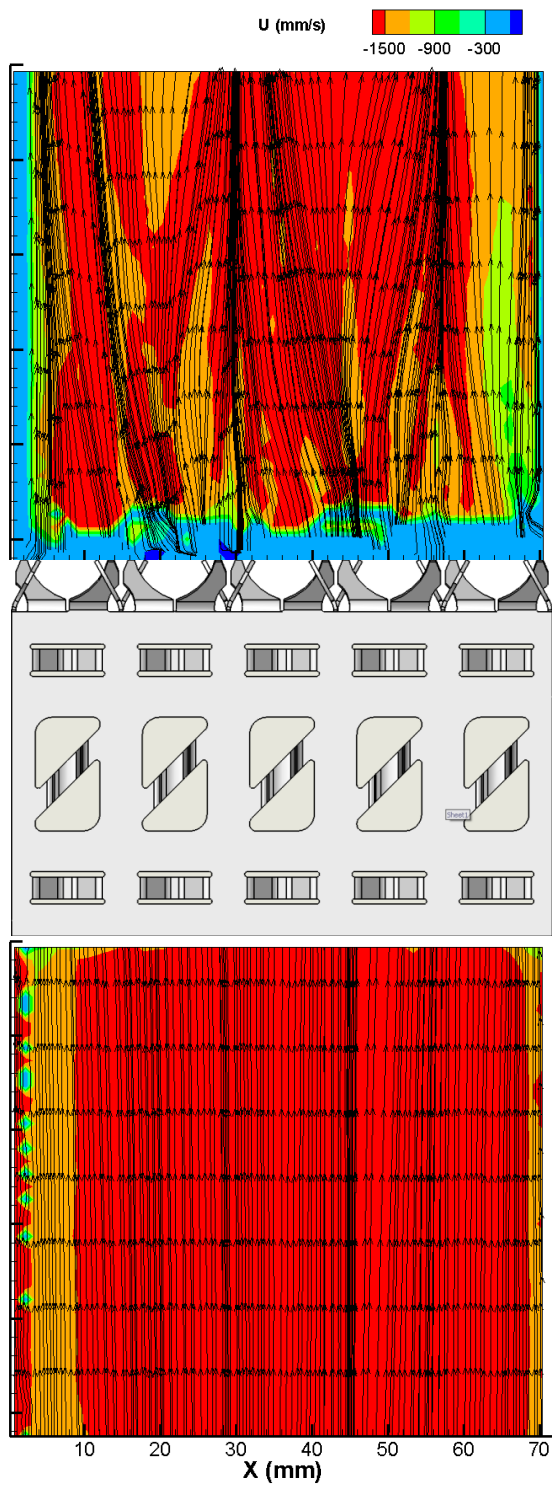


Figure B7. Streamwise average velocity before and after grid. Plane 7. $Re=16,300$

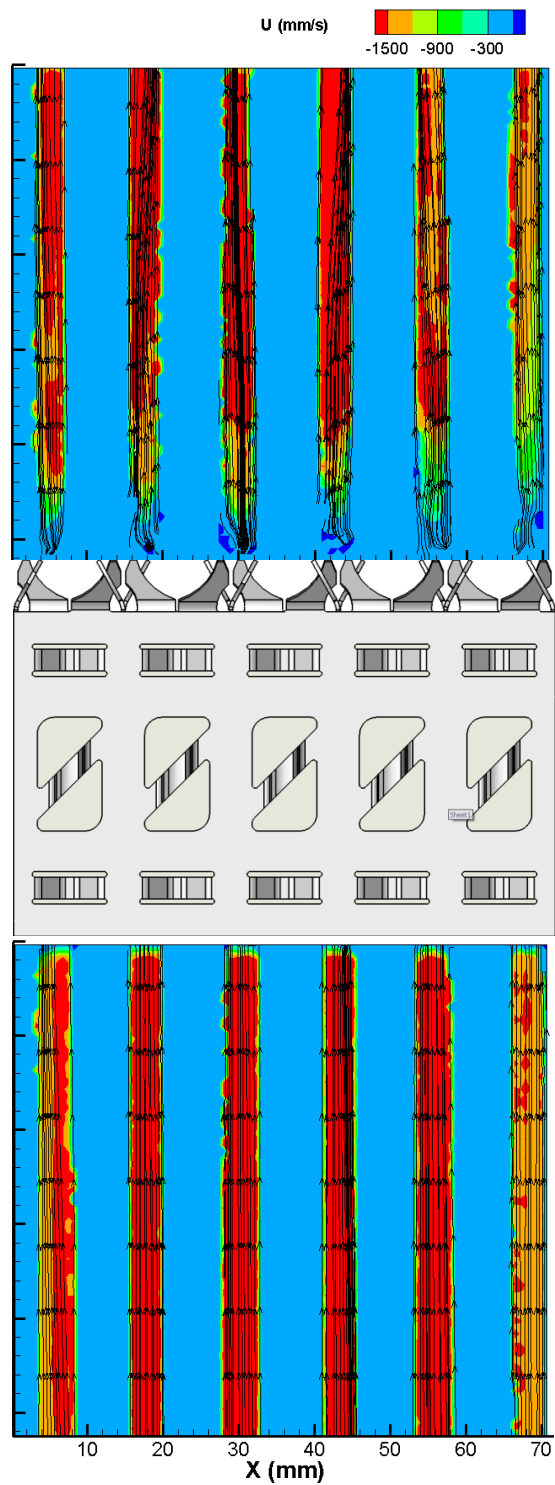


Figure B8. Streamwise average velocity before and after grid. Plane 8. $Re=16,300$

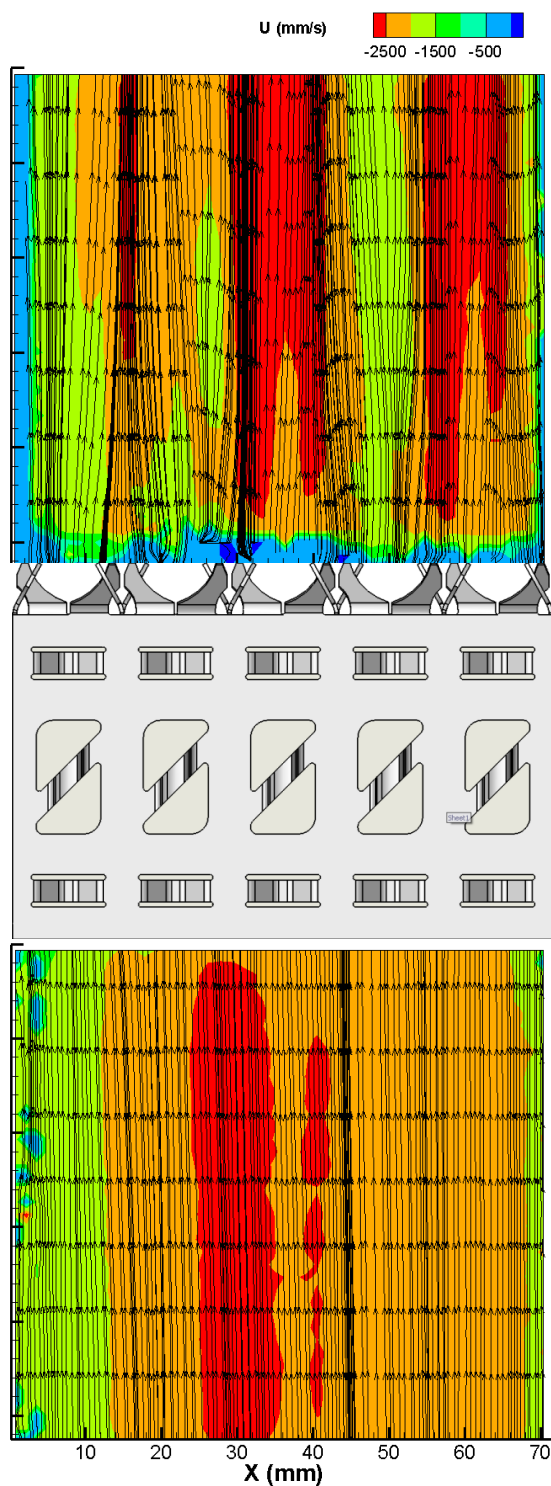


Figure B9. Streamwise average velocity before and after grid. Plane 9. $Re=16,300$

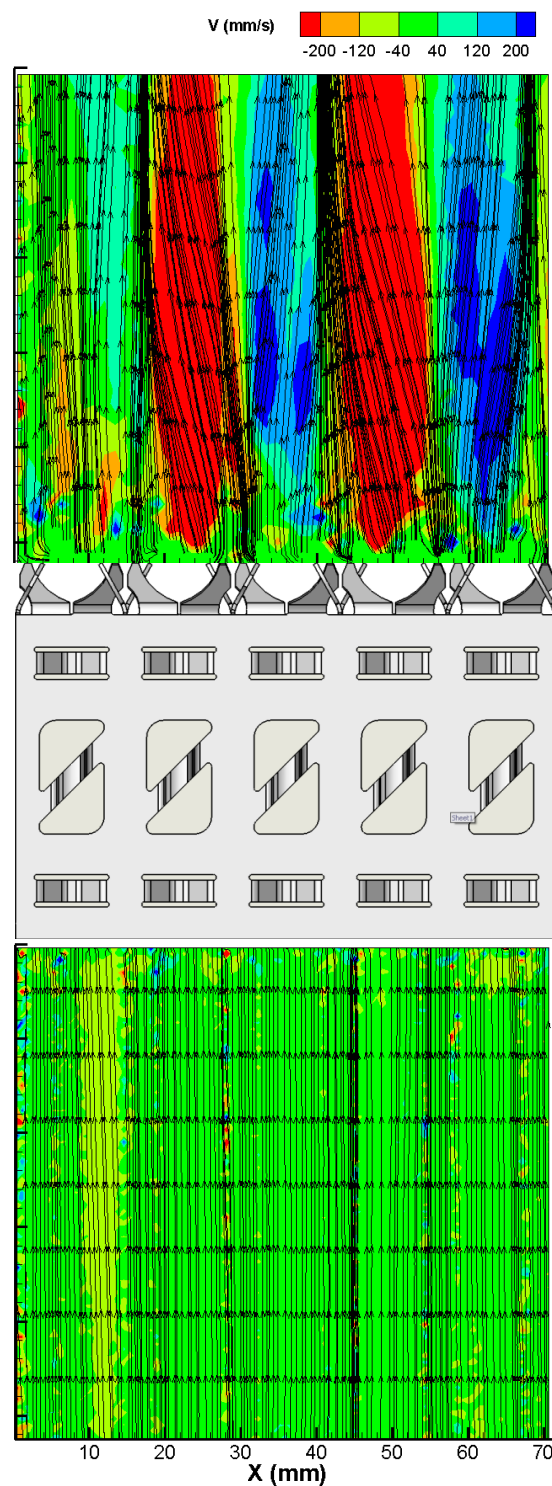


Figure B10. Normal average velocity before and after grid. Plane 1. $Re=16,300$

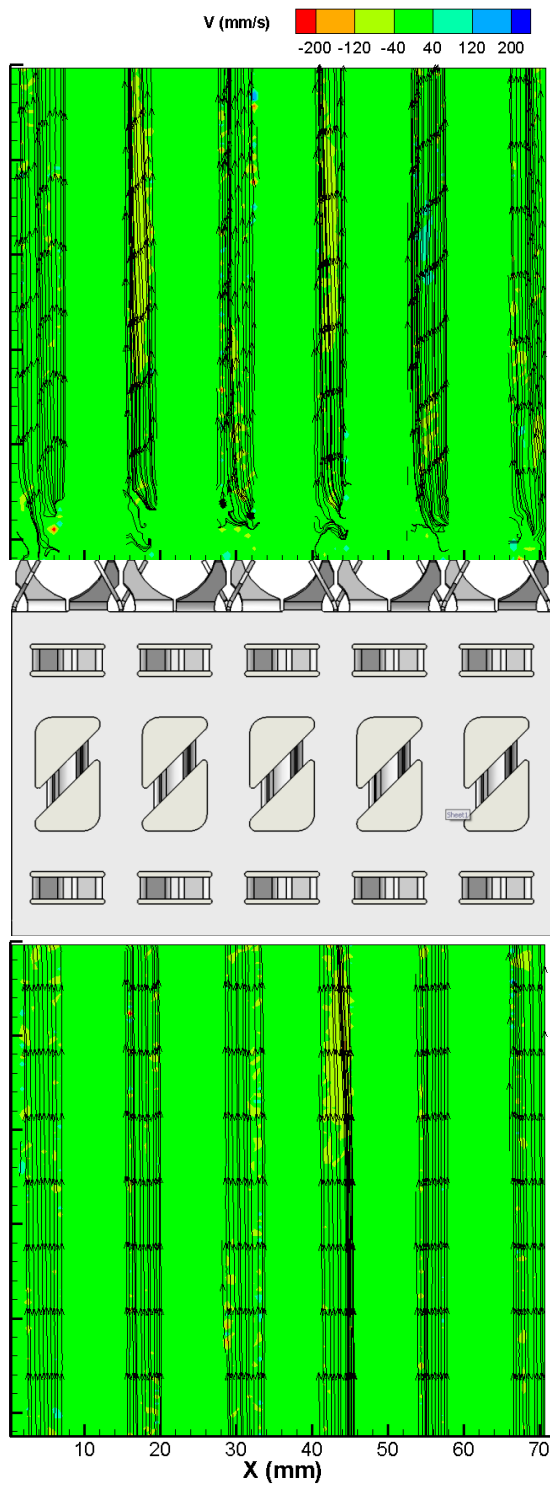


Figure B11. Normal average velocity before and after grid. Plane 2. $Re=16,300$

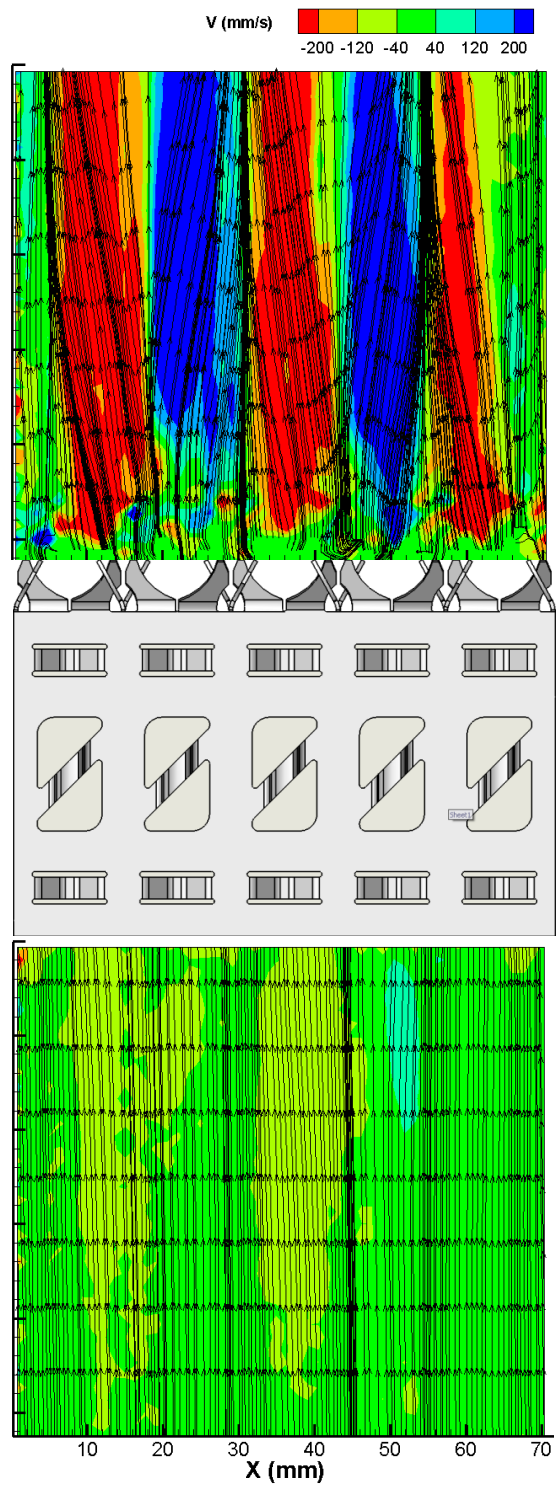


Figure B12. Normal average velocity before and after grid. Plane 3. $Re=16,300$

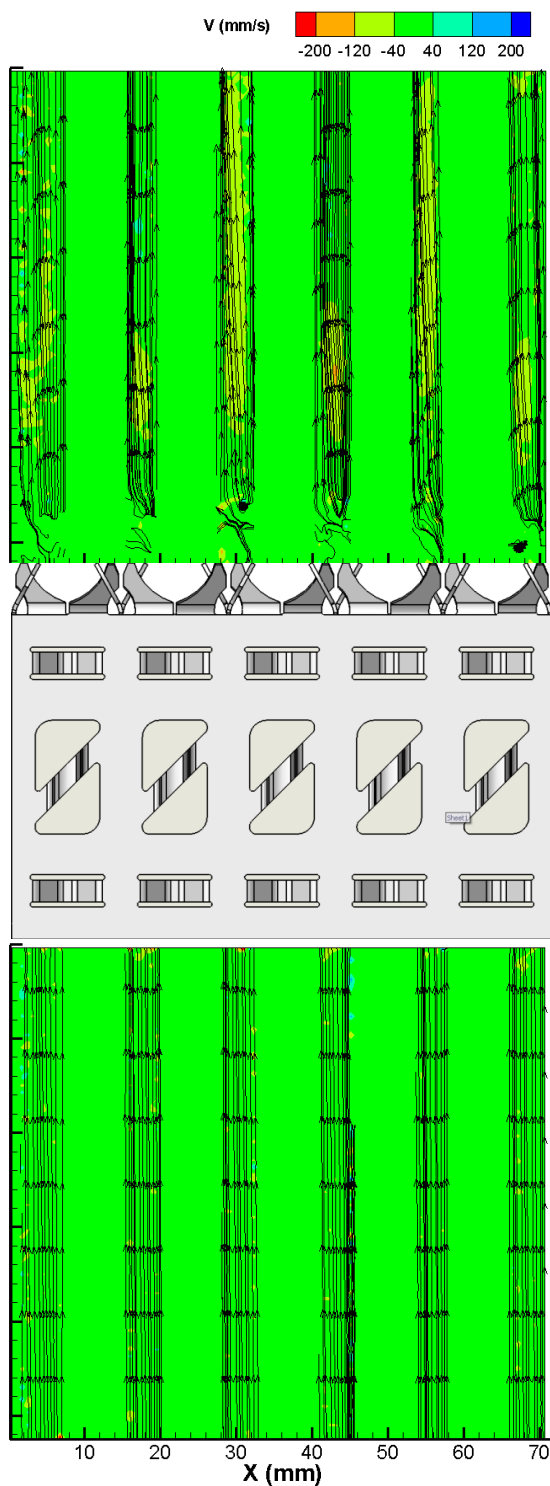


Figure B13. Normal average velocity before and after grid. Plane 4. $Re=16,300$

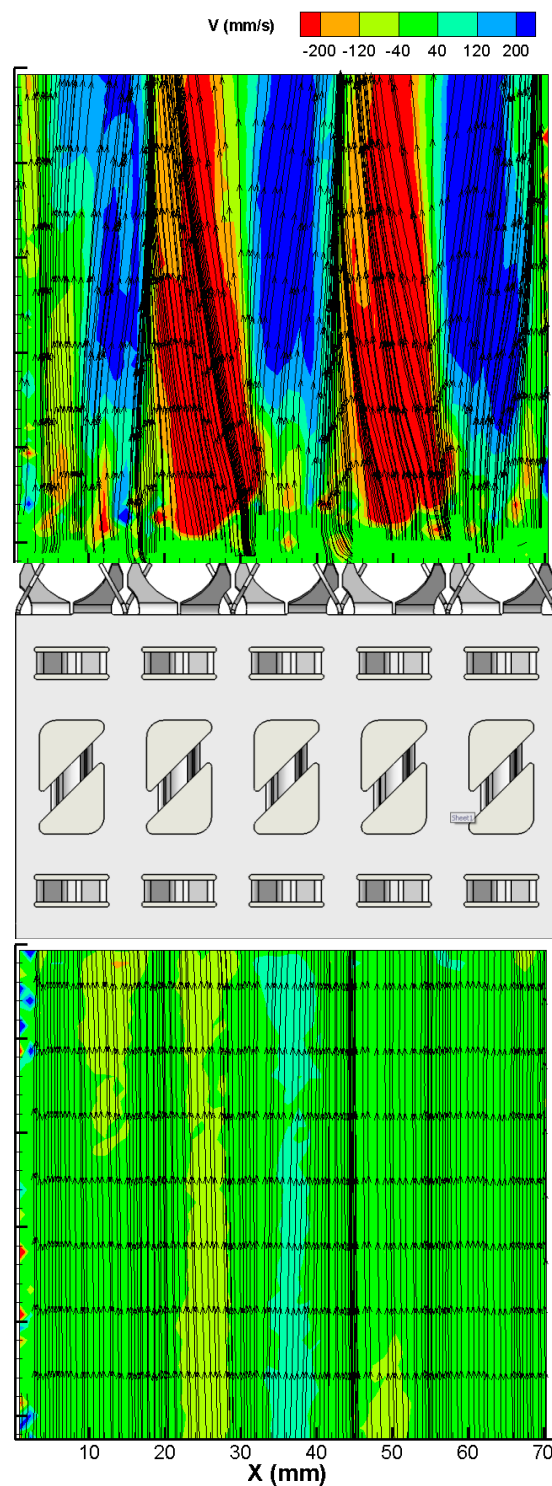


Figure B14. Normal average velocity before and after grid. Plane 5. $Re=16,300$

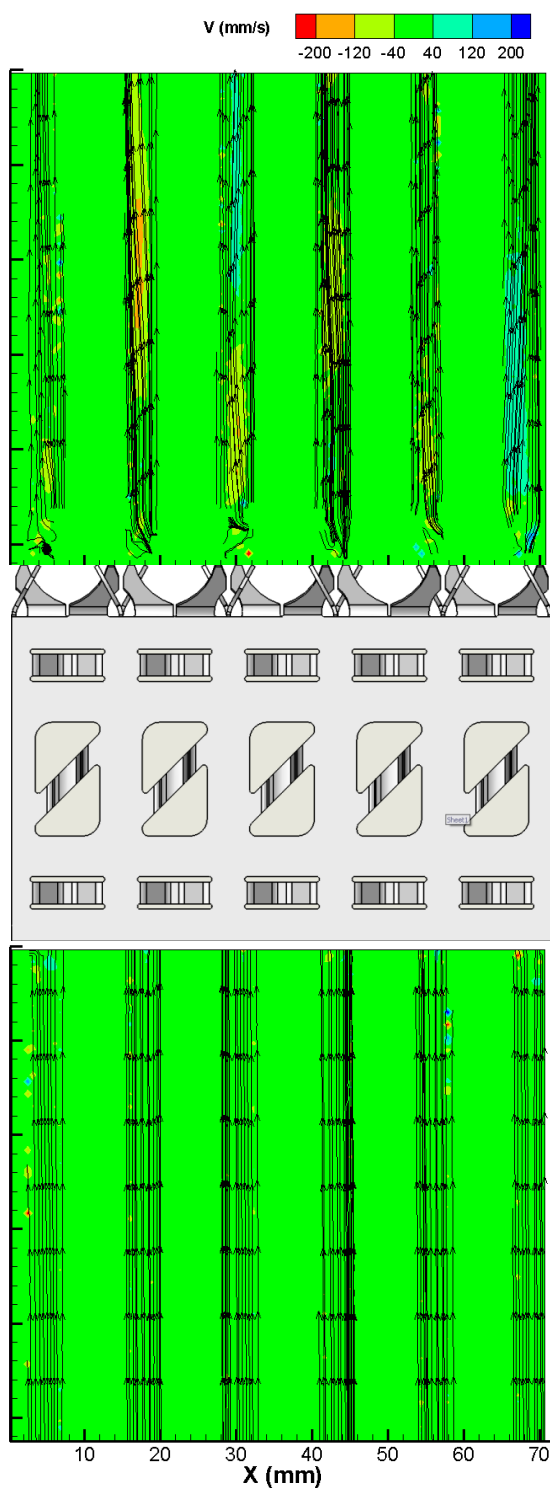


Figure B15. Normal average velocity before and after grid. Plane 6. $Re=16,300$

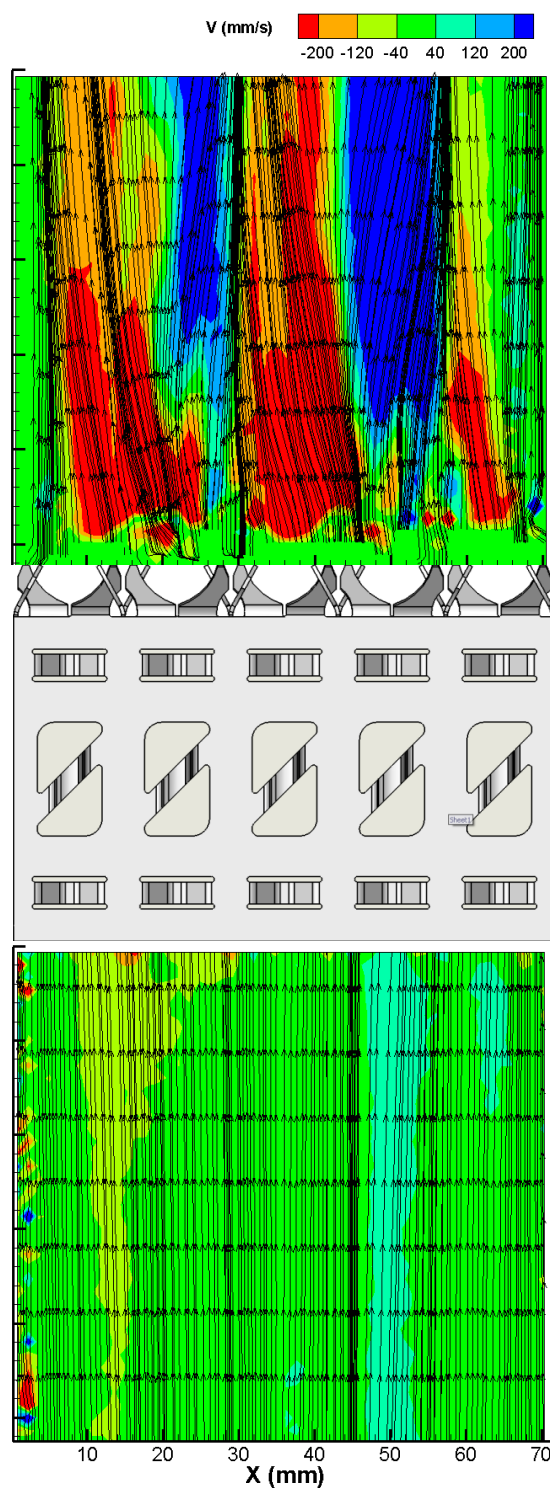


Figure B16. Normal average velocity before and after grid. Plane 7. $Re=16,300$

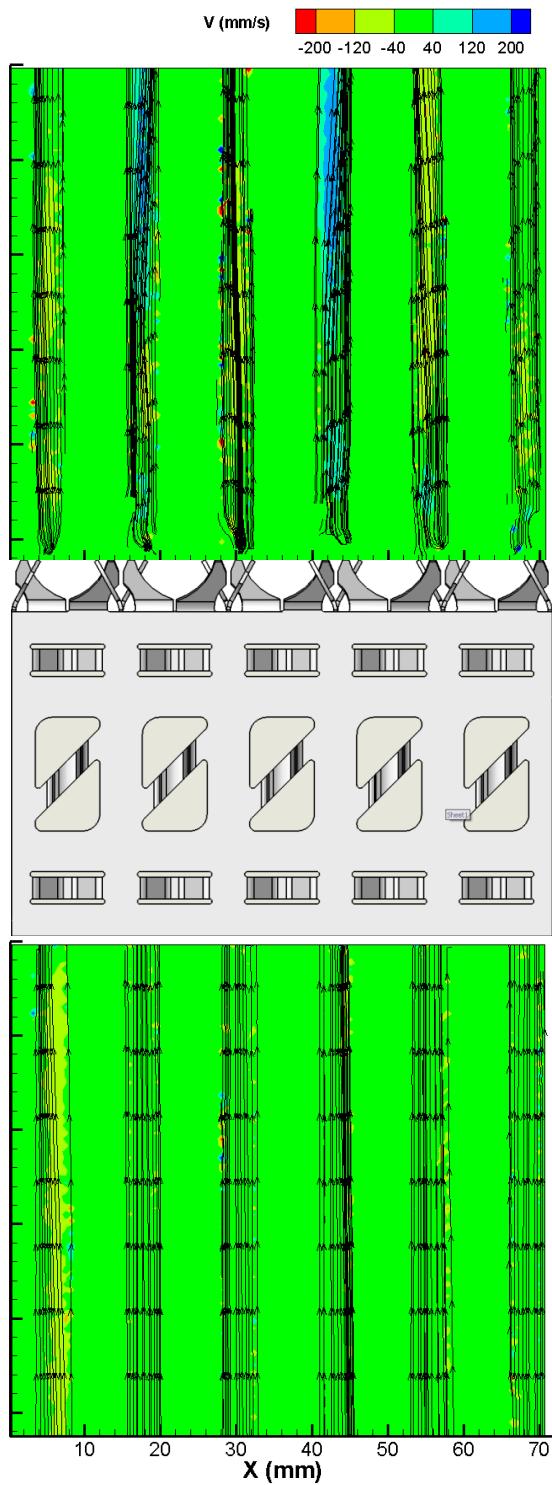


Figure B17. Normal average velocity before and after grid. Plane 8. $Re=16,300$

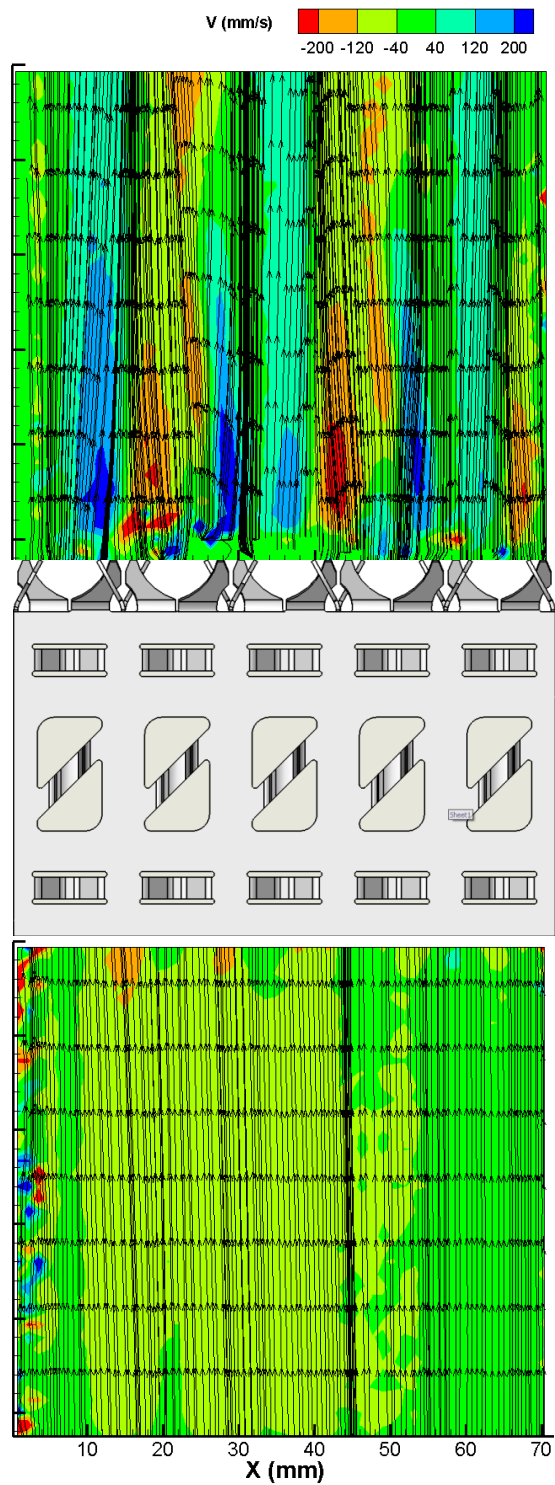
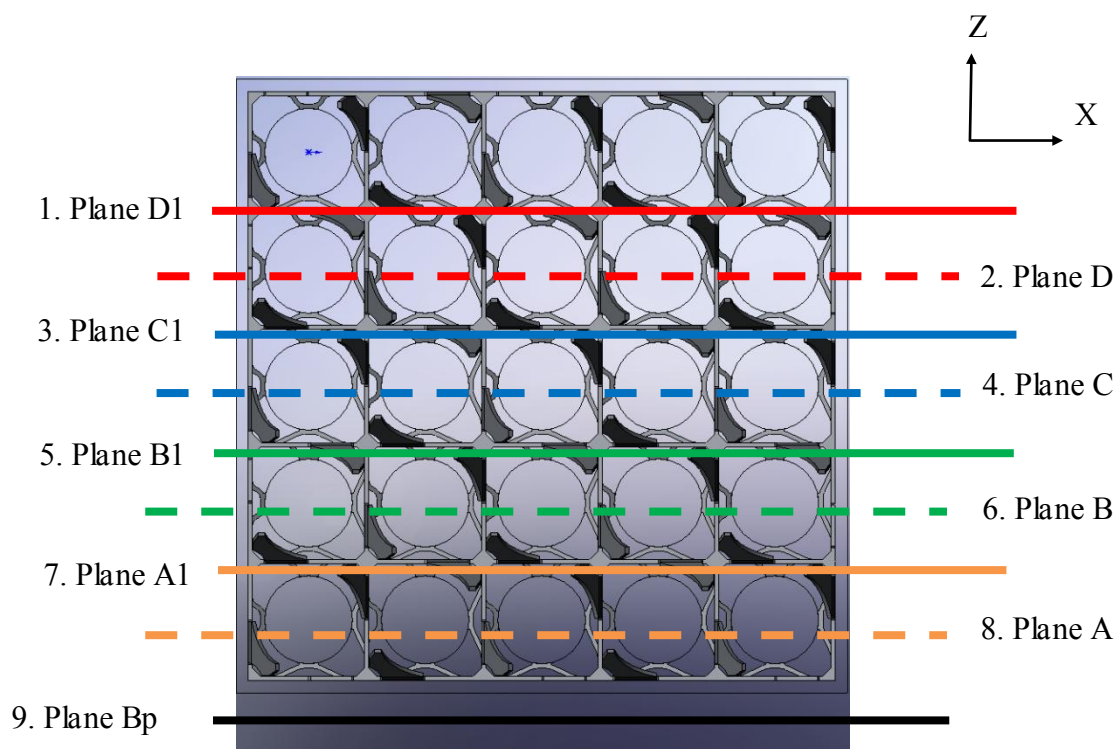


Figure B18. Normal average velocity before and after grid. Plane 9. $Re=16,300$

APPENDIX C

This appendix shows the velocity fields for each measured plane using test grid 2 for the sub-channel scale. The measurements were performed under a Reynolds number condition of 16300. The color code represents the magnitude of the streamwise component of the velocity vector (Y-axis direction) or the magnitude of the normal component of the velocity vector (X-axis direction) respectively. The following figure shows the position of each measured plane with respect to the bundle.



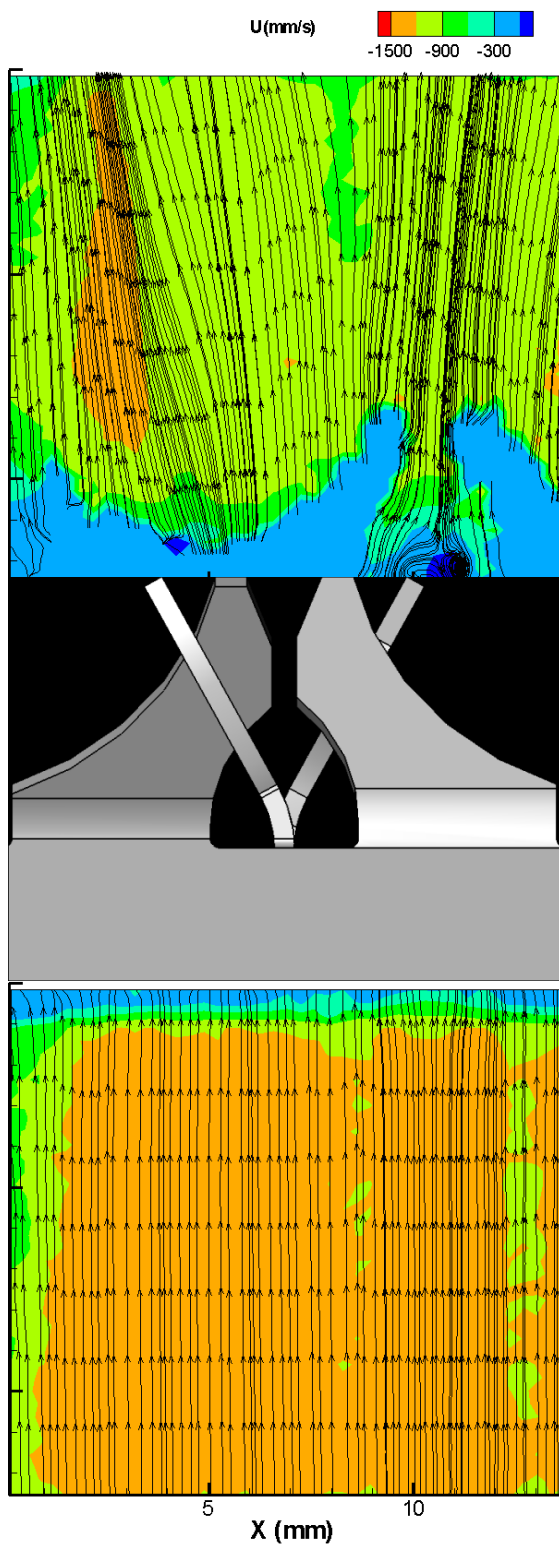


Figure C1. Streamwise average velocity before and after grid. Plane 1. $Re=16,300$

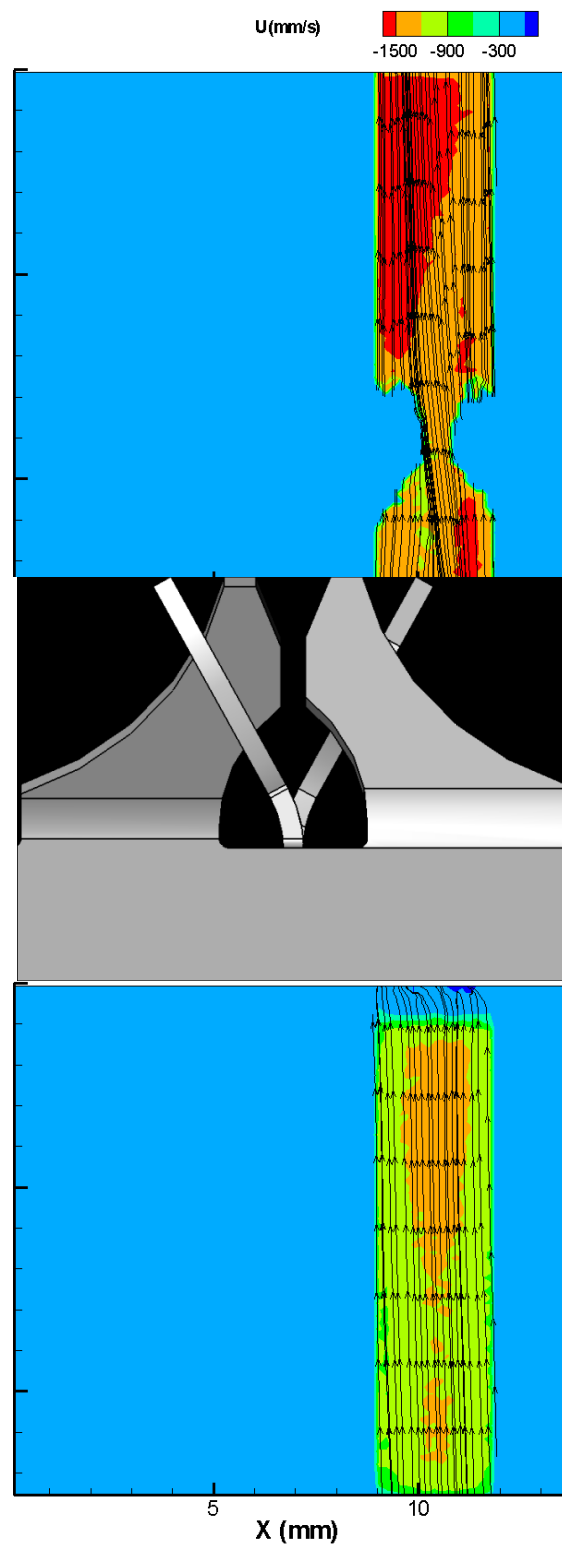


Figure C2. Streamwise average velocity before and after grid. Plane 2. $Re=16,300$

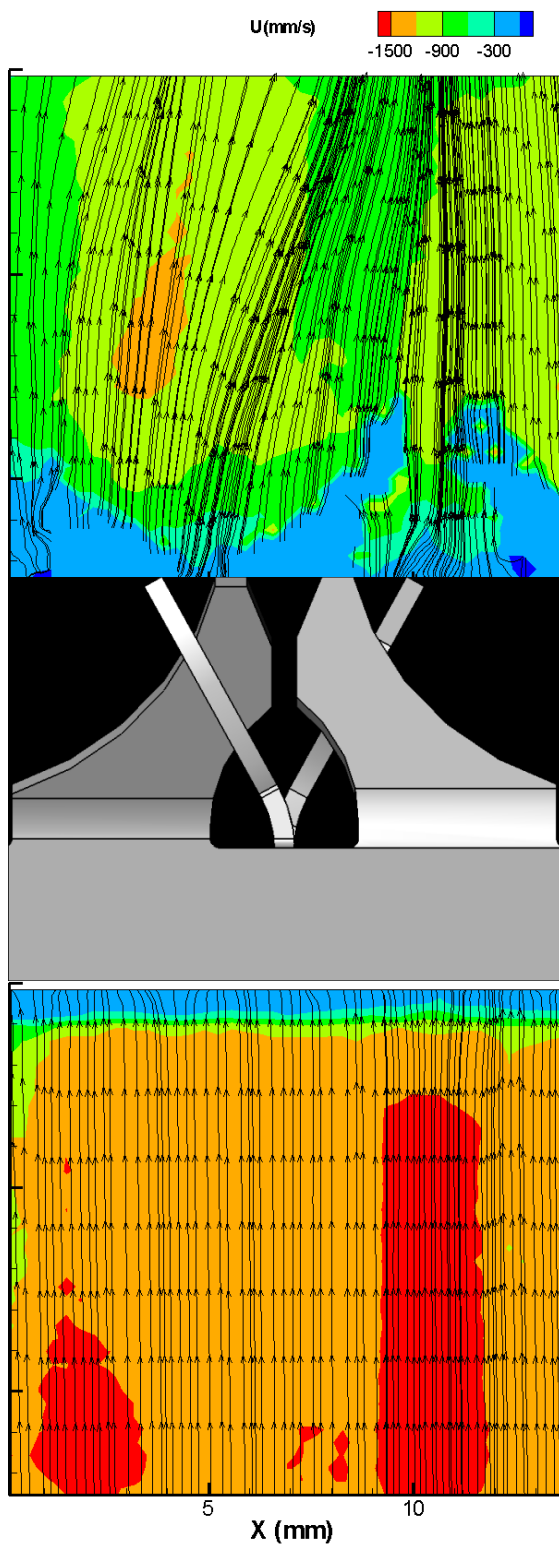


Figure C3. Streamwise average velocity before and after grid. Plane 3. $Re=16,300$

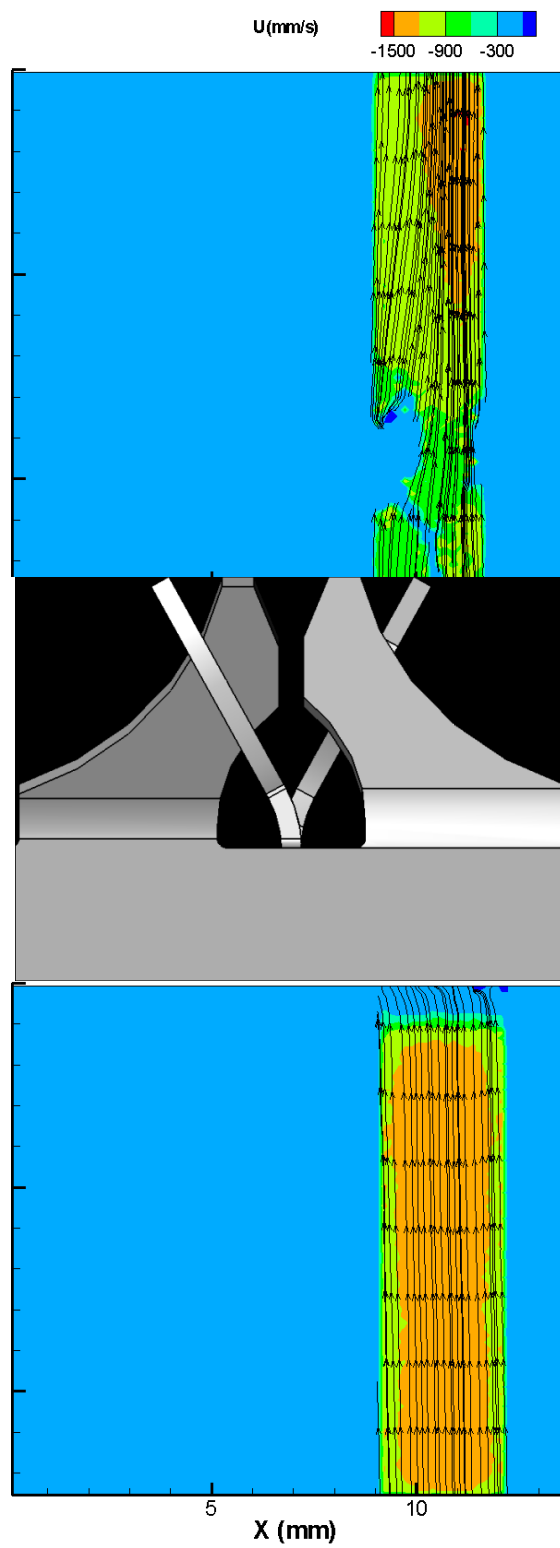


Figure C4. Streamwise average velocity before and after grid. Plane 4. $Re=16,300$

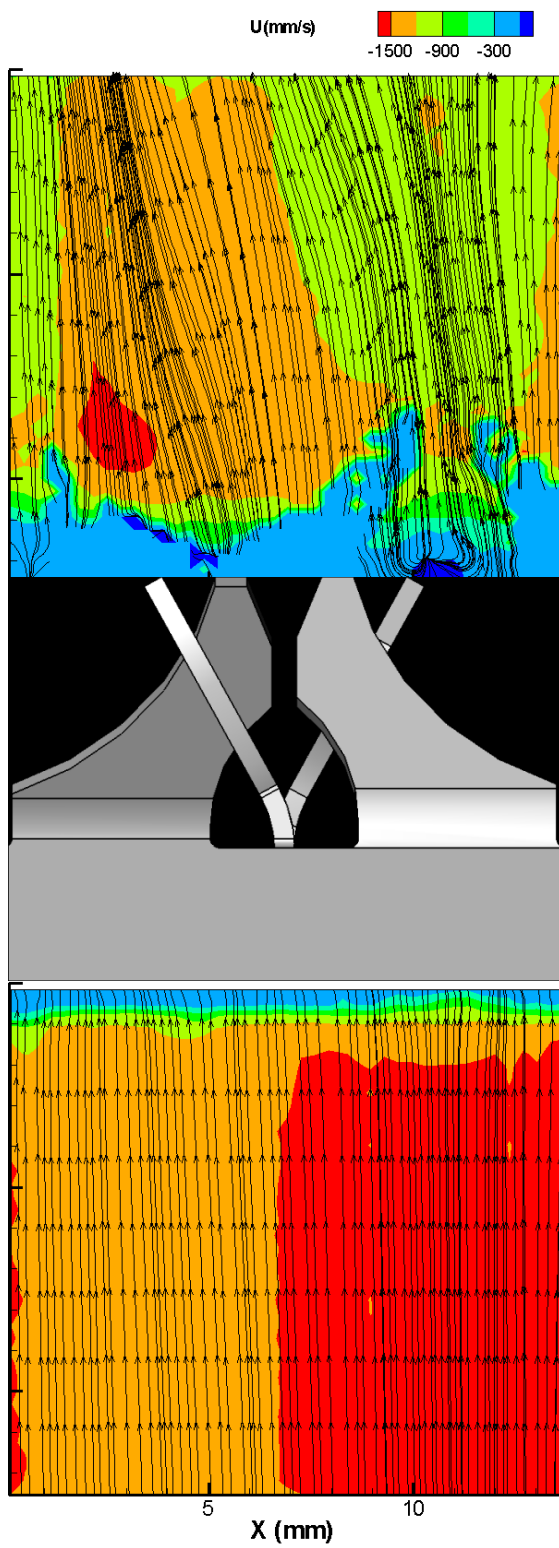


Figure C5. Streamwise average velocity before and after grid. Plane 5. $Re=16,300$

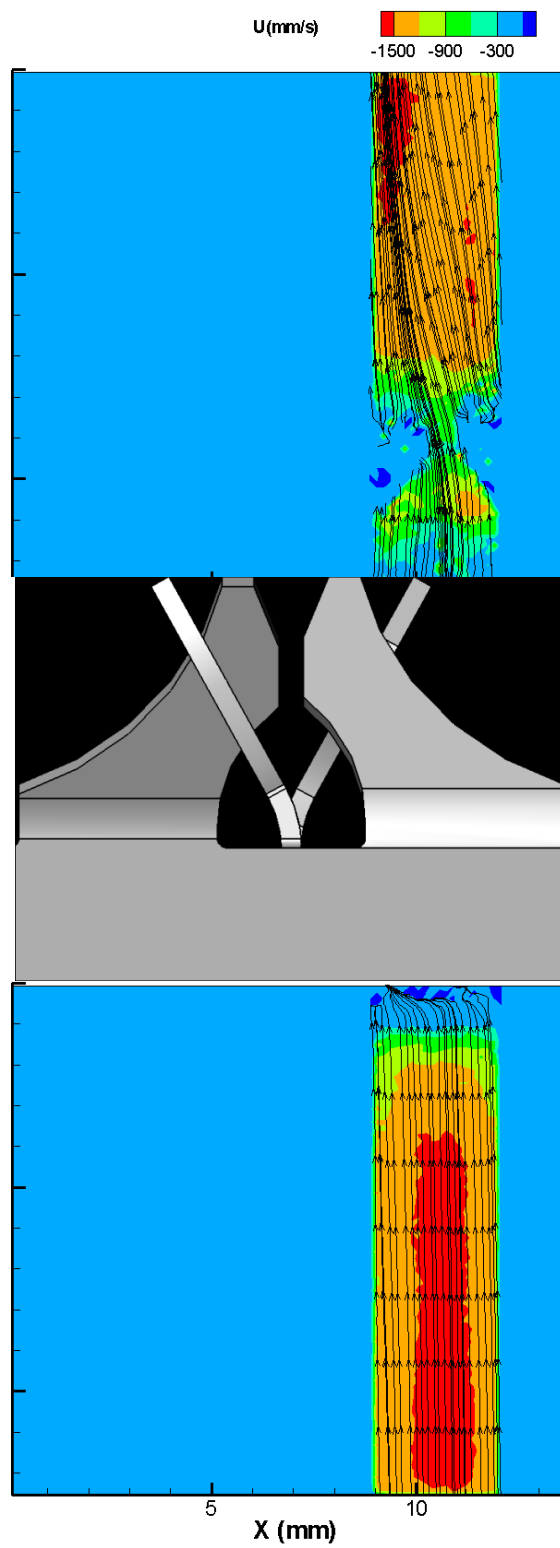


Figure C6. Streamwise average velocity before and after grid. Plane 6. $Re=16,300$

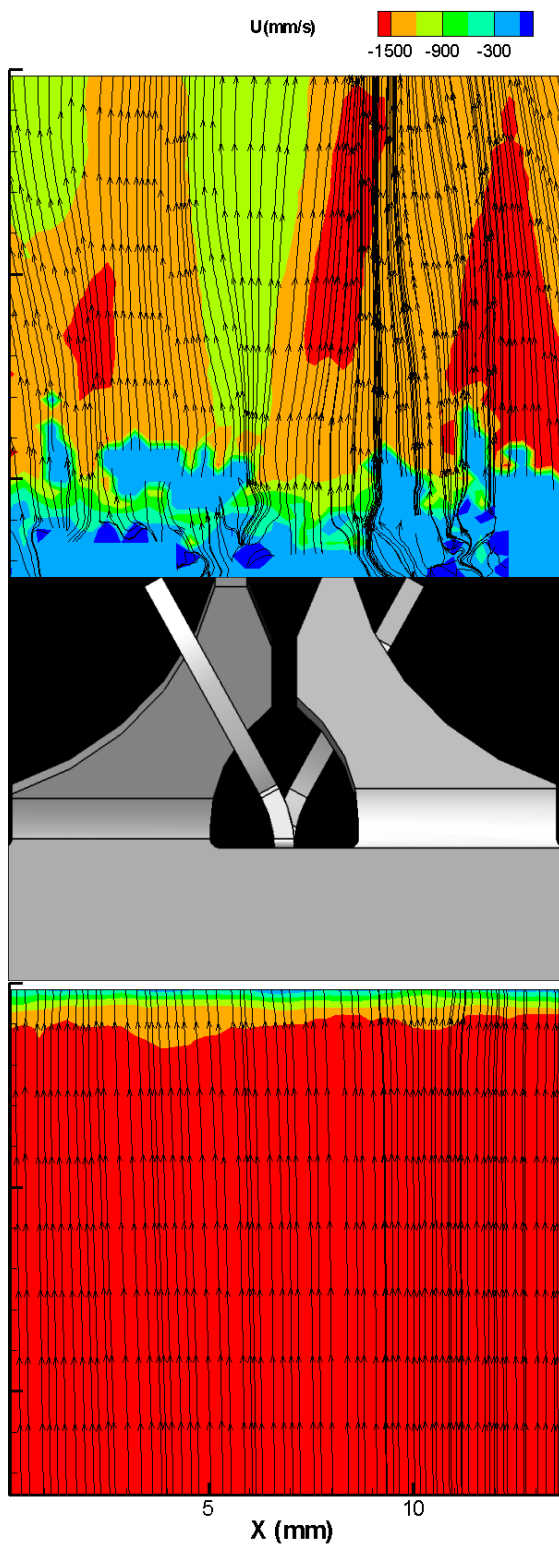


Figure C7. Streamwise average velocity before and after grid. Plane 7. $Re=16,300$

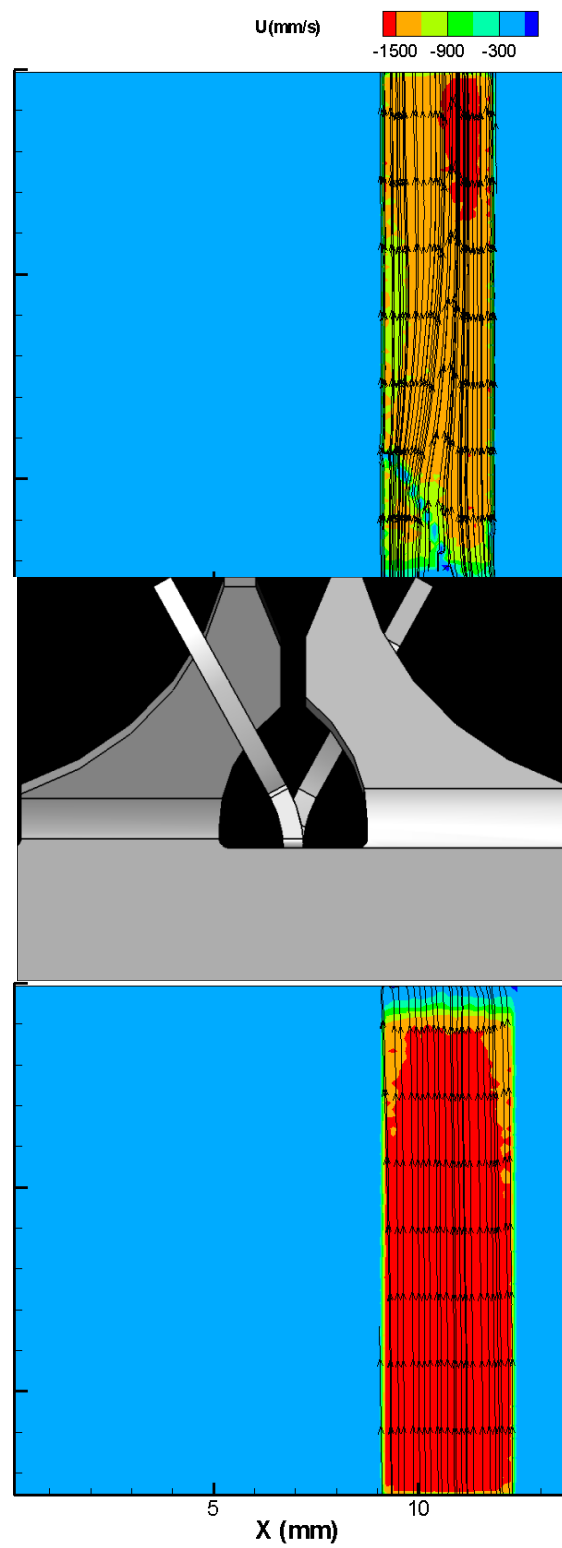


Figure C8. Streamwise average velocity before and after grid. Plane 8. $Re=16,300$

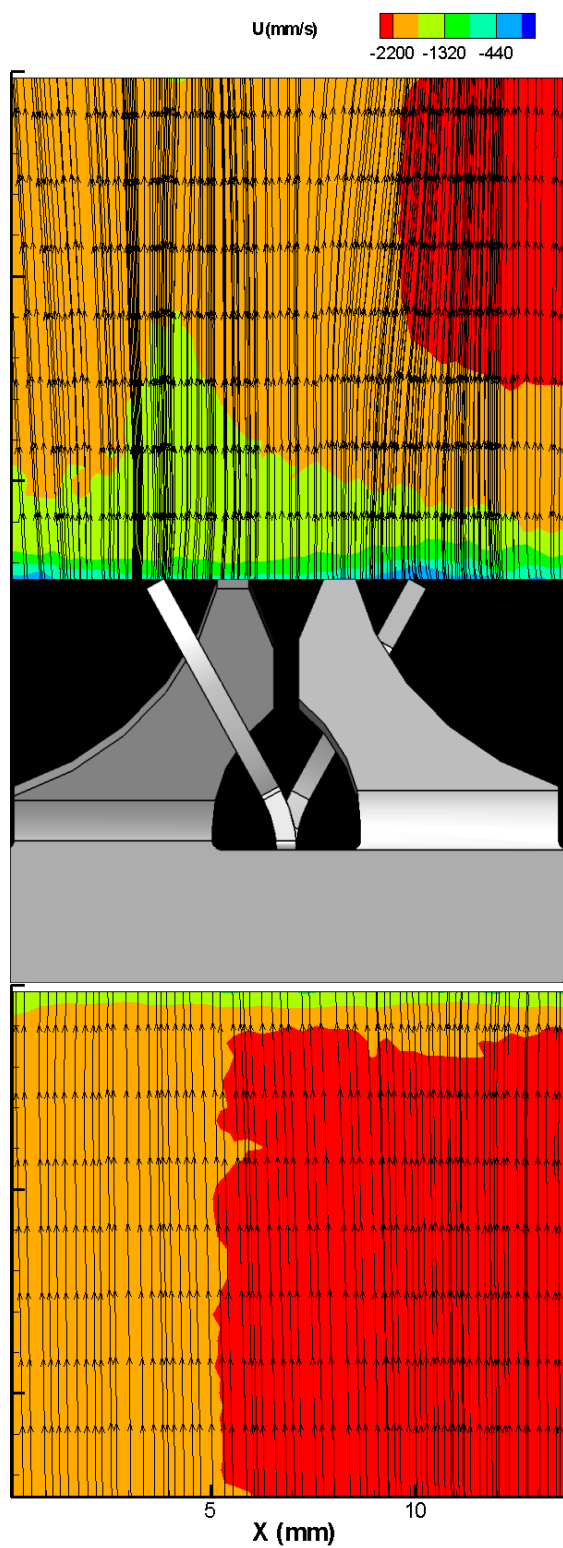


Figure C9. Streamwise average velocity before and after grid. Plane 9. $Re=16,300$

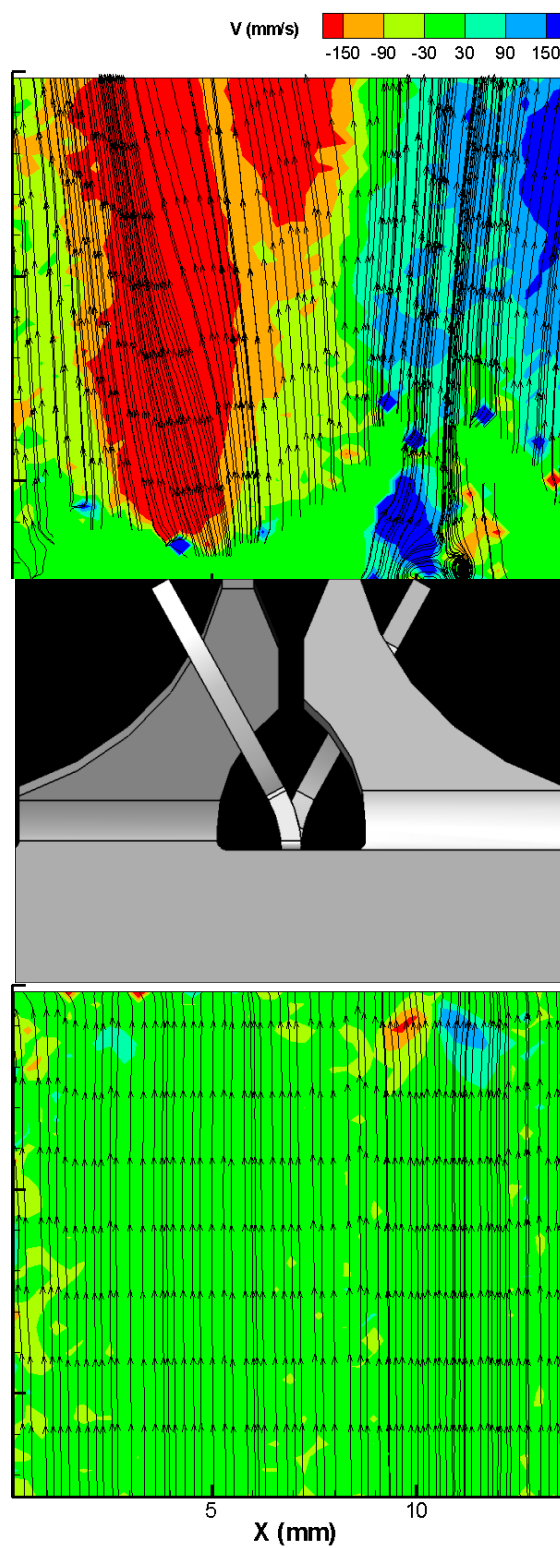


Figure C10. Normal average velocity before and after grid. Plane 1. $Re=16,300$

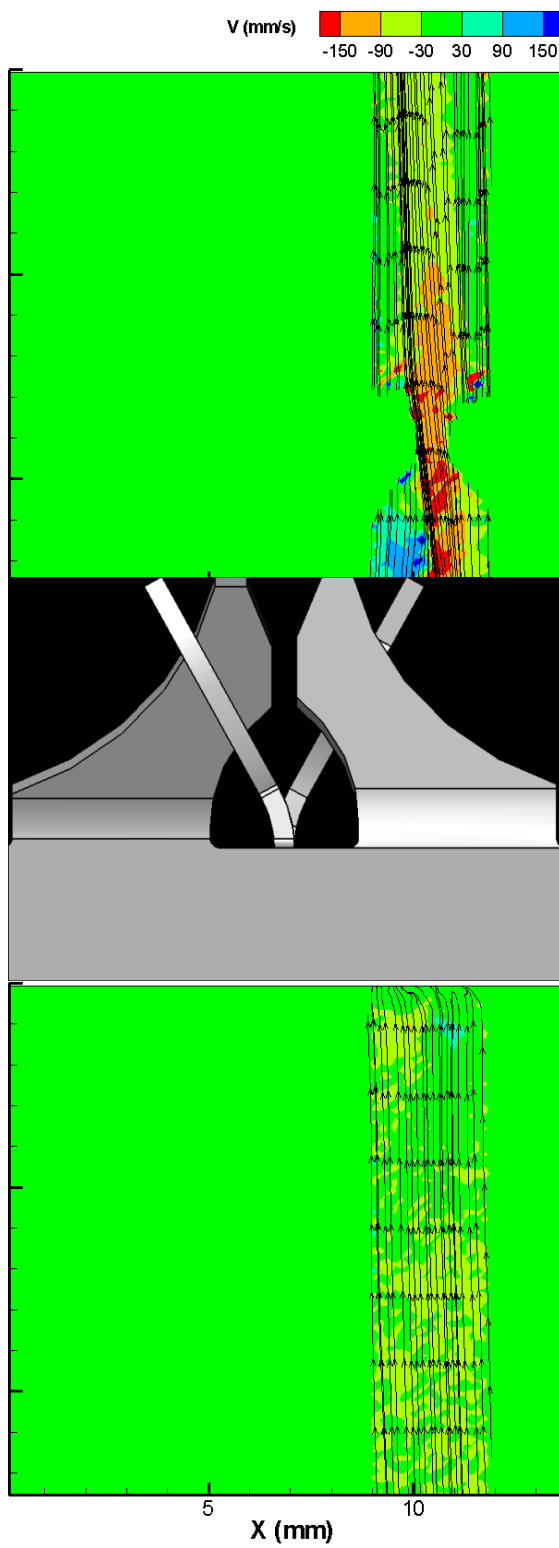


Figure C11. Normal average velocity before and after grid. Plane 2. $Re=16,300$

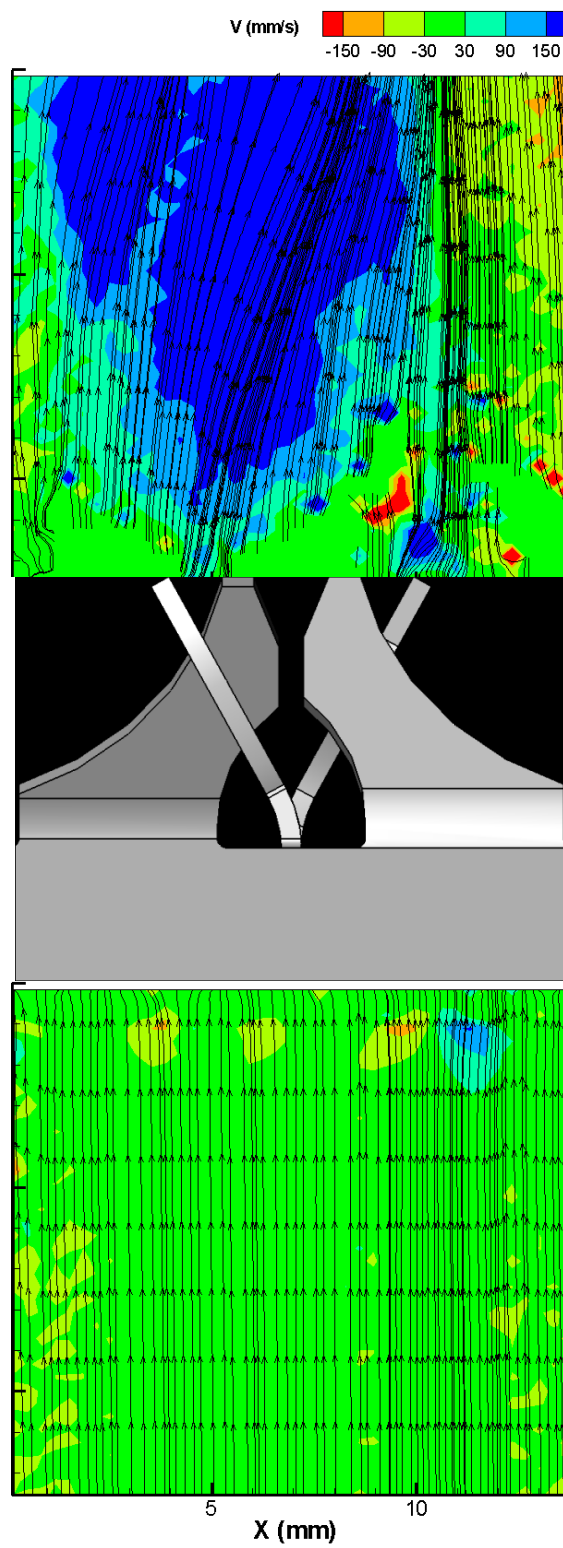


Figure C12. Normal average velocity before and after grid. Plane 3. $Re=16,300$

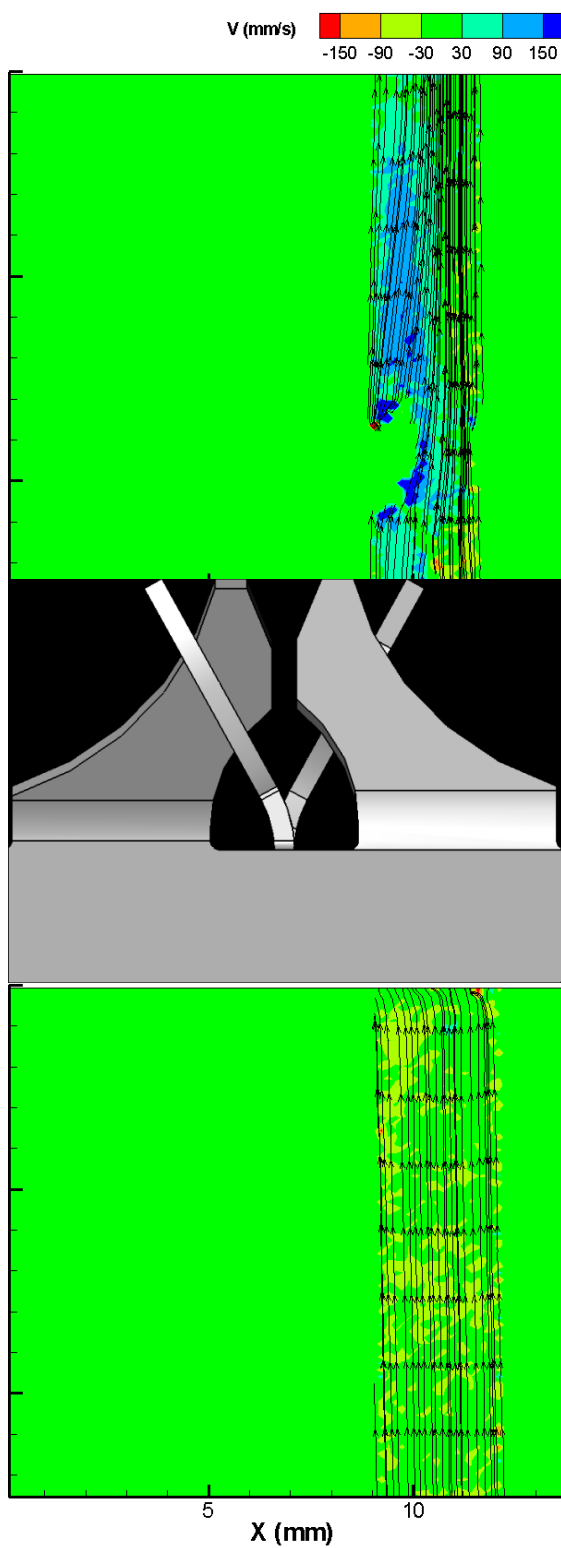


Figure C13. Normal average velocity before and after grid. Plane 4. $Re=16,300$

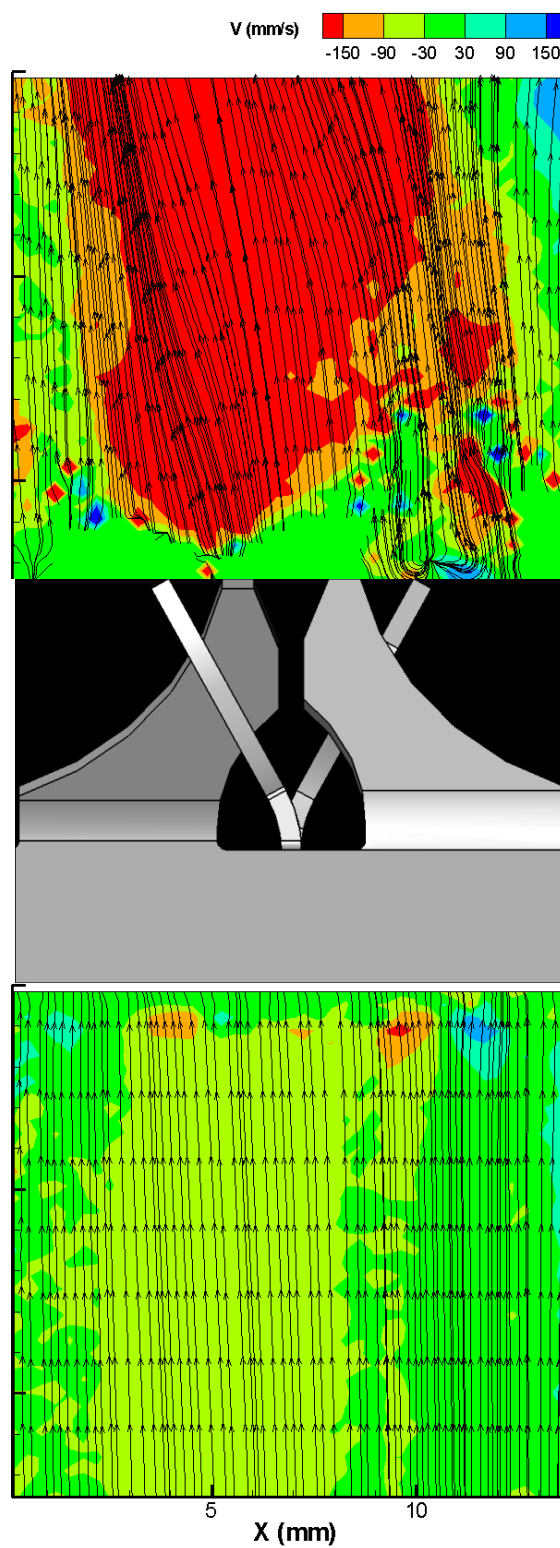


Figure C14. Normal average velocity before and after grid. Plane 5. $Re=16,300$

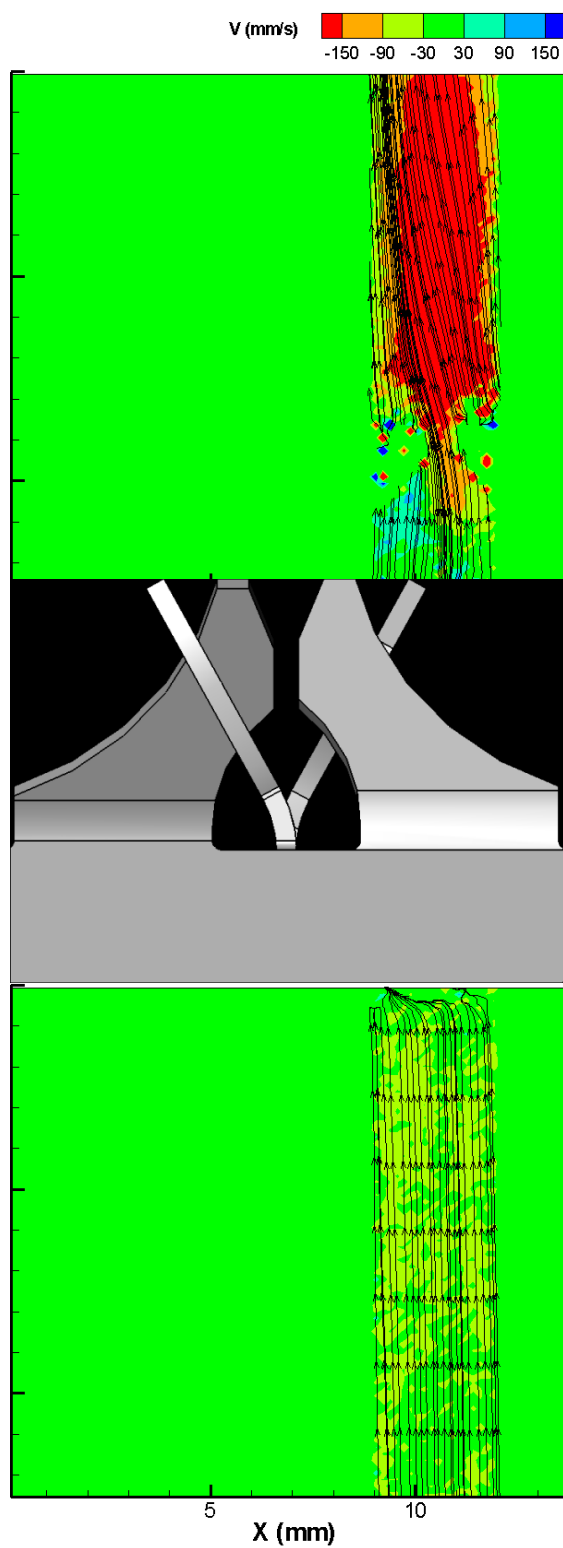


Figure C15. Normal average velocity before and after grid. Plane 6. $Re=16,300$

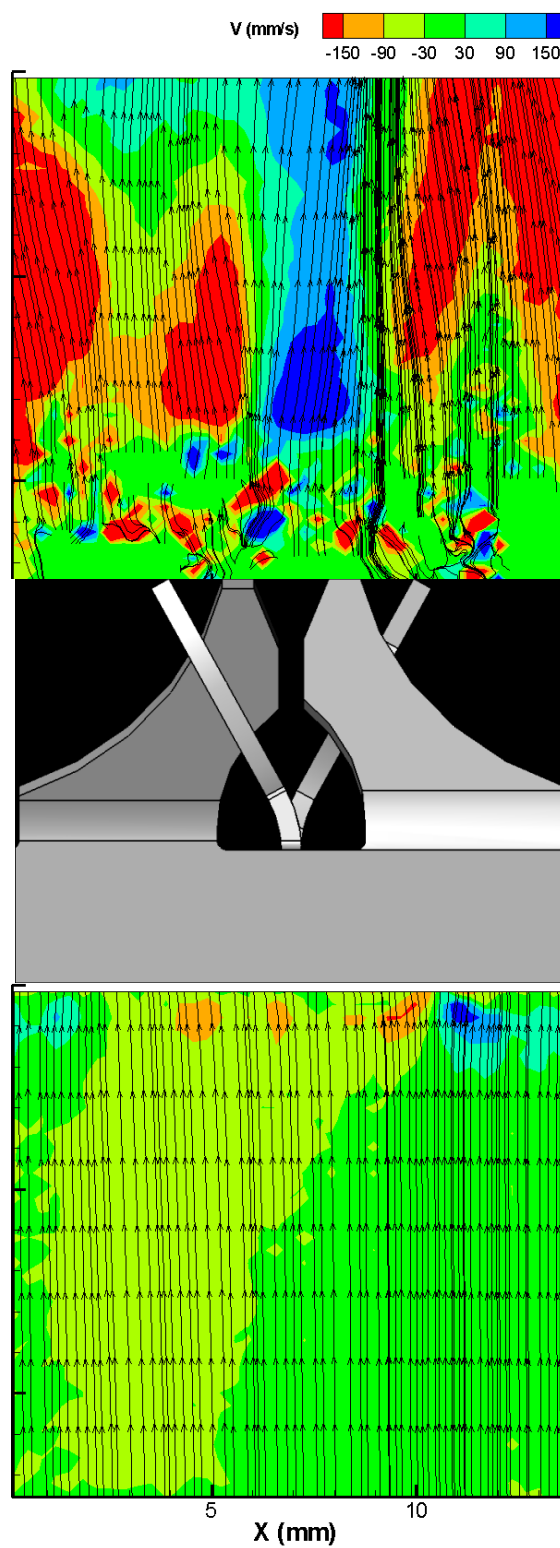


Figure C16. Normal average velocity before and after grid. Plane 7. $Re=16,300$

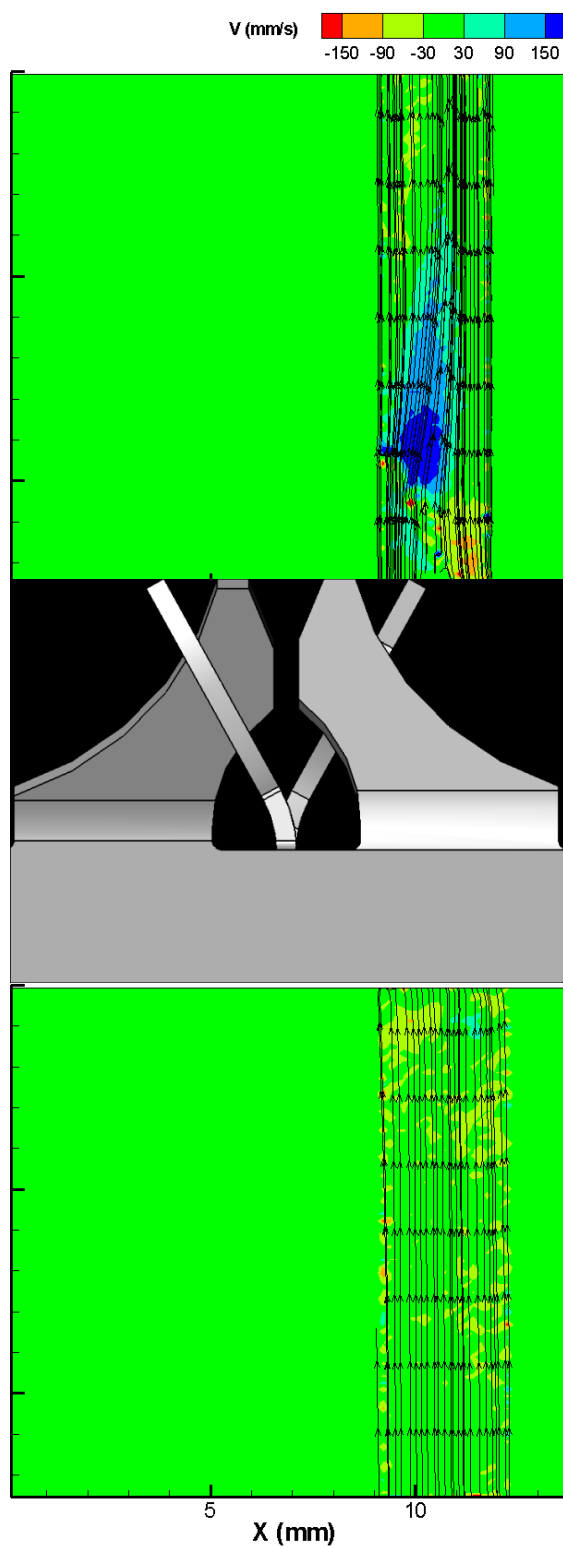


Figure C17. Normal average velocity before and after grid. Plane 8. $Re=16,300$

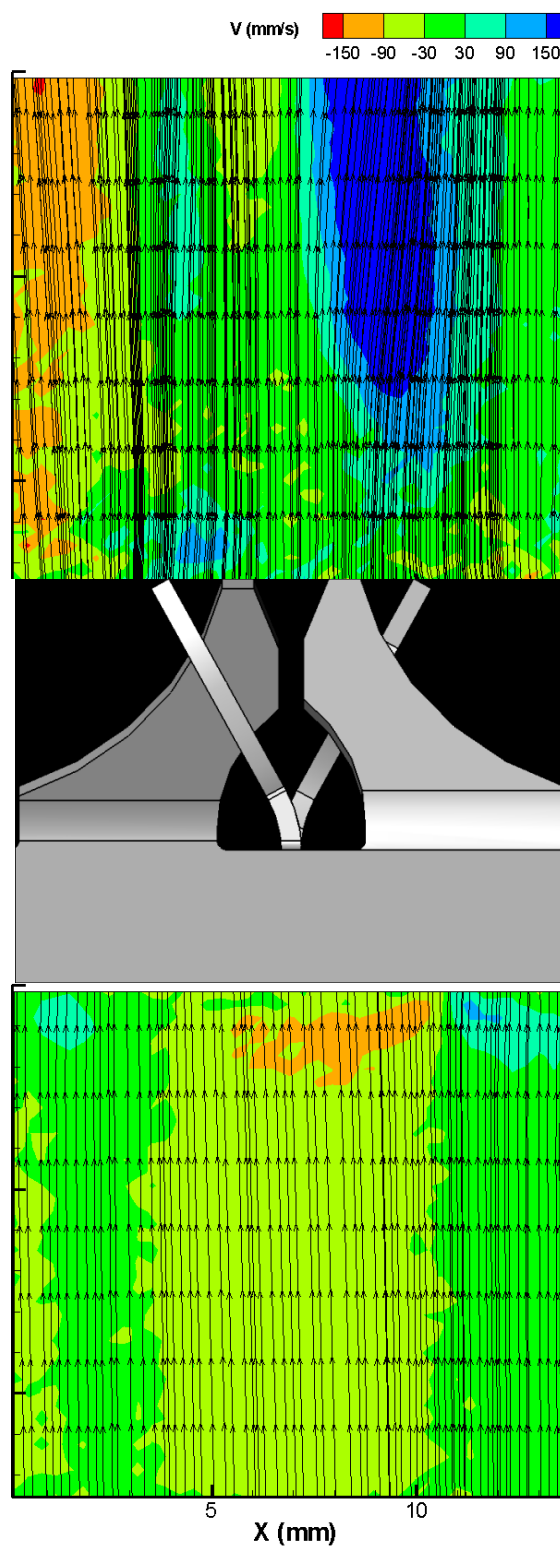


Figure C18. Normal average velocity before and after grid. Plane 9. $Re=16,300$

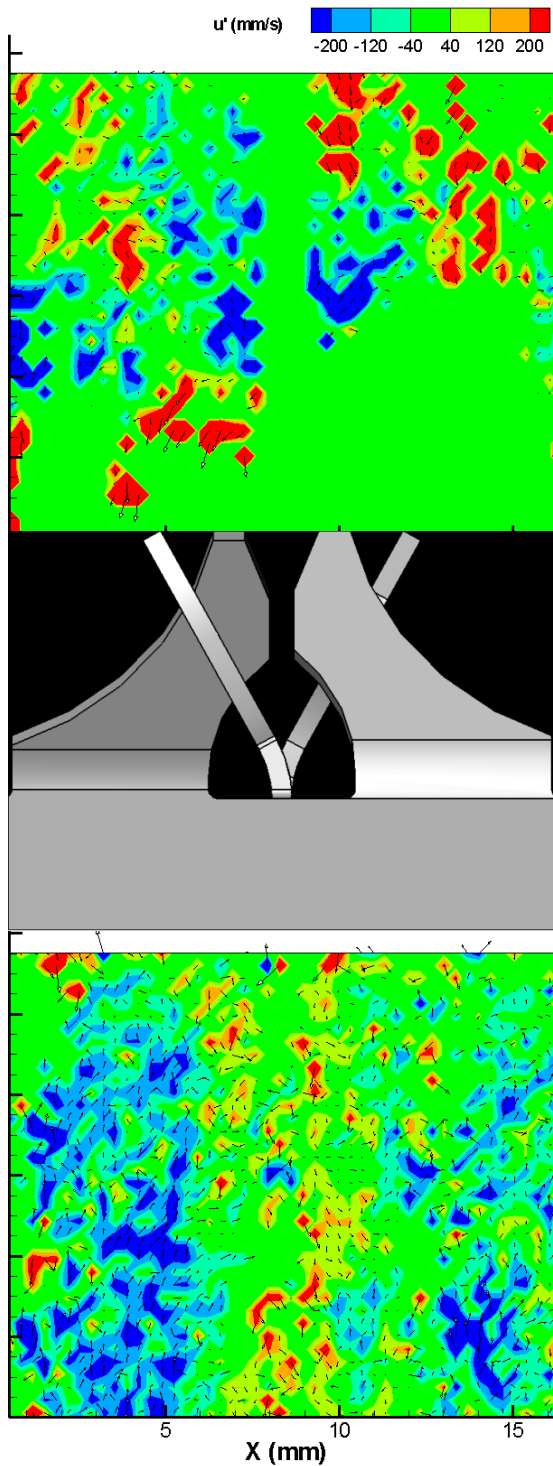


Figure C19. Streamwise velocity fluctuation before and after grid. Plane 1. $Re=16,300$

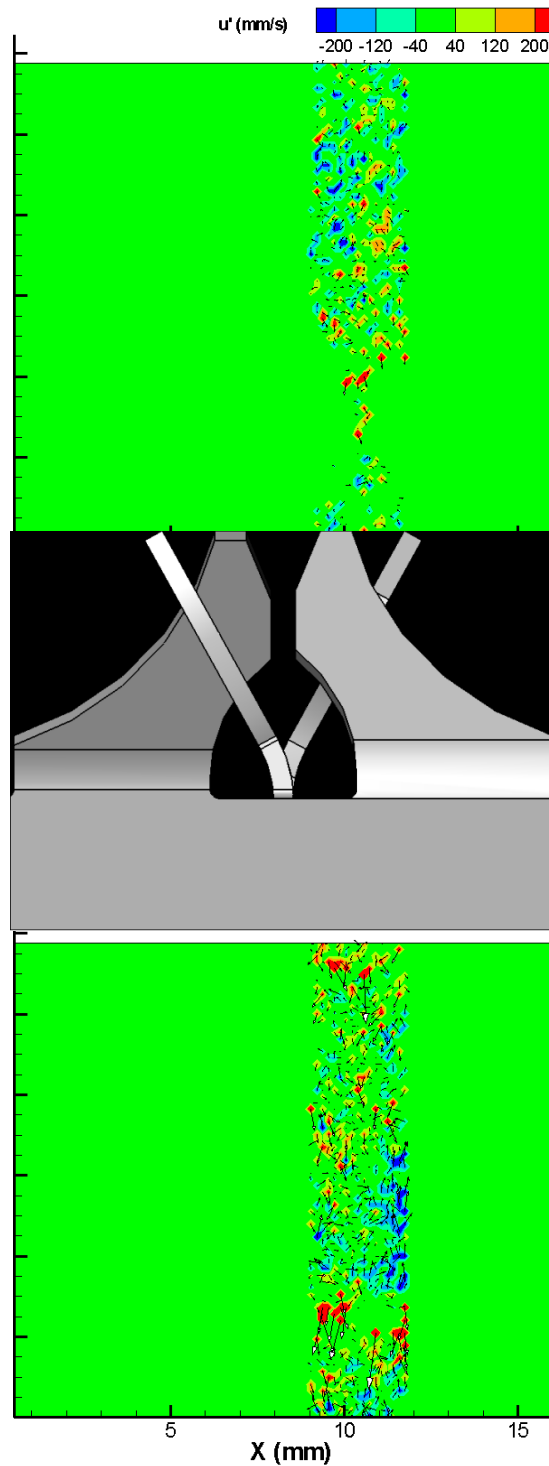


Figure C20. Streamwise velocity fluctuation before and after grid. Plane 2. $Re=16,300$

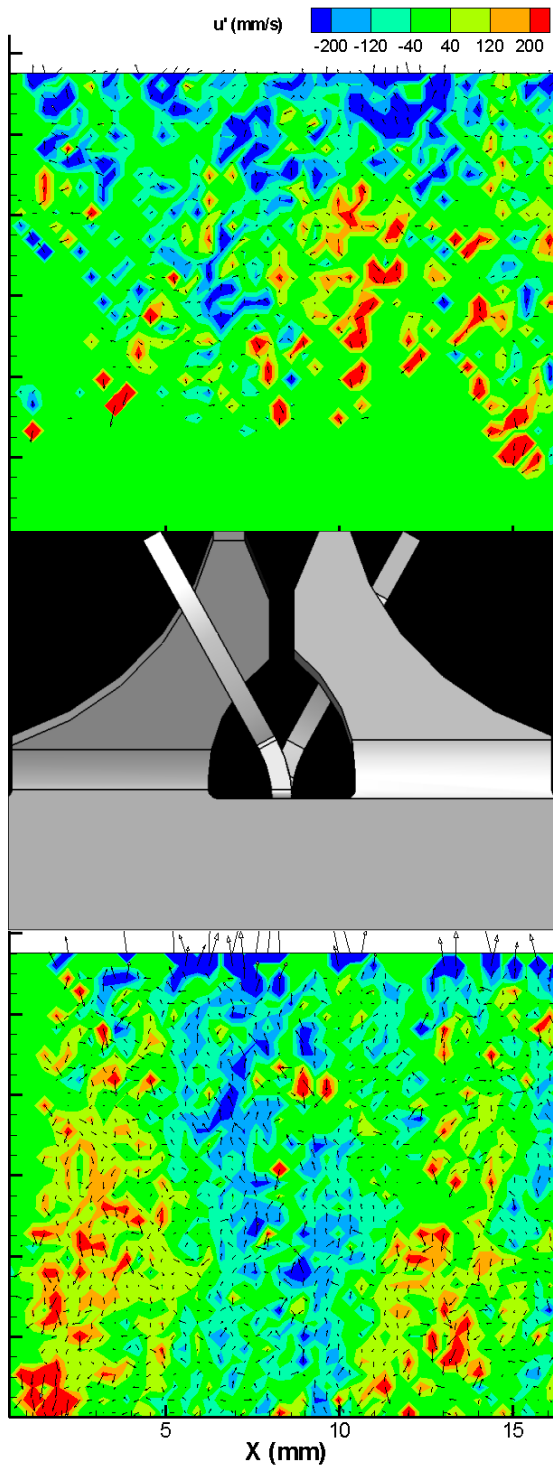


Figure C21. Streamwise velocity fluctuation before and after grid. Plane 3. $Re=16,300$

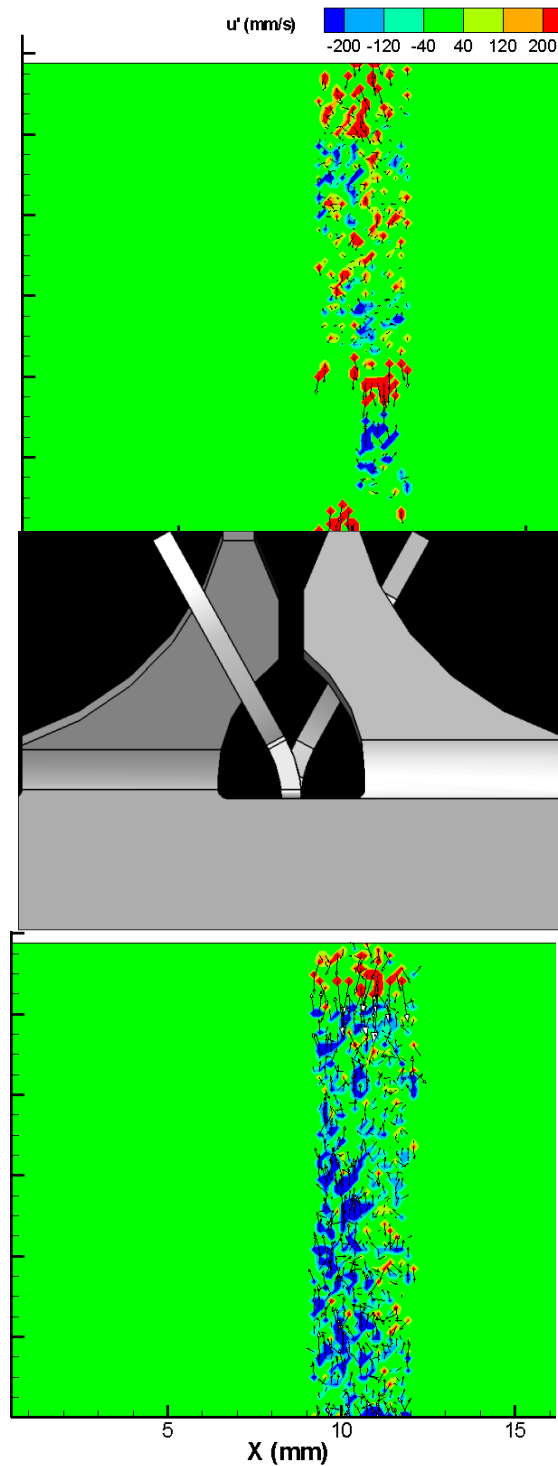


Figure C22. Streamwise velocity fluctuation before and after grid. Plane 4. $Re=16,300$

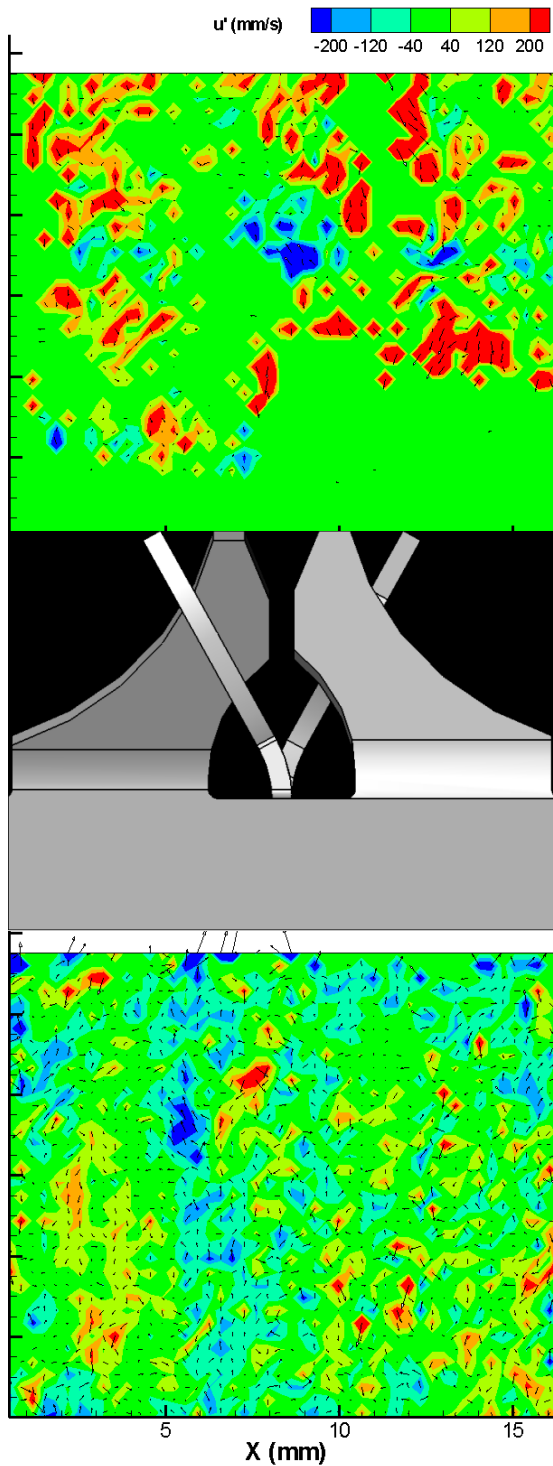


Figure C23. Streamwise velocity fluctuation before and after grid. Plane 5. $Re=16,300$

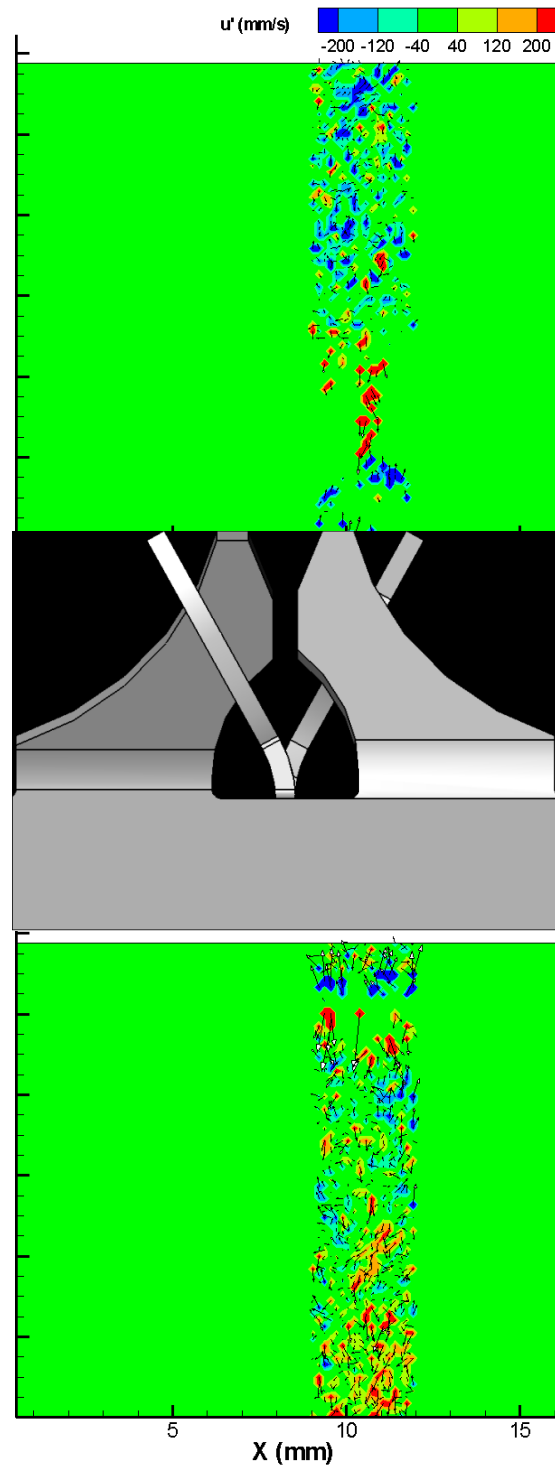


Figure C24. Streamwise velocity fluctuation before and after grid. Plane 6. $Re=16,300$

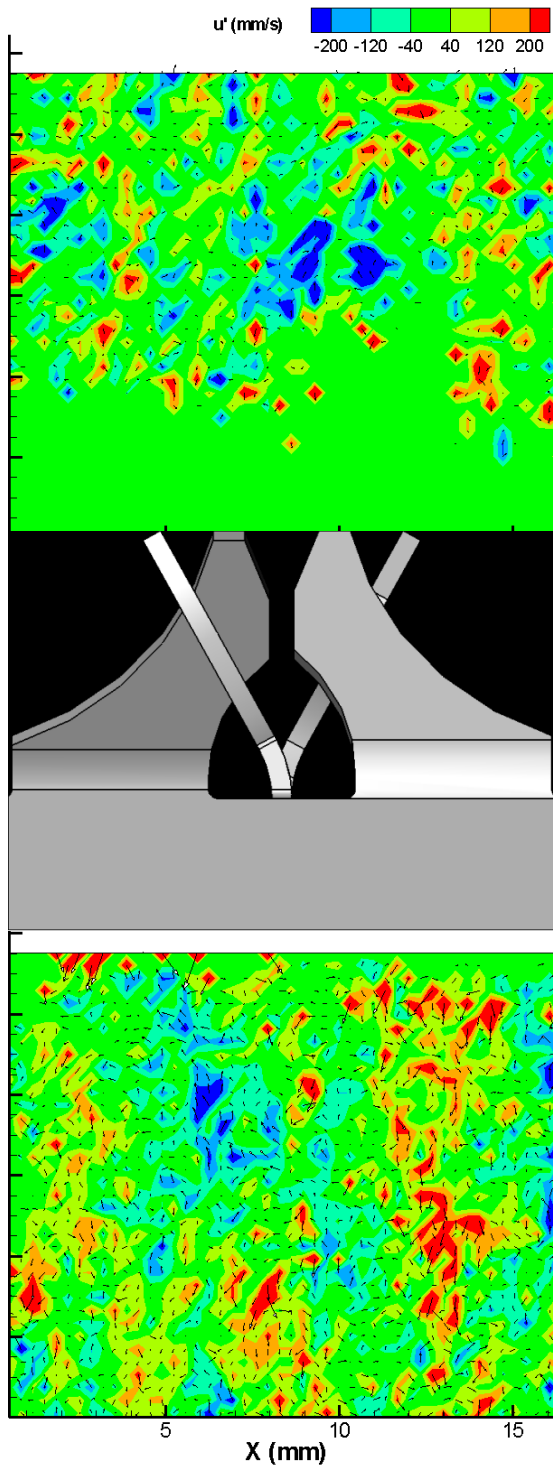


Figure C25. Streamwise velocity fluctuation before and after grid. Plane 7. $Re=16,300$

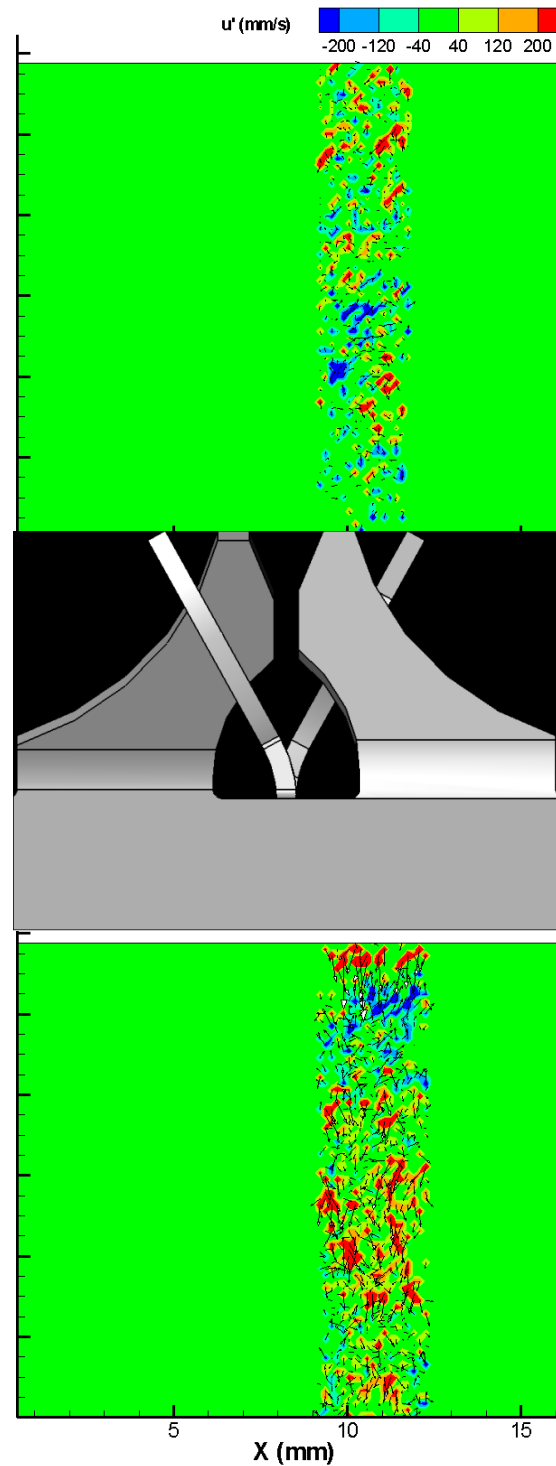


Figure C26. Streamwise velocity fluctuation before and after grid. Plane 8. $Re=16,300$

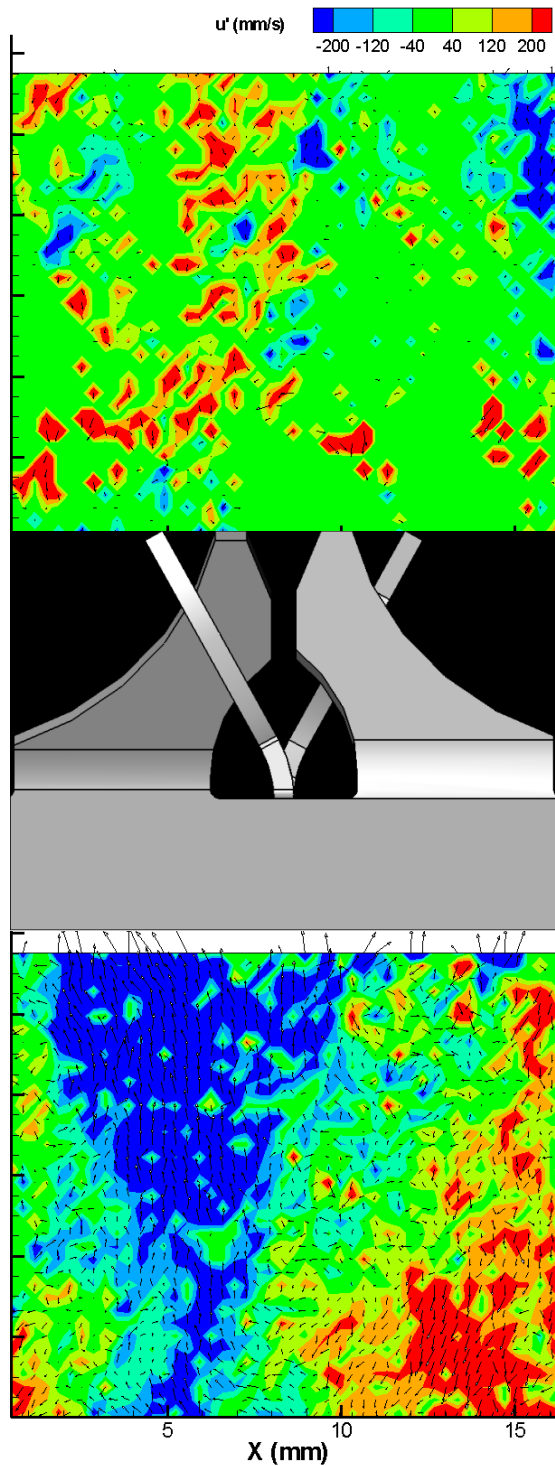


Figure C27. Streamwise velocity fluctuation before and after grid. Plane 9. $Re=16,300$

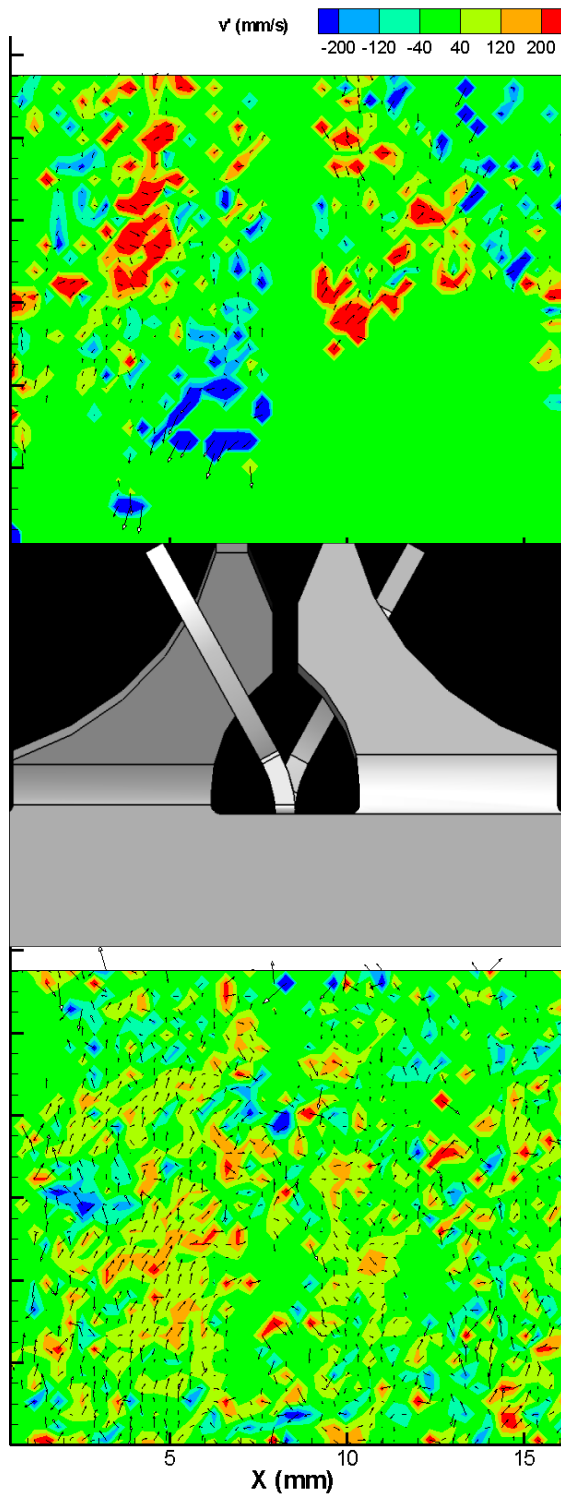


Figure C28. Normal velocity fluctuation before and after grid. Plane 1. $Re=16,300$

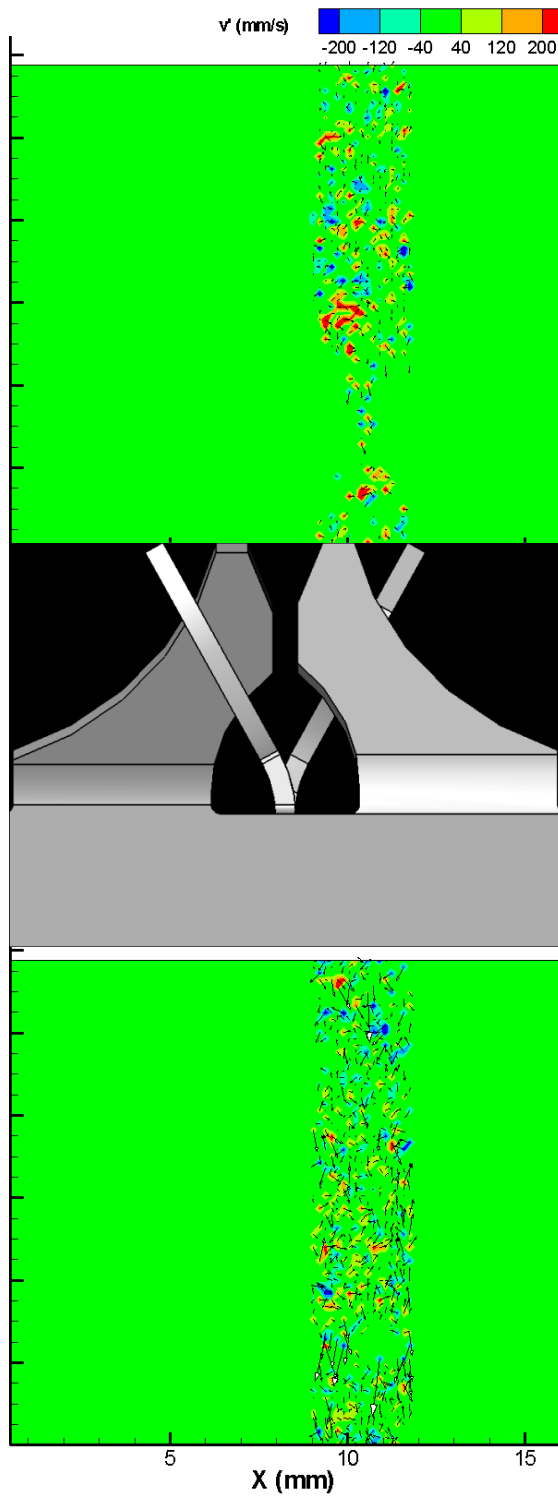


Figure C29. Normal velocity fluctuation before and after grid. Plane 2. $Re=16,300$

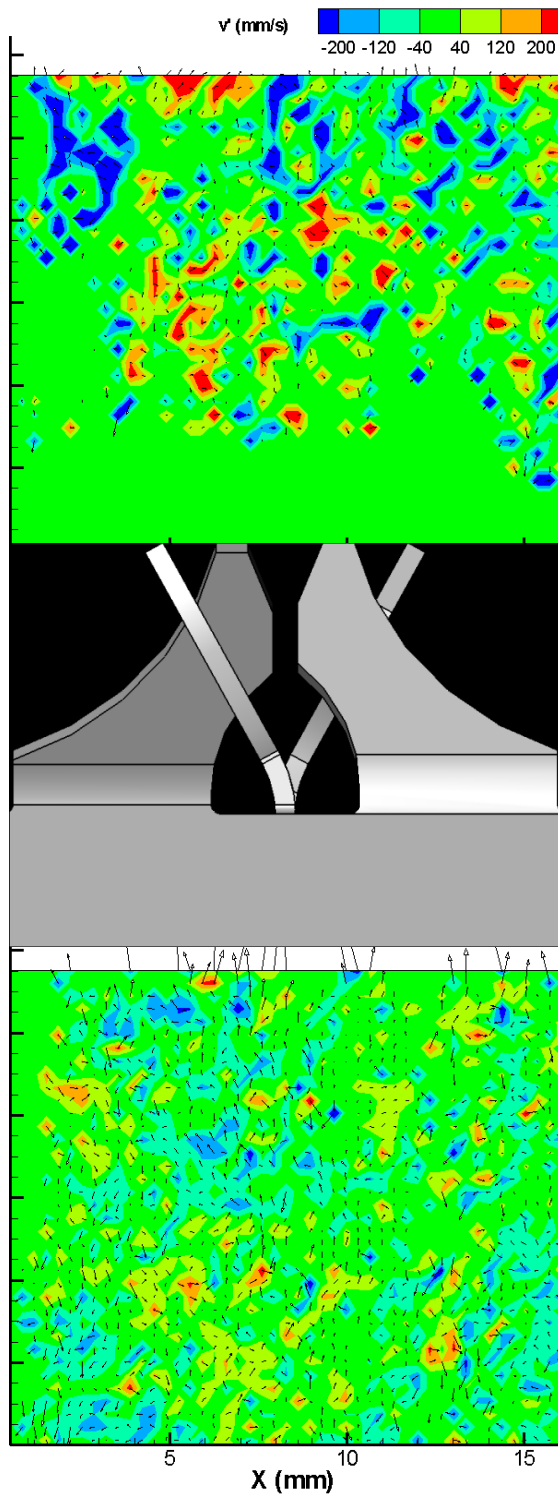


Figure C30. Normal velocity fluctuation before and after grid. Plane 3. $Re=16,300$

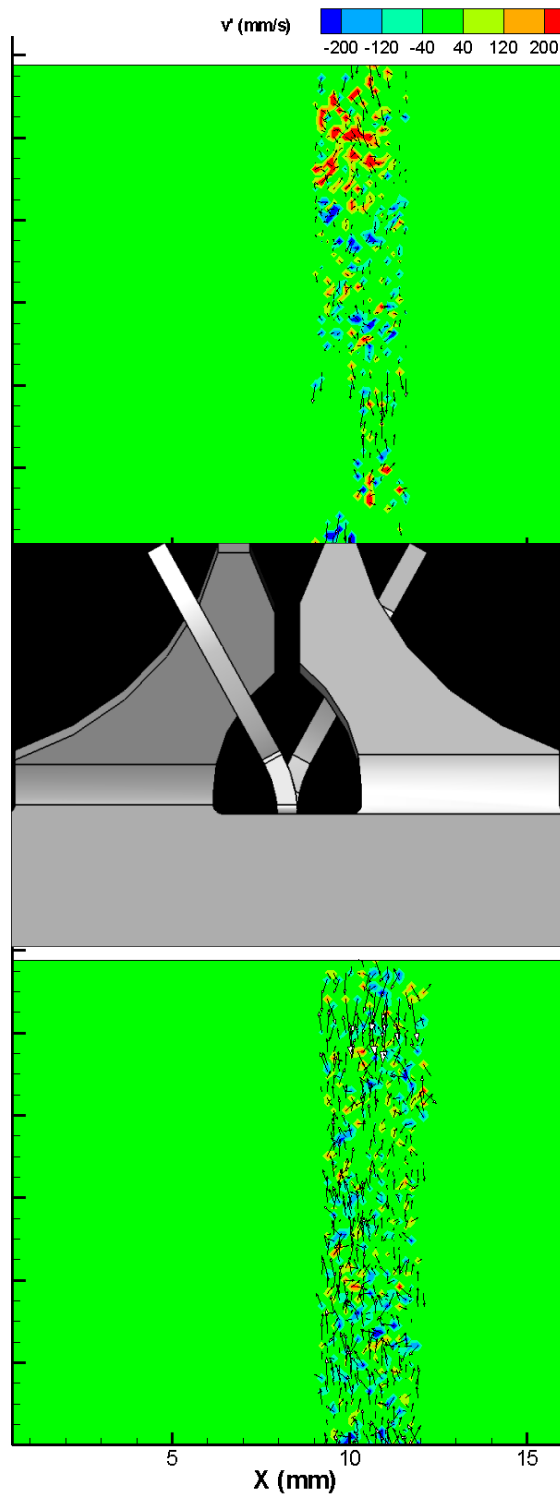


Figure C31. Normal velocity fluctuation before and after grid. Plane 4. $Re=16,300$

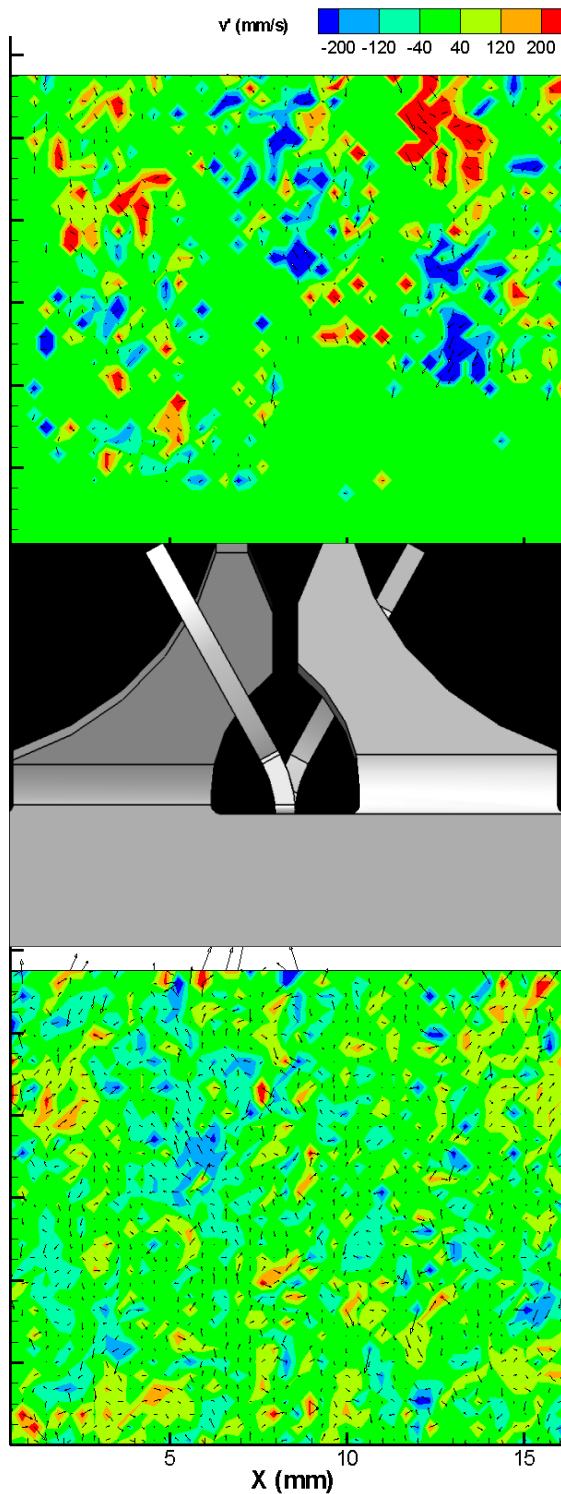


Figure C32. Normal velocity fluctuation before and after grid. Plane 5. $Re=16,300$

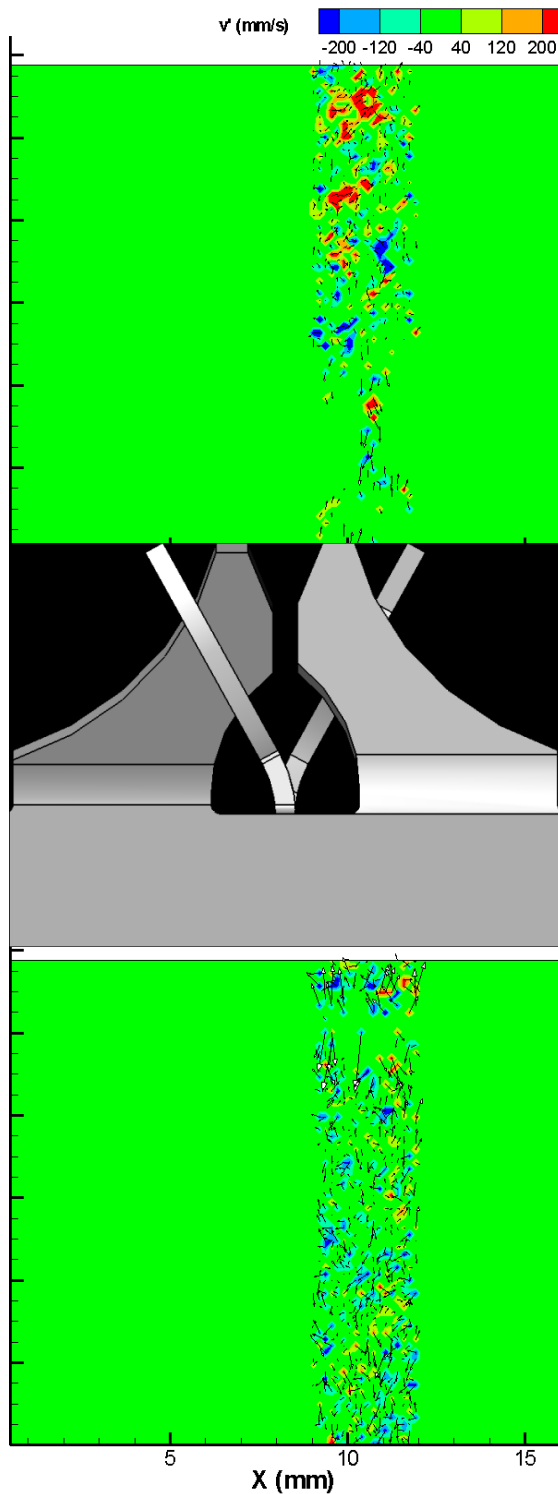


Figure C33. Normal velocity fluctuation before and after grid. Plane 6. $Re=16,300$

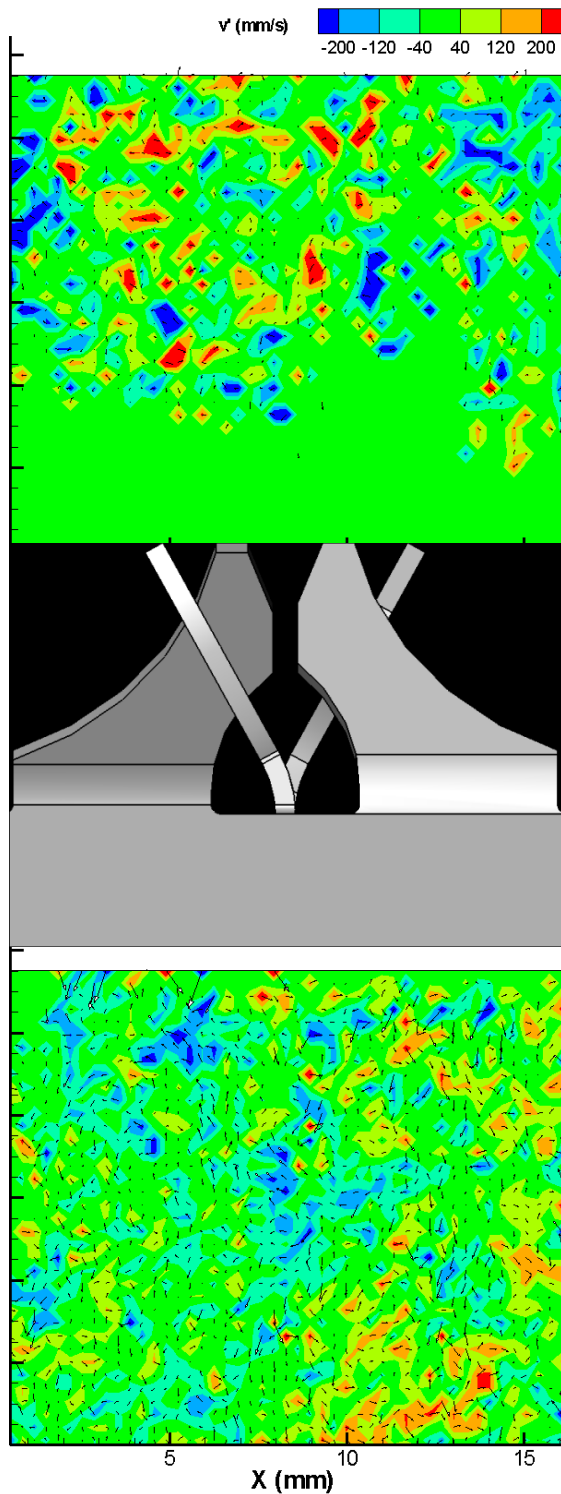


Figure C34. Normal velocity fluctuation before and after grid. Plane 7. $Re=16,300$

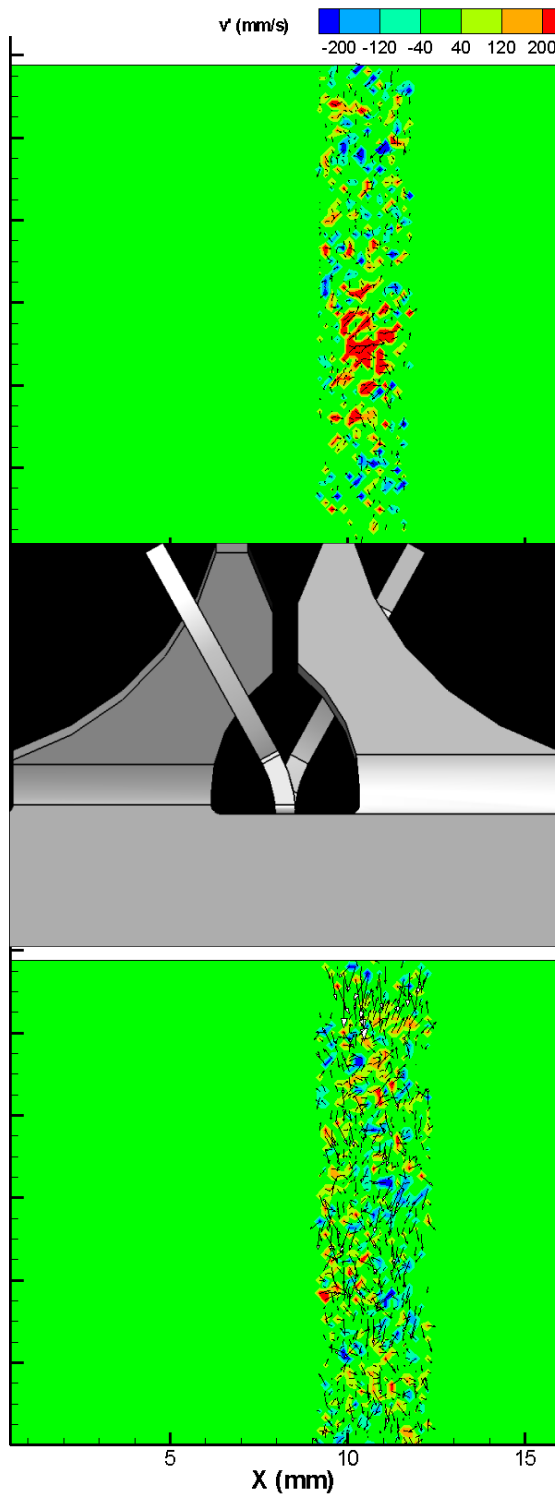


Figure C35. Normal velocity fluctuation before and after grid. Plane 8. $Re=16,300$

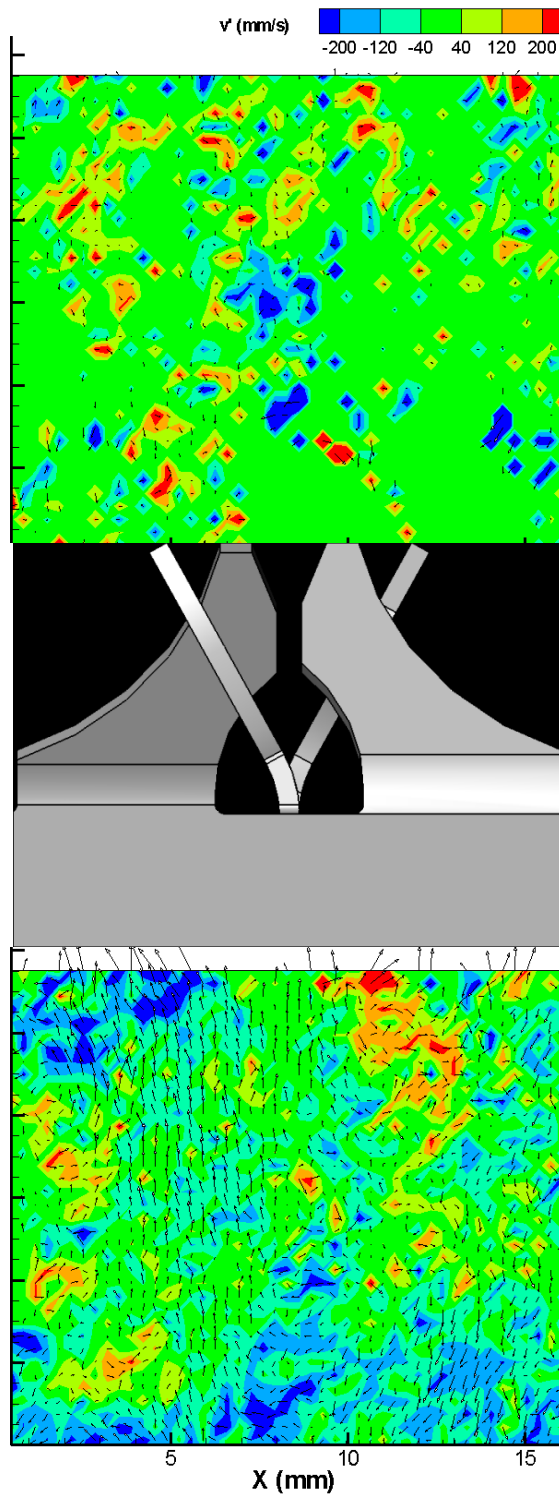


Figure C36. Normal velocity fluctuation before and after grid. Plane 9. $Re=16,300$

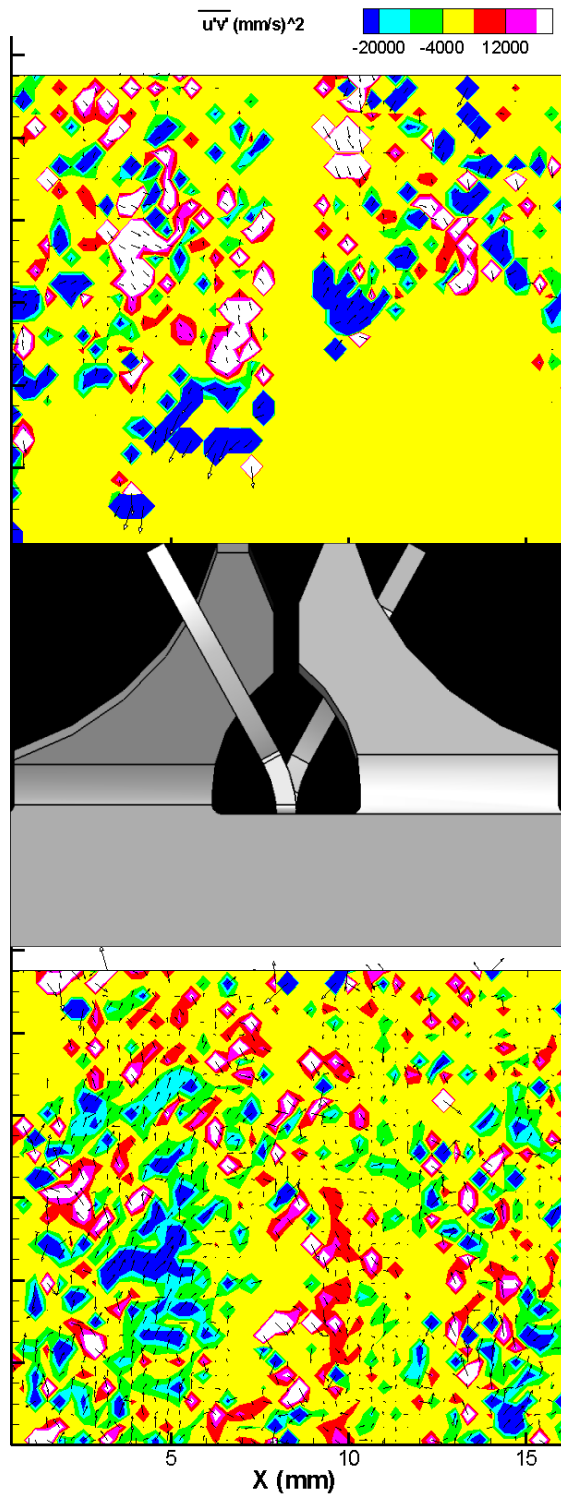


Figure C37. Reynolds stress before and after grid. Plane 1. $Re=16,300$

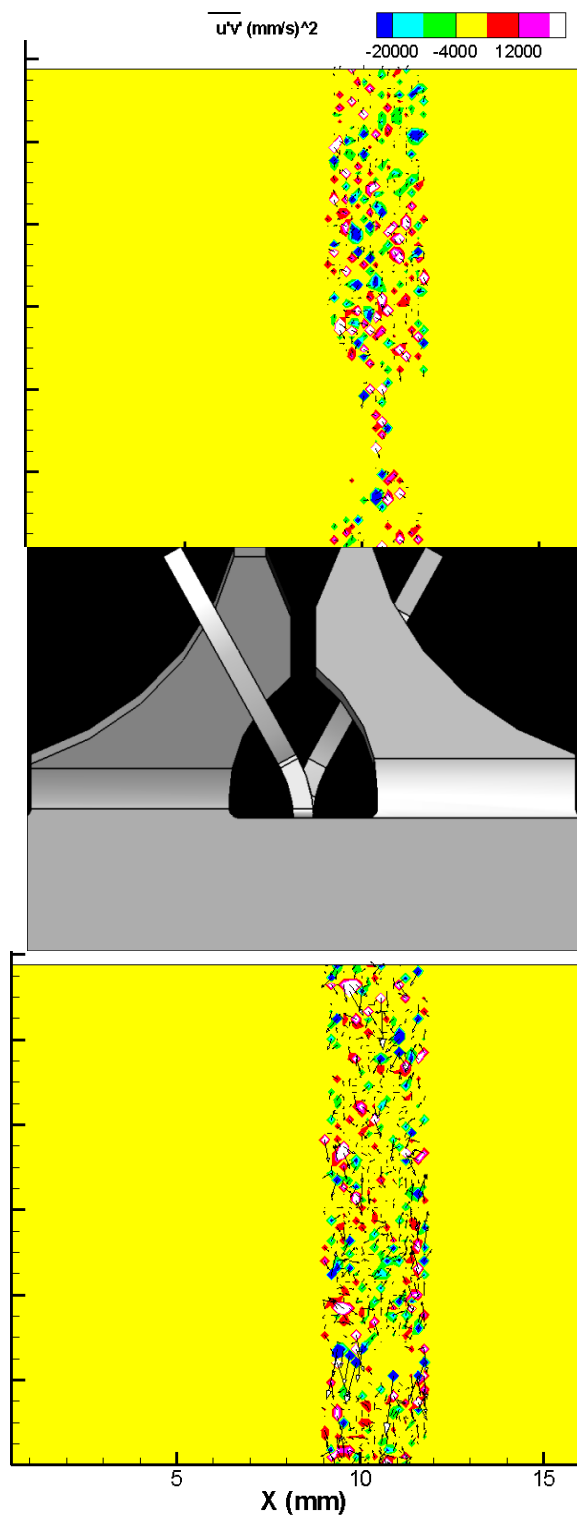


Figure C38. Reynolds stress before and after grid. Plane 2. $Re=16,300$

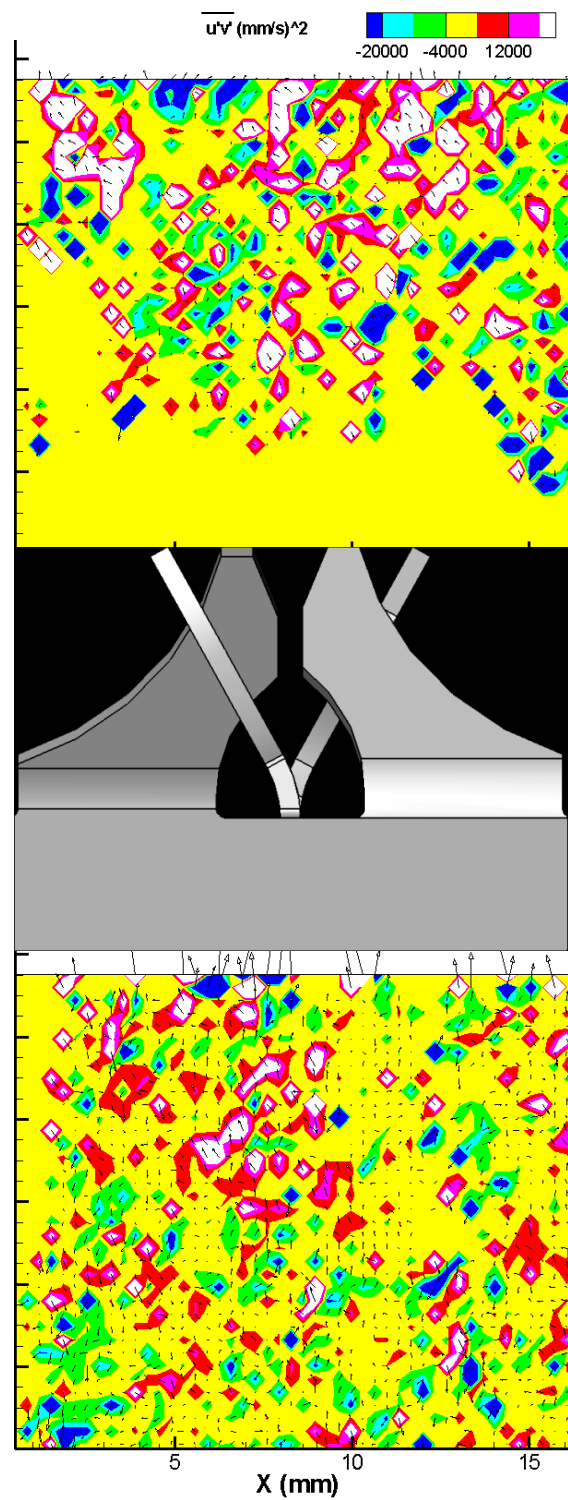


Figure C39. Reynolds stress before and after grid. Plane 3. $Re=16,300$

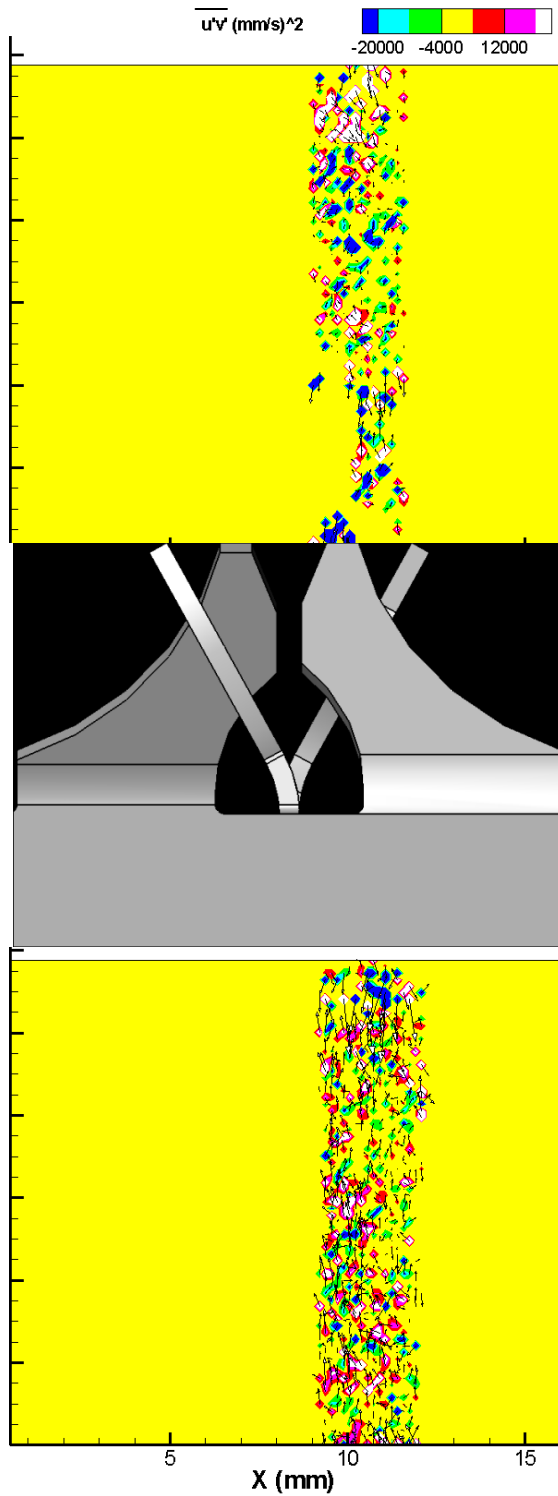


Figure C40. Reynolds stress before and after grid. Plane 4. $Re=16,300$

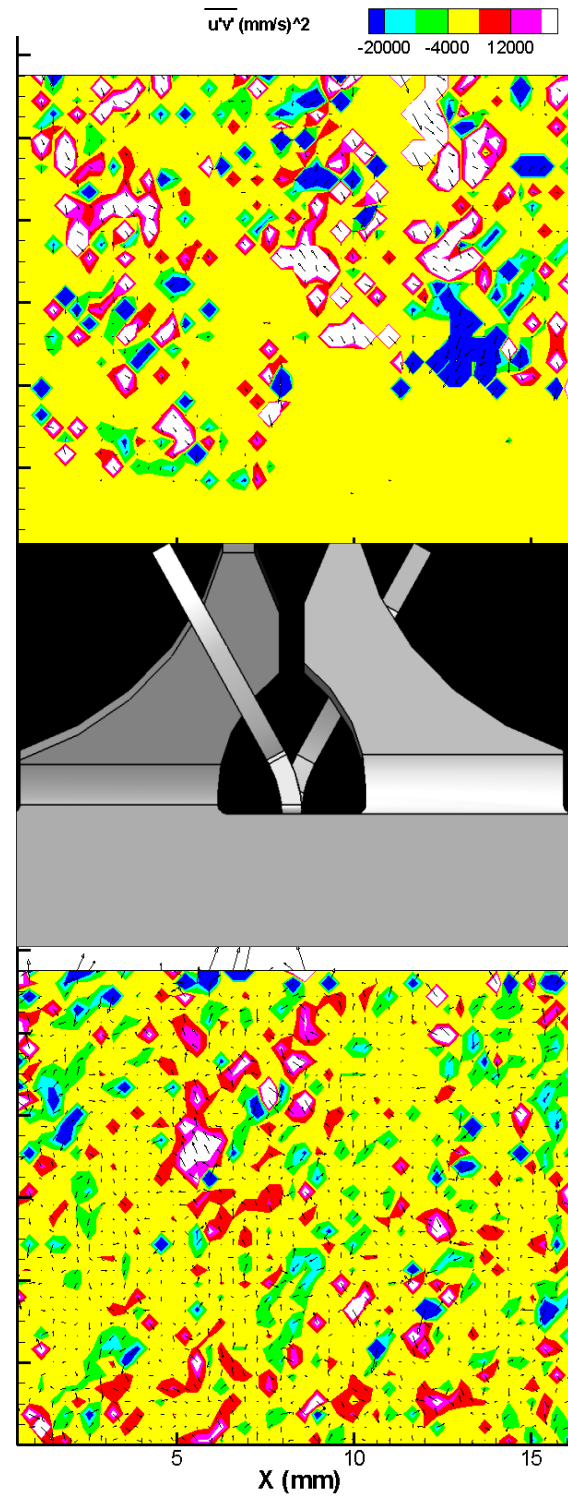


Figure C41. Reynolds stress before and after grid. Plane 5. $Re=16,300$

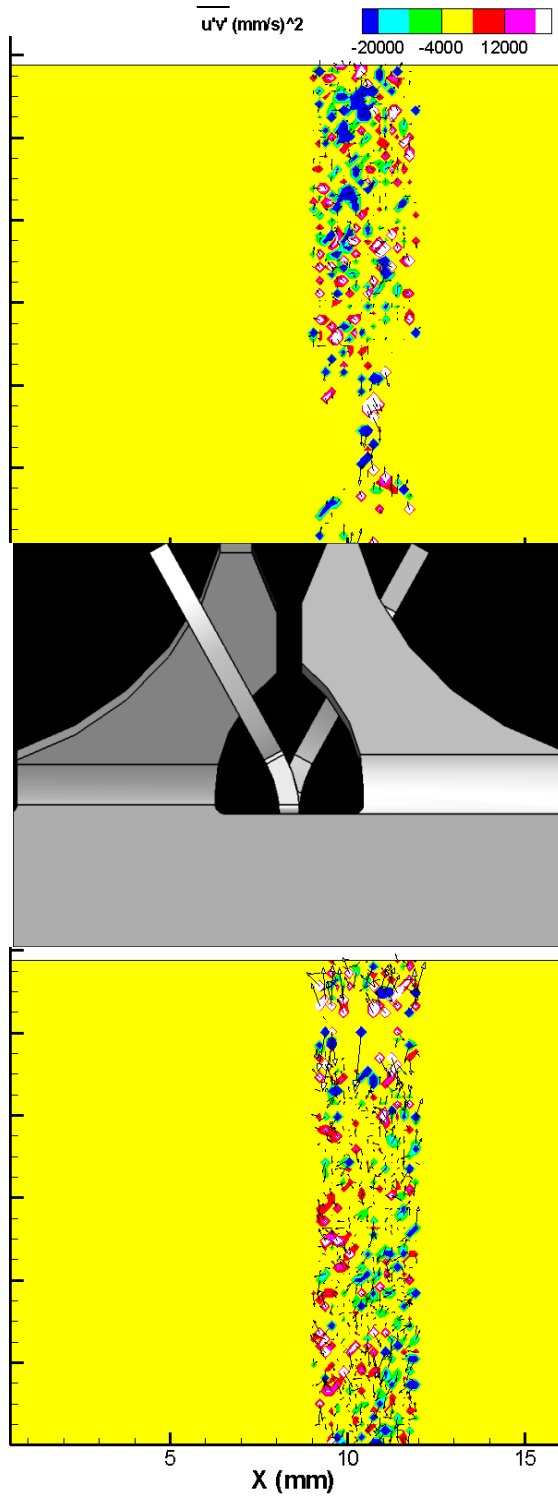


Figure C42. Reynolds stress before and after grid. Plane 6. $Re=16,300$

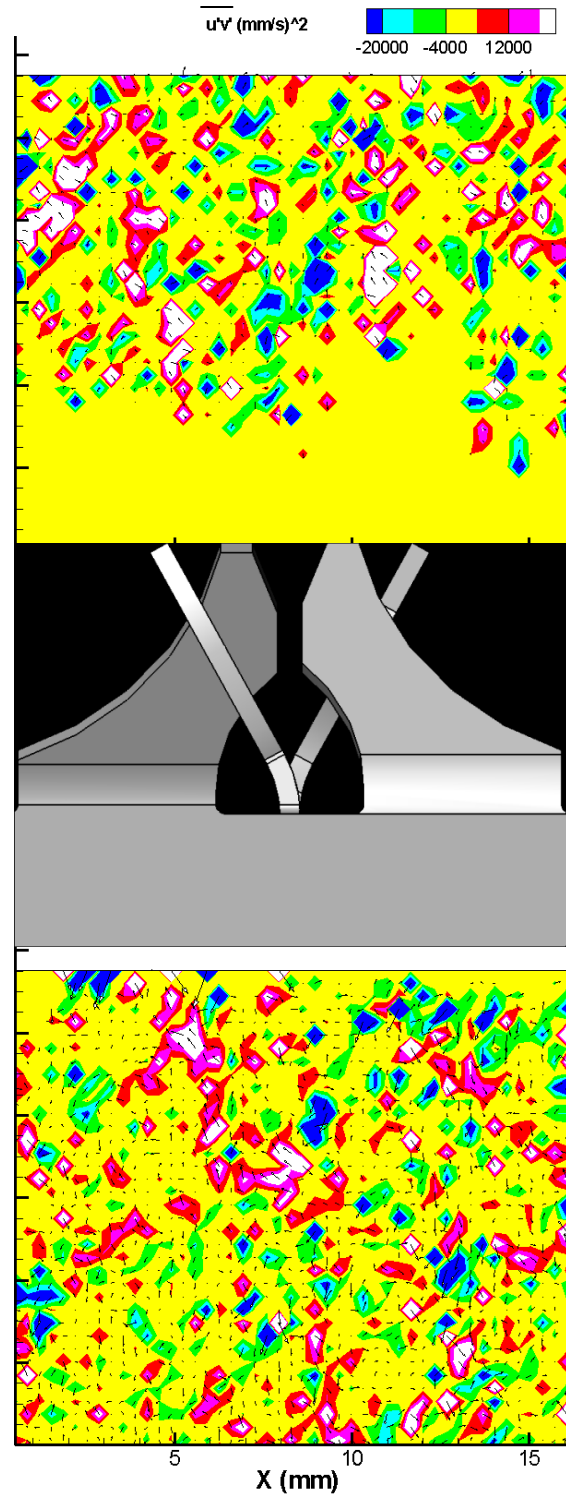


Figure C43. Reynolds stress before and after grid. Plane 7. $Re=16,300$

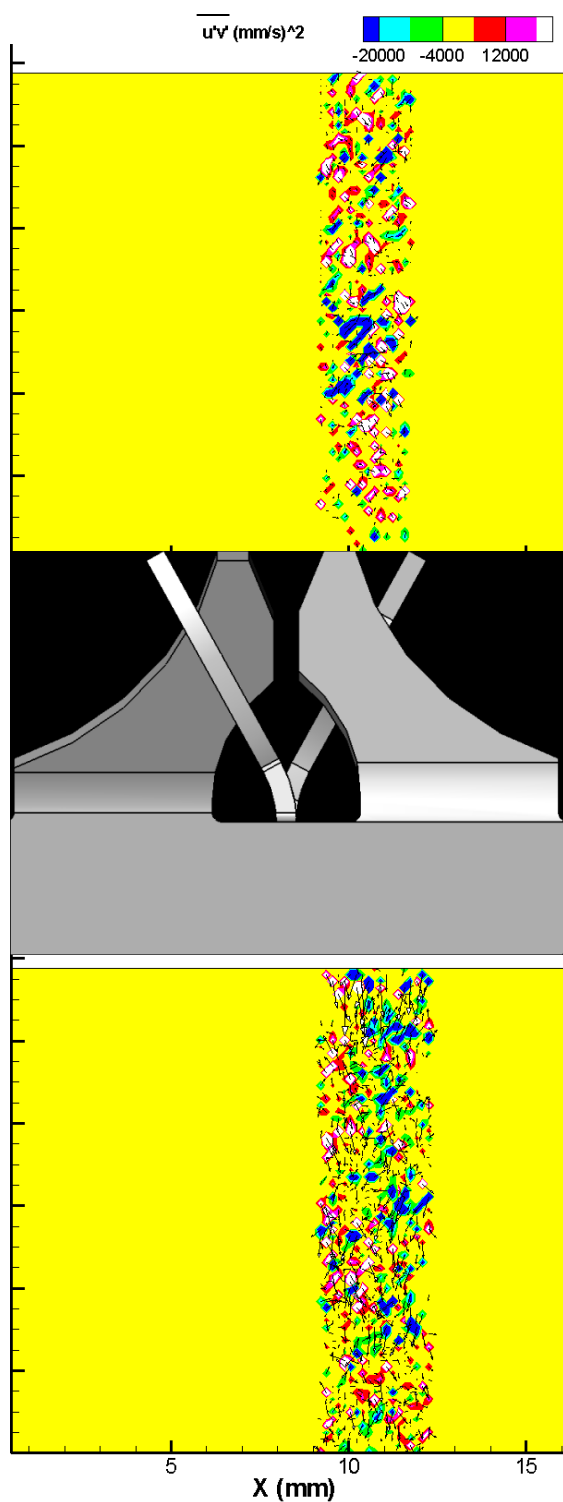


Figure C44. Reynolds stress before and after grid. Plane 8. $Re=16,300$

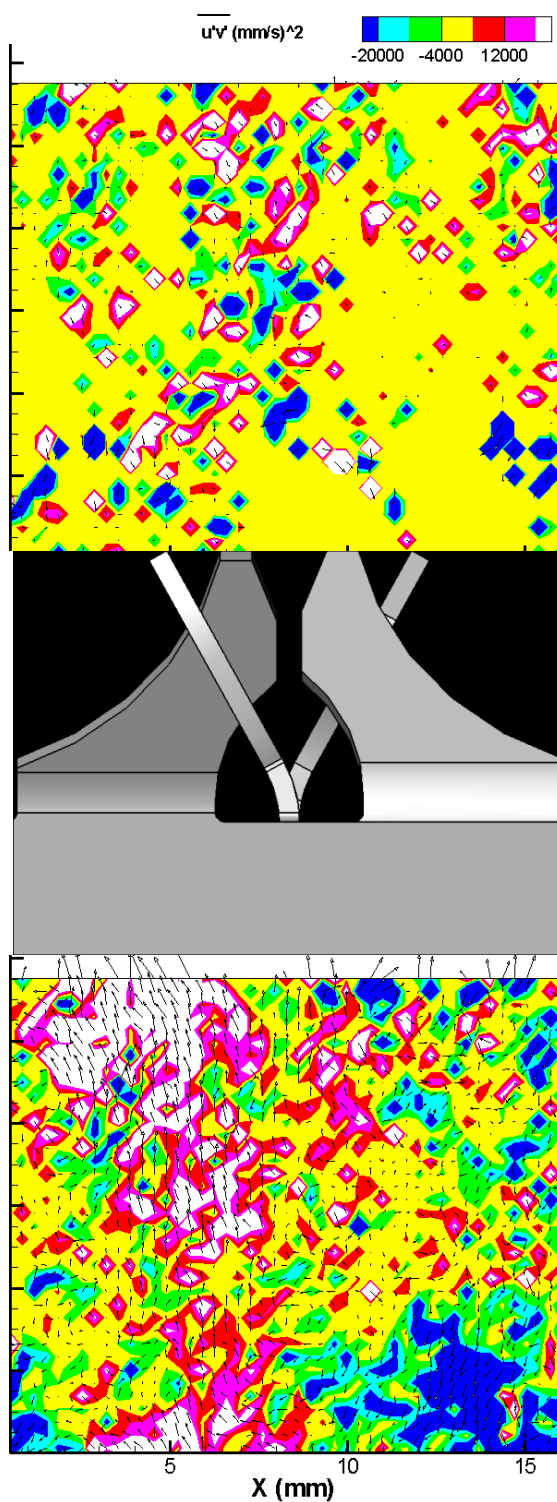


Figure C45. Reynolds stress before and after grid. Plane 9. $Re=16,300$

VITA

Elvis Efren Dominguez Ontiveros was born in Mexico. He received a Bachelor of Science in electrical engineering from Instituto Politecnico Nacional (IPN), Mexico City, Mexico in December 2000.

He received a Master of Science in Nuclear Engineering from Texas A&M University in August 2004. He joined the doctoral program in Mechanical Engineering at Texas A&M University under the direction of Dr. Yassin A. Hassan. He graduated in May 2010 with his Ph.D. His research interests include two-phase flow, heat transfer, fluid mechanics, thermal hydraulics of nuclear reactor, measuring techniques. He can be reached or contacted at 129 Zachary building, College Station, Texas, 77843-3133, elvisdom@yahoo.com.